Visualizing bacterial protein organization at the nanoscale using DNA-PAINT super-resolution microscopy

Dissertation der Fakultät für Biologie

der Ludwig-Maximilians-Universität München

vorgelegt von

Kimberly Alison Cramer

aus Savannah, Georgia, Vereinigte Staaten von Amerika

am 27. Mai 2024

München

Erstgutachter: Prof. Dr. Ralf Jungmann
Zweitegutachter: Prof Dr. Heinrich Leonhardt

Tag der Abgabe: 27.05.2024
Tag der mündlichen Prüfung: 03.12.2024

Eidesstattliche Erklärung

Ich versichere hiermit an Eides statt, dass die vorgelegte Dissertation von mir selbständig und ohne unerlaubte Hilfe angefertigt ist.

München, den 27.05.2024 Kimberly Alison Cramer

Erklärung

Hiermit erkläre ich

dass die Dissertation nicht ganz oder in wesentlichen Teilen einer anderen Prüfungskommission vorgelegt worden ist.

dass ich mich anderweitig einer Doktorprüfung ohne Erfolg nicht unterzogen habe.

dass ich ohne Erfolg versucht habe, eine Dissertation einzureichen oder mich der Doktorprüfung zu unterziehen.

München, den 27.05.2024 Kimberly Alison Cramer

Table of Contents

Summary

Fluorescence microscopy has evolved to enable researchers to visualize cells and subcellular structures at unprecedented resolutions. The super-resolution microscopy methods STED, PALM, STORM, PAINT, and DNA-PAINT enable researchers to resolve targets at resolutions higher than the diffraction limit of light (~250 nm). Recently, one nanometer resolution of cellular proteins was achieved. DNA-PAINT is a fluorescence based super-resolution microscopy method that can readily achieve nanoscale resolutions in cells (<20 nm) and has spectrally unlimited multiplexing capabilities. Elucidating the organization and spatial arrangement of the biomolecules responsible for bacterial division will enable a comprehensive understanding of the division process. In spore-forming bacteria one of two modes of division can occur, vegetative division or sporulation. How and if division is performed differently dependent on division mode is unknown. Imaging of divisome components at the nanoscale remains relatively unexplored, particularly in sporulating cells. Comparing divisome architecture between division modes could reveal insights into fundamental mechanisms governing division in vegetative and sporulating cells and shed light on potential differences.

The first part of this thesis presents a methodology for visualizing bacterial proteins labeled with fluorescent protein tags and nanobody binders using STED super-resolution microscopy (Publication 1). Nanobody binders targeting the commonly used GFP or RFP tags were used to label DivIVA fusion proteins in *Bacillus subtilis*. Screening of anti-GFP and anti-RFP nanobody binders conjugated to different STED dyes identified optimal combinations for *B. subtilis* imaging in green and red spectrums.

In the second part, the nanoscale organization and distribution of divisome proteins FtsZ, SepF, DivIVA, and ZapA was compared between the vegetative and sporulating division modes of *Bacillus subtilis* (Publication 2) via multiplexed DNA-PAINT. The optimized intracellular bacterial protein labeling protocol from Publication 1 was used as a starting point for DNA-PAINT sample preparation. DNA-PAINT imaging revealed that the divisome is positioned differently within the division plane dependent on *B. subtilis* division mode. Specifically, vegetative cells positioned the divisome at the mid-septa while sporulating cells positioned the divisome towards their mother cell compartment. Quantitative analyses revealed protein content of FtsZ, DivIVA, SepF, and ZapA rings at division septa differed dependent on division mode. Additionally, SepF was revealed to form arc shaped assemblies at division septa *in cellulo.*

The third part of this thesis studied the role of the nanoscale distribution of fibronectin on the adhesion of the common pathogen *Staphylococcus aureus* (Publication 3). DNA-PAINT was used to calculate the density of Fibronectin binding protein (FnBP) receptors on bacteria and *in vitro* nanopattern experiments found the minimal circular fibronectin patch size necessary for bacterial

adhesion. This combined approach enabled calculation of the minimum number of FnBP receptors required for *S. aureus* attachment to fibronectin-coated surfaces.

List of Figures

List of Publications

This thesis discusses the following publications:

1. **Cramer K*,** Bolender AL*, Stockmar I, Jungmann R, Kasper R[#], and Shin JY[#].
   Visualization of Bacterial Protein Complexes Labeled with Fluorescent Proteins and Nanobody Binders for STED Microscopy.
   International Journal of Molecular Sciences. 2019. 20(14):3376

2. **Cramer K**, Reinhardt SCM, Auer A, Shin JY[#], and Jungmann R[#].
   Comparing Divisome Organization between Vegetative and Sporulating Bacillus subtilis at the Nanoscale using DNA-PAINT.
   Science Advances. 2024. 10:eadk5847

3. Khateb H, Sørensen R, **Cramer K**, Eklund A, Kjems J, Meyer R, Jungmann R, and Sutherland D.
   The Role of Nanoscale Distribution of Fibronectin in the Adhesion of Staphylococcus aureus Studied by Protein Patterning and DNA-PAINT.
   ACS Nano. 2022. 16(7)10392-10403

Further publications:

4. O'Neill AC, Uzbas F, Antognolli G, Merino F, Draganova K, Jäck A, Zhang S, Pedini G, Schessner JP, **Cramer K**, Schepers A, Metzger F, Esgleas M, Smialowski P, Guerrini R, Falk S, Feederle R, Freytag S, Wang Z, Bahlo M, Jungmann R, Bagni C, Borner GHH, Robertson SP, Hauck SM and M Götz M.
   Spatial Centrosome Proteome of Human Neural Cells Uncovers Disease-Relevant Heterogeneity. Science. 2022. 376(6599):eabf9088

* Co-first authors
# Co-corresponding authors

Declaration of contributions as a co-author

Publication 1: Visualization of Bacterial Protein Complexes Labeled with Fluorescent Proteins and Nanobody Binders for STED Microscopy

My contributions to this manuscript include the following: Methodology development with Jae Yen Shin, Iris Stockmar, and Robert Kasper. Microscopy sample preparation. Experimental investigations with Anna-Lena Bolender, Robert Kasper, Jae Yen Shin. Data analysis with Anna-Lena Bolender, Robert Kasper, Jae Yen Shin. Producing the original draft with Jae Yen Shin and Robert Kasper. Manuscript review and editing with all authors.

Publication 2: Comparing Divisome Organization Between Vegetative and Sporulating Bacillus subtilis at the Nanoscale using DNA-PAINT

My contributions to this manuscript include the following: Conceiving and performing experiments. Analyzing and interpreting data. Producing the original draft with Ralf Jungmann. Manuscript editing and review with all authors.

Publication 3: The Role of Nanoscale Distribution of Fibronectin in the Adhesion of Staphylococcus aureus Studied by Protein Patterning and DNA-PAINT

My contributions to this manuscript include the following: DNA-PAINT image acquisition with Heba Kateb, Alexandra Eklund and Rasmus Sorensen. Manuscript editing and review with all authors.

A description of the contributions of all co-authors can be found in the respective publications (Results).

Supervisor Signature

Prof. Dr. Ralf Jungmann

Abbreviations

bp	Base pair
CLEM	Correlative light and electron microscopy
cryo-FIB-ET	Cryogenic focused-ion-beam milling electron tomography
DNA	Deoxyribonucleic acid
DNA-PAINT	DNA points accumulation for imaging in nanoscale topography
dSTORM	Direct stochastic optical reconstruction microscopy
ECM	Extracellular matrix proteins
Em.	Emission
Epi	Epifluorescence
Ex.	Excitation
Fn	Fibronectin
FP	Fluorescent protein
FnBP	Fibronectin binding protein
GFP	Green fluorescent protein
HILO	Highly inclined and laminated optical sheet
IM	Inner membrane
LED	Light emitting diode
LPS	Lipopolysaccharides
min	Minute
MINFLUX	Minimal photon fluxes
MSCRAMM	Microbial surface component recognizing adhesive matrix molecule
NB	Nanobody
NBS	Noc-binding sites
nt	Nucleotide
NO	Nucleoid occlusion
OM	Outer membrane
PA-FP	Photoactivatable fluorescent protein
PAINT	Point accumulation for imaging in nanoscale topography
PALM	Photo-activated localization microscopy
PBS	Phosphate-buffered saline
PBPs	Penicillin binding proteins
POC	Proof-of-concept

PSF	Point spread function
RFP	Red fluorescent protein
SIM	Structured illumination microscopy
SMLM	Single molecule localization microscopy
SNR	Signal-to-noise ratio
SRM	Super-resolution microscopy
STED	Stimulated emission depletion
STORM	Stochastic optical reconstruction microscopy
TIRF	Total internal reflection fluorescence
qPAINT	Quantitative DNA-PAINT
ZBPs	Z-ring binding proteins
Z-ring	FtsZ ring

Introduction

1.1 Fluorescence

Fluorescence microscopy is an essential tool that is extensively used in life sciences to study molecules of interest within cells. It has enabled researchers to visualize target assemblies, map cellular trafficking, and characterize target distribution and molecular mechanisms of action within the cellular context. The principle of fluorescence is key to understanding how target molecules can be visualized under the microscope.

Fluorescence is the rapid relaxation of an excited molecule to a lower energy state by emitting a photon. The Jablonski diagram depicts the most common ways fluorescence occurs (Fig. 1) [1]. Molecules can exist in ground, first, or second electronic state and each state has several vibrational energy levels. When a laser or light source is first switched on and directed to the sample, electrons of a fluorophore absorb light energy (hv_A) and are excited from their ground state (S_0) to a higher energy level or excited singlet state (S_1 or S_2). Vibrational relaxation occurs when an electron at an energy level higher than S_1 relaxes to level S_1. Excited electrons at energy level S_1 can release the energy gained as photons and move from their higher energy level to the original ground state [2]. The emitted photon (hv_F) has less energy and a longer wavelength of light than the absorbed photon, a phenomenon referred to as Stokes Shift [3], which can place the emitted light from the photon in the visible spectrum of light. Fluorescence microscopy relies on the Stokes Shift principle to separate excitation light from emission light. Alternatively, intersystem crossing can occur, in which electrons at a higher energy level (S_1) transition into a triplet or dark state (T_1) and fail to emit photons upon returning to the ground state (S_0). Intersystem crossing is undesirable because it prevents or hinders target detection. The quantum yield of a molecule refers to the efficiency of a molecule in converting photons into fluorescence events and higher quantum yields indicate increased efficiency.

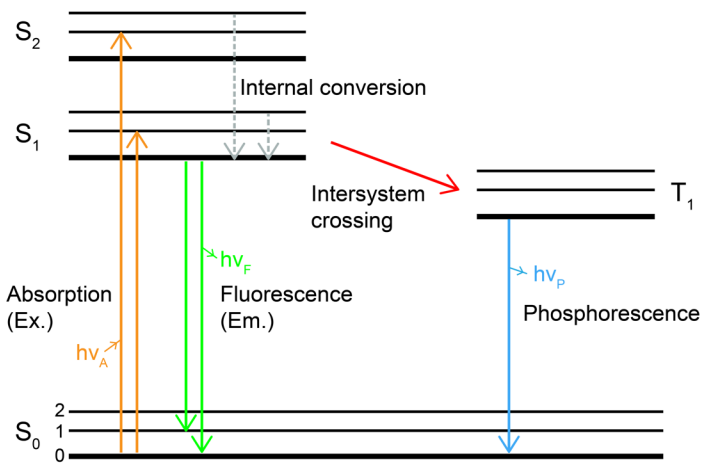

Figure 1.1. Jablonski diagram of fluorescence. A fluorophore can exist in a ground state (S_0), excited singlet states (S_1 or S_2), or excited triplet state (T_1). Each has a number of vibrational energy levels. Orange: When an electron absorbs light (hv_A), it goes from a ground state S_0 to an excited singlet state S_1 or S_2. Grey: Molecules excited to a higher excited singlet state undergo internal conversion and relax to S_1. Green: Fluorescence occurs when photons emit from S_1 to S_0. Red: Alternatively, an electron enters a triplet state (T_1) during intersystem crossing. Blue: Once at T_1, no fluorescence occurs, but the electron can emit a photon (hv_P) during phosphorescence, which returns it to the ground state S_0. Ex., Excitation. Em., Emission.

To visualize a cellular target with a fluorescence microscope, researchers must attach a fluorescence emitter to the target they want to visualize. The attached fluorescence emitter is typically a fluorophore, a molecule which becomes fluorescent upon activation with specific wavelengths of light. When investigating biological systems, targets can be visualized by direct or indirect labeling.

For direct labeling, fluorescent proteins (FPs) are fused to the target of interest via genetic engineering. In 1962, the first fluorescent protein, green fluorescent protein (GFP), was discovered in the jellyfish *Aequorea Victoria* [4]. In 2008 the Nobel Prize in Chemistry went to Tsien, Shimomura, and Chalfie for their discovery and development of GFP for a variety of applications, including microscopy. Since GFP, tens of other FPs have been discovered that emit fluorescence in different spectrums and have been engineered for various microscopy applications [5]. A more recent innovation in direct labeling approaches is genetic code expansion, in which dye-labeled unnatural amino acids are incorporated into the protein of interest *in vivo* [6].

In indirect target labeling, labeling probes with high affinities for the target molecule are used for selective identification of targets. A commonly used affinity protein is an antibody binder. Antibodies are proteins produced by the animal and human immune systems after exposure to a foreign object and bind to specific molecules with high affinity. Researchers create antibodies against specific molecules by injecting animals such as rabbit, mouse, rat, donkey or goat, with a target molecule. This evokes a high expression of antibodies in the blood serum which are then affinity purified [7]. Fluorescent dyes can be covalently coupled to antibodies to enable downstream target identification. Probes indirectly label targets as the fluorescent emitter, the dye, is not attached directly to the target molecule under investigation. When using indirect labeling approaches one should consider that larger probe sizes result in larger displacements between the target under investigation and the signal from the fluorescent emitter. For example, the commonly used immunolabeling approach of primary and secondary antibodies can introduce a displacement of up to 30 nm between the detected signal and the target [8]. Recent innovations in labeling probe development have equip researchers with smaller probes to mitigate this effect [9-12].

1.2 Fluorescence microscopes

Microscopes are used to visualize objects not visible to the naked eye. When biomolecules are labeled with fluorescence emitter molecules, they can be visualized using a fluorescence microscope.

The epi-fluorescence microscope is one of the basic microscope set-ups used today, Fig. 1.2. Its components are arranged so that both the illuminated and emitted light travels though the same objective lens. A light source, such as a lamp of LED, emits a broad spectrum of light that serves as the excitation source for fluorescent molecules in the samples. An excitation filter is placed in the light path to allow only the desired wavelengths of light to pass through and reach the sample. The excitation light then enters a dichroic mirror that reflects it to the sample and transmits the resulting emitted fluorescence from the sample. Emitted fluorescence is filtered through an emission filter prior to reaching the camera or detector system. The excitation and emission filters of a microscope should always be checked to verify their compatibility with the imaged fluorophore.

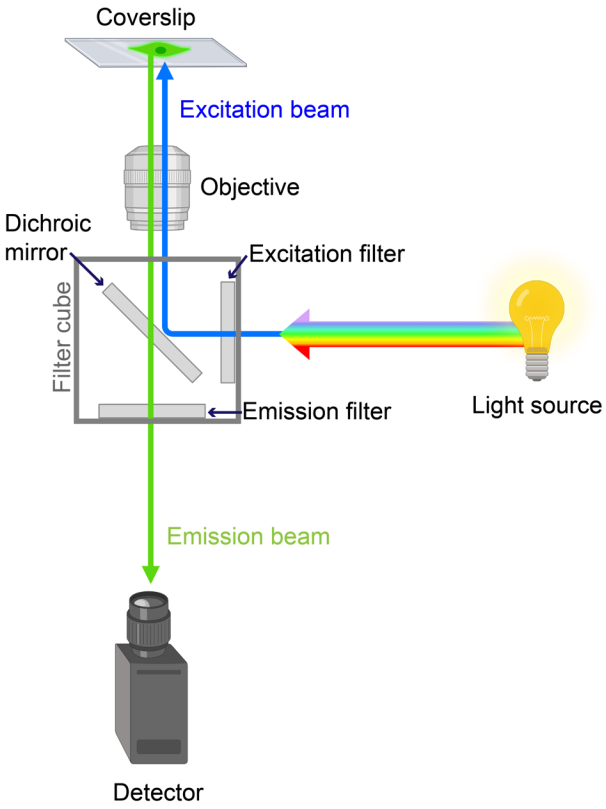

Figure 1.2. Basic epi-fluorescence microscope set-up. An excitation beam (blue) from a light source, *e.g.* LED lightbulb, is filtered by an excitation filter and reflected by the dichroic mirror through the objective. Once the excitation beam reaches the coverslip containing the biological sample, fluorescence is emitted from labeled biomolecules, the emission beam (green). The emission beam passes through the objective and dichroic mirror, and is detected by a detector, *e.g.* camera. A filter cube contains the excitation filter, emission filter, and the dichroic mirror. Figure made with Biorender.com.

Light propagates at different rates through different types of mediums. The refractive index (n) of a material is a measure of how much light is bent or refracted when it enters that material from a vacuum (or air). Refractive index gives researchers an indication of the light bending abilities of a medium. Immersion oils containing various refractive indexes are used to correct for the different refractive indexes of the mediums used during image acquisition on microscopes. Snell's law describes how much light will refract as it crosses the interface of two mediums. This change is determined by the angles at which the light approaches and leaves the interface and the different mediums:

$$n_1 * \sin\theta_1 = n_2 * \sin\theta_2$$

Modes of sample illumination can be classified depending on how the excitation beam of a microscope passes through the sample. The three illumination modes include Epifluorescence (Epi), Total internal reflection (TIRF), and highly inclined and laminated optical sheet (HILO) [13], Fig 1.3. In Epi, the light beam (from the laser) passes upwards through the entire sample. Since significant background fluorescence signal can occur as a result of whole sample illumination, Epi-fluorescence imaging isn't ideal to detect single molecules. HILO occurs when the light path is moved parallel to the coverslip, resulting in the illumination path entering the sample at a sharp angle, creating a highly inclined optical sheet of light that results in less sample penetration and improved background signal compared to Epi. TIRF occurs when the light path is moved even further parallel, until the laser hits the coverslip at an angle larger than the so called critical angle. The light beam then undergoes total reflection at the interface of glass and buffer, instead of penetrating through the sample and refracting as described in Snell's Law. Total internal reflection fluorescence (TIRF) microscopy can only be achieved when passing a light beam from a high refractive index medium (*e.g.,* coverslip) into a lower refractive index medium (*e.g.*, sample). Reflection results in the formation of an electromagnetic field (~200 nm in height) within the aqueous medium. The generated evanescent wave specifically illuminates and activates fluorophores within this small area adjacent to the glass-water (or glass-buffer) interface [14]. The critical angle depends on the refractive index of the coverslip n_1 and the imaging buffer n_2 as follows:

$$\theta_{critical} = \sin 1\ (n_1/n_2)$$

At the critical angle, the light beam is reflected and an evanescent wave propagates parallel to the coverslip of the sample and decays exponentially. The evanescent wave can be described with the following function:

$$I_Z = I_0\, e^{z/d}$$

I_Z is the intensity at depth and I_0 is the initial intensity. TIRF is commonly used for imaging of single-molecules or targets at the cell surface, while HILO and Epi illumination modes are used to image targets deeper inside cells.

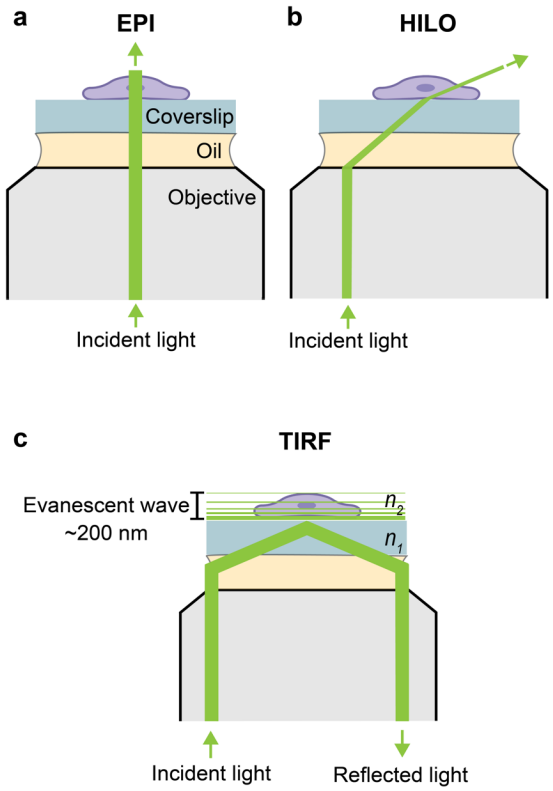

Figure 1.3. EPI, HILO, and TIRF modes of illumination. **a**) Epifluorescence (EPI) occurs when incident light is centered in the objective and results in a vertical illumination column that penetrates through the coverslip and sample. **b**) Highly inclined and laminated optical sheet (HILO) occurs when the incident light is shifted towards the edge of the objective. HILO results in sample illumination at a steep angle. **c**) Total internal reflection fluorescence (TIRF) occurs when the incident light is shifted enough towards the objective edge enough to reach a critical angle. Light is reflected back into the coverslip and induces an evanescent wave with sample penetration depth of approximately 200 nm. TIRF is only possible when propagating light goes from a medium of higher refractive index (n_1) to a medium of a lower refractive index (n_2). Purple cell made using Biorender.com.

1.3 The Resolution Limit

While microscopes allow us to see targets not visible to the naked eye, traditional optical microscopy has limitations on how well two objects can be distinguished from one another or resolved. A fundamental concept is the Abbe limit [15], which states the minimum resolvable distance between two objects or points in a sample cannot be smaller than half the wavelength of the imaging light. This limit exists because of the diffraction of light as it passes through the aperture at the back of the back focal plane of the objective. The Abbe limit was defined by Ernst Abbe as the following:

$$d = \frac{\lambda}{2NA}$$

NA refers to the numerical aperture of the objective lens on a microscope and λ is the wavelength of light. For example, if imaging a sample using a red laser (641 nm) and using an objective with an NA of 1.49, the resolution would be 215 nm.

In fluorescence microscopy, the Rayleigh criterion [16] is an accepted criteria to determine the minimum resolvable points in an image. It takes into account that the emission and excitation wavelengths are shifted. Rayleigh described entities as point like emitters and defined entities as resolved when the center of the diffraction pattern of one point coincides with the first zero of the second point's diffraction pattern, as in the equation:

$$R = 1.22 * \lambda / 2 * NA$$

Thus, resolution depends on the numerical aperture of the objective of the microscope and the emitted wavelength of light. Traditional fluorescence microscopes can achieve approximately 250 nm lateral resolution and 500 nm axial resolution. Such resolution allows researchers to visualize entire cells of many organisms and even distinguish organelles. However, studying biomolecules and their assemblies on a molecular scale requires resolutions of at least tens of nanometers.

2.1 SIM and STED super-resolution microscopy

Multiple super-resolution microscopy methods have been developed that bypass the Abbe resolution limit. Of these methods, two main groups have emerged. The first group modifies the illumination pattern of the microscope and comprises stimulated emission depletion microscopy (STED) and structured illumination microscopy (SIM). The second group uses single molecules as emitters and includes photo-activated localization microscopy (PALM), stochastic optical reconstruction microscopy (STORM), point accumulation for imaging in nanoscale topography (PAINT), and DNA point accumulation for imaging in nanoscale topography (DNA-PAINT).

Structured illumination microscopy (SIM) is a super-resolution microscopy method that achieves approximately 2-fold improvement in resolution compared to diffraction-limited imaging [17]. When an illumination pattern is applied to a sample that contains structures smaller than the diffraction limit, interference between the sample and pattern results in a moiré effect. SIM works by imaging the same area multiple times with different patterns of illumination to enable the spatial information of target molecules to be extracted from Fourier transformations of each image. During post-processing, images are combined into one reconstruction. The main advantages of SIM compared to other SRM methods is that it can be performed on samples that have been prepared for diffraction limited microscopy and the required imaging duration for one field-of-view is on the scale of seconds. Indeed, the fast imaging acquisition times of SIM enables live-cell imaging.

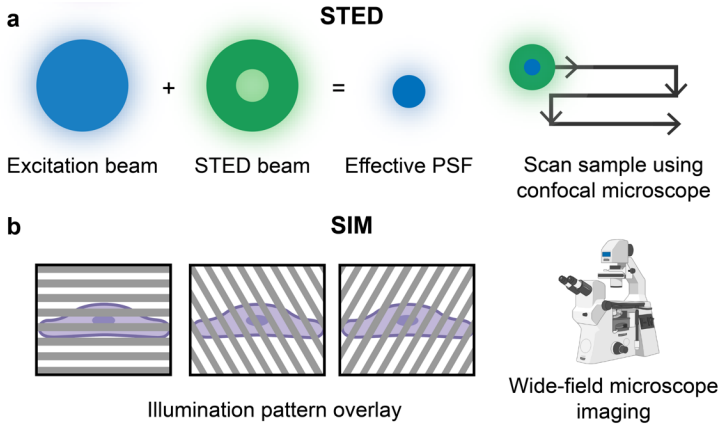

Figure 2.1. Basic principles of SIM and STED super-resolution microscopy methods. a) STED microscopy uses an excitation beam (blue) and a donut shaped STED beam (green) during image acquisition. The STED beam is overlaid on the excitation path, creating a depletion ring that prevents fluorophore activation beyond the central zero point. This results in a smaller effective Point Spread Function (PSF) compared to the excitation PSF. Samples are imaged via scanning of a confocal microscope. **b**) For SIM an illumination pattern is applied to the sample, which contains structures finer than the diffraction limit and introduces interference, manifesting as a moiré effect. Sample is imaged with different illumination patterns, allowing spatial details of target molecules to be extracted from Fourier transformations. Wide-field microscopes are used for SIM.

Stimulated emission depletion (STED) microscopy is a super-resolution microscopy method that decreases the central focal area of the emission beam by selectively depleting the fluorophores around the focal center [18]. STED uses an excitation beam and a donut-shaped depletion beam or STED beam. The STED beam prevents fluorophores from transitioning to an excited state or ON state, except for those located within the zero intensity point at its center. The size of the zero intensity region is smaller than the diffraction limit. Consequently when the beams scan across the sample together they can achieve spatial resolution proportional to the size of the effective fluorescent region in the zero intensity area [19]. Due to these inherent properties, STED microscopy typically requires sophisticated microscopy equipment. The achievable resolution can be described with the following formula:

$$\Delta x = \frac{\lambda}{2\,NA} * \frac{1}{\sqrt{1 + \frac{I}{I\,sat}}}$$

Δx denotes the smallest resolvable feature, λ denotes excitation wavelength, and I denotes the STED beam intensity. Thus the limiting factor is no longer the diffraction limit of light but rather the intensity of the STED laser, which must be strong enough to produce a small PSF. Fixed and live cell cells samples can be imaged via STED, and live cell imaging was first recorded in 2008 [20].

2.2 Single molecule localization microscopy

The second class of super-resolution microscopy methods fall under single molecule localization microscopy (SMLM). SMLM overcomes the diffraction limit of light by temporally separating

fluorescent molecules that spatially overlap and accurately determining fluorescent molecule positions. In SMLM, target molecules stochastically switch from a fluorescence emitting state (ON state) to a dark state (OFF state), which results in characteristic SMLM "blinking" (Figure 2.2). The PSF of a microscope refers to the characteristic blob within an image that represents a singular point-like object. Stochastic blinking enables observation of individual molecules, effectively isolating point-spread-functions (PSFs) since it is unlikely that overlapping molecules are activated at the same time. A wide-field microscope can be used to acquire images over a long enough period of time to collect sufficient sampling from point-emitters or until fluorescent proteins or dyes bleach. The PSFs from emitter molecules in individual images are fitted to determine their center position with sub-diffraction precision. Finally, all images are superimposed and reconstructed into a final super-resolution image. In SMLM, the attainable localization precision scales inversely with the square root of the number of photons fitted [21]:

$$\Delta x \approx \frac{1}{\sqrt{N}}$$

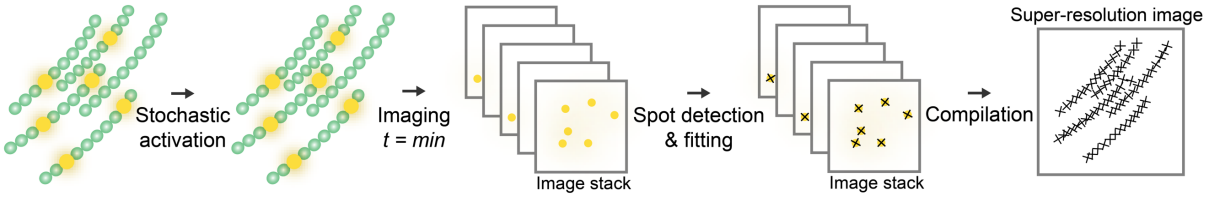

Figure 2.2. Single molecule localization microscopy concept. Fluorophores attached to a target structure (green) are stochastically activated to create characteristic single molecule localization blinking. During sample imaging, activated fluorophores (yellow) are detected by a camera over a period of time, typically minutes (*t = min*), and appear as spots in the image stack. Spots are detected and fitted during post-processing with sub-diffraction precision. A super-resolution image is reconstructed by compiling fitted localizations of images within the stack and performing post-processing, *e.g.* drift correction.

SMLM methods can be distinguished by the way blinking is created in each method. PALM, established by Eric Betzig and colleges in 2006 uses photo-activatable fluorescent proteins (PA-FPs) that are fused to target molecules [22] and activated with specific wavelengths of light to blink until sufficient sampling is reached or PA-FPS are bleached. Here, users need to adjust the intensity of the activation laser to create optimal blinking. STORM was developed in 2006. STORM blinking was first created using Cy3-Cy5 dye pairs to enable dye switching between ON and OFF states [23]. A few years later, direct STORM (dSTORM) was developed, which uses a single photo-switchable dye species [24]. Optimization of (d)STORM buffer components and concentrations are required to generate optimal blinking densities of organic dyes. In both PALM and (d)STORM, once a photo-switchable dye or fluorescent protein is bleached by the laser, it remains in the dark state and can no longer be imaged.

Points accumulation for imaging in nanoscale topography (PAINT) mitigates this limitation by utilizing fluorophores that freely diffuse in the imaging solution [25]. PAINT was introduced in 2006 using the dye

Nile Red, which is a lipid stain. Nile Red fluorescence is not observed when diffusing in the imaging buffer, but strong fluorescence appears when it is bound to the target. Once bound, the dye can be detected by the camera until it either bleaches or falls off the target. The main advantage of PAINT is that the large quantity of dyes in the imaging solution enables constant probe binding to the target. Additionally, photo-switching dyes or proteins isn't required to generate super-resolution images.

Most recently in 2017, a method called minimal photon fluxes (MINFLUX) was established by Francisco Balzarotti and Stefan Hell. MINFLUX combines the stochastic fluorophore switching that is characteristic of SMLM with the donut-shaped depletion beam used in STED microscopy to yield unprecedented localization precisions of ~ 1 nm in cells[26].

2.3 DNA-PAINT super-resolution microscopy

Deoxyribonucleic acid (DNA) is foundational to DNA-PAINT super-resolution (DNA-PAINT) microscopy. The genetic information for all living organisms is stored as DNA, which is a polymer comprised of nucleotides. Each nucleotide contains three main components; a phosphate group, one of four nitrogenous bases, and a sugar group. The four possible nitrogenous bases include cytosine (C), adenine (A), guanine (G), or thymine (T), which from a glycosidic bond with the deoxyribose sugar group that is linked to a phosphate. The nitrogenous base A pairs with T via two hydrogen bonds and bases G and C pair via three hydrogen bonds. DNA bases can be further classified into pyrimidines or purines based on their chemical structure. The larger purines A and G have two carbon rings and the smaller pyrimidines T and C have one carbon ring. Two polymers of DNA run anti-parallel to one another, or in the opposite direction, with nitrogenous bases pairing in the center followed by the sugar-phosphate backbone (Figure 2.3). The nucleotide chains coil around each other like a twisted ladder, creating a double helix structure. The Nobel Prize in Physiology and Medicine was awarded to James Watson, Francis Crick, and Maurice Wilkins for their work discovering the structure of DNA in 1962 [27].

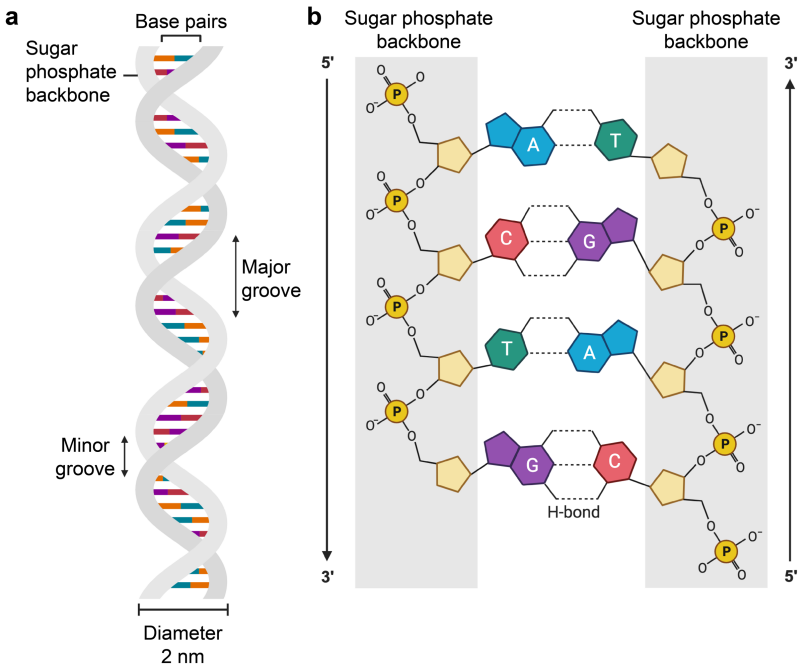

Figure 2.3. DNA structure. a) The double helix structure of DNA. Two polynucleotide DNA strands wrap around each other to form a double helix with larger major and smaller minor grooves. Base pairing between nucleotides in the center of the structure creates the double stranded nature of DNA. DNA diameter is 2 nm. **b**) DNA is comprised of two sugar phosphate backbones running in opposite directions, one strand runs 5' to 3' while the other runs 3' to 5'. Base pairing occurs between adenosine (A) and thymine (T) or guanine (G) and cytosine (C) via hydrogen bonds (H-bond). Phosphate groups in orange. Deoxyribose sugars in yellow. Created with Biorender.com.

DNA-PAINT takes advantage of the predictable binding kinetics of DNA nucleotides to create super-resolution images. DNA-PAINT was developed in 2010 [28] and combines the predictable and programmable properties of DNA-DNA interactions with the strengths of PAINT based imaging. Instead of dyes, DNA is used as a tool to create the blinking signal essential for single molecule localization microscopy. A docking strand, which is a short oligonucleotide, is attached to the target under investigation or to a labeling probe that binds the target. The imager strand, an oligonucleotide that is complementary to docking strand and dye-conjugated, is delivered to the sample in an imaging buffer (Figure 2.4). When unbound, the imager strand diffuses in solution too fast for the camera to capture. When the imager strand transiently binds to its complementary docking strand, the dye attached to the imager strand is immobilized long enough to generate a fluorescent signal with a much higher signal-to-noise ratio than the diffusing imager strands. The resulting blinking signals are captured by the camera as spots during an image acquisition, typically tens of minutes. The raw image file can then be analyzed and rendered into a super-resolution image using the open source software Picasso, which was developed specifically for DNA-PAINT image analysis by the Ralf Jungmann laboratory [29]. Alternatively, other single-molecule localization microscopy analysis programs such as ThunderSTORM [30] can be used. 3D DNA-PAINT can be implemented by the addition of an cylindrical lens to the microscope [31].

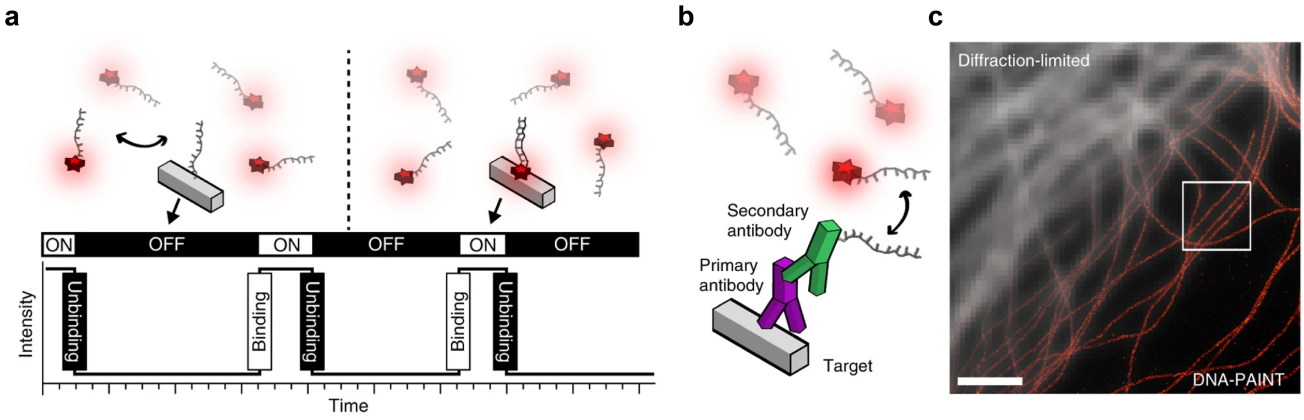

Figure 2.4. DNA-PAINT concept. a) Schematic depicting transient binding of a dye-labeled imager to its complementary docking site attached to a target of interest. When unbound or OFF, no blinking is detected in the intensity vs. time trace. When bound or ON, a blinking signal is detected. **b**) General labeling strategy for cellular protein targets. Targets can be visualized using a primary antibody against the cellular protein of interest and a DNA-conjugated secondary antibody against the primary antibody species. **c**) A diffraction-limited image of α-tubulin is overlayed with its DNA-PAINT super-resolution counterpart. 2 µm scale bar. Reprinted with permission from Springer Nature [29], Copyright 2017.

The kinetics of imager-docking strand interactions in DNA-PAINT have been described. The association and dissociation rate of the imager to the docking strand follow a second order kinetic model:

$$[c_i] + [c_d] \underset{k_{off}}{\overset{k_{on}}{\rightleftarrows}} [c_i c_d]$$

c_i and c_d corresponds to the concentration of the imager and docking strands, respectively.

The "bright time" or "ON time" refers to the duration of time an imager is bound to the docking strand and the "dark time" or "OFF time" refers to the duration of time in which no imager is bound to the docking strand. Bright time, τ_b, is described by the following formula:

$$\tau_b = \frac{1}{k_{off}}$$

The dark time, τ_d, or the time during which the docking strand has no imager bound, is described as:

$$\tau_d = \frac{1}{k_{on} \times c_i}$$

In which c_i refers to the concentration of imager strands in solution.

The dissociation rate, k_{off}, is calculated based on the imager bright time:

$$k_{off} = \frac{1}{\tau_b}$$

The association rate k_{on} is described using imager concentration (c_i) and the mean dark time (τ_d):

$$k_{on} = \frac{1}{c_i \times \tau_d}$$

The stability of DNA interaction influences the mean bright time of the imager-docking strand duplex and can be programmed. This is easily done by changing the length and GC content of the imager-docking strand sequence and or changing the salinity of imaging buffer. Increasing the sample temperature during DNA-PAINT imaging will increase the dissociation rate and vice versa. To collect the highest number of photons per localization and thus achieve the highest resolutions, the integration time of the camera should be tuned to a similar length as the bright time of the imager strand.

DNA-PAINT does not require spectrally distinct dyes to identify different target molecules. Instead, the number of identifiable targets depends on the number of orthogonal DNA sequences that can be used to encode target identity. Since DNA-PAINT docking strands are typically 8 – 16 nt long, theoretically unlimited multiplexing can be achieved with a single dye. In an experiment, the user can image docking site P1 with imager strand P1*, then P1* can be washed out the sample using buffers such as PBS. Imager P2* can then be added to the sample to image docking site P2 (Figure 2.5). This can be repeated for *n* number of docking sites during a process called Exchange-PAINT[32]. Ten target Exchange-PAINT was performed on ten different DNA origami structures exhibiting the numbers 0 – 9 as a proof-of-concept experiment. For cell imaging DNA-PAINT docking sites are conjugated to affinity reagents like nanobodies or antibodies that bind a target of interest. Recently, DNA-PAINT was used to image 30 targets in neurons at single protein resolution [33]. In contrast, other super-resolution microscopy methods (*e.g.* PALM, STORM, and STED) rely on spectrally distinct dyes for target identification, which typically limits multiplexing capabilities to ~ 3 targets.

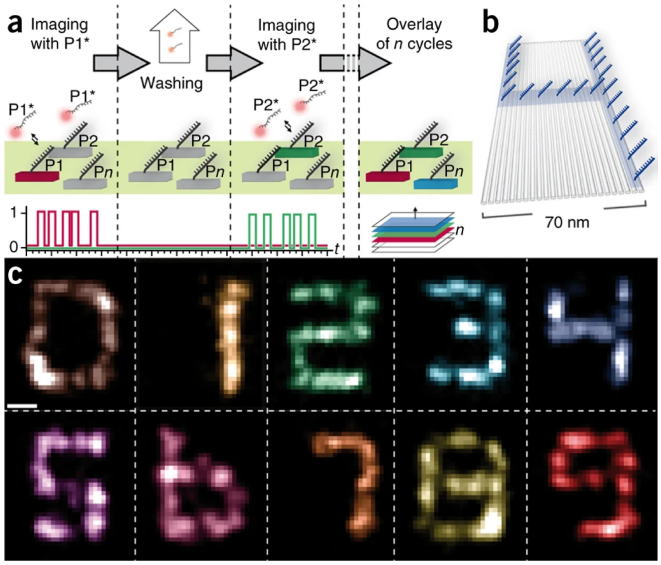

Figure 2.5. Exchange-PAINT. a) Schematic of the Exchange-PAINT cycle. The first target is imaged using P1* imager which transiently binds to P1 docking site. P1* is washed out of the sample after imaging is completed and P2* imager is introduced, imaged, and washed out. This is repeated for n cycles. **b**) Schematic of DNA origami structure used for proof-of-concept experiment in c. **c**) Ten target Exchange-PAINT was performed on DNA origami structures. DNA-PAINT images of the ten different DNA origami structures displaying numbers 0 - 9 are shown. Reprinted with permission from Springer Nature [32], Copyright 2014.

DNA-PAINT has inherent quantitative capabilities. The copy numbers of proteins or targets can be accurately predicted by analyzing the binding kinetics between imager and docking strands, a method termed quantitative DNA-PAINT (qPAINT) [34] (Figure 2.6). With a constant influx rate, if a single target molecule labeled with one docking strand is visited by an imager strand twice in a certain time frame, an imager strand will visit three target molecules with three docking strands at three times the frequency. For absolute quantification of target molecules, a calibration sample with a known imager concentration (c_i) and association rate (k_{on}) should be used to calculate imager influx rate (ξ):

$$\xi = k_{on} \times c_i$$

For cellular samples, a DNA origami with a known number of bindings sites can be used a calibration sample *in situ*. The number of binding sites present on a targets is determined with the following formula:

$$binding\ sites = \frac{1}{\tau_{d*} \times \xi}$$

The mean dark time (τ_{d*}) of localizations within an area of interest is extracted from the measurement by determining the cumulative distribution function of dark times and fitting this function with the exponential function:

$$P(t) = \exp(\ 1/\tau_{d*}\ )$$

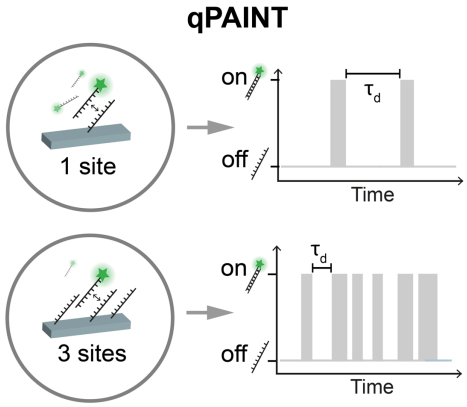

Figure 2.6. Quantitative DNA-PAINT (qPAINT) principle. Target molecules are labeled with 1 and 3 docking sites within the same area (circle). Intensity vs. time traces show DNA-PAINT blinking patterns in the presence of 1 and 3 docking sites. With a constant influx rate, one docking site exhibits a certain time, τ_d, between binding events. Three docking sites present exhibit three times shorter τ_d. Reprinted with permission from Science AAAS [35], Copyright 2024.

DNA-PAINT docking and imager sequences were recently optimized to enable up to 100-fold faster imaging [36]. A limiting factor of DNA-PAINT imaging has been the required image acquisition time per target. When using first generation DNA-PAINT sequences [29,32,34] imaging a single cellular target within one field-of-view could require image acquisition times of 30 minutes to several hours. Speed optimized sequences, called SPEED sequences, work by concatenating repetitive sequence motifs to create overlapping docking sites that enable up to 100-fold faster image acquisitions. Indeed, 5 – 7 potential imager binding sites are present on a single SPEED docking site. Six different SPEED sequences have been developed, enabling up to six target multiplexing using Exchange-PAINT. Furthermore, SPEED sequences enable DNA-PAINT imaging using lower imager concentrations, resulting in increased signal-to noise ratios and biological sampling when compared to first generation sequences. SPEED sequences are used in Results, Publication 2.

3.1 Introduction to spore-forming bacteria

Bacteria are single-celled prokaryotic microorganisms. They are classified into two major classes, gram-negative and gram-positive, which differ in the architecture and composition of the bacterial cell envelope (Figure 3.1) [37]. Gram-negative bacteria have an inner cytoplasmic membrane (IM) that is surrounded by a thinner cell wall (5 – 10 nm) that is in turn surrounded by an outer membrane (OM). In contrast, gram-positive bacteria have a single cytoplasmic membrane surrounded by a thick cell wall (20 – 80 nm). Peptidoglycan is a key component of bacterial cell envelopes and is composed of glycan strands of alternating N-acetylglucosamine and N-acetylmuramic acid sugars, which are fully or partially crosslinked by peptide bridges in gram-positive and gram-negative bacteria, respectively. The composition of biomolecules at the cell envelope differs between gram-negative and gram-positive bacteria [38]. The OM of gram-negative bacteria includes glycolipids including

lipopolysaccharides, porins, surface proteins, and integral membrane proteins. The OM and IM sandwich a thin layer of peptidoglycan in the gram-negative periplasm. The IM contains integral membrane proteins. The gram-positive cell envelope contains a thick peptidoglycan layer, teichoic acids, lipoteichoic acids, and integral and peripheral membrane proteins.

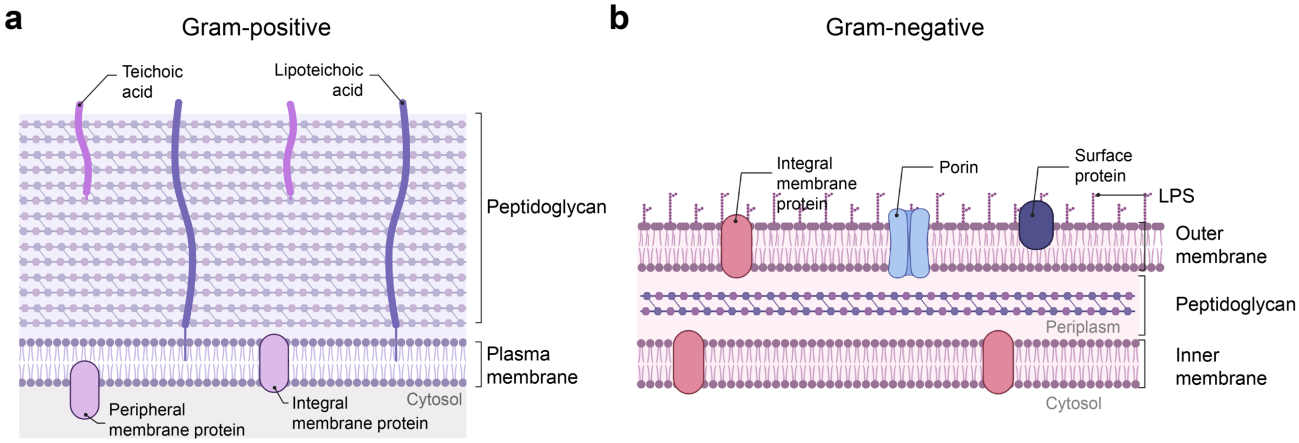

Figure 3.1. The bacterial cell envelope. a) The gram-positive cell envelope consists of a plasma membrane and thick layer of peptidoglycan (20 – 80 nm). Teichoic and lipoteichoic acids weave through peptidoglycan layers. Integral and peripheral membrane proteins decorate the plasma membrane. **b**) The gram-negative cell envelope consists of an inner membrane closest to the cytosol and an outer membrane. The area between the outer and inner membranes is the periplasm, in which a thin peptidoglycan layer (5 – 10 nm) resides. Various molecules such as LPS, porins, surface proteins, and integral membrane proteins are present on the outer membrane. Integral membrane proteins are also present on the inner membrane. LPS: lipopolysaccharide. Figure created with Biorender.com.

Gram-positive bacteria of the species *Bacillus* and *Clostridium* have the ability to form spores, or sporulate. Between 50% to 60% of the bacterial genera found in gut microbiota of a healthy individuals can produce spores [39]. Spore-forming bacteria have two modes of division that are can be defined by their end products (Figure 3.2). During symmetric division, called vegetative division, the cell is split into two identical daughter cells. Vegetative division is the standard or normal mode of division and occurs under favorable nutrient conditions. Upon exposure to stressful environments, the survival mechanism of sporulation is initiated, which produces a dormant and resistant cell type called a "spore". Sporulation begins when division initiates asymmetrically near one bacterial cell pole, resulting in a septum that divides the cell into side-by-side compartments. The larger compartment is called the mother cell compartment and the smaller compartment the forespore or spore. As the division septum is synthesized, a genome is segregated into each compartment. The mother cell helps the spore reach maturity by engulfing it in a mechanism similar to phagocytosis and coating it in protective layers. Lastly, the mother releases the spore into the environment via self-lysis. Spores remain dormant until they reach an environment that supports normal growth. They then germinate, *i.e.* begin vegetatively dividing. Spores are extremely resistant to harsh environments including extreme heat, ultraviolent radiation, and harsh chemicals. Sporulation is used as simple model to investigate cellular differentiation and morphogenesis [40].

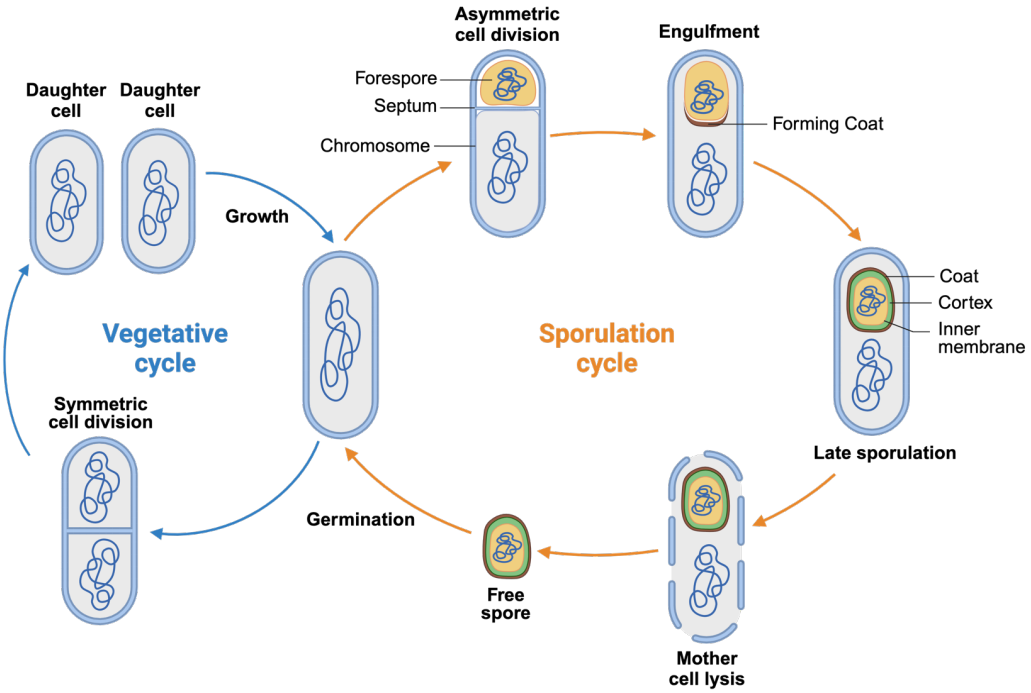

Figure 3.2. The vegetative and sporulation cycles of spore-forming bacteria. During the vegetative cycle (blue), the genome is replicated and segregated to opposite cell poles. Bacteria undergo symmetric cell division, during which the division septum is synthesized at the mid-cell and two identical daughter cells are created. Daughter cells mature and repeat the vegetative cycle. The sporulation cycle (orange) is activated in response to environmental stress. During sporulation, cell division occurs asymmetrically near a single cell pole, creating a smaller forespore compartment and a larger mother cell compartment separated by a division septum. A chromosome is segregated into the forespore and mother cell compartments during division. The mother cell engulfs the forespore and helps cover it in a protective coat. Upon late sporulation, the spore is comprised of an inner cortex, and inner membrane, and a coat. Finally, the mother cell releases the spore into the environment via self-lysis. Free spores germinate and enter the vegetative life cycle upon exposure to favorable environmental conditions. Figure created with Biorender.com.

This PhD thesis primarily investigates *Bacillus subtilis,* which is a spore-forming aerobic rod-shaped bacteria found in the soil, and human and animal guts. *B. subtilis* is the major model organism for gram-positive bacteria and sporulation studies, and has a diameter of ~0.85 μm and a length of 2 – 5 μm [41].

3.2 The *Bacillus subtilis* division machinery

The divisome is a macromolecular machine consisting of tens of different of proteins that assemble at the future division site and splits the cell in two. The most studied division protein is FtsZ, which is highly conserved in bacteria. FtsZ is a tubulin-like protein with a GTP-binding motif. In 1991, the visualization of FtsZ as a ring-like structure (termed the Z-ring) at the mid-cell in gram-negative *Escherichia coli* marked the first time a cell division component was seen using microscopy [42]. Shortly after, FtsZ was also visualized as a ring-like structure in gram-positive *B. subtilis* at the mid-cell [43]. The Z-ring is considered the foundational component of the divisome in almost all bacteria, acting as an essential scaffold for other divisome components. FtsZ monomers assemble in a head-to-tail fashion

to form single-stranded protofilaments, which condense into the Z-ring at the future division site (Figure 3.3). FtsZ protofilaments treadmill circumferentially around the division plane. GTP hydrolysis regulates FtsZ polymerization rate [44].

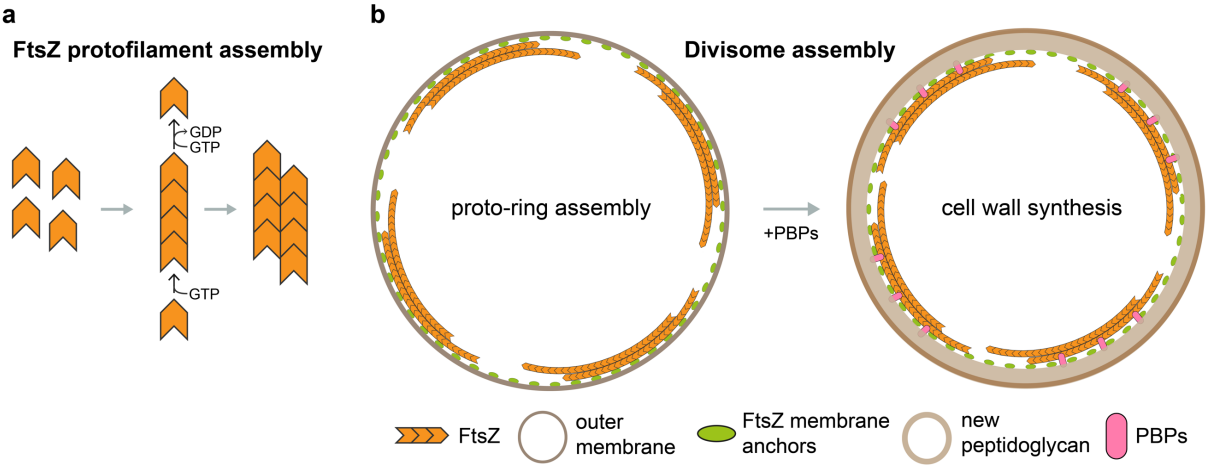

Figure 3.3. FtsZ protofilament and divisome assembly. a) FtsZ monomers treadmill to form protofilaments. GTP is required for addition of a FtsZ monomer. GTP is hydrolyzed to GDP for monomer removal. FtsZ protofilaments condense via lateral interactions to create the Z-ring. **b**) Latitudinal bisections of the mid-cell show divisome components during the first and second steps of divisome assembly. Left: In the first step of divisome assembly FtsZ protofilaments are stabilized and tethered to the membrane by FtsZ membrane anchors, which comprise ZBPs and FtsA. A proto-ring is formed. Right: PBPs localize to the division site during the second step of divisome assembly and enable cell wall synthesis. FtsZ membrane anchors continue to tether the constricting Z-ring to the membrane until division is completed. PBPs: penicillin binding proteins. ZBPs: Z-ring binding proteins.

In *B. subtilis*, the division machinery components assemble in two major steps (Figure 3.3) [45]. In the first step, the protein FtsZ assembles simultaneously with "early" cell division proteins FtsA, ZapA, SepF, and EzrA proteins. Of these, the proteins ZapA, SepF, and EzrA are the FtsZ binding proteins (ZBPs), which condense FtsZ filaments into the Z-ring and are required for functional Z-ring assembly. FtsA and SepF anchor FtsZ filaments to cellular membrane. ZapA and is a cytoplasmic protein that laterally crosslinks FtsZ filaments comprising the Z-ring. EzrA helps the Z-ring associate with the membrane and prevents aberrant Z-ring formation. This first step of division forms the "proto-ring", comprising a Z-ring that is stabilized and tethered to the membrane by early divisome proteins. While FtsA treadmills with FtsZ protofilaments, the ZBPs are stationary [46] and don't affect FtsZ filament dynamics. In the second step of divisome assembly, "late" cell division proteins, including GspB, FtsL, DivIB, FtsW, Ppb2B, and DivIVA localize to the division plane after a delay of approximately 20% of the cell cycle [45]. These proteins are involved in processes such as peptidoglycan and cell wall biosynthesis. Exactly how the division septum is built isn't fully understood. FtsZ treadmilling around the division ring was shown to drive the motions of peptidoglycan (PG) synthesizing enzymes and thus control septal constriction rate [44,47]. However, more recent research suggests that cell constriction is driven by a multimeric PG synthesis complex dependent on septal PG synthesis and not FtsZ treadmilling [48]. While the overall assembly steps and functional roles of many divisome proteins are well studied, how

proteins work together remains elusive. Moreover, the organization and relative positioning of divisome proteins in vegetative *B. subtilis* remains unknown, resulting in an incomplete picture of bacterial cell division.

How divisome proteins organize, interact, and work together and is even less understood during sporulation than in vegetative division. At the onset of sporulation, the Z-ring at the mid-cell forms a spiral-like intermediate which becomes a Z-ring at one or both cell poles [49]. Then, through an unknown process, the cell "decides" which Z-ring will be used for asymmetric division. It is unclear if the exact same divisome components responsible for vegetative division perform division in sporulating cells. Interestingly, several studies suggest the divisome is different between cell types. The protein DivIVA (discussed below) was found to be distributed differently across the division plane dependent on division mode [50]. Recently, cryogenic focused-ion-beam milling electron tomography (cryo-FIB-ET) revealed that unlike vegetative cells, filaments of FtsZ and FtsA don't localize at the mid-point of the invaginating septum in sporulating cells, but asymmetrically towards the mother cell compartment. Thus, the placement of the Z-ring within the division plane differs between vegetative and sporulating cells and it remains unclear if and how division is performed differently between vegetative and sporulating cells.

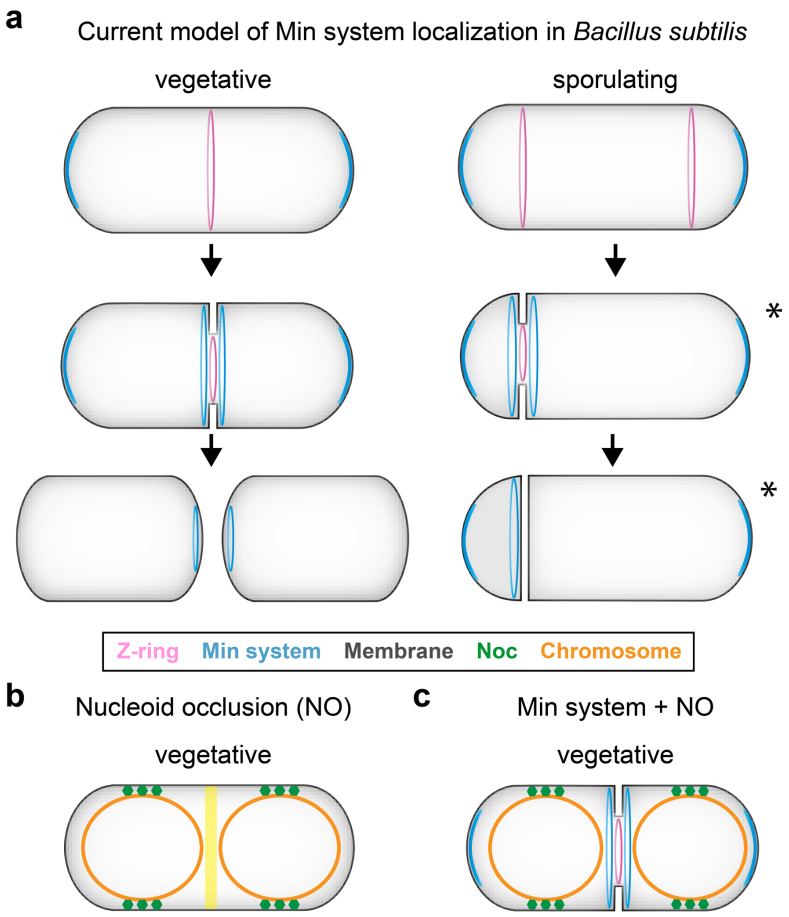

Figure 3.4. Current models of the Min and Nucleoid occlusion systems of B. subtilis. a) Vegetative: The Z-ring localizes to the mid-cell and initiates division. Min proteins localize at the extreme cell poles. Upon membrane constriction, the Min system localizes to the mid-cell as dual rings flanking the constricting Z-ring. Upon cell separation, the Min system remains at the old cell poles and no Z-ring is present. Sporulating: Upon sporulation cycle activation, the Z-ring redeploys to cell poles. DivIVA localizes at the extreme cell poles. Upon asymmetric division, DivIVA is believed to form dual rings sandwiching the constricting Z-ring. DivIVA retains its localization at extreme cell poles. After septation, only the DivIVA ring in the forespore is present. **b**) Noc protein tethers the chromosome to the cell membrane to create a physical barrier against Z-ring formation. **c**) Schematic of both the Min and Noc systems in a dividing vegetative cell. * indicates protein localization that has not been experimentally confirmed. NO: nucleoid occlusion.

In *B. subtilis*, the cell division machinery is regulated by two main systems: nucleoid occlusion (NO) and the Min system (Figure 3.4). These systems are believed to operate independently of one another. NO functions to prevent the cell from dividing over the chromosome. The protein Noc was the first nucleoid occlusion protein identified in *B. subtilis* [51]. Noc is a membrane binding protein which binds to 74 specific noc-binding sequences (NBS) that are distributed throughout the chromosome, with the exception of its terminus [52]. Noc binding to NBS and the cell membrane functions to physically prevent the formation of a Z-ring within proximity. Thus, Noc-bound DNA must be recruited to the membrane for functional NO. When additional noc-binding sites (NBS) were added to the terminus of the chromosome, cell division was delayed suggesting a potential role for NO in temporal regulation of division. Thus far, evidence of direct interactions between Noc and cell division proteins has not been found.

The *B. subtilis* Min system prevents aberrant assembly of the divisome near the cell poles and next to the dividing septum [53]. In the absence of the Min system the division machinery is placed aberrantly, resulting in small DNA-free cells called mini-cells. The Min system is composed of the proteins DivIVA, MinJ, MinC and MinD. DivIVA is the topological determinant of the Min system and assembles as two rings, dual rings, that sandwich active division sites in vegetative cells [54] and is believed to form dual rings in sporulating cells[50]. DivIVA is recruited to division sites via its high affinity for negative membrane curvature, which appears at division sites upon membrane constriction. DivIVA dual rings sequester MinCDJ proteins away from the divisome to prevent FtsZ re-assembly next to active division sites. DivIVA also localizes to the extreme cell poles, where it prevents aberrant cell division. The most recently discovered protein in the Min system is MinJ, which acts as a bridge between DivIVA and the division inhibitor MinCD [55,56]. MinC protein directly inhibits FtsZ assembly by preventing its polymerization.

3.3 Super-resolution microscopy imaging of bacteria

The first papers that reported super-resolution imaging of bacteria were published in the late 2000s. PALM was first used in 2008 to investigate the structural protein MreB in *Caulobacter cresentus* [57]. Other early uses of PALM include investigations of the *Escherichia coli* chemotaxis network [58] and visualizing the Z-ring in live *E. coli* [59]. STED microscopy was first performed on bacteria to visualize the membrane [60] and subsequently used to image the Z-ring [61]. STORM was first used to image the tubular stalk of the bacteria *Caulobacter crescentus* in 2008 [57]. Most recently, MINFLUX was used in bacteria for the first time to image a pore protein on the injectisome of *Yersinia enterocolitica* [62]. Since their introduction, super-resolution microscopy (SRM) methods have been used to investigate a variety of bacterial proteins and processes in various species.

The dense and complex structure of the bacterial cell envelopes presents a challenge for microscopists performing immunolabeling of intracellular bacterial proteins. While a plethora of receptor proteins and bacterial secretion systems harbor components that localize extracellularly, a large portion of bacterial systems use intracellular proteins. Interestingly, studies using indirect labeling are scare in comparison to studies that use direct labeling (see 1.1 Fluorescence)[63] and image extracellular proteins. This is likely in part because using FPs precludes the need for intricate sample preparation as specimens can be imaged live or immediately after fixation. Furthermore, since protein tags have been used in microbiology for decades, bacterial strains expressing tagged targets are typically readily available or easy to produce in microbiology labs. SRM microscopy has been extensively preformed with FPs to image various bacterial targets including the cytoskeleton, membrane targets, and the cell division machinery. However, FPs emit relatively fewer photons than organic dyes, which results in

comparatively worse localization precisions [63]. For studies requiring nanoscale resolution of targets (<20 nm) a more beneficial approach would be imaging via organic dyes.

In *B. subtilis*, cell division machinery proteins FtsZ and DivIVA have been imaged using super-resolution microscopy (SRM) methods. 3D-SIM and STED microscopy revealed the Z-ring was an irregular and discontinuous structure [61,64]. Additionally, 3D-SIM and PALM imaging resolved the protein DivIVA as a dual ring structure that sandwiches the constricting division septum in vegetative cells [54,65]. Applying SRM methods to the remaining divisome components could help reveal their ensemble nanoscale architecture, distribution, and relative positioning. Ultimately, mapping divisome organization during vegetative and sporulating division modes of *B. subtilis* could uncover fundamental insights on how bacteria divide and enable researchers to compare division mechanisms between modes.

Aims and Objectives of the Thesis

Understanding how bacteria divide is a fundamental biological question. The divisome, a macromolecular complex made up of tens of proteins, performs division. However, essential questions about its nanoscale architecture and 3D component organization limit our understanding of bacterial division. In phylum Firmicutes, division can occur through vegetative growth, producing identical daughter cells, or sporulation, a survival mechanism producing a single spore.

This primary aim of this thesis is to reveal the nanoscale organization and architecture of the divisome and explore whether division-mode specific differences exist between vegetative and sporulating cells, which could reveal insights into fundamental mechanisms governing division in vegetative and sporulating cells and shed light on divergences. To achieve this aim, DNA-PAINT super-resolution microscopy (DNA-PAINT) will be used for divisome component visualization at the nanoscale.

The secondary aim of this thesis is to demonstrate the potential of DNA-PAINT super-resolution microscopy as a general tool for bacterial imaging.

The aims of this thesis will be achieved by accomplishing the following objectives:

(1) Optimizing sample preparation for intracellular bacterial protein labeling

First, a methodology for visualizing bacterial intracellular proteins labeled with nanobody binders for structured illumination microscopy (SIM) and stimulated emission depletion (STED) super-resolution microscopy will be established. The divisome protein DivIVA will be used as the proof-of-concept protein and the performance of nanobodies conjugated to STED dyes will be evaluated to determine the best nanobody-STED dye combination for bacterial imaging *in situ*.

(2) Comparing nanoscale organization of divisome components between division modes in Bacillus subtilis

The spatial organization of key divisome proteins (FtsZ, SepF, ZapA, and DivIVA) in the gram-positive bacteria *B. subtilis* will be investigated in vegetative and sporulating cells using the intracellular labeling protocol from objective (1) to perform DNA-PAINT. The relative nanoscale positioning and organization of divisome proteins will be mapped to determine differences in their placement, distribution, and or assemblies between division modes.

(3) Performing DNA-PAINT to reveal Staphylococcus aureus protein distribution

DNA-PAINT will be used to determine the distribution of the extracellular membrane protein fibronectin-binding protein (FnBP) in *Staphylococcus aureus*. This objective involves quantifying the

density of FnBP on bacterial surfaces to determine the minimum number of FnBPs required for bacterial adhesion. This will demonstrate the applicability of DNA-PAINT for extracellular bacterial protein studies and as a tool for bacterial imaging.

By completing these objectives, this thesis will advance our understanding of bacterial cell division and present DNA-PAINT as a useful tool for nanoscale imaging of bacterial proteins.

Results

Publication 1: Visualization of Bacterial Protein Complexes Labeled with Fluorescent Proteins and Nanobody Binders for STED Microscopy

Visualization of Bacterial Protein Complexes Labeled with Fluorescent Proteins and Nanobody Binders for STED Microscopy

Kimberly Cramer*, Anna-Lena Bolender*, Iris Stockmar, Ralf Jungmann, Robert Kasper[#], and Jae Yen Shin[#]

International Journal of Molecular Sciences
2019
20(14),3376
doi: 10.3390/ijms20143376

*These authors contributed equally to this work
#Authors to whom correspondence can be addressed

International Journal of
Molecular Sciences

MDPI

Article

Visualization of Bacterial Protein Complexes Labeled with Fluorescent Proteins and Nanobody Binders for STED Microscopy

Kimberly Cramer [1,2,†], Anna-Lena Bolender [3,†], Iris Stockmar [1,2], Ralf Jungmann [1,2], Robert Kasper [3,*] and Jae Yen Shin [1,2,*]

1 Max Plank Institute of Biochemistry, 82152 Martinsried, 82152 Munich, Germany
2 Faculty of Physics and Center for Nanoscience, Ludwig Maximilian University, 80539 Munich, Germany
3 Max Plank Institute of Neurobiology, 82152 Martinsried, 82152 Munich, Germany
* Correspondence: rkasper@neuro.mpg.de (R.K.); jshin@biochem.mpg.de (J.Y.S.)
† These authors contributed equally to this work.

Received: 14 June 2019; Accepted: 8 July 2019; Published: 10 July 2019

Abstract: In situ visualization of molecular assemblies near their macromolecular scale is a powerful tool to investigate fundamental cellular processes. Super-resolution light microscopies (SRM) overcome the diffraction limit and allow researchers to investigate molecular arrangements at the nanoscale. However, in bacterial cells, visualization of these assemblies can be challenging because of their small size and the presence of the cell wall. Thus, although conceptually promising, successful application of SRM techniques requires careful optimization in labeling biochemistry, fluorescent dye choice, bacterial biology and microscopy to gain biological insights. Here, we apply Stimulated Emission Depletion (STED) microscopy to visualize cell division proteins in bacterial cells, specifically *E. coli* and *B. subtilis*. We applied nanobodies that specifically recognize fluorescent proteins, such as GFP, mCherry2 and PAmCherry, fused to targets for STED imaging and evaluated the effect of various organic fluorescent dyes on the performance of STED in bacterial cells. We expect this research to guide scientists for in situ macromolecular visualization using STED in bacterial systems.

Keywords: STED; bacteria; super-resolution microscopy; fluorescent proteins; nanobody; cell division

1. Introduction

The expression of targets of interest fused to fluorescent proteins (FPs) is one of the labeling approaches utilized to indirectly or directly visualize proteins with diffraction-limited and super-resolution microscopy (SRM) such as stimulated emission depletion (STED) [1,2], structured illumination microscopy (SIM) [3,4], DNA points accumulation for imaging in nanoscale topography (DNA-PAINT) [5], (direct)stochastic optical reconstruction ((d)STORM) [6,7] and photoactivatable localization (PALM) [8] microscopies. While imaging of targets in bacterial cells has mostly used genetically encoded fluorescent proteins for direct visualization, indirect visualization of FPs using binders with organic dyes could provide higher versatility and higher spatial resolution due to often superior photophysical properties [9]. However, in the latter approach, it remains challenging to achieve a high labeling efficiency of intracellular proteins because of the limited cell wall permeability [9,10] (see Figure 1).

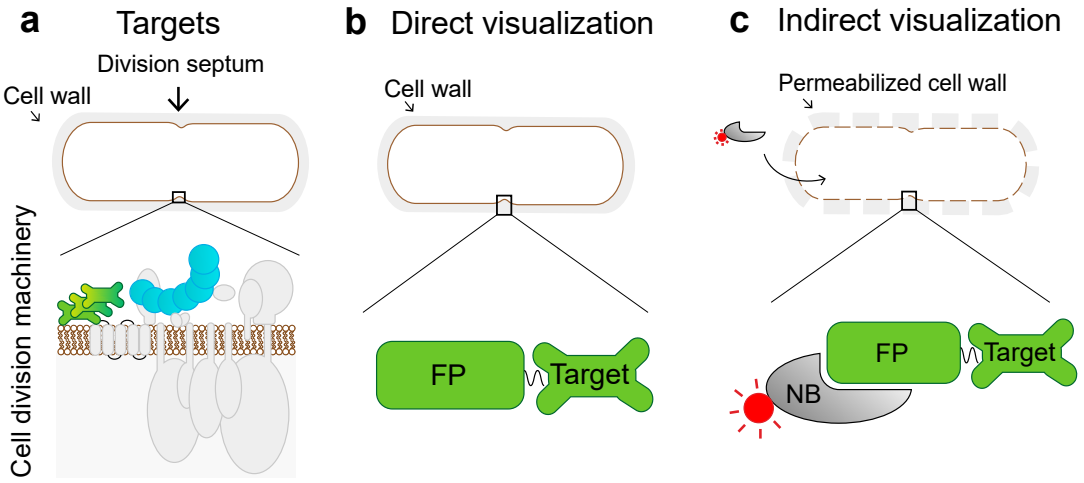

Figure 1. Schematic diagram of the bacterial protein complex and methods for visualization. (**a**) Cartoon representation of the *B. subtilis* cell featuring cell wall (gray), cell membrane (brown), and cell division proteins forming the cell division machinery. Proteins FtsZ and DivIVA visualized in this study are highlighted in blue and green, respectively. (**b**) The signal from a fluorescent protein (FP) fused to the target protein is directly visualized or (**c**) the target is indirectly visualized by fluorescently (red) labeled nanobodies (NB).

The direct visualization of FPs, expressed as fusion proteins in bacterial targets, has been widely implemented in super-resolution light microscopies [9,11,12]. One of the most beneficial aspects of this method is that bacterial samples can be directly imaged—even live—without intensive sample preparation. Using direct visualization of FPs with SRM, researchers have observed protein assemblies, such as the cell division machinery [9,13–17], membrane microdomains [18–20], and the cytoskeleton [21,22] in various bacterial organisms such as *Escherichia coli*, *Bacillus subtilis*, *Staphylococcus aureus* and *Caulobacter crescentus*. In addition, recent developments of dual-color imaging using FPs for SIM [15,23] and STED [24] have led scientists to gain biological insights into the relationship between the ultrastructure of protein assemblies and their function, which would otherwise not been accessible.

On the other hand, imaging immunolabeled samples using super-resolution microscopy has been performed to a lesser extent in bacterial cells, most likely due to the limited labeling efficiency of intracellular proteins given by low cell wall permeability [9,10]. In this indirect visualization method, binders, i.e., primary antibodies that bind the target of interest, followed by secondary antibodies carrying a fluorescent molecule, need to enter bacteria. For binders to successfully reach intracellular targets, the cell wall must be at least partly digested using enzymes such as lysozyme. Although limited, there are a few examples in the literature that implemented antibodies to visualize bacterial proteins with SRM. For instance, FtsZ, one of the most essential cell division proteins, was visualized with STED and SIM microscopy using primary and secondary antibody binders in *B. subtilis* cells [25,26]. Most recently, two different cell division proteins, FtsZ and FtsN, were simultaneously visualized using antibody binders in *E. coli* cells [24].

Although valuable, indirect immunolabeling using primary and secondary antibodies increases the apparent size of the visualized structure or introduces a localization bias of 10–20 nm when using SRM [27–29]. One way of reducing the distance between the target of interest and fluorescent label (linkage error) is by using significantly smaller binders, such as nanobodies (~2 nm) or FAB fragments (a smaller version of an antibody) [30]. To this extent, Vedyaykin et al. visualized FtsZ in *E. coli* cells using a conventional primary antibody and a secondary FAB fragment with STORM [31]. Recently, the use of dye-labeled nanobodies as nanoscale detection tools has been implemented to visualize protein complexes in eukaryotic cells with SRM [30].

Another crucial aspect to consider when performing SRM is dye properties. Some properties (e.g., high brightness, photostability, low phototoxicity) are universally desired among all SRM techniques,

however, some specific properties are of higher or lower importance depending on the imaging modality. For instance, STORM requires dyes that blink, i.e., switch between fluorescence ON- and OFF-states, such as Cy5 derivatives [32]. For STED, however, it is advantageous that dyes do not blink [33]. Additionally, a particular property of a dye (e.g., hydrophobicity, net charge) might influence the specificity of a binder. Thus, the identification of a functional combination of dyes and binders most likely depends on the organism under investigation and even upon the target of interest.

Despite great strides in bacterial SRM, research using the direct visualization of targets greatly outweighs that using indirect visualization methods, which is mainly due to the comparably more complex sample preparation requirements and the limited availability of good binders. In this study, we sought to assay labeling approaches for STED microscopy, increase the number of imageable targets in *B. subtilis* by using nanobody binders that recognize fluorescent proteins, such as green fluorescent protein (GFP) or red fluorescent protein (RFP) and their derivatives, and identify combinations of binders and dyes that are suitable for STED imaging in bacterial cells.

2. Results

2.1. Nanobodies Recognizing Fluorescent Proteins Enable Visualization of Target Proteins in Bacteria with STED Microscopy

Targets under investigation can be visualized indirectly using binders that specifically detect targets or fluorescent proteins fused to a target. Here, we implement a visualization method based on nanobodies that bind FPs for conventional confocal and STED microscopy (Figure 1). Our workflow comprises three main steps: (1) evaluation of whether FPs fused to target proteins are innocuous to the target protein function; (2) optimization for cell-wall permeabilization; (3) visualization of the target proteins using fluorescently labeled nanobodies.

To establish this, we chose DivIVA as a candidate protein. DivIVA is a cell division protein in the Gram-positive model bacterium *B. subtilis*, and its ultrastructure can only be visualized with super-resolution microscopy [14,34]. *B. subtilis* expressing either GFP or mCherry2 [35] fused to DivIVA and showed a fluorescent band at the division septa when imaged using diffraction-limited microscopy (Figure 2a,b). As expected, these proteins showed double bands (hereafter referred to as "DivIVA dual band") when visualized with SIM microscopy. The distances between the two bands (ranging from ~80 nm to ~200 nm) were similar to previous reports (Figure 2a,b, Figure S1) [14,34].

Unlike eukaryotic cells, bacterial cells contain a cell wall that impedes the intracellular delivery of exogenous molecules, in our case nanobodies conjugated to fluorophores, potentially "trapping" these molecules and preventing their intracellular delivery. Thus, to efficiently deliver molecules, we first optimized the cell wall digestion step by treating fixed cells with various concentrations of lysozyme and delivering a fluorescently labeled binder that recognizes FPs. Specifically, we employed *B. subtilis* strains expressing photoactivatable mCherry (PAmCherry) fused to the DivIVA protein. The condition in which the cells presented the highest fluorescent signal from the nanobody at the cell division septa was considered the best for cell-wall permeabilization (Figure S2b). The optimal cell permeabilization condition might differ from species to species and even strain to strain.

Visualization of GFP and mCherry2—fused to DivIVA—using the respective Atto647n-conjugated nanobody binders (NB^{GFP}-Atto647n and NB^{RFP}-Atto647n) shows a similar DivIVA dual-band localization pattern when compared to the direct visualization of FPs (Figure 2). These results indicate that both binders specifically bind the corresponding fluorescent proteins. As expected from our confocal imaging results and the property of Atto647n for STED imaging [36], Atto647n was suitable to image bacterial proteins and resolve the dual band of DivIVA with STED microscopy. In contrast, confocal microscopy was not able to resolve the dual band of DivIVA (Figure 2c,d). As a control experiment, we compared STED performance for organic dye (NB^{RFP}-Atto647n) and fluorescent protein, specifically mCherry2. Our results showed that the use of organic dye, specifically Atto647n (i.e., NB-Atto647n) significantly enhanced the STED signal (Figure S3).

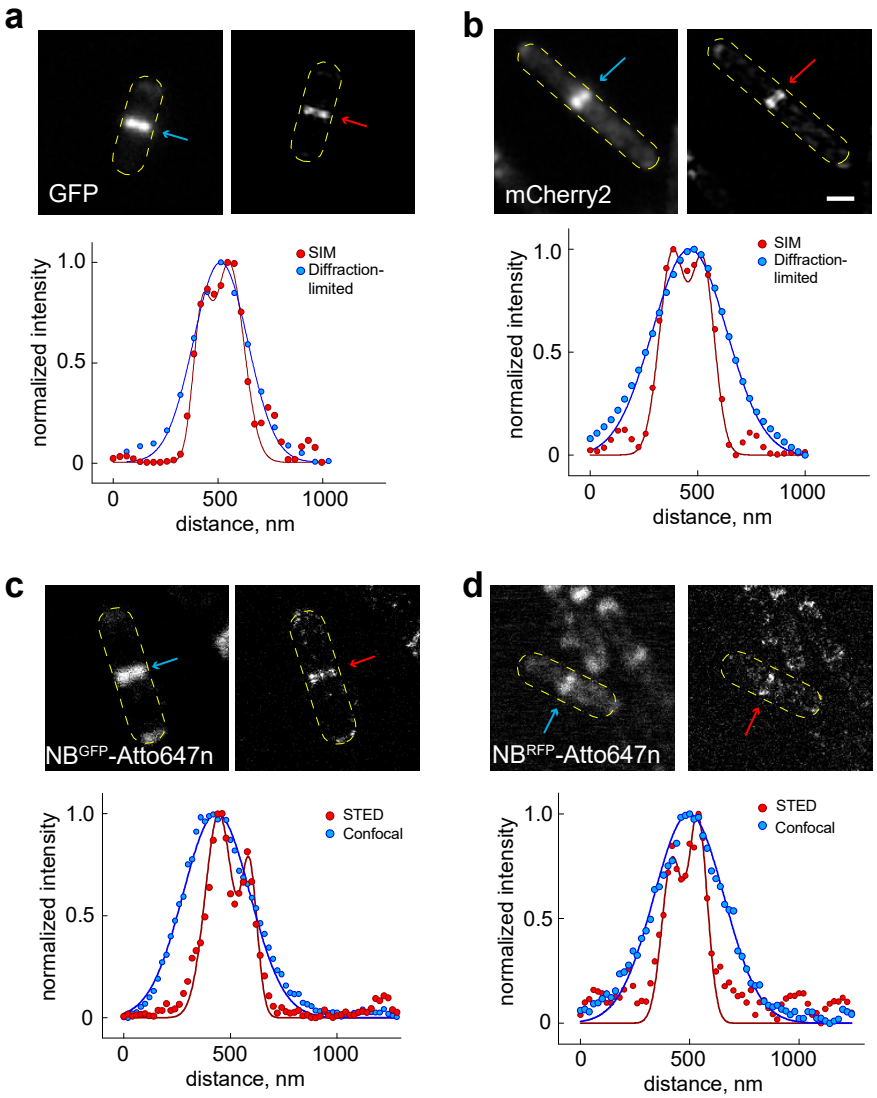

Figure 2. Visualization of the cell division protein DivIVA using SIM and STED microscopy. (**a**,**b**) Fluorescent signal from cells expressing either GFP or mCherry2 fused to DivIVA was imaged using diffraction-limited (left panel) and SIM (right panel) microscopies. Intensity profile of the signal along the longitudinal axis of the cell is shown in the lower panel. (**c**,**d**) Fluorescent signal from cells incubated with the Atto647n conjugated to either GFP nanobody (NB^{GFP}-Atto647n) or RFP nanobody (NB^{RFP}-Atto647n) was imaged using a conventional confocal (left panel) and STED (right panel) microscopy. The intensity profile of the signal along the longitudinal axis of the cell is shown in the lower panel. Scale bar 1 µm.

Thus, our established protocol using binders for RFP and GFP allowed us to efficiently image bacterial protein complexes with STED microscopy (Figures 2 and 3). Although we could clearly resolve the DivIVA dual band at the division septa using both binders, the cellular background appeared higher upon visual inspection when using the RFP binder, NB^{RFP}-Atto647n (Figure 3). To quantify this background, we determined the fluorescent signal at the cell division septa (A) and outside of the septa (B) (Figure S4), and used these values to calculate a signal-to-background ratio (A/B) and the percentage of the cellular background (B/A*100). Interestingly, NB^{RFP}-Atto647n exhibited three times more background than the GFP binder, NB^{GFP}-Atto647n (Table 1).

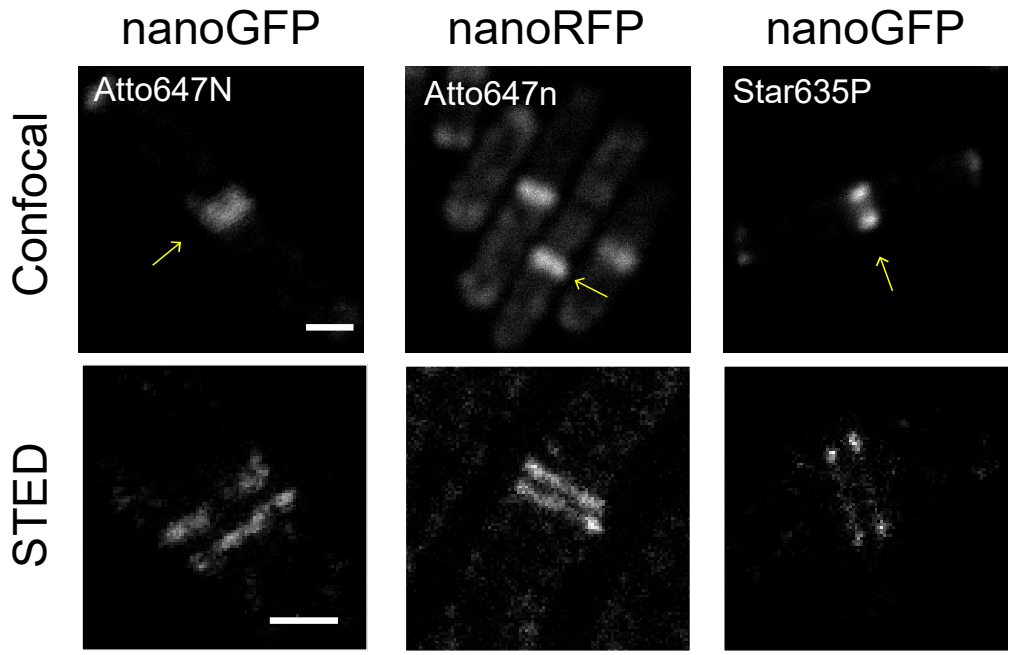

Figure 3. Comparison of Atto647n and Star635p for bacterial STED imaging. *B. subtilis* cells expressing either DivIVA-GFP or DivIVA-mCherry2 were visualized using nanobodies conjugated with Atto647n or Star635p. STED images show an enlarged field of view of the object marked with an arrow in the confocal image. Scale bars 1 µm and 0.5 µm, for confocal and STED images, respectively.

Table 1. Summary of Dyes Performance for STED Imaging in Bacterial Cells.

Nanobody-Dye	Target	Signal-to-Background Ratio	Cellular Background
NB^{GFP}-Atto647n	GFP	12	11 %
NB^{RFP}-Atto647n	mCherry2	3	36 %
NB^{GFP}-Atto594	GFP	n.a. *	n.a. *
NB^{RFP}-Atto594	mCherry2	3	38 %
NB^{RFP}-Star600	PAmCherry	2.4	42 %
NB^{GFP}-Star635p	GFP	3	34 %

All targets were fused to DivIVA protein. Signal-to-cellular background ratio and cellular background were calculated as described in the main text and in Figure S4. * not applicable (n.a.), values corresponding to signal and cellular background could not be determined due to high cellular background.

2.2. Evaluation of Unspecific Binding for GFP and RFP Nanobodies in Bacterial Cells

We reasoned that the higher cellular background of the RFP binder could be due to either (1) higher cytoplasmic contents in actual DivIVA-mCherry2 molecules compared to the *B. subtilis* strain expressing the DivIVA-GFP protein, or (2) unspecific binding of the NB^{RFP}-Atto647n. To rule out these two possibilities, we quantified, as described above, the background fluorescence of mCherry2 and GFP in bacillus strains that either expressed DivIVA-mCherry2 or DivIVA-GFP. Contrary to the cellular background observed in STED images, both strains showed similar backgrounds of approximately 40% and 35% for DivIVA-GFP and DivIVA-mCherry2, respectively (Table S1). Interestingly, the RFP binder, NB^{RFP}-Star600, also recognized the PAmCherry fusion protein, although with a higher cellular background than the mCherry2 fusion protein (Table 1). Altogether, these results indicate that (1) both the GFP and RFP binders are suitable for STED microscopy, (2) the GFP binder presents higher specificity to GFP than the RFP binder does to mCherry2, and (3) the RFP binder binds unspecifically to *B. subtilis* cells.

2.3. Evaluation of Fluorescent Dyes for STED Imaging in Bacterial Cells

Next, we systematically evaluated the suitability and performance of various dyes to image proteins in bacteria using STED microscopy. Furthermore, we investigated the effect of the dye on unspecific nanobody binding. To this end, we imaged DivIVA-mCherry2 or DivIVA-GFP expressing bacillus strains using nanobodies conjugated with various fluorophores that are reported to be suitable for STED microscopy. However, these dyes have mostly been evaluated for suitability in eukaryotic cells [36,37]. Specifically, we employed Atto647n, Atto594, Star600 and Star635p dyes (properties compiled in Table S2) conjugated either to the RFP or GFP nanobodies.

Our STED results show that NB^{GFP}-Atto647n produced images with at least four times higher signal-to-background than the RFP binders conjugated with the same dye (Table 1). Interestingly, the background for the GFP nanobody altered when conjugated with different dyes. The cellular background when using NB^{GFP} increased as follows: Atto647n < Star635p < Atto594 (Figure 4, Table 1). This result indicates that all the tested dyes induced unspecific binding of NB^{GFP} in *B. subtilis* cells. In contrast, we did not observe significant differences in the cellular background for the NB^{RFP} when conjugated with different dyes (Figure 4, Table 1), indicating that the specificity of the NB^{RFP} is less influenced by the dyes compared to the GFP nanobody. Note that the spectral overlap between Atto594 and mCherry2 might have increased the signal-to-background ratio (Table 1). However, STED microscopy directly observing the mCherry2 fusion protein qualitatively showed a poorer signal-to-background ratio (Figure S3).

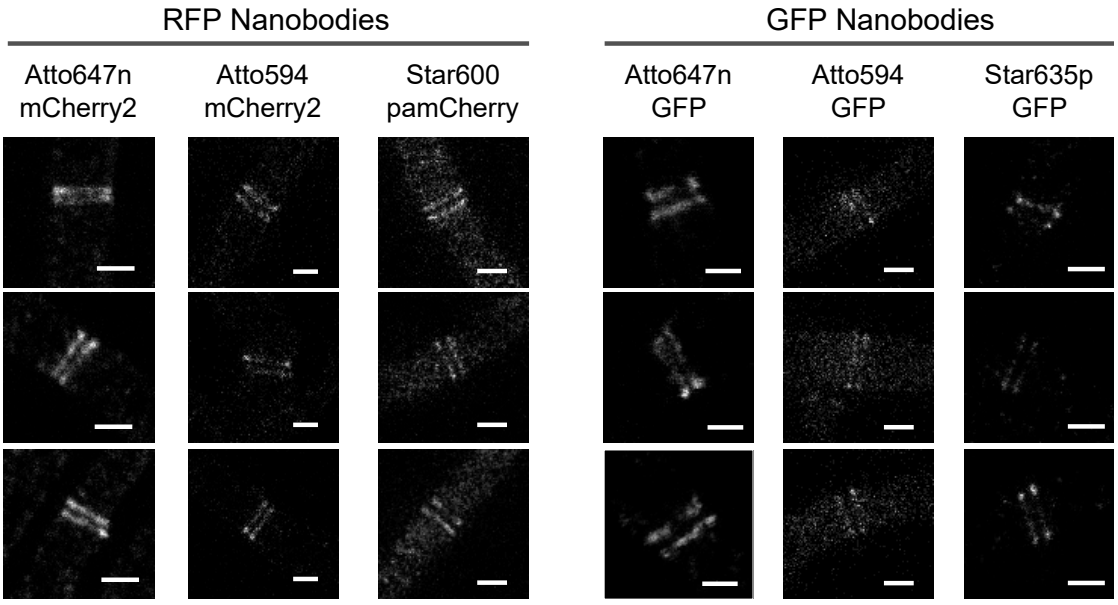

Figure 4. STED images of DivIVA dual bands visualized with nanobodies. *B. subtilis* cells expressing GFP, mCherry2 or PAmCherry fused to DivIVA were imaged using nanobodies containing the indicated organic fluorescent dyes. Scale bars 500 nm.

3. Discussion

In this study, we implemented for the first time a methodology for STED super-resolution microscopy to visualize bacterial protein complexes using nanobodies that bind fluorescent proteins. Interestingly, good STED dye performers for eukaryotic cells were not necessarily equally good for bacterial cells. Although we implemented nanobody-based STED in bacterial cells, we expect this research to be useful to the implementation of experimental design and sample preparation workflow for other species containing cell walls such as yeasts, plant cells and archaea.

To assay our approach, we visualized FtsZ and DivIVA cell division proteins because both form assemblies that are well described with super-resolution microscopies, e.g., SIM, STED, PALM and

STORM [9,12,14,25]. Our super-resolved DivIVA dual band presented similar dimensions (Figure S1) to previously reported values [14,34]. However, results indicate different degrees of unspecific binding (background values in Table S1), most likely due to the properties of the organic dye attached to the nanobodies. All nanobodies employed here resolved the DivIVA dual band (Figures 2–4). In good agreement with the literature, our STED protocol also visualized the FtsZ protein localized in a "patchy" distribution along the circumference of the cell division plane in *E. coli* cells (Figure S5) [12,25].

Although STED can be performed in live bacteria [20,24,38,39], our aim was to establish a method based on immunolabeling, since organic fluorescent dyes exhibit higher photostability compared to fluorescent proteins [38]. Consequently, these dyes tolerate higher STED beam intensities, which is directly related to the resolution that STED microscopy can achieve [37,39]. The benefits of organic dyes in comparison to FPs were further demonstrated here when STED images of mCherry2 and NB^{RFP}-Atto647n were directly compared in the same cell (Figure S3). In addition, development efforts have increased the number of suitable STED dyes for cell imaging [37,38], which, when used in combination with the immunolabeling method, offers higher versatility. In this regard, the ideal dye–nanobody pair should be innocuous to the specificity of the nanobody. However, this appears to not always be the case, as we have shown here (Figure 4 and Table 1). Additionally, the performance and suitability of a dye–nanobody pair might vary according to the targets and organisms under investigation. For example, while Atto594 dye performs well for eukaryotic cell imaging [40,41], it performed poorly in bacterial cell imaging (Figure 4 and Table 1). However, Atto647n performed equally well in bacterial cells, as previously reported for imaging of eukaryotic targets [37].

Our immunolabeling approach should be particularly interesting to labs that already have large strain collections of organisms expressing target proteins fused to FPs. Additionally, the growing repertoire of nanobodies can be used not only for STED microscopy, but also other imaging modalities such as STORM [30]. Furthermore, one could also employ nanobodies that directly or indirectly recognize their targets using primary and secondary nanobodies. Likewise, direct and indirect methods using FPs, nanobodies, and combinations of primary and secondary antibodies can be combined to make imaging much more versatile and used for implementation of multi-color imaging.

Finally, and most importantly, the presence of the cell wall in bacteria is an essential organelle to consider since it must be digested for the intracellular delivery of binders. As shown in this study, identifying a digestion condition that favors the delivery of exogeneous molecules while preserving cell morphology allowed us to visualize protein assemblies, namely DivIVA and FtsZ, with STED microscopy (Figure 2, Figures S2 and S5). Additionally, another factor to consider is identifying suitable and better performing fluorescent dyes for a particular target and the organism under investigation. The literature on STED microscopy for bacterial cells is much more limited compared to the literature available on STED microscopy for eukaryotic cells. Ideally, dyes should be innocuous to the specific binding of nanobodies and antibodies to their targets. However, this is not always the case, as it was shown that coupling Star635p or Atto594 dye to the GFP nanobody increases unspecific binding (compare cellular backgrounds in Table 1). Thus, we expect our table of signal-to-background ratio and the cellular background to be useful in improving experimental design (Table 1, Table S1).

4. Materials and Methods

4.1. Reagents and Cell Culture

Bacterial strains used in this study are listed in the Supplementary Materials (Table S3). Luria Bertani broth, and SMG ([15 mM (NH4)2SO4, 61 mM K2HPO4, 44 mM KH2PO4, 3.4 mM sodium citrate 2xH2O, 1.7 mM MgSO4, 5.9 mM glutamate and 27 mM glucose] supplemented with 1.0 mM tryptophan) were used to grow bacteria. The cells were fixed with paraformaldehyde (P6148, Merck, Kenilworth, NJ, USA), immobilized with poly-L-lysine (Sigma P8920, St. Louis, MO, USA), and permeabilized with lysozyme (ThermoFisher, 90082, Waltham, MA, USA). PBSG (PBS + 20nM glucose) and PBST (PBS + 0.02% Tween20) were used for washing. ProLong Diamond Antifade

Mountant (ThermoFisher, P36965, Waltham, MA, USA) or Abberior Mount Liquid Antifade (MM-2009, Abberior Instruments, Göttingen, Germany) were used as mounting media.

4.2. SIM Imaging

4.2.1. Bacterial Sample Preparation

Cell Growth. Strains BHF3 and 1803 were streaked onto LB plates. Single colonies were grown overnight in LB medium at 30 °C, 220 rpm.

Live Cell Sample Preparation. Strain 1803 was inoculated 1:100 into fresh LB medium the next morning and grown at 30 °C and 150 rpm until OD_{600} = 0.5. An amount of 200 µL of cell culture was centrifuged for 20–30 s at 2000 xg. A cellular pellet was resuspended in 3 µL of LB medium and spotted on a 1.5% (*w*/*v*) agarose pad. A glass coverslip was placed on the agarose pad and cells were immediately imaged.

Fixed Cell Sample Preparation. Strain BHF3 was grown, fixed, and immobilized as performed in Stockmar et al. (2018). An amount of 2% paraformaldehyde was used for fixation. The maximum cellular density per fixation reaction was OD_{600} = 0.25. Cells were immobilized in multi-well chambers (µ-Slide Well Glass Bottom, Ibidi 80827, Gräfeling, Germany).

4.2.2. SIM Data Acquisition and Processing

SIM images were acquired with a commercial Zeiss Elyra PS.1 microscope (Zeiss, Oberkochen, Germany) using an PCO pco.edge 4.2 m sCMOS Camera. An alpha Plan-Apochromat 100x/1,46 Oil DIC objective lens was used for fixed cell imaging and a C-Apochromat 63x/1,2 W Corr objective lens for live cell imaging. Images of strains BHF3 and strain 1803 appearing in Figure 2 are individual slices within a 2D z-stack. Exposure time was 200 ms for both GFP and mCherry2 imaging. GFP and mCherry2 were excited with a 488 nm OPSL Diode laser and a 561 nm OPSL Diode laser, respectively. Image analysis was done using Zeiss ZEN 2.1 software (Zeiss, Oberkochen, Germany). A noise filter of −3.2447 with a Max Isotrop was applied on the DivIVA-GFP image (Figure 2a), and a noise filter of −5 with a Max Isotrop of 1 was applied for the DivIVA-mCherry2 image (Figure 2b).

4.3. STED Imaging

4.3.1. Bacterial Sample Preparation

Cell Growth. Strains 1803 and BHF3 were grown as previously described [34], except that the cells were grown overnight in LB medium.

Fixation and Immobilization. The cells were fixed as described in Section 4.2, via SIM Imaging. The maximum cellular density per fixation reaction was OD_{600} = 0.25. The fixed cells were immobilized on coverslips that had been incubated for 30 min with 0.01% poly-L-lysine solution and washed three times with Milli-Q water. Amounts of 150–200 µL of fixed cells containing a cellular density of ~OD_{600} 0.8 were added to each coverslip and left to settle for 30 min. The cells were then gently washed three times with PBSG.

Immunolabeling Protocol. The immobilized cells were permeabilized using 0.2 mg/mL lysozyme in PBSG for 5 min at 30 ºC, then immediately blocked for 1 h in 2% BSA. Nanobody binders were incubated overnight at 4 ºC. The following day, the cells were washed three times with PBST. All binders with their corresponding dilutions, targets and figures are found in Table S4. Abberior Mount Liquid Antifade or ProLong® Diamond Antifade Mountant was then added to glass microscope slides and coverslips were placed on top. After 30 min, the slides were sealed with clear or tan nail polish.

4.3.2. STED and Confocal Data Acquisition and Processing

Confocal and STED images were acquired using a STEDYCON nanoscope system (Abberior Instruments, Göttingen, Germany) mounted on a Leica DMR X2 microscope and equipped with

a specialized STED 100x oil immersion objective, NA 1.4 (Leica Microsystems). The excitation wavelengths were used according to the dye of the fluorescent protein specification: GFP with 488 nm, Atto594 and STAR600 with 561 nm, and 640 nm for Atto647N and Star635P. For both emission channels, a depletion laser at 775 nm was used. Fluorescent signals were detected on 3 separate APD detectors using standard bandpass filters (APD1: 650–700 nm, APD2: 575–625 nm, APD3: 505–545 nm) and a gated detection window starting at 1 ns after the laser pulse and closing after 6 ns. Finally, 2D STED images as single planes or as z-stacks with a slice distance of 200 nm were recorded and regions of interest were identified and processed using Fiji software [42,43] and OriginPro 9.1G (OriginLab, Northampton, MA, USA).

Supplementary Materials: Supplementary materials can be found at http://www.mdpi.com/1422-0067/20/14/3376/s1.

Author Contributions: Conceptualization, J.Y.S.; Data curation, K.C.; Formal analysis, K.C., A.-L.B., R.K. and J.Y.S.; Funding acquisition, R.J., R.K.; Investigation, J.Y.S., K.C., A.-L.B. and R.K.; Methodology, K.C., R.K., I.S. and J.Y.S.; Project administration, R.J. and J.Y.S.; Resources; Writing—original draft, K.C., R.K. and J.Y.S.; Writing—review and editing, K.C., A.-L.B., R.J., R.K. and J.Y.S.

Funding: This work was supported in part by the German Research Foundation through the Emmy Noether Program (DFG JU 2957/1-1 to R.J.), the European Research Council through an ERC Starting Grant (MolMap; grant agreement number 680241 to R.J.) and the Max Planck Society (R.J. and R.K.)

Acknowledgments: We thank Hartmann Harz, Andreas Maiser and Katharina Brandstetter for Nano^{RFP}-Star600; Marc Bramkamp and Petra Schwille for strains.

Conflicts of Interest: The authors declare no conflict of interest.

References

1. Hell, S.W.; Wichmann, J. Breaking the diffraction resolution limit by stimulated emission: Stimulated-emission-depletion fluorescence microscopy. *Opt. Lett.* **1994**, *19*, 780–782. [CrossRef] [PubMed]
2. Klar, T.A.; Jakobs, S.; Dyba, M.; Egner, A.; Hell, S.W. Fluorescence microscopy with diffraction resolution barrier broken by stimulated emission. *Proc. Natl. Acad. Sci. USA* **2000**, *97*, 8206–8210. [CrossRef] [PubMed]
3. Frohn, J.T.; Knapp, H.F.; Stemmer, A. True optical resolution beyond the Rayleigh limit achieved by standing wave illumination. *Proc. Natl. Acad. Sci. USA* **2000**, *97*, 7232–7236. [CrossRef] [PubMed]
4. Gustafsson, M.G. Surpassing the lateral resolution limit by a factor of two using structured illumination microscopy. *J. Microsc.* **2000**, *198*, 82–87. [CrossRef] [PubMed]
5. Strauss, S.; Nickels, P.C.; Strauss, M.T.; Jimenez Sabinina, V.; Ellenberg, J.; Carter, J.D.; Gupta, S.; Janjic, N.; Jungmann, R. Modified aptamers enable quantitative sub-10-nm cellular DNA-PAINT imaging. *Nat. Methods* **2018**, *15*, 685–688. [CrossRef] [PubMed]
6. Rust, M.J.; Bates, M.; Zhuang, X. Sub-diffraction-limit imaging by stochastic optical reconstruction microscopy (STORM). *Nat. Methods* **2006**, *3*, 793–796. [CrossRef] [PubMed]
7. Heilemann, M.; van de Linde, S.; Schüttpelz, M.; Kasper, R.; Seefeldt, B.; Mukherjee, A.; Tinnefeld, P.; Sauer, M. Subdiffraction-resolution fluorescence imaging with conventional fluorescent probes. *Angew. Chem. Int. Ed. Engl.* **2008**, *47*, 6172–6176. [CrossRef]
8. Betzig, E.; Patterson, G.H.; Sougrat, R.; Lindwasser, O.W.; Olenych, S.; Bonifacino, J.S.; Davidson, M.W.; Lippincott-Schwartz, J.; Hess, H.F. Imaging intracellular fluorescent proteins at nanometer resolution. *Science* **2006**, *313*, 1642–1645. [CrossRef]
9. Coltharp, C.; Xiao, J. Superresolution microscopy for microbiology. *Cell. Microbiol.* **2012**, *14*, 1808–1818. [CrossRef]
10. Schoen, I.; Ries, J.; Klotzsch, E.; Ewers, H.; Vogel, V. Binding-activated localization microscopy of DNA structures. *Nano Lett.* **2011**, *11*, 4008–4011. [CrossRef]
11. Schneider, J.P.; Basler, M. Shedding light on biology of bacterial cells. *Philos. Trans. R. Soc. Lond. B Biol. Sci.* **2016**, *371*, 20150499. [CrossRef] [PubMed]
12. Holden, S. Probing the mechanistic principles of bacterial cell division with super-resolution microscopy. *Curr. Opin. Microbiol.* **2018**, *43*, 84–91. [CrossRef] [PubMed]

13. Shin, J.Y.; Lopez-Garrido, J.; Lee, S.-H.; Diaz-Celis, C.; Fleming, T.; Bustamante, C.; Pogliano, K. Visualization and functional dissection of coaxial paired SpoIIIE channels across the sporulation septum. *eLife* **2015**, *4*, 3253. [CrossRef] [PubMed]
14. Eswaramoorthy, P.; Erb, M.L.; Gregory, J.A.; Silverman, J.; Pogliano, K.; Pogliano, J.; Ramamurthi, K.S. Cellular architecture mediates DivIVA ultrastructure and regulates min activity in Bacillus subtilis. *MBio* **2011**, *2*, e00257-11. [CrossRef] [PubMed]
15. Eswaramoorthy, P.; Winter, P.W.; Wawrzusin, P.; York, A.G.; Shroff, H.; Ramamurthi, K.S. Asymmetric division and differential gene expression during a bacterial developmental program requires DivIVA. *PLoS Genet.* **2014**, *10*, e1004526. [CrossRef] [PubMed]
16. Holden, S.J.; Pengo, T.; Meibom, K.L.; Fernandez Fernandez, C.; Collier, J.; Manley, S. High throughput 3D super-resolution microscopy reveals Caulobacter crescentus in vivo Z-ring organization. *Proc. Natl. Acad. Sci. USA* **2014**, *111*, 4566–4571. [CrossRef]
17. Buss, J.; Coltharp, C.; Shtengel, G.; Yang, X.; Hess, H.; Xiao, J. A multi-layered protein network stabilizes the Escherichia coli FtsZ-ring and modulates constriction dynamics. *PLoS Genet.* **2015**, *11*, e1005128. [CrossRef]
18. Schneider, J.; Klein, T.; Mielich-Süss, B.; Koch, G.; Franke, C.; Kuipers, O.P.; Kovács, Á.T.; Sauer, M.; Lopez, D. Spatio-temporal remodeling of functional membrane microdomains organizes the signaling networks of a bacterium. *PLoS Genet.* **2015**, *11*, e1005140. [CrossRef]
19. Bach, J.N.; Giacomelli, G.; Bramkamp, M. Sample Preparation and Choice of Fluorophores for Single and Dual Color Photo-Activated Localization Microscopy (PALM) with Bacterial Cells. *Methods Mol. Biol.* **2017**, *1563*, 129–141.
20. Dempwolff, F.; Schmidt, F.K.; Hervás, A.B.; Stroh, A.; Rösch, T.C.; Riese, C.N.; Dersch, S.; Heimerl, T.; Lucena, D.; Hülsbusch, N.; et al. Super Resolution Fluorescence Microscopy and Tracking of Bacterial Flotillin (Reggie) Paralogs Provide Evidence for Defined-Sized Protein Microdomains within the Bacterial Membrane but Absence of Clusters Containing Detergent-Resistant Proteins. *PLoS Genet.* **2016**, *12*, e1006116. [CrossRef]
21. Olshausen, P.V.; Defeu Soufo, H.J.; Wicker, K.; Heintzmann, R.; Graumann, P.L.; Rohrbach, A. Superresolution imaging of dynamic MreB filaments in B. subtilis—A multiple-motor-driven transport? *Biophys. J.* **2013**, *105*, 1171–1181. [PubMed]
22. Billaudeau, C.; Yao, Z.; Cornilleau, C.; Carballido-López, R.; Chastanet, A. MreB Forms Subdiffraction Nanofilaments during Active Growth in Bacillus subtilis. *MBio* **2019**, *10*, e01879–e01918. [PubMed]
23. Lesterlin, C.; Ball, G.; Schermelleh, L.; Sherratt, D.J. RecA bundles mediate homology pairing between distant sisters during DNA break repair. *Nature* **2014**, *506*, 249–253. [CrossRef] [PubMed]
24. Söderström, B.; Chan, H.; Shilling, P.J.; Skoglund, U.; Daley, D.O. Spatial separation of FtsZ and FtsN during cell division. *Mol. Microbiol.* **2018**, *107*, 387–401. [CrossRef] [PubMed]
25. Jennings, P.C.; Cox, G.C.; Monahan, L.G.; Harry, E.J. Super-resolution imaging of the bacterial cytokinetic protein FtsZ. *Micron* **2011**, *42*, 336–341. [CrossRef] [PubMed]
26. Strauss, M.P.; Liew, A.T.F.; Turnbull, L.; Whitchurch, C.B.; Monahan, L.G.; Harry, E.J. 3D-SIM super resolution microscopy reveals a bead-like arrangement for FtsZ and the division machinery: Implications for triggering cytokinesis. *PLoS Biol.* **2012**, *10*, e1001389. [CrossRef] [PubMed]
27. Ries, J.; Kaplan, C.; Platonova, E.; Eghlidi, H.; Ewers, H. A simple, versatile method for GFP-based super-resolution microscopy via nanobodies. *Nat. Methods* **2012**, *9*, 582–584. [PubMed]
28. Deschout, H.; Cella Zanacchi, F.; Mlodzianoski, M.; Diaspro, A.; Bewersdorf, J.; Hess, S.T.; Braeckmans, K. Precisely and accurately localizing single emitters in fluorescence microscopy. *Nat. Methods* **2014**, *11*, 253–266. [PubMed]
29. Bates, M.; Huang, B.; Dempsey, G.T.; Zhuang, X. Multicolor super-resolution imaging with photo-switchable fluorescent probes. *Science* **2007**, *317*, 1749–1753. [CrossRef]
30. Beghein, E.; Gettemans, J. Nanobody Technology: A Versatile Toolkit for Microscopic Imaging, Protein-Protein Interaction Analysis, and Protein Function Exploration. *Front. Immunol.* **2017**, *8*, 771. [CrossRef]
31. Vedyaykin, A.D.; Vishnyakov, I.E.; Polinovskaya, V.S.; Khodorkovskii, M.A.; Sabantsev, A.V. New insights into FtsZ rearrangements during the cell division of Escherichia coli from single-molecule localization microscopy of fixed cells. *Microbiologyopen* **2016**, *5*, 378–386. [CrossRef] [PubMed]
32. Heilemann, M.; Margeat, E.; Kasper, R.; Sauer, M.; Tinnefeld, P. Carbocyanine dyes as efficient reversible single-molecule optical switch. *J. Am. Chem. Soc.* **2005**, *127*, 3801–3806. [CrossRef] [PubMed]

33. Kasper, R.; Harke, B.; Forthmann, C.; Tinnefeld, P.; Hell, S.W.; Sauer, M. Single-molecule STED microscopy with photostable organic fluorophores. *Small* **2010**, *6*, 1379–1384. [CrossRef] [PubMed]
34. Stockmar, I.; Feddersen, H.; Cramer, K.; Gruber, S.; Jung, K.; Bramkamp, M.; Shin, J.Y. Optimization of sample preparation and green color imaging using the mNeonGreen fluorescent protein in bacterial cells for photoactivated localization microscopy. *Sci. Rep.* **2018**, *8*, 10137. [CrossRef] [PubMed]
35. Thomaides, H.B.; Freeman, M.; El Karoui, M.; Errington, J. Division site selection protein DivIVA of Bacillus subtilis has a second distinct function in chromosome segregation during sporulation. *Genes Dev.* **2001**, *15*, 1662–1673. [CrossRef] [PubMed]
36. Oracz, J.; Westphal, V.; Radzewicz, C.; Sahl, S.J.; Hell, S.W. Photobleaching in STED nanoscopy and its dependence on the photon flux applied for reversible silencing of the fluorophore. *Sci. Rep.* **2017**, *7*, 11354. [CrossRef] [PubMed]
37. Wurm, C.A.; Kolmakov, K.; Göttfert, F.; Ta, H.; Bossi, M.; Schill, H.; Berning, S.; Jakobs, S.; Donnert, G.; Belov, V.N.; et al. Novel red fluorophores with superior performance in STED microscopy. *Opt. Nanoscopy* **2012**, *1*, 7. [CrossRef]
38. Grotjohann, T.; Testa, I.; Leutenegger, M.; Bock, H.; Urban, N.T.; Lavoie-Cardinal, F.; Willig, K.I.; Eggeling, C.; Jakobs, S.; Hell, S.W. Diffraction-unlimited all-optical imaging and writing with a photochromic GFP. *Nature* **2011**, *478*, 204–208. [CrossRef]
39. Delcanale, P.; Pennacchietti, F.; Maestrini, G.; Rodríguez-Amigo, B.; Bianchini, P.; Diaspro, A.; Iagatti, A.; Patrizi, B.; Foggi, P.; Agut, M.; et al. Subdiffraction localization of a nanostructured photosensitizer in bacterial cells. *Sci. Rep.* **2015**, *5*, 15564. [CrossRef]
40. Meyer, S.A.; Ozbay, B.N.; Potcoava, M.; Salcedo, E.; Restrepo, D.; Gibson, E.A. Super-resolution imaging of ciliary microdomains in isolated olfactory sensory neurons using a custom two-color stimulated emission depletion microscope. *J. Biomed. Opt.* **2016**, *21*, 66017. [CrossRef]
41. Winter, F.R.; Loidolt, M.; Westphal, V.; Butkevich, A.N.; Gregor, C.; Sahl, S.J.; Hell, S.W. Multicolour nanoscopy of fixed and living cells with a single STED beam and hyperspectral detection. *Sci. Rep.* **2017**, *7*, 46492. [CrossRef] [PubMed]
42. Vicidomini, G.; Bianchini, P.; Diaspro, A. STED super-resolved microscopy. *Nat. Methods* **2018**, *15*, 173–182. [CrossRef] [PubMed]
43. Schindelin, J.; Arganda-Carreras, I.; Frise, E.; Kaynig, V.; Longair, M.; Pietzsch, T.; Preibisch, S.; Rueden, C.; Saalfeld, S.; Schmid, B.; et al. Fiji: An open-source platform for biological-image analysis. *Nat. Methods* **2012**, *9*, 676–682. [CrossRef] [PubMed]

Supplementary Materials

Visualization of bacterial protein complexes labeled with fluorescent proteins and nanobody binders for STED microscopy

Kimberly Cramer[1,2,*], Anna-Lena Bolender[3,*] , Iris Stockmar[1,2], Ralf Jungmann[1,2], Robert Kasper[3,#], Jae Yen Shin[1,2,#]

[1]Max Plank Institute of Biochemistry, 82152 Martinsried, Munich, Germany.
[2]Faculty of Physics and Center for Nanoscience, Ludwig Maximilian University, 80539 Munich, Germany.
[3]Max Plank Institute of Neurobiology, 82152 Martinsried, Munich, Germany.
*Equally contributed authors: Kimberly Cramer and Anna-Lena Bolender.
[#]Correspondence: rkasper@neuro.mpg.de (R.K.) jshin@biochem.mpg.de (J.Y.S.)

SM Figure 1.

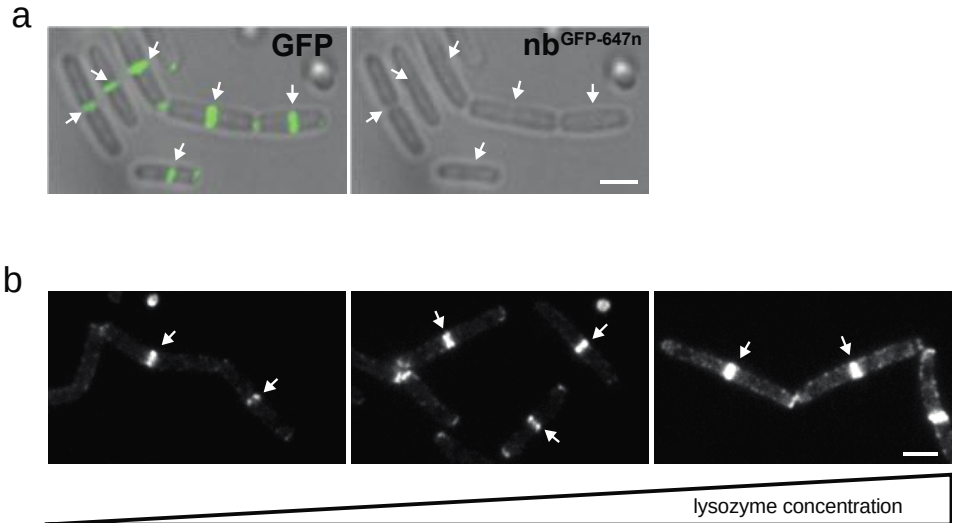

SM Figure 1. Effect of lysozyme treatment on nanobody binder entry into *B. subtilis*. (a) Overlay of bright field (gray) and fluorescence signal from GFP (left) in green, and NB^{GFP}-Atto647n (right) in *B. subtilis* cells expressing DivIVA-GFP (1803) treated with 0 mg/ml of lysozyme. Arrows indicate division septa where DivIVA-GFP is localized Scale bar 2 μm. **(b)** Fluorescence signal from NB^{RFP}-Atto647n in *B. subtilis* cells expressing DivIVA-PAmCherry *(*JB37) treated with 0.04, 0.2, and 0.4 mg/ml of lysozyme, left to right. Arrows indicate NB^{RFP}-atto647n signal at division septa. Scale bar 3 μm. Images were taken with a diffraction-limited microscope. In (a), GFP imaging was performed with an exposure of 0.2s, ND filter = 32%, and NB^{GFP}-Atto647n imaging was performed with an exposure time of 0.5s, ND filter = 32%. In (b), exposure was 0.2s, ND filter = 50% for NB^{GFP}-atto647n imaging.

SM Figure 2.

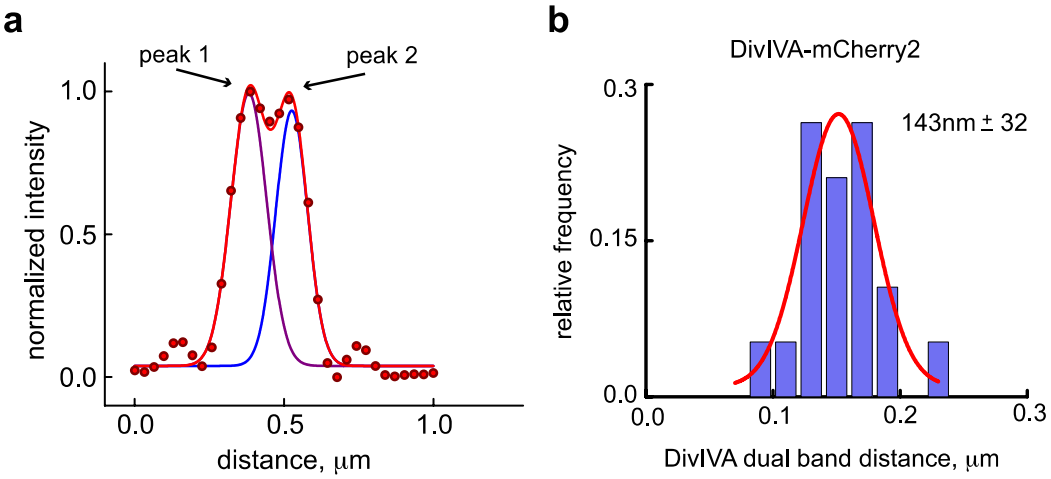

SM Figure 2. Histogram of distance between the DivIVA dual band in SIM images. Intensity profiles of the mCherry2 fluorescent signal along the longitudinal axis of cells from *B. subtilis* cells expressing DivIVA-mCherry2 were obtained using Fiji. **(a)** To extract the center position of each band along the longitudinal axis, the sum of two Gaussian functions were fitted (solid line) to this intensity profile (circles), using the software OriginPro 9.1G. Then, the values for the two center parameters (peak 1 and peak 2) of the Gaussians were subtracted to calculate their distance. **(b)** Mean and STD of the distance distribution are indicated in the histogram.

SM Figure 3

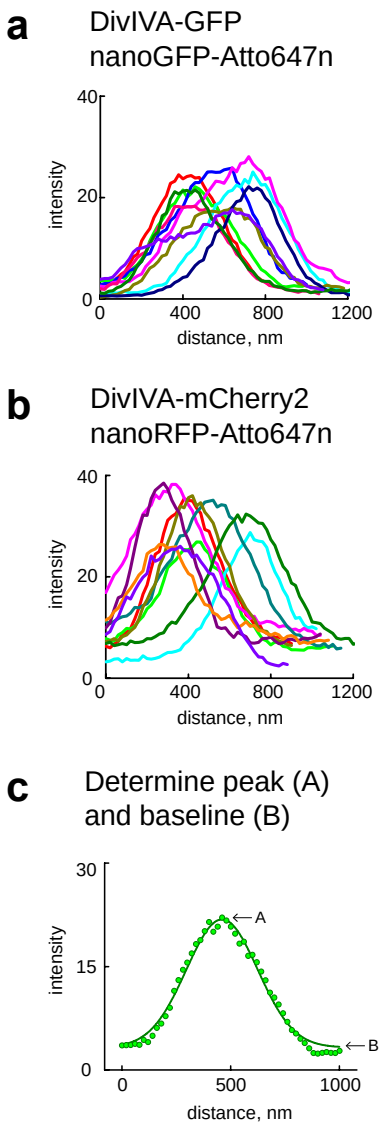

SM Figure 3. Determination of signal-to-background ratio. (a, b) Intensity profiles of the fluorescent signal from the fluorophore conjugated nanobody-along the longitudinal axis of cells from *B. subtilis* cells expressing either DivIVA-GFP or DivIVA-mCherry2. Each line represents the signal distribution from one cell, which was obtained by drawing a line along the longitudinal axis of cells using ImageJ. **(c)** Each intensity profile (circles) was fitted with a single peak gaussian function (continuous line), peak height at center point (A) and baseline (B) were obtained using the software OriginPro 9.1G.

SM Figure 4

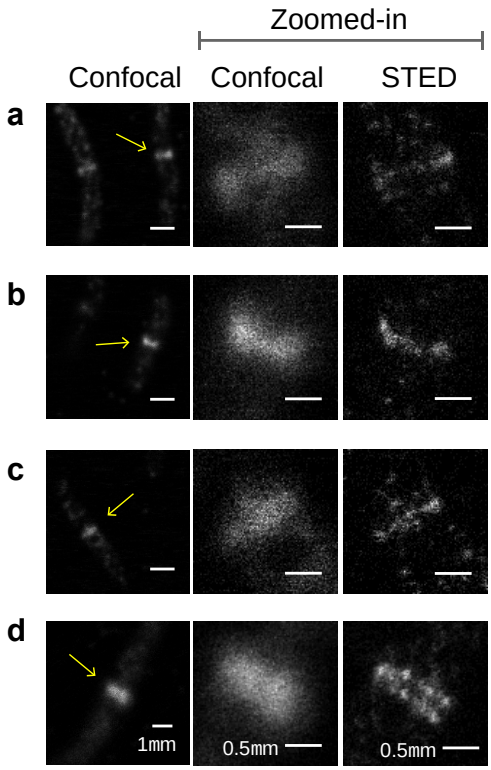

SM Figure 4. Visualization of FtsZ in *Escherichia coli with STED microscopy.* Strain EC484 containing GFP tagged FtsZ was visualized using NB^{GFP}-Atto647n via confocal and STED microscopy. Four examples are shown in **(a-d).** Confocal images in the Left column show FtsZ localization in single cells. Yellow arrows indicate FtsZ localization at division septa for **(a-d)**, and their corresponding zoomed-in confocal and STED images are shown in the Middle and Right columns, respectively.

SM Figure 5

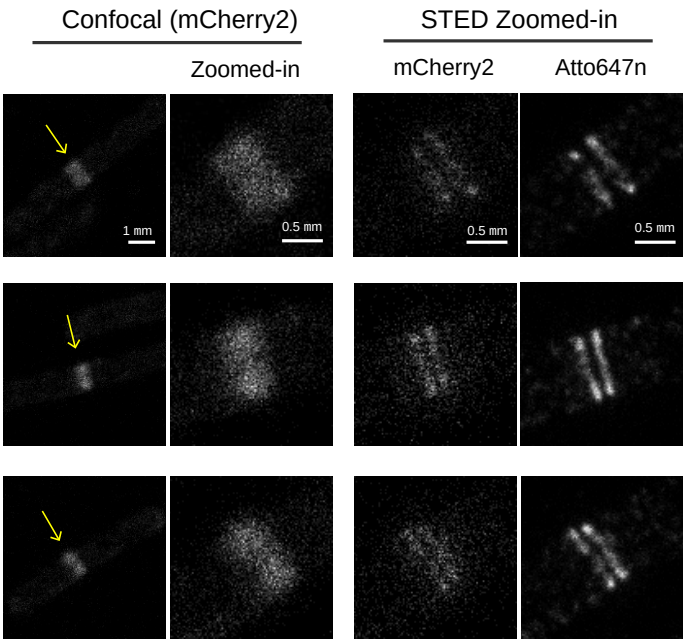

SM Figure 5. Comparison of mCherry2 and Atto647n for STED imaging. *B. subtilis* expressing DivIVA-mCherry2 treated with the immunolabeling protocol using the binder NB^{RFP}-Atto647n (as described in Material and Methods) were imaged with STED microscopy. Yellow arrows indicate DivIVA localization at division septa, and their corresponding zoomed-in confocal and STED images are shown in the Middle and Right columns.

SM Table I. Cellular background for *B. subtilis* expressing mCherry2 and GFP fusion protein

FP	Fused to	Signal to background ratio (A/B)	Cellular Background (B/A*100)
GFP	DivIVA	2.6	40 %
mCherry2	DivIVA	2.9	35 %

Signal-to-background ratio and Cellular background were calculated as described in the main text and SM Figure 3. n = 31.

SM Table II: STED sample preparation reagents and conditions. Lists of nanobodies binders used in this study, the targets the binders imaged, the dilutions employed, Figures in the Main Text where imaging using each binder appears, and their Cat. No.

Binder	Target imaged	Dilution	Corresponding Figure	Cat. No. *
NB^{GFP}-atto594	DivIVA-GFP	1:250	3, 4	gba594
NB^{GFP}-atto647n	DivIVA-GFP	1:250	2, 3, 4	gba647n
NB^{GFP}-star635p	DivIVA-GFP	1:250	3, 4	gbas635p
NB^{RFP}-atto594	DivIVA-mCherry2	1:250	3, 4	rba594
NB^{RFP}-atto647n	DivIVA-mCherry2	1:250	2, 3, 4	rba647n
NB^{RFP}-star600	DivIVA-PAmCherry	1:250	4	n/a$

*Cat. No. for Chromotek GmbH products.
$ Gifted

SM Table III: Properties of STED dyes used in this study. Lists of dye molecules and their net charge, hydrophobicity, molecular weight, $\lambda_{excitation}$ and $\lambda_{emission}$.

Dye	Net charge (after coupling)	Hydrophobicity	Molecular weight (g/mol)	λ_{abs}, nm	λ_{fl}, nm	*REF
Atto595	-1	Very hydrophilic	1,389	603	626	Atto-tec
Atto647n	+1	Moderately hydrophilic	843	646	664	Atto-tec
Star600	0 (zwitterionic)	hydrophilic	880.9	604	623	Abberior
Star635p	-3	hydrophilic	1,030.8	638	651	Abberior
mCherry2	n.a.	n.a.	26,700	585	610	[43]

*obtained from dye information pages provided by Atto-tec of Abberior companies

SM Materials and Methods

SM Table III: Lists bacterial strains used in this study.

Name	Genotype	Species	Citation
1803	*divIVA::(PdivIVA*-gfp *divIVA* $^{+}$ cat*)*	*B. subtilis*	[44]
JS99	*divIVA*::divIVA-mCherry2 spec	*B. subtilis*	This study
JB37	*divIVA*::divIVA-PAmCherry spec	*B. subtilis*	[45]
EC484	P_{208}-*ftsZ-gfp leu*::Tn*10*	*E. coli*	[46]

SM References (also in Main Text):

43. Shen, Y.; Chen, Y.; Wu, J.; Shaner, N. C.; Campbell, R. E. Engineering of mCherry variants with long Stokes shift, red-shifted fluorescence, and low cytotoxicity. *PLoS One* **2017**, *12*, 1–14.
44. Hamoen, L. W.; Meile, J.-C.; de Jong, W.; Noirot, P.; Errington, J. SepF, a novel FtsZ-interacting protein required for a late step in cell division. *Mol Microbiol* **2006**, *59*, 989–999.
45. Stockmar, I.; Feddersen, H.; Cramer, K.; Gruber, S.; Jung, K.; Bramkamp, M.; Shin, J. Y. Optimization of sample preparation and green color imaging using the mNeonGreen fluorescent protein in bacterial cells for photoactivated localization microscopy. *Sci Rep* **2018**, 1–11.
46. Weiss, D. S.; Chen, J. C.; Ghigo, J. M.; Boyd, D.; Beckwith, J. Localization of FtsI (PBP3) to the septal ring requires its membrane anchor, the Z ring, FtsA, FtsQ, and FtsL. *J Bacteriol* **1999**, *181*, 508–520.

Publication 2: Comparing Divisome Organization Between Vegetative and Sporulating Bacillus subtilis at the Nanoscale using DNA-PAINT

Comparing Divisome Organization Between Vegetative and Sporulating Bacillus subtilis at the Nanoscale using DNA-PAINT

Kimberly Cramer, Susanne CM Reinhardt, Alexander Auer, Jae Yen Shin[#], and Ralf Jungmann[#]

Science Advances
2024
10:eadk5847
doi: 10.1126/sciadv.adk5847

#Authors to whom correspondence can be addressed

BIOPHYSICS

Comparing divisome organization between vegetative and sporulating *Bacillus subtilis* at the nanoscale using DNA-PAINT

Kimberly Cramer[1,2], Susanne C. M. Reinhardt[1,2], Alexander Auer[1,2], Jae Yen Shin[1]*†, Ralf Jungmann[1,2]*

Spore-forming bacteria have two distinct division modes: sporulation and vegetative division. The placement of the foundational division machinery component (Z-ring) within the division plane is contingent on the division mode. However, investigating if and how division is performed differently between sporulating and vegetative cells remains challenging, particularly at the nanoscale. Here, we use DNA-PAINT super-resolution microscopy to compare the 3D assembly and distribution patterns of key division proteins SepF, ZapA, DivIVA, and FtsZ. We determine that ZapA and SepF placement within the division plane mimics that of the Z-ring in vegetative and sporulating cells. We find that DivIVA assemblies differ between vegetative and sporulating cells. Furthermore, we reveal that SepF assembles into ~50-nm arcs independent of division mode. We propose a nanoscale model in which symmetric or asymmetric placement of the Z-ring and early divisome proteins is a defining characteristic of vegetative or sporulating cells, respectively, and regulation of septal thickness differs between division modes.

INTRODUCTION

Bacterial cell division is a fundamental process in which a complex macromolecular protein machine, the divisome, splits the cell in two. *Bacillus subtilis*, the gram-positive model organism, exhibits two distinct modes of cell division: vegetative and sporulation. Vegetative cells divide symmetrically at the mid-cell to produce two daughter cells. During sporulation, the cell divides asymmetrically near a single-cell pole, generating a larger mother cell compartment and a smaller compartment called the forespore (Fig. 1A). In both division modes, the tubulin homolog FtsZ assembles into filaments that create a ring-like structure, the Z-ring, at the future division site (*1*). The Z-ring forms a scaffold upon which tens of other proteins assemble, forming the divisome (*2*).

In *B. subtilis*, divisome assembly occurs in two steps (*3*). The first step is an assembly of so-called "early proteins" that bind and support Z-ring formation at the division site (*4*–*6*). The early divisome protein ZapA stabilizes the Z-ring by acting as a protein cross-linker between FtsZ filaments (*7*). Early proteins FtsA and SepF promote Z-ring formation by anchoring FtsZ filaments to the membrane using an amphipathic alpha helix (*5*, *8*, *9*). SepF is widely conserved across not only gram-positive bacteria but also archaea and cyanobacteria (*10*). In vitro, SepF polymers form regular rings with 50-nm diameters that can bundle FtsZ filaments. SepF ring diameter both correlates with and controls septal thickness in vegetatively dividing bacteria (*11*). However, it is unlikely that SepF forms 50-nm rings in cells since the N-terminal membrane-binding domain is located inside the ring (*5*). Therefore, SepF was hypothesized to form arcs encircling the invaginating membrane (*5*, *11*). In the second divisome assembly step, "late proteins" arrive after Z-ring assembly and are involved in cell wall synthesis or remodeling and divisome regulation (*3*).

A major difference in divisome organization between vegetative and sporulating cells is the localization of the Z-ring and FtsA within the division plane. FtsA and FtsZ were found to be symmetrically placed at constricting septa in vegetative cells and asymmetrically placed in the mother cell compartment in sporulating cells (*12*). Whether other early divisome proteins also localize asymmetrically with the Z-ring is not yet determined. The protein DivIVA distributes differently across the division plane dependent on division mode (*13*). DivIVA is the localizer of *B. subtilis* Min system proteins, which prevent aberrant Z-ring assembly and help determine the division site (*14*–*16*). Thus, it is likely that regulatory proteins also assemble differently between division modes. Further knowledge about cell type–dependent differences in the three-dimensional (3D) nanoscale assemblies and localizations of division proteins and their regulators remain sparse. Super-resolution microscopy studies visualizing divisome proteins in sporulating cells remain relatively unexplored (*13*, *17*). However, super-resolution approaches could help understand divisome organization by providing insights into the underlying mechanisms governing division during vegetative growth and sporulation and help reveal if mechanisms differ between division modes.

Here, we use DNA-PAINT super-resolution microscopy (*18*) in combination with quantitative analyses to map the nanoscale cellular localization and spatial arrangement of several cell division proteins and determine potential differences in cell division machinery between vegetative and sporulating *B. subtilis*. We reveal that the Z-ring anchoring protein SepF forms arcs and measure similar SepF arc diameters in both cell types, indicating that SepF arcs do not regulate septal thickness in sporulating cells. We determine DivIVA ring assemblies differ between cell types. In addition, we map the positioning of the Z-ring, SepF, ZapA, and DivIVA rings at division septa and compare ring protein amounts between cell types. Together, our results show the asymmetric placement of divisome proteins toward the mother cell compartment as a key characteristic of sporulating cells and strongly suggest septal thickness regulation differs between division modes.

[1]Faculty of Physics and Center for Nanoscience, Ludwig Maximilian University, Munich, Germany. [2]Max Planck Institute of Biochemistry, Martinsried, Germany.
*Corresponding author. Email: shinjaeyen@gmail.com (J.Y.S.); jungmann@biochem.mpg.de (R.J.)
†Present address: Spermosens AB, Scheelevägen 4, 223 63 Lund, Sweden.

RESULTS

Geometric and stoichiometric analysis of DivIVA at the division plane in vegetative and sporulating cells

First, to investigate regulation of Z-ring placement, we determined the nanoscale arrangement of DivIVA in sporulating and vegetative cells, which might suggest different localization of the Min system. To this end, we set out to characterize the 3D assembly of DivIVA, which serves as a localizer for Min system proteins to the division site (*14*, *15*). To visualize DivIVA in individual cells, we developed a protocol to image bacterial proteins with DNA-PAINT super-resolution microscopy (see Materials and Methods). Briefly, for DNA-PAINT, an oligonucleotide (docking strand) is conjugated to a target binder (e.g., antibody) and its complementary dye-labeled oligonucleotide (imager strand) diffuses through the solution. When these transiently bind, a blinking signal is created, captured by a microscope, and rendered as a super-resolution image (*18*). To implement DNA-PAINT, we first constructed a *B. subtilis* strain (KCB300) that expresses DivIVA protein fused to the super-folder green fluorescent protein (sfGFP) from the DivIVA native locus (fig. S1 and table S1). DivIVA-sfGFP localized at the division septa in vegetative and sporulating cells (Fig. 1, C and F), indicating that sfGFP did not affect the location of DivIVA. Next, we used DNA-conjugated GFP nanobodies for DNA-PAINT imaging (Fig. 1B). DNA-PAINT data revealed that DivIVA localized as two distinct bands at the division plane of vegetative cells (Fig. 1D) and organized as dual rings when visualized in 3D (Fig. 1E), agreeing with previous results (*13*). Notably, we report that the 3D dual ring assembly of DivIVA is retained at the polar division site in sporulating cells (Fig. 1, G and H). In both cell types, DivIVA rings localize on opposite sides of the septum (fig. S2). Thus, dual DivIVA rings flank the division septum in vegetative and sporulating cells.

To further investigate DivIVA dual rings in individual cells, we developed an image analysis framework (see Materials and Methods). Briefly, after interactive selection in the Picasso software (*18*), an automated fitting procedure first separates the DivIVA rings in an *xy*

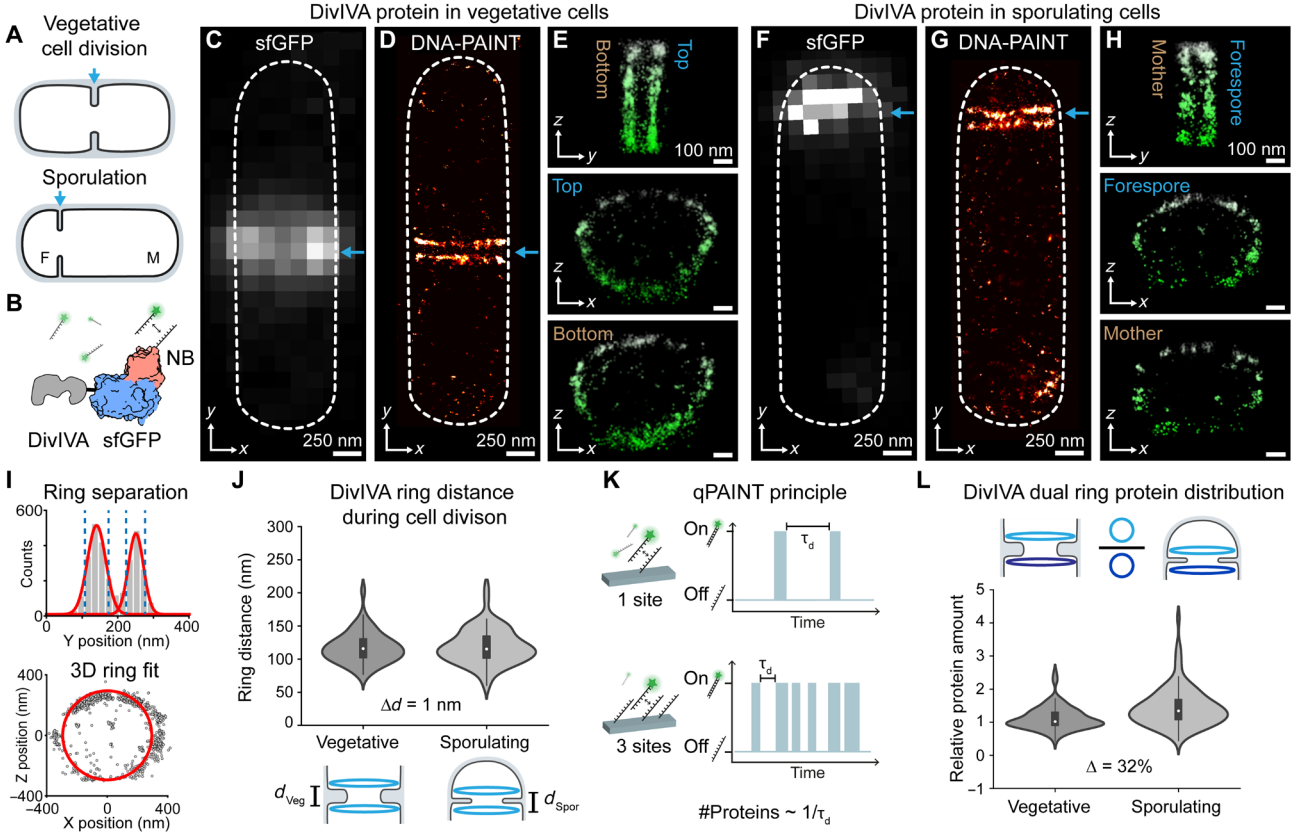

Fig. 1. Geometric and stoichiometric analysis of DivIVA at the division plane in vegetative and sporulating cells. (**A**) Cell division, blue arrows, occurs at mid-cell during vegetative division and asymmetrically during sporulation. Sporulating cells contain a smaller forespore (F) and a larger mother cell (M) compartment. (**B**) Labeling schematic of DivIVA-sfGFP with DNA-conjugated nanobody (NB). (**C** to **E**) DivIVA localization in a vegetative cell (arrows). (C) Diffraction-limited super-folder green fluorescent protein (sfGFP) imaging shows one band of DivIVA at mid-cell. (D) DNA-PAINT reveals that DivIVA forms two distinct bands. (E) Top: The *zy* projection of DivIVA reveals distinct bands. Middle and bottom: *zx* views unveil DivIVA as two separate rings. (**F** to **H**) DivIVA localization in a sporulating cell (arrows). (**I**) Analysis framework extracting ring-to-ring distances (top) and ring radii (bottom). (**J**) Distance between DivIVA rings in dividing vegetative (d_{Veg}) and sporulating (d_{Spor}) cells. Median values in vegetative and sporulating cells were 116 nm (IQR 103 to 131 nm, $n = 53$) and 115 nm (IQR 101 to 145 nm, $n = 64$), respectively, indicating d_{Veg} and d_{Spor} are similar. Medians are not significantly different (Mood's test). (**K**) qPAINT principle stating protein amount correlates with $1/\tau_d$. One docking site (on one protein) exhibits a certain time, τ_d, between binding events while three docking sites (on three proteins) yield three times shorter τ_d. (**L**) DivIVA dual ring protein distribution comparison between cell types. Median values in vegetative and sporulating cells were 1.02 (IQR 0.89 to 1.29, $n = 97$) and 1.34 (IQR 1.09 to 1.69, $n = 98$), respectively. Medians are significantly different (Mood's test), $P = 8.5 \times 10^{-6}$. Thus, the DivIVA protein amount is similar in rings in vegetative cells but in sporulating cells, the DivIVA ring in the forespore contains more protein. Plots (J) and (L): Boxes represent IQR (interquartile range), 25 and 75% data quartiles. Whiskers show 1.5 × IQR. White dots indicate median values.

projection using two-component Gaussian fits with appropriate thresholds (see Materials and Methods and Fig. 1I). Next, a 3D ring fit extracts ring properties for analysis. Using this analysis framework, parameters such as the distance between the dual rings, their radii, and further quantitative DNA-PAINT characteristics can be extracted. We first determined the distance between DivIVA dual rings in individual vegetative and sporulating *B. subtilis* undergoing division (i.e., the Z-ring was also present) and calculated median values of 116 nm [interquartile range (IQR) 103 to 131 nm] and 115 nm (IQR 101 to 145 nm), respectively (Fig. 1J). Thus, the distance between DivIVA dual rings is similar between dividing vegetative and sporulating cells.

Previous work showed DivIVA localized in a biased manner across the division plane in sporulating cells, with more DivIVA present in the forespore compartment (*13*). Considering our newfound assembly of DivIVA into dual rings (Fig. 1H), we wanted to quantify if more DivIVA protein is present in the DivIVA ring assembling within the forespore. We used qPAINT (*19*), which is a method to assess protein amounts via DNA-PAINT. In qPAINT, the time between two imager binding events, called dark time τ_d (Fig. 1K), inversely scales with the amount of protein present in rings (#proteins ~$1/\tau_d$). Using this relation, we compared the relative protein amounts between both rings for vegetative and sporulating cells (Fig. 1L). We found a median ratio of 1.02 (IQR 0.89 to 1.29) for vegetative cells and 1.34 (IQR 1.09 to 1.69) for sporulating cells, respectively, indicating a higher protein amount in the forespore DivIVA ring in sporulating cells (Fig. 1L). This suggests reduced localization of the Min system in the mother cell compartment where the asymmetric Z-ring is placed.

Z-ring placement between dual DivIVA differs between cell types

To test this hypothesis, we then wanted to determine the proximity of the Z-ring to the DivIVA dual rings and, by extension, the Min system. Close proximities would suggest increased probabilities of interaction between the Min system and Z-ring. We were especially curious about sporulating cells, in which the Z-ring is placed toward the mother cell compartment (*12*). To visualize the Z-ring together with DivIVA in individual cells, we implemented two-target Exchange-PAINT (*20*). A combination of a primary antibody anti-FtsZ and DNA-conjugated secondary nanobody allowed us to visualize the Z-ring (fig. S3). We visualized DivIVA as before (Fig. 1). DNA-PAINT revealed two bands of DivIVA sandwiching one FtsZ band at the division plane in both vegetative and sporulating cells (Fig. 2, A to C and F to H). The *zy* and *zx* views clearly show that FtsZ localizes as a ring (Z-ring) flanked by a DivIVA ring on each side in vegetative (Fig. 2D) and sporulating cells (Fig. 2I).

To determine where DivIVA dual rings localize relative to the Z-ring, we quantified the location of DivIVA rings and the FtsZ ring in the *xy* plane using two- and one-component Gaussian fits, respectively (Fig. 2, E and J). In vegetatively dividing cells, we defined −1, 0, and +1 as the position of the first DivIVA ring ($ring_1$), the mid-septum, and the second DivIVA ring ($ring_2$), respectively. Notably, in vegetative cells, we found the Z-ring is placed at the midpoint between the dual DivIVA rings, or equidistant from each ring (mean position 0.0 ± 0.2) (Fig. 2E). In sporulating cells, we defined −1, 0, and +1 as the position of the DivIVA ring in the forespore compartment ($ring_F$), the mid-septum, and the DivIVA ring in the mother cell compartment ($ring_M$), respectively. We determined that the Z-ring is placed closer to the DivIVA ring in the mother cell compartment (mean position: 0.3 ± 0.3) (Fig. 2J). In sporulating cells, the Z-ring is on average 48 ± 33 nm (d_2) away from $ring_M$ and 71 ± 38 nm (d_1) away from $ring_F$. Therefore, the Z-ring localizes approximately 25 nm closer to the DivIVA ring in the mother cell.

Nanoscale positioning of SepF and ZapA rings relative to the Z-ring does not change between cell types

We then turned our attention to the relative placement of ZapA and SepF to the Z-ring, as both proteins are early divisome components involved in Z-ring stabilization. We were especially curious about the placement of SepF, as current models predict localization on the invaginating septum. However, it stabilizes the Z-ring, which also suggests an asymmetric placement in sporulating cells.

We constructed a *B. subtilis* strain expressing ZapA protein fused to ALFA-tag (*21*) from the ZapA native locus (KCB328; fig. S1 and table S1). DNA-conjugated anti–ALFA-tag nanobodies (NB-ALFA) were used for ZapA visualization. Two-target Exchange-PAINT on the Z-ring and ZapA (Fig. 3, A to D) revealed ZapA assembles in 2D as a band (Fig. 3, A and C) and in 3D as a ring structure (Fig. 3, B and D) that appears to localize with the Z-ring in both vegetative and sporulating cells. We then measured the relative distances between FtsZ and ZapA rings along the *y* axis (see Materials and Methods and Fig. 3E and fig. S4). We determined the ZapA ring typically localized within 2 ± 11 nm and 1 ± 12 nm of the Z-ring at vegetative and sporulating division septa, respectively (Fig. 3E). Thus, ZapA rings are positioned together with the Z-ring in both division modes.

We visualized SepF in vegetative and sporulating cells using a bacterial strain expressing the fusion protein SepF-sfGFP from the endogenous loci (strain KCB1113; fig. S1 and table S1) and DNA-conjugated anti-GFP nanobodies to target SepF-sfGFP. SepF was resolved as a band (Fig. 3, F and H) in 2D and as a ring in 3D (Fig. 3, G and I) at division sites in both vegetative and sporulating cells and appeared to localize with the Z-ring. In the same manner, as described above (Fig. 3E), we analyzed the positioning of SepF rings to the Z-ring. SepF was typically localized within 3 ± 10 nm and 2 ± 15 nm of the Z-ring at vegetative and sporulating division septa, respectively (Fig. 3J). Thus, our data show that the SepF ring localizes with the Z-ring at division septa. To further verify SepF and Z-ring colocalization, we sliced our multiplexed data into ~40-nm sections in the *z* direction. At the cellular cross section of dividing vegetative and sporulating cells, FtsZ was bordered by or localized in close proximity to SepF (fig. S5). We conclude the nanoscale placement of SepF and ZapA relative to the Z-ring remains the same at vegetative and sporulating division septa despite the asymmetric placement of the Z-ring. Thus, SepF and ZapA are asymmetrically placed at division septa in sporulating cells.

Next, we compared the radii of the Z-ring, ZapA, and SepF rings. Larger or smaller ring radii would suggest rings assemble closer or further from the cell membrane than others, respectively. The radius of the SepF or ZapA rings was subtracted from the Z-ring radius in individual vegetative or sporulating cells. Positive values indicate that ZapA or SepF rings had smaller radii than the Z-ring and negative values indicate that the ZapA or SepF rings had larger radii. We determined that the relative radii of ZapA rings were −5 ± 14 nm and −9 ± 13 nm (means ± SD) in vegetative and sporulating cells, respectively (Fig. 3K). We determined that the difference between the Z-ring and SepF radii was −20 ± 11 nm and −21 ± 22 nm (means ± SD) in vegetative and sporulating cells, respectively (Fig. 3L), indicating that SepF rings have ~20-nm-larger radii than the Z-ring. We suspect the displacement of ZapA relative to the Z-ring to be caused by an offset due to the nanobody and antibody labeling approach. However, the larger displacement

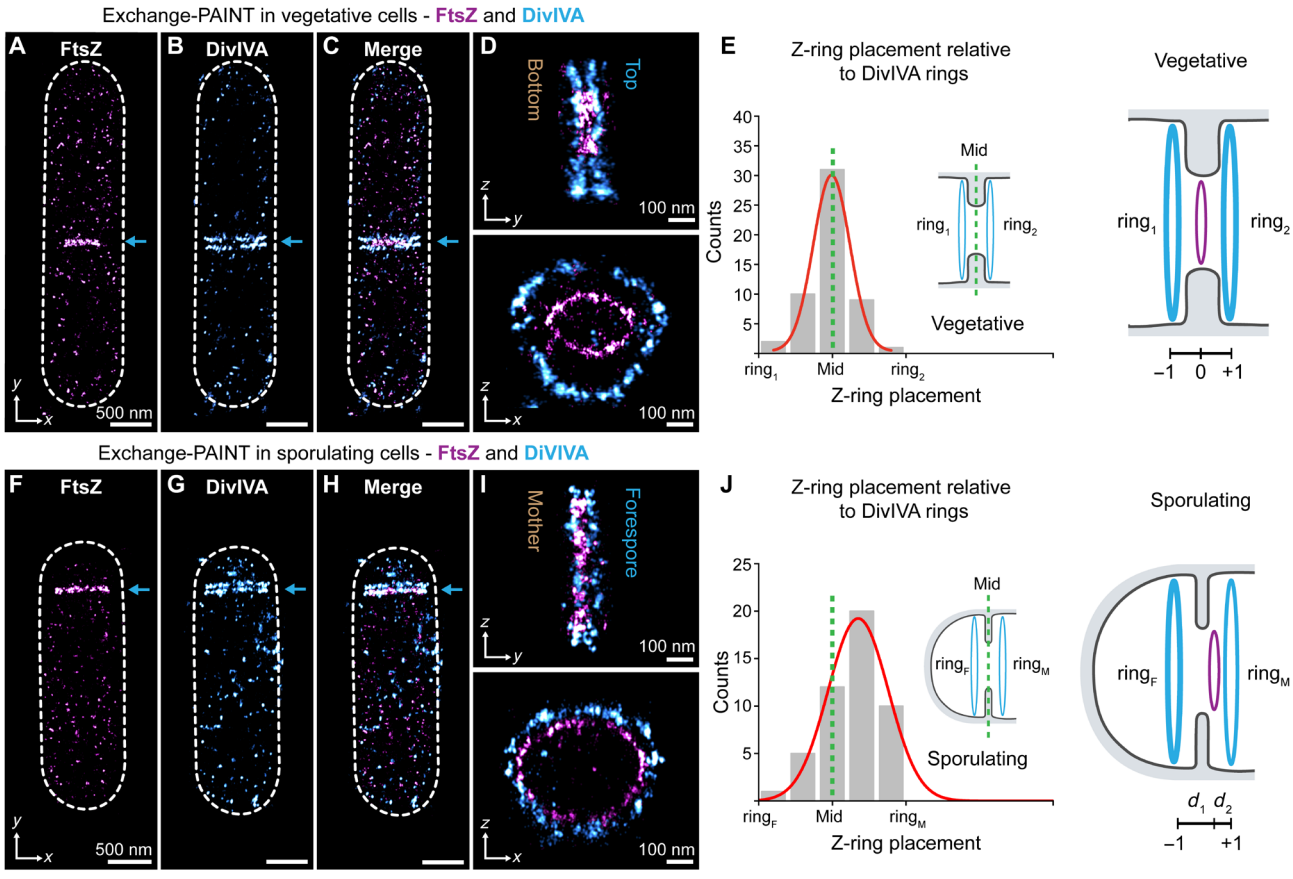

Fig. 2. Z-ring placement relative to DivIVA dual rings differs between cell types. Two-target Exchange-PAINT imaging of FtsZ (magenta) and DivIVA (cyan) in dividing vegetative (**A** to **D**) and sporulating (**F** to **I**) *B. subtilis*. [(A) and (F)] FtsZ localization. [(B) and (G)] DivIVA localization. [(C) and (H)] Merged Exchange-PAINT image of an entire cell. Arrows point to protein localization at division sites. [(D) and (I)] Top: The *zy* view of DivIVA and FtsZ. Bottom: The *zx* view of DivIVA and Z-ring "sandwich" arrangement showing the slightly smaller diameter of the (constricting) Z-ring compared to DivIVA. (**E**) Distribution of Z-ring position relative to dual DivIVA rings in vegetative cells. $ring_1$ and $ring_2$ are DivIVA rings in separate daughter cells. A green dotted line marks the center point between DivIVA rings. Corresponding Gaussian fit yields 0.0 ± 0.2 nm (means ± SD, $n = 53$, 0 marks a centered Z-ring position with ±1 corresponding to the DivIVA ring positions) revealing that the Z-ring is positioned at the center point between DivIVA rings. (**J**) Distribution of Z-ring position relative to dual DivIVA rings in sporulating cells. A green dotted line marks the center point between DivIVA rings. $ring_F$ and $ring_M$ are DivIVA rings in the forespore or mother cell compartment, respectively. Gaussian fit yields 0.3 ± 0.3 (means ± SD, $n = 64$, again 0 marks a centered Z-ring position with ±1 corresponding to the DivIVA ring positions), revealing that the Z-ring is positioned toward the DivIVA ring in the mother cell compartment. d_1 (71 ± 38 nm, means ± SD, $n = 64$) and d_2 (48 ± 33 nm, means ± SD, $n = 64$) correspond to different distances between a DivIVA ring and the Z-ring. Scale bars, 500 nm [(B), (C), (G), and (H)].

of SepF relative to the Z-ring indicates a true radius difference. Together, data determined that the relative radii of the protein rings are similar in both sporulating and vegetative cells, and data strongly suggest that the SepF ring assembles closest to the cell membrane, followed by the ZapA and FtsZ rings.

Next, we determined if the protein density within the Z-ring, SepF, and ZapA rings differed between vegetative and sporulating cells. To this end, as described above (Fig. 1), we used $1/\tau_d$ as a proxy for protein amounts. We compared protein amounts in the rings of each cell type within the same field of view (FOV) (see Materials and Methods and fig. S6). A ring density ratio was created to compare protein densities of sporulating cells to vegetative cells. Ring density refers to the protein amount normalized by the ring circumference. When the ring density ratio is smaller than 1, protein density is larger in vegetative cell rings. When the ratio is >1, it is larger in sporulating cells. While the mean ratio of ZapA rings was 0.9 ± 0.4, the data range and spread indicate no clear trend. Contrarily, the Z-ring and SepF rings presented mean values of 0.9 ± 0.1 and 0.7 ± 0.1, respectively. Thus, indicating SepF rings contain fewer proteins (~30%) in sporulating cells than in vegetative cells and the Z-ring contains slightly fewer proteins (~10%) in sporulating cells than in vegetative cells. Hence, the ring protein density of the Z-ring and SepF ring typically differs between vegetative and sporulating cells.

SepF assembles as arcs at vegetative and sporulating division septa

We noticed SepF bands exhibiting "protruding edges" in our images. Thus, we next focused our attention on testing the hypothesis that SepF proteins form arcs with diameters correlating with and influencing the division septum thickness in vegetative cells (*11*). SepF-sfGFP and the Z-ring were labeled as previously described (Fig. 3 and fig. S3). Similar to the organization observed in Fig. 3, DNA-PAINT imaging revealed that SepF assembled as a band at the division plane in sporulating and vegetative cells (Fig. 4, A and D) and forms a ring structure

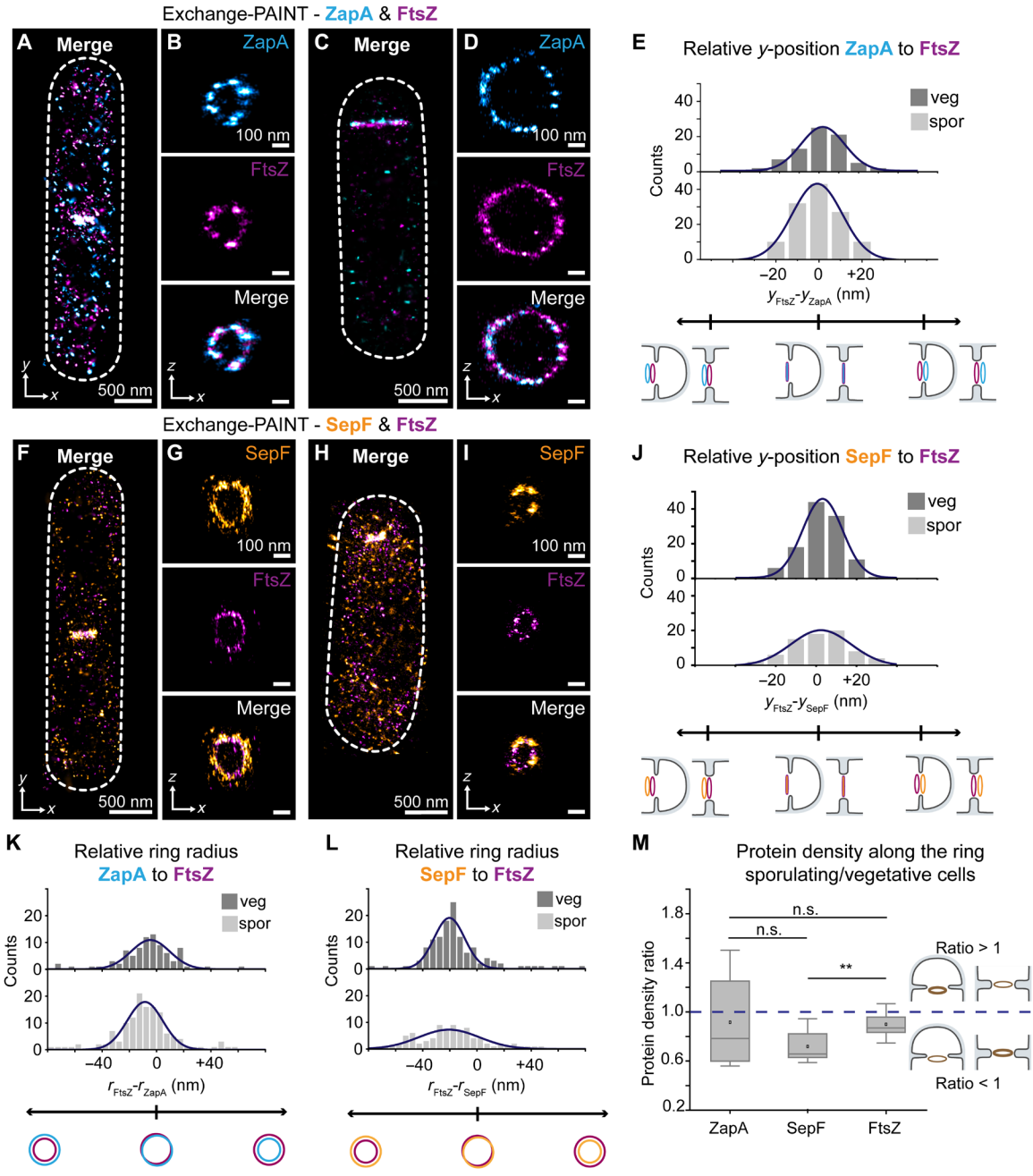

Fig. 3. Nanopositioning of SepF and ZapA rings relative to FtsZ. (**A**) Vegetative cells displaying ZapA and FtsZ localization as a band at the mid-cell. (**B**) The *zx* view of ZapA and FtsZ, showing both form rings. (**C** and **D**) Results for a sporulating cell. (**E**) Relative *y*-position distribution of the ZapA ring to the Z-ring in cells shows mean values of 2 ± 11 nm in vegetative and 1 ± 12 nm in sporulating cells, indicating close positioning of the Z-ring and ZapA ring in both division modes. (**F**) Vegetative cells displaying SepF and FtsZ localization as a band at the mid-cell. (**G**) The *zx* view of SepF and FtsZ, showing both form rings. (**H** and **I**) Respective results in a sporulating cell. (**J**) Relative *y*-position distribution of SepF to the Z-ring shows mean values of 3 ± 10 nm in vegetative and 2 ± 15 nm in sporulating cells, indicating close positioning in both division modes. (**K**) Relative ring radius of ZapA to FtsZ (r_{FtsZ}-r_{ZapA}): −5 ± 14 nm in vegetative, −9 ± 13 nm in sporulating. (**L**) SepF to FtsZ (r_{FtsZ}-r_{SepF}): −20 ± 11 nm vegetative, −21 ± 22 nm sporulating, showing a larger SepF ring radius than Z-ring. (**M**) Ring density ratios of ZapA, SepF, and FtsZ in vegetative and sporulating cells were compared and visualized as box plots. Mean ratios are 0.9 ± 0.4 for ZapA, 0.7 ± 0.1 for SepF, and 0.9 ± 0.1 for Z-rings. Ratios above 1 indicate higher densities in sporulating cells, while below 1 indicates higher densities in vegetative cells. Statistical tests reveal significant differences for SepF and FtsZ (but not ZapA) from a ratio of 1, and significant differences between Z-ring and SepF, but not between ZapA and SepF or FtsZ. Data from 16 (ZapA and SepF) and 56 (FtsZ) fields of view.

in 3D (Fig. 4, B and E). Notably, we noticed the edges of SepF bands consistently protruded into an arc shape. Therefore, we sliced SepF rings into 35- to 55-nm sections in the *z* plane. We then looked at the SepF assembly at the midpoint, the center of the cell in the *z* direction, and found that SepF forms clear arc structures at this cellular cross section (Fig. 4, C and F). We found arcs consistently at the cross section of multiple dividing *B. subtilis* (Fig. 4G), further indicating that SepF rings at division septa are composed of arc-shaped protein assemblies. Since the diameter of SepF protein rings in vitro correlates with division septum thickness, we set out to determine whether the SepF arc diameter corresponded with the reported thickness of the dividing septa in sporulating and vegetative cells. We defined the distance between the two endpoints on SepF arcs as arc diameter, which was measured by determining the distance between the two arc endpoints (see Materials and Methods). The 3D arrangement of SepF-sfGFP in combination with its labeling probe, NB-GFP, at the septum, should be considered for the true SepF arc diameter (Fig. 4H). NB-GFP is 4 to 5 nm long and GFP is fused to the C terminus of SepF. Thus, anti-GFP nanobodies would create a displacement of approximately 5 nm from their binding site to the true SepF position, adding up to 10 nm to the total arc diameter. Distribution centers indicate that typical SepF arc diameter is 64.7 nm (median, IQR 57.1 to 70.8) and 59.6 nm (median, IQR 55.5 to 64.1) for vegetative and sporulating cells, respectively (Fig. 4I). Thus, true SepF arc diameter is likely ~50 nm in both cell types (Fig. 4I), in good agreement with reported septal thickness in vegetative (50 nm) but not sporulating (25 nm) cells (*12*).

DISCUSSION

On the basis of our findings, we are now able to present a nanoscale model (Fig. 5) for the localization of FtsZ, early divisome proteins, and DivIVA in vegetative and sporulating cells.

In vegetative cells, the Z-ring is placed at the mid-septa. SepF assembles as arcs with ~50-nm diameters (Fig. 4) that encircle and line the invaginating septum (Fig. 3), creating a ring-like structure (Figs. 3 and 4) (*5*, *22*). SepF stabilizes and aligns FtsZ protofilaments that treadmill with associated peptidoglycan synthesis machinery (*23*, *24*), ultimately affecting septal thickness. ZapA tetramers laterally cross-link FtsZ filaments (*4*, *25*) to stabilize the Z-ring at the division site (Fig. 3). After membrane invagination begins, DivIVA rings flank the septum equidistant from the Z-ring (Fig. 2). DivIVA localizes the Min system that functions to inhibit aberrant Z-ring assembly near the division site (*26*).

In sporulating cells, dual DivIVA rings also flank the division site (Fig. 2). The Z-ring is asymmetrically placed ~25 nm closer to the DivIVA ring in mother cell compartment (Fig. 2). Similar to vegetative cells, SepF colocalizes with the Z-ring and assembles as 50-nm arcs (Fig. 3). However, SepF arcs are asymmetrically placed across the thinner (~25 nm) invaginating membrane toward the mother cell compartment (Figs. 3 and 4). Here, SepF arcs stabilize FtsZ protofilaments (*5*, *22*) but do not regulate septal thickness. Again, ZapA tetramers cross-link FtsZ filaments (Fig. 4) to promote its assembly (*7*). In addition, we calculated the longitudinal positioning of the Z-ring, SepF, ZapA, and DivIVA rings relative to cell length in sporulating cells (fig. S7) based on findings in Figs. 2 and 3.

Our results strongly suggest that SepF arcs do not function to regulate septum thickness in sporulating cells. Previous "clamp models" postulated SepF forms arcs that wrap around the leading edge of the constricting septa in vegetative cells (*11*, *22*). These models were derived from experiments involving purified SepF and FtsZ polymers and cryo–electron microscopy of the cell membrane, during which ring-shaped polymers of SepF were observed. We determined that SepF forms arcs in situ (Fig. 4), and the SepF ring localizes closer to the cell membrane than the Z-ring (Fig. 3) and is placed at the same position as the Z-ring within the dividing septum (Fig. 3). Thus, the clamp model of SepF assembly seems extremely likely. We propose that the thickness of the septa is controlled by

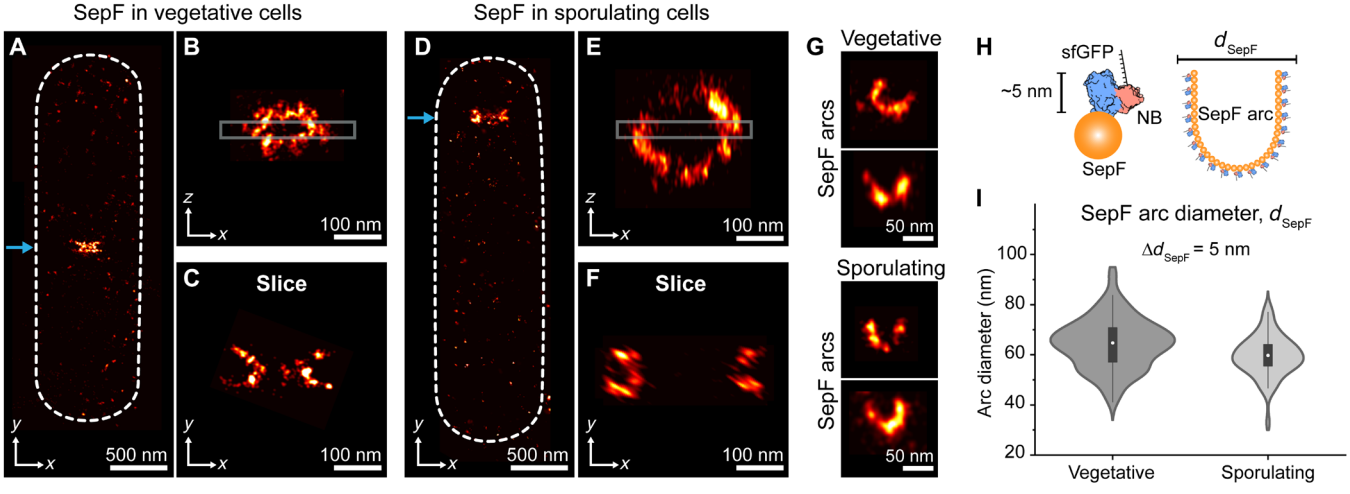

Fig. 4. SepF assembles as arcs at vegetative and sporulating division septa. (**A**) DNA-PAINT imaging reveals SepF localizes as a band with "protruding edges" (similar to a half torus) in vegetative cells. The blue arrow points to SepF localization at mid-cell. (**B**) Projection in *zx* of the SepF band in (A) shows that SepF assembles as a ring-like structure. (**C**) Fifty-nanometer slice [as indicated in (B)] shows that SepF forms arcs. (**D** to **F**) Respective results in a sporulating cell. SepF assembles at the asymmetric division site in sporulating cells (blue arrow). (**G**) Further examples of SepF arcs (50-nm slices) in vegetative and sporulating cells. (**H**) Schematic of SepF-sfGFP labeling strategy via DNA-conjugated anti-GFP (sfGFP) NBs. d_{SepF}, or SepF arc diameter, is defined as the distance between endpoints of SepF arcs. NBs face outward when bound to SepF arcs. (**I**) The distribution of SepF arc diameters, d_{SepF}, in each division mode is shown as violin plots. d_{SepF} is 64.7 nm (median, IQR 57.1 to 70.8, $n = 96$) and 59.6 nm (median, IQR 55.5 to 64.1, $n = 55$) for vegetative and sporulating cells, respectively. Boxes represent IQR (interquartile range), 25% and 75% quartile of data. Whiskers show 1.5 × IQR. White dots indicate median values.

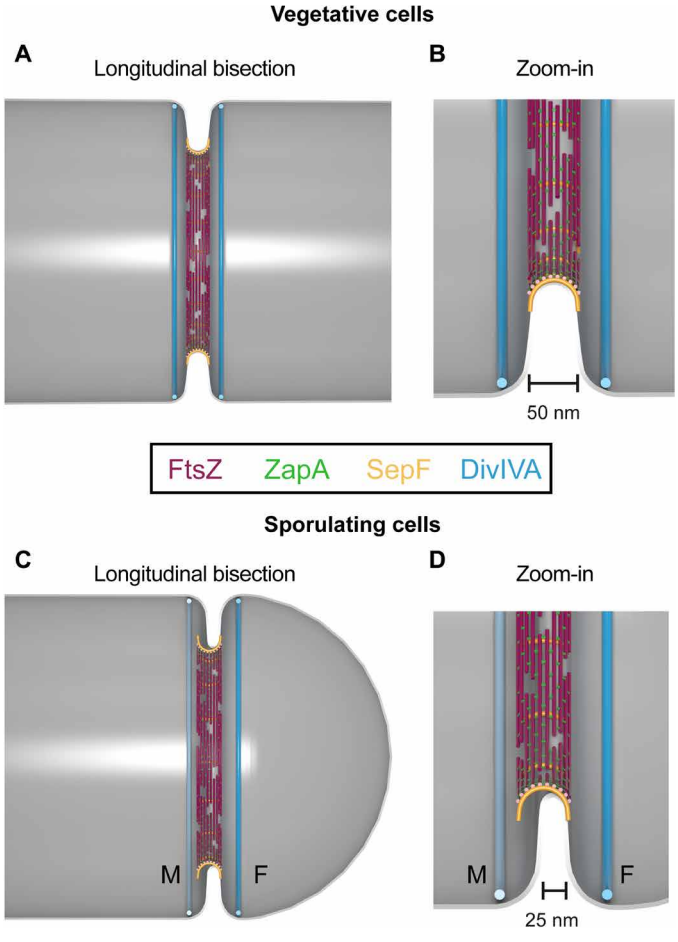

Fig. 5. Nanoscale model of SepF, FtsZ (Z-ring), ZapA, and DivIVA 3D assembly and placement within vegetative and sporulating septa. (**A**) Model of divisome protein assembly and placement within a longitudinal bisection of a vegetatively dividing cell. The invaginating septum is approximately 50 nm thick. FtsZ filaments, which form the Z-ring, localize at the septum. SepF assembles as arcs with ~50-nm diameters that encircle the invaginating septum. SepF arcs stabilize and align the FtsZ filaments that lie perpendicularly across them. "Dog bone–shaped" ZapA tetramers stabilize the Z-ring by acting as a protein cross-linker between FtsZ filaments. DivIVA rings sandwich the active divisome, placed equidistant from the Z-ring, preventing aberrant Z-ring formation. DivIVA protein distributes evenly between its dual rings. (**B**) Zoom-in of the bottom portion of the division plane in (A). (**C**) Model of divisome protein assembly and placement within a longitudinal bisection of a sporulating cell. The invaginating septum is approximately 25 nm thick. M is the mother cell compartment. F is forespore. The Z-ring, composed of FtsZ filaments, is placed asymmetrically on the septum toward M and contains 10% less protein than in vegetative cells. SepF and ZapA are asymmetrically placed with the Z-ring. SepF forms 50-nm arcs which cannot perfectly encircle the thinner (25 nm) invaginating septum in sporulating cells. This enables asymmetric localization of SepF arcs toward the M. ZapA cross-links FtsZ filaments. DivIVA rings flank the active divisome. The Z-ring localizes ~25 nm closer to the DivIVA ring in M, enabling quick divisome disassembly for relocation of FtsZ to the division site at the opposite cell pole. DivIVA ring in M has ~30% less protein than its counterpart. (**D**) Zoom-in of the bottom portion of the division plane in (C). FtsZ, magenta; SepF, orange; DivIVA, cyan; ZapA, green. The cell membrane is gray.

SepF arc diameter (*11*) in vegetative cells, in which both dividing septum thickness and SepF arc diameter of ~50 nm correlate. We show that arc diameters of ~50 nm (Fig. 4) are present in sporulating cells, which contain a 25-nm-thick septum (*12*). Thus, SepF arc diameter most likely does not regulate septum thickness in sporulating cells. The protein SpoIIE, which is only expressed in sporulating cells and shown to modulate septal thickness (*12*, *27*, *28*), could offer a potential explanation.

Our results indicate that the asymmetric placement of Z-ring stabilizing proteins toward the mother cell compartment is characteristic of sporulating *B. subtilis* (Fig. 3). This was especially interesting because the cell places the Z-ring asymmetrically during sporulation (*12*). Our results are expected for ZapA, which functions as a protein cross-linker between FtsZ filaments (*4*, *29*). However, it was unclear if SepF would colocalize with the Z-ring toward the mother cell compartment (*12*) or at the mid-septum in sporulating cells. While SepF recruitment to the division site depends on FtsZ (*30*), its N terminus binds cellular membranes (*5*) and SepF arcs in vegetative cells localized at the mid-septa (Fig. 3). We show that the SepF ring localizes asymmetrically in sporulating cells. It is possible that SepF interaction with the Z-ring promotes the asymmetric positioning of SepF at the division site. FtsA was also shown to localize with the Z-ring in sporulating cells (*12*). Thus, all known divisome proteins involved in promoting functional Z-ring assembly early in division (SepF, ZapA, and FtsA) assemble asymmetrically with the Z-ring in sporulating cells.

DNA-PAINT imaging revealed both differences and similarities between DivIVA dual rings in division modes (Figs. 1 and 2). We calculated that the DivIVA ring in the forespore ($ring_F$) contained ~30% more DivIVA than its counterpart in the mother cell compartment ($ring_M$) in dividing cells. A previous study (*13*) reported that DivIVA was present only in the forespore compartment after division. A geometric factor that might promote DivIVA protein localization in $ring_F$ is the geometry of the membrane in the forespore compartment. DivIVA has a high affinity for negative, i.e., concave, membrane curvature, which is present where the septum meets the lateral edge of the cell (*31*). We note that the forespore side of the septum appears to present higher concavity than the mother cell side due to the rounded shape of the forespore, which could promote DivIVA assembly. We also note that divisome components begin septum synthesis at a second short-lived division site (*32*) at the opposite end of the mother cell. Thus, DivIVA in $ring_M$ might redistribute there upon the synthesis of the partial septum, which is eventually abolished (*13*). Since the invaginating septum is thinner in sporulating than vegetative cells, we expected shorter distances between DivIVA dual rings in sporulating cells. We determined the distance between DivIVA rings was similar in vegetative and sporulating cells (Fig. 1J). Our results suggest differences in forespore compartment membrane curvature or additional protein factors might influence DivIVA dual ring localization in sporulating cells. Lastly, we determined that the Z-ring localizes closer (~25 nm) to DivIVA $ring_M$ (Fig. 2) and, by extension, the Min system, which disassembles the divisome after division (*33*). We predict that closer proximity to Min proteins enables faster divisome disassembly for the relocalization of FtsZ to the second division site.

We found that the ring assemblies of SepF and FtsZ rings contain different protein amounts between division modes. SepF rings in sporulating cells contained approximately 30% less protein compared to vegetative cells (Fig. 3). SepF, EzrA, and FtsA bind the same 20–amino acid FtsZ protein domain (*8*, *34*, *35*). Thus, there might be competition for Z-ring binding between early divisome proteins. Furthermore, in sporulation, additional proteins localize to the division plane for processes like DNA translation or septal thinning (*12*) and compete for space at the septum. It was proposed that the number of FtsZ filaments at the division site correlates with septum thickness in dividing cells (*12*). We observed that Z-rings in sporulating cells contained about 10% less FtsZ compared to vegetative

cells (Fig. 3). However, the division septum is 50% thinner in sporulating cells. Our results suggest that the amount of FtsZ filaments at the constricting septum is not a key determinant of septal thickness. Previous work compared FtsZ protofilament length at active division sites via cryo-focused ion beam cryo-electron tomography (cryo-FIB-ET) slices (*12*). In contrast, our analysis pipeline normalized protein density in rings for Z-ring diameter and analyzed the entire 3D Z-ring assembly with improved statistics.

The nanometer-scale resolution in combination with the quantitative nature of DNA-PAINT allowed us to reveal differences and similarities between the organization and distribution of division proteins in vegetative and sporulating *B. subtilis*. It is very likely that additional divisome components distribute, organize, and assemble differently between modes of division and certainly across species. It will be interesting to see whether the asymmetric placement of divisome proteins is specific to sporulating *B. subtilis* or a universal mechanism across spore-forming bacteria. The ability to simultaneously image and quantify divisome proteins in hundreds of bacteria at nanoscale resolution with high labeling and detection efficiency in situ opens up avenues for mapping the nanoscale structure of the complete divisome and other multicomponent bacterial complexes in the future.

MATERIALS AND METHODS

Bacterial culture conditions

Competent *B. subtilis* was created as previously described (*36*). Strains were plated on LB agar plates and grown overnight in LB at 30°C. Sporulating cells and samples for microscopy were prepared as described previously (*37*). Briefly, cells were grown in diluted LB media (1:4) to OD_{600} (optical density at 600 nm) ~ 0.5 to 0.7 and then induced to sporulate using Sterlini and Mandelstam medium at 37°C. Sporangia were fixed at time points between 1.75 and 2.6 hours. Vegetative cells were diluted 1:1000 in SMG media and grown at 30°C until OD_{600} ~ 0.15 then fixed.

Strain construction

See *B. subtilis* strains used in this study in table S1. *B. subtilis* 168 was used as the background for all strain construction. Primer sequences are found in table S3. A five-part Gibson assembly (*38*) was performed to create plasmids pKCB300 and pKCB1113. pKCB300 contains genes coding for sfGFP and a spectinomycin resistance marker flanked by the DivIVA gene and its downstream region for site-directed homologous recombination. pKCB1113 contains genes coding for sfGFP and a kanamycin resistance marker flanked by the SepF gene and its downstream region for site-directed homologous recombination. A linker was inserted before sfGFP and ALFA-tag by adding codons codifying for 3× glycine to the forward primer used for amplification. After Gibson assembly, plasmids were transformed into competent *B. subtilis* 168 and colony-purified. gDNA was sequenced to verify correctness. pKCB328 was created via a blunt-end cloning kit (NEB, catalog no. E1202S) of a custom gene block (IDT Technologies) (table S6). Strains and plasmids are available upon request.

Buffers

The following buffers were used for sample preparation and imaging:

1) PBSG: 1× phosphate-buffered saline (PBS; pH 7.4) and 20 nM glucose

2) PBST: 1× PBS (pH 7.4) and 0.02% (w/v) Tween 20

3) SDS buffer: 1× PBS (pH 7.4) and 0.01% (w/v) SDS

4) Blocking buffer: 3% (w/v) bovine serum albumin, 0.02% (v/v) Tween 20, and 1% (w/v) dextran sulfate (Sigma-Aldrich, catalog no. D4911-10G) in 1× PBS (pH 7.4)

5) Buffer C: 500 mM NaCl in 1× PBS (pH 7.4)

6) SMG media: 15 mM $(NH_4)_2SO_4$, 61 mM K_2HPO_4, 44 mM KH_2PO_4, 3.4 mM sodium citrate 2× H_2O, 1.7 mM $MgSO_4$, 5.9 mM glutamate, and 27 mM glucose supplemented with 1.0 mM tryptophan

DNA-PAINT sample preparation vegetative cells

Cells were fixed, immobilized, permeabilized, and blocked as previously described (*39*). Protein targets were labeled as described below (DNA-PAINT immunolabeling). Cells were washed three times with PBST. Gold nanoparticles (Cytodiagnostics, catalog no. G-90-100) were diluted 1:4 in PBS and added to the sample for 5 min. Cells were then washed three times with PBS. Imager strands were diluted into buffer C containing the PCA (3,4-dihydroxybenzoic acid), PCD (protocatechuate 3,4-dioxygenase pseudomonas), and Trolox oxygen scavenging system and added to samples directly before DNA-PAINT imaging. If vegetative and sporulating cells were to be imaged together, then they were fixed and permeabilized separately before cell immobilization and immunolabeling in the same sample.

DNA-PAINT sample preparation of sporulating cells

Cells were fixed and immobilized as previously described (*39*). The bacterial cell wall was permeabilized by incubating samples with lysozyme (2 mg/ml; Thermo Fisher Scientific, catalog no. 90082) for 60 s at 30°C. Cells were then washed with SDS buffer three times. Next, a blocking solution was added for 20 min at room temperature (RT). Immunolabeling was performed as described below (DNA-PAINT immunolabeling).

DNA-PAINT immunolabeling

DivIVA labeling

Anti-GFP nanobody (Nano-Tag, catalog no. N0305-250 μg) conjugated with a DNA-PAINT handle was added in a 1:200 dilution and incubated at 4°C overnight (ON).

ALFA-tag labeling

Anti-ALFA nanobody (Nano-Tag, catalog no. N1505-250 μg) conjugated with a DNA-PAINT handle was added in a 1:200 dilution and incubated at 4°C ON.

FtsZ labeling

Primary rabbit anti-FtsZ antibody (Biozol, catalog no. GTX36253) was added in a 1:100 dilution and incubated at 4°C ON. A secondary anti-rabbit nanobody conjugated with a DNA-PAINT handle was added in a 1:200 dilution and incubated for 90 min at RT.

Multiplexed labeling

Binders were added as explained above and incubated ON at 4°C. If imaging FtsZ, the secondary anti-rabbit nanobody conjugated with a DNA-PAINT handle was added the next day in a 1:200 dilution and incubated for 90 min at RT.

Cells were washed three times with PBST. Gold nanoparticles (Cytodiagnostics, catalog no. G-90-100) were diluted 1:4 in PBS and added to the sample for 5 min. Cells were washed three times with PBSG. Imager strands were diluted into buffer C containing PCA, PCD, and Trolox oxygen scavenging system and added to samples directly before DNA-PAINT imaging. Exchange-PAINT was performed by washing samples three times with PBS between imaging rounds, or until no blinking was observed.

Nile Red imaging

Nile Red (Invitrogen, catalog no. N1142) was added to the sample after all DNA-PAINT imaging was completed. Nile Red was diluted to a concentration of 1 to 1.5 nM in buffer C containing the PCA, PCD, and Trolox oxygen scavenging system and incubated for 5 min before imaging. Once Nile Red was added, no more DNA-PAINT imaging was performed in the sample.

Preparation of PCA, PCD, and Trolox

40× PCA: 154 mg PCA (Sigma-Aldrich, catalog no. 37580-25G-F) was dissolved in 10 ml of water and adjusted to pH 9.0 using NaOH (Merck, catalog no. 1091361000). 100× PCD: 9.3 mg PCD (Sigma-Aldrich, catalog no. P8279) was dissolved in 13.3 ml of buffer [100 mM tris-HCl (pH 8), 50 mM KCl (Merck, catalog no. 7647-14-5), 1 mM EDTA, and 50% glycerol (Sigma-Aldrich, catalog no. 65516-500ml)]. 100X Trolox: 100 mg (±)-6-hydroxy-2,5,7,8-tetramethylchromane-2-carboxylic acid (Trolox, Sigma-Aldrich, catalog no. 238813-5G) was dissolved in 3.2 ml of H_2O complemented with 430 µl 100% methanol (Sigma-Aldrich, catalog no. 32213-2.5L) and 345 µl of 1 M NaOH.

DNA-binder conjugation

The nanobody binder FluoTag-Q anti-GFP (NanoTag, catalog no. N0301) was used to target sfGFP. Nanobody anti-ALFA nanobody (NanoTag, catalog no. N1505) was used to target ALFA-tag. A custom-made anti-rabbit nanobody was used to target primary FtsZ antibodies. All nanobodies contained a single cysteine that was coupled with DNA oligonucleotides functionalized with an azide group at the 5′-end (Metabion, Planegg, Germany), as described previously (*40*).

Affinity purification of anti-FtsZ antibody

FtsZ was purified on the basis of an affinity purification method by following the protocol from the manufacturer https://tinyurl.com/y5zutwhd. Since FtsZ antibodies (Biozol, catalog no. GTX36253) were only available in small volumes (microliters), bead coupling and purification were performed in 1.5-ml Eppendorf tubes. Thus, washing is defined as centrifugation and removal of supernatant. Elution fractions were dialyzed using the Slide-A-Lyzer Mini Dialysis device (Thermo Fisher Scientific, catalog no. 69550) into PBS (w/v) 50% glycerol for storage at −20°C.

DNA-PAINT microscope setup

DNA-PAINT imaging was carried out on an inverted microscope (Nikon Instruments, Eclipse Ti2) with the Perfect Focus System, applying an objective-type total internal reflection fluorescence (TIRF) configuration equipped with an oil-immersion objective (Nikon Instruments, Apo SR TIRF 100×, NA 1.49, oil). A 488-nm (200 mW, Toptica iBeam smart) or 561-nm laser (Coherent Sapphire, 200 mW) was used for excitation and was coupled into a single-mode fiber. The laser beam was passed through cleanup filters (Chroma Technology, ZET561/10) and coupled into the microscope objective using a beam splitter (Chroma Technology, ZT561rdc). Fluorescence light was spectrally filtered with an emission filter (Chroma Technology, ET600/50 m) and imaged with a scientific complementary metal-oxide semiconductor camera (Andor, Zyla 4.2plus) without further magnification, resulting in an effective pixel size of 130 nm after 2 × 2 binning. The camera readout sensitivity was set to 16-bit, and readout bandwidth to 540 MHz. Three-dimensional imaging was performed using a cylindrical lens (Nikon Instruments, N-STORM) in the detection path.

Image analysis

Raw fluorescence data from DNA-PAINT imaging was subjected to super-resolution reconstruction using the "Picasso" software package (*18*) (latest version available on https://github.com/jungmannlab/picasso). Drift correction was performed with a redundant cross-correlation and gold nanoparticles as fiducials. Gold nanoparticles were also used to align the FtsZ and DivIVA signals, FtsZ and SepF signals, and FtsZ and ZapA signals in Exchange-PAINT. Regions of interest (whole cells or septa) were selected manually using Picasso's "Pick tool" and the rectangle pick option. Cells and septa were picked along the main axis of the bacterial cell, in sporulating cells in the direction from the forespore ring to the mother ring, yielding rotated *xy* coordinates. Statistical analyses were performed and graphs were created using the software Origin 2019b from OriginLab. The notation of *P* values is as follows: * indicates $1.00 \times 10^{-02} < P \leq 5.00 \times 10^{-02}$. ** indicates $1.00 \times 10^{-03} < P \leq 1.00 \times 10^{-02}$. *** indicates $1.00 \times 10^{-04} < P \leq 1.00 \times 10^{-03}$. **** indicated $P \leq 1.00 \times 10^{-04}$. IQR refers to the second and third data quartiles (middle 50% of data). Localization precisions were calculated using a nearest neighbor–based analysis (*41*) and are listed in table S8. The mean localization precision for all DNA-PAINT measurements was 6 ± 1 nm (means ± SD, $n = 414$).

Ring analysis workflow

First, the longitudinal position of the Z-ring in sporulating cells was determined by a unimodal Gauss fit in a histogram (bin size, 20 nm) representing frequency counts of localizations along the main axis of each picked cell. The location of the cell within the picked ROI was identified using the signal from cytosolic FtsZ: In the histogram, a bin was considered to show the signal if it contained more than 10% of the median number of counts in nonzero bins. Identifying the first and last block of 10 consecutive bins above this threshold allows us to identify the cell edges as the outermost bins of these blocks. In this way, noise at the edges of the picked ROI will not induce artifacts in the identification of the longitudinal position of the cell within the region of interest. Subsequently, the relative position of the Z-ring within the cell was calculated.

First, individual rings were identified using frequency counts along the rotated *y* axis of every picked septum. The distributions were fitted using unimodal (FtsZ, SepF, and ZapA) or bimodal (DivIVA) Gaussian distributions. The fits were initialized using the height and width estimations obtained from the mean shift algorithm (*42*), which is implemented in the Python package scikit-learn (*43*). For dual-band data, the identified rings were mutually filtered using the values for width, amplitude, and distance to exclude picks where the two bands could not be successfully identified. Distances between DivIVA rings (Fig. 1, I and L), between DivIVA and FtsZ rings (Fig 2, E and J), between FtsZ and SepF, and between FtsZ and ZapA (Fig. 3, E and J, and fig. S4) were calculated from the center-to-center distance of the respective Gauss peaks.

Localizations from individual rings were selected in a corridor around the center of the Gaussian fit of the frequency count. Here, the corridor width is scaled with the width of the Gaussian fit (fig. S6).

Selected localizations were further used to perform a tilt correction of single-band data and individual DivIVA rings: Therefore, a singular value decomposition (SVD) was used to estimate the transformation

matrix. Subsequently, Rodrigues' rotations were applied to the original set of localizations resulting in a corrected alignment of the ring plane with the *xz* plane. Recalculating the frequency count and the unimodal Gauss fit yields a narrower curve width, thus allowing for a more precise selection of ring localizations in a corridor around the center of the Gauss fit.

Next, the rings were fitted using a circle fit in the *xz* plane. The circle fits revealed ring radii and ring center information. For single-band data, only localizations with *xz* distances to the ring center being within ±100 nm of the fitted ring radius were kept for further analysis. If less than 80% of the localizations are within this region, then the ring was discarded. Furthermore, a ring was excluded if it was not sampled all around: To this aim, 12 segments were defined along the ring. A segment is considered to be sampled if it contains at least a fourth of the localizations that it would contain if the localizations N_{locs} were evenly distributed $[N_{\mathrm{locs}}/(4N_{\mathrm{segments}})]$. If this criterium is fulfilled by less than eight segments, then the ring is discarded.

For the qPAINT analysis, selected localizations were linked, and kinetic information including the dark time τ_d was determined for every ring using the algorithm described earlier (*18*, *19*).

To identify whether one of the DivIVA rings contained more protein copies than the other, the ratio of the dark time of the forespore ring and the mother ring (sporulating cells) or ring 1 and ring 2 (vegetative cells) was calculated. A value larger than 1 indicates a higher protein amount in the forespore ring than in the mother ring or in ring 1 compared to ring 2. These ratios were calculated for all cells in all imaged FOVs and lastly compared between vegetative and sporulating cells.

To identify whether sporulating or vegetative cells contain more protein in their respective FtsZ, SepF, and ZapA rings, ring radii need to be considered because the protein amount in a ring scales with the radius.

In addition, protein amounts of sporulating and vegetative cells can only be compared within the same FOV because the dark times τ_d become incomparable if experimental conditions minimally differ between experiments. Therefore, for each FOV, the dark times are first plotted against their respective ring radius *r*. Then, a linear fit was performed for sporulating and vegetative data points, respectively: $1/\tau_d = a * r$, where *a* is the slope of the fitted line. A larger slope indicates a higher protein density across the ring. The ratio of these slopes ($a_{\mathrm{spor}}/a_{\mathrm{veg}}$) can be compared across FOVs. The statistical significance of the calculated mean ratios displayed in Fig. 3M was first determined with a one-sampled *t* test, which found that SepF and FtsZ means are significantly different from a ratio of 1 (SepF: $P = 4.49736 \times 10^{-4}$; FtsZ: $P = 2.05054 \times 10^{-5}$), but not ZapA ($P = 0.56196$). In addition, a two-sampled *t* test (Welch's test) determined that the Z-ring and SepF have statistically significant distributions ($P = 0.00456$), while ZapA and SepF ($P = 0.20666$) as well as ZapA and FtsZ ($P = 0.90987$) do not. SVD and circular fitting were performed using the SciPy package (*44*) (v.1.4.1).

SepF arc diameter

First, the tip of SepF arcs was manually selected using Picasso's Pick tool. Second, a *z* slice of 100-nm thickness is selected by fitting a unimodal Gaussian to a histogram along the *z* axis of the pick. Only localizations within ±50 nm around the Gauss peak are considered further. Last, a histogram along the *x* axis of the rectangle pick is calculated and SepF arc tips are identified by a bimodal Gauss fit. Using the values for width, amplitude, and distance, picks are discarded if the two peaks cannot be successfully identified. The arc diameter is the distance between both Gauss peaks.

Supplementary Materials

This PDF file includes:

Figs. S1 to S7
Tables S1 to S8
References

REFERENCES AND NOTES

1. E. F. Bi, J. Lutkenhaus, FtsZ ring structure associated with division in Escherichia coli. *Nature* **354**, 161–164 (1991).
2. J. Errington, L. J. Wu, Cell cycle machinery in *Bacillus subtilis*. *Subcell. Biochem.* **84**, 67–101 (2017).
3. P. Gamba, J. W. Veening, N. J. Saunders, L. W. Hamoen, R. A. Daniel, Two-step assembly dynamics of the *Bacillus subtilis* divisome. *J. Bacteriol.* **191**, 4186–4194 (2009).
4. L. G. Monahan, A. Robinson, E. J. Harry, Lateral FtsZ association and the assembly of the cytokinetic Z ring in bacteria. *Mol. Microbiol.* **74**, 1004–1017 (2009).
5. R. Duman, S. Ishikawa, I. Celik, H. Strahl, N. Ogasawara, P. Troc, J. Lowe, L. W. Hamoen, Structural and genetic analyses reveal the protein SepF as a new membrane anchor for the Z ring. *Proc. Natl. Acad. Sci. U.S.A.* **110**, E4601–E4610 (2013).
6. P. Szwedziak, Q. Wang, T. A. Bharat, M. Tsim, J. Lowe, Architecture of the ring formed by the tubulin homologue FtsZ in bacterial cell division. *eLife* **3**, e04601 (2014).
7. T. Mohammadi, G. E. Ploeger, J. Verheul, A. D. Comvalius, A. Martos, C. Alfonso, J. van Marle, G. Rivas, T. den Blaauwen, The GTPase activity of Escherichia coli FtsZ determines the magnitude of the FtsZ polymer bundling by ZapA in vitro. *Biochemistry* **48**, 11056–11066 (2009).
8. S. O. Jensen, L. S. Thompson, E. J. Harry, Cell division in *Bacillus subtilis*: FtsZ and FtsA association is Z-ring independent, and FtsA is required for efficient midcell Z-Ring assembly. *J. Bacteriol.* **187**, 6536–6544 (2005).
9. S. Pichoff, J. Lutkenhaus, Tethering the Z ring to the membrane through a conserved membrane targeting sequence in FtsA. *Mol. Microbiol.* **55**, 1722–1734 (2005).
10. N. Pende, A. Sogues, D. Megrian, A. Sartori-Rupp, P. England, H. Palabikyan, S. K. R. Rittmann, M. Grana, A. M. Wehenkel, P. M. Alzari, S. Gribaldo, SepF is the FtsZ anchor in archaea, with features of an ancestral cell division system. *Nat. Commun.* **12**, 3214 (2021).
11. M. Wenzel, I. N. Celik Gulsoy, Y. Gao, Z. Teng, J. Willemse, M. Middelkamp, M. G. M. van Rosmalen, P. W. B. Larsen, N. N. van der Wel, G. J. L. Wuite, W. H. Roos, L. W. Hamoen, Control of septum thickness by the curvature of SepF polymers. *Proc. Natl. Acad. Sci. U.S.A.* **118**, e2002635118 (2021).
12. K. Khanna, J. Lopez-Garrido, J. Sugie, K. Pogliano, E. Villa, Asymmetric localization of the cell division machinery during *Bacillus subtilis* sporulation. *eLife* **10**, e62204 (2021).
13. P. Eswaramoorthy, P. W. Winter, P. Wawrzusin, A. G. York, H. Shroff, K. S. Ramamurthi, Asymmetric division and differential gene expression during a bacterial developmental program requires DivIVA. *PLOS Genet.* **10**, e1004526 (2014).
14. J. H. Cha, G. C. Stewart, The divIVA minicell locus of *Bacillus subtilis*. *J. Bacteriol.* **179**, 1671–1683 (1997).
15. D. H. Edwards, J. Errington, The *Bacillus subtilis* DivIVA protein targets to the division septum and controls the site specificity of cell division. *Mol. Microbiol.* **24**, 905–915 (1997).
16. I. Barak, P. Prepiak, F. Schmeisser, MinCD proteins control the septation process during sporulation of *Bacillus subtilis*. *J. Bacteriol.* **180**, 5327–5333 (1998).
17. A. Lablaine, M. Serrano, C. Bressuire-Isoard, S. Chamot, I. Bornard, F. Carlin, A. O. Henriques, V. Broussolle, The morphogenetic protein CotE positions exosporium proteins CotY and ExsY during sporulation of Bacillus cereus. *mSphere* **6**, e00007-21 (2021).
18. J. Schnitzbauer, M. T. Strauss, T. Schlichthaerle, F. Schueder, R. Jungmann, Super-resolution microscopy with DNA-PAINT. *Nat. Protoc.* **12**, 1198–1228 (2017).
19. R. Jungmann, M. S. Avendano, M. Dai, J. B. Woehrstein, S. S. Agasti, Z. Feiger, A. Rodal, P. Yin, Quantitative super-resolution imaging with qPAINT. *Nat. Methods* **13**, 439–442 (2016).
20. R. Jungmann, M. S. Avendano, J. B. Woehrstein, M. Dai, W. M. Shih, P. Yin, Multiplexed 3D cellular super-resolution imaging with DNA-PAINT and Exchange-PAINT. *Nat. Methods* **11**, 313–318 (2014).
21. H. Gotzke, M. Kilisch, M. Martinez-Carranza, S. Sograte-Idrissi, A. Rajavel, T. Schlichthaerle, N. Engels, R. Jungmann, P. Stenmark, F. Opazo, S. Frey, The ALFA-tag is a highly versatile tool for nanobody-based bioscience applications. *Nat. Commun.* **10**, 4403 (2019).
22. M. E. Gundogdu, Y. Kawai, N. Pavlendova, N. Ogasawara, J. Errington, D. J. Scheffers, L. W. Hamoen, Large ring polymers align FtsZ polymers for normal septum formation. *EMBO J.* **30**, 617–626 (2011).

23. A. W. Bisson-Filho, Y. P. Hsu, G. R. Squyres, E. Kuru, F. Wu, C. Jukes, Y. Sun, C. Dekker, S. Holden, M. S. VanNieuwenhze, Y. V. Brun, E. C. Garner, Treadmilling by FtsZ filaments drives peptidoglycan synthesis and bacterial cell division. *Science* **355**, 739–743 (2017).
24. X. Yang, Z. Lyu, A. Miguel, R. McQuillen, K. C. Huang, J. Xiao, GTPase activity-coupled treadmilling of the bacterial tubulin FtsZ organizes septal cell wall synthesis. *Science* **355**, 744–747 (2017).
25. R. Pacheco-Gomez, X. Cheng, M. R. Hicks, C. J. Smith, D. I. Roper, S. Addinall, A. Rodger, T. R. Dafforn, Tetramerization of ZapA is required for FtsZ bundling. *Biochem. J.* **449**, 795–802 (2013).
26. P. Eswaramoorthy, M. L. Erb, J. A. Gregory, J. Silverman, K. Pogliano, J. Pogliano, K. S. Ramamurthi, Cellular architecture mediates DivIVA ultrastructure and regulates min activity in *Bacillus subtilis*. *MBio* **2**, e00257-11 (2011).
27. P. Guzman, J. Westpheling, P. Youngman, Characterization of the promoter region of the *Bacillus subtilis* spoIIE operon. *J. Bacteriol.* **170**, 1598–1609 (1988).
28. I. Barak, P. Youngman, SpoIIE mutants of *Bacillus subtilis* comprise two distinct phenotypic classes consistent with a dual functional role for the SpoIIE protein. *J. Bacteriol.* **178**, 4984–4989 (1996).
29. P. Caldas, M. Lopez-Pelegrin, D. J. G. Pearce, N. B. Budanur, J. Brugues, M. Loose, Cooperative ordering of treadmilling filaments in cytoskeletal networks of FtsZ and its crosslinker ZapA. *Nat. Commun.* **10**, 5744 (2019).
30. L. W. Hamoen, J. C. Meile, W. de Jong, P. Noirot, J. Errington, SepF, a novel FtsZ-interacting protein required for a late step in cell division. *Mol. Microbiol.* **59**, 989–999 (2006).
31. K. S. Ramamurthi, R. Losick, Negative membrane curvature as a cue for subcellular localization of a bacterial protein. *Proc. Natl. Acad. Sci. U.S.A.* **106**, 13541–13545 (2009).
32. J. Pogliano, N. Osborne, M. D. Sharp, A. Abanes-De Mello, A. Perez, Y. L. Sun, K. Pogliano, A vital stain for studying membrane dynamics in bacteria: A novel mechanism controlling septation during *Bacillus subtilis* sporulation. *Mol. Microbiol.* **31**, 1149–1159 (1999).
33. S. van Baarle, M. Bramkamp, The MinCDJ system in *Bacillus subtilis* prevents minicell formation by promoting divisome disassembly. *PLOS ONE* **5**, e9850 (2010).
34. E. Cendrowicz, S. P. van Kessel, L. S. van Bezouwen, N. Kumar, E. J. Boekema, D. J. Scheffers, *Bacillus subtilis* SepF binds to the C-terminus of FtsZ. *PLOS One* **7**, e43293 (2012).
35. R. M. Cleverley, J. R. Barrett, A. Basle, N. K. Bui, L. Hewitt, A. Solovyova, Z. Q. Xu, R. A. Daniel, N. E. Dixon, E. J. Harry, A. J. Oakley, W. Vollmer, R. J. Lewis, Structure and function of a spectrin-like regulator of bacterial cytokinesis. *Nat. Commun.* **5**, 5421 (2014).
36. G. A. Wilson, K. F. Bott, Nutritional factors influencing the development of competence in the *Bacillus subtilis* transformation system. *J. Bacteriol.* **95**, 1439–1449 (1968).
37. J. M. Sterlini, J. Mandelstam, Commitment to sporulation in *Bacillus subtilis* and its relationship to development of actinomycin resistance. *Biochem. J.* **113**, 29–37 (1969).
38. D. G. Gibson, L. Young, R. Y. Chuang, J. C. Venter, C. A. Hutchison III, H. O. Smith, Enzymatic assembly of DNA molecules up to several hundred kilobases. *Nat. Methods* **6**, 343–345 (2009).
39. K. Cramer, A. L. Bolender, I. Stockmar, R. Jungmann, R. Kasper, J. Y. Shin, Visualization of bacterial protein complexes labeled with fluorescent proteins and nanobody binders for STED microscopy. *Int. J. Mol. Sci.* **20**, 3376 (2019).
40. S. Sograte-Idrissi, N. Oleksiievets, S. Isbaner, M. Eggert-Martinez, J. Enderlein, R. Tsukanov, F. Opazo, Nanobody detection of standard fluorescent proteins enables multi-target DNA-PAINT with high resolution and minimal displacement errors. *Cell* **8**, 48 (2019).
41. U. Endesfelder, S. Malkusch, F. Fricke, M. Heilemann, A simple method to estimate the average localization precision of a single-molecule localization microscopy experiment. *Histochem. Cell Biol.* **141**, 629–638 (2014).
42. D. Comaniciu, P. Meer, Mean shift: A robust approach toward feature space analysis. *IEEE Trans. Pattern Anal. Mach. Intell.* **24**, 603–619 (2002).
43. F. Pedregosa, G. Varoquaux, A. Gramfort, V. Michel, B. Thirion, O. Grisel, M. Blondel, P. Prettenhofer, R. Weiss, V. Dubourg, J. Vanderplas, A. Passos, D. Cournapeau, M. Brucher, M. Perrot, E. Duchesnay, Scikit-learn: Machine learning in Python. *J Mach. Learn. Res.* **12**, 2825–2830 (2011).
44. P. Virtanen, R. Gommers, T. E. Oliphant, M. Haberland, T. Reddy, D. Cournapeau, E. Burovski, P. Peterson, W. Weckesser, J. Bright, S. J. van der Walt, M. Brett, J. Wilson, K. J. Millman, N. Mayorov, A. R. J. Nelson, E. Jones, R. Kern, E. Larson, C. J. Carey, I. Polat, Y. Feng, E. W. Moore, J. VanderPlas, D. Laxalde, J. Perktold, R. Cimrman, I. Henriksen, E. A. Quintero, C. R. Harris, A. M. Archibald, A. H. Ribeiro, F. Pedregosa, P. van Mulbregt; SciPy 1.0 Contributors, SciPy 1.0: Fundamental algorithms for scientific computing in Python. *Nat. Methods* **17**, 261–272 (2020).
45. P. R. Burkholder, N. H. Giles Jr., Induced biochemical mutations in *Bacillus subtilis*. *Am. J. Bot.* **34**, 345–348 (1947).
46. T. J. Kenney, C. P. Moran Jr., Organization and regulation of an operon that encodes a sporulation-essential sigma factor in *Bacillus subtilis*. *J. Bacteriol.* **169**, 3329–3339 (1987).

Acknowledgments: We thank P. Schwille and M. Bramkamp for helpful discussions. We thank A. Strasser for providing affinity purification protocols, S. Strauss for producing DNA-conjugated nanobodies, and T. Schlichthaerle for help with the labeling cartoon creation. We thank the Carlos Bustamante laboratory for providing strain KP161. We thank M. Spitaler from the MPIB Imaging Facility for live-cell imaging support. K.C. and S.C.M.R. acknowledge support from the International Max Planck Research School for Molecules of Life (IMPRS-ML). **Funding:** This research was funded in part by the European Research Council through an ERC Consolidator Grant (ReceptorPAINT, grant agreement no. 101003275), the German Research Foundation through SFB1032 (project A11, no. 201269156), the Danish National Research Foundation (Centre for Cellular Signal Patterns, DNRF135), the Max Planck Foundation and the Max Planck Society. **Author contributions:** K.C. conceived and performed experiments, analyzed and interpreted data, and wrote the manuscript. S.C.M.R. and A.A. conceived and wrote Python analysis scripts and A.A. helped with DNA-PAINT image acquisition. J.Y.S. conceived and supervised the study, performed experiments, and edited the manuscript. R.J. conceived and supervised the study, analyzed and interpreted data, and wrote the manuscript. All authors reviewed and approved the manuscript. **Competing interests:** The authors declare that they have no competing interests. **Data and materials availability:** All data needed to evaluate the conclusions in the paper are present in the paper and/or the Supplementary Materials. Localization datasets from this study are available at https://doi.org/10.5281/zenodo.10144266; software scripts used to analyze the data are available at https://doi.org/10.5281/zenodo.10144506.

Submitted 13 September 2023
Accepted 11 December 2023
Published 10 January 2024
10.1126/sciadv.adk5847

ScienceAdvances

Comparing divisome organization between vegetative and sporulating *Bacillus subtilis* at the nanoscale using DNA-PAINT

Kimberly Cramer, Susanne C. M. Reinhardt, Alexander Auer, Jae Yen Shin, and Ralf Jungmann

Sci. Adv. **10** (2), eadk5847. DOI: 10.1126/sciadv.adk5847

Science Advances (ISSN 2375-2548) is published by the American Association for the Advancement of Science. 1200 New York Avenue NW, Washington, DC 20005. The title *Science Advances* is a registered trademark of AAAS.

Science Advances
AAAS

Supplementary Materials for

Comparing divisome organization between vegetative and sporulating *Bacillus subtilis* at the nanoscale using DNA-PAINT

Kimberly Cramer *et al.*

Corresponding author: Jae Yen Shin, shinjaeyen@gmail.com; Ralf Jungmann, jungmann@biochem.mpg.de

Sci. Adv. **10**, eadk5847 (2024)
DOI: 10.1126/sciadv.adk5847

This PDF file includes:

Supplementary Figure 1 | Sporulation assay of strains. A sporulation assay was performed on strains KCB300, KCB1113, KCB328, and KCB102. WT (168) strain was used as a positive control and KP161 used as a negative control. Sporulation positive strains become opaque after nutrient depletion (see WT), indicating spore formation. Sporulation negative strains become transparent, indicating cell death (see KP161). Strains KCB300, KCB1113, KCB328, and KCB102 resemble the WT strain, indicating successful sporulation.

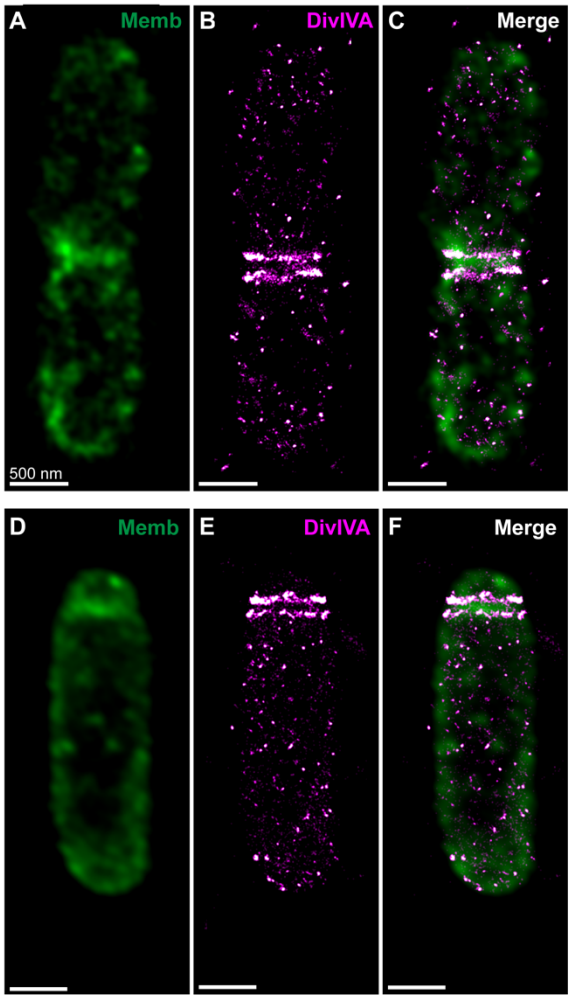

Supplementary Figure 2 | Dual DivIVA rings flank the division septum in vegetative and sporulating *B. subtilis*. DNA-PAINT was performed on DivIVA and PAINT imaging on the cell membrane. DivIVA imaging implemented in strain KCB300 via anti-GFP nanobodies conjugated with a DNA-PAINT handle. Membrane imaging performed using Nile Red PAINT dye. (**A–C**) Imaging results in a vegetative cell. (**A**) Nile Red imaging of the cell membrane in a vegetative cell shows the division septum as a band at mid-cell. (**B**) DNA-PAINT imaging reveals DivIVA localizes as one band on each side of the division septum. (**C**) Merge image of **A** and **B**. (**D–F**) Respective results for a sporulating cell.

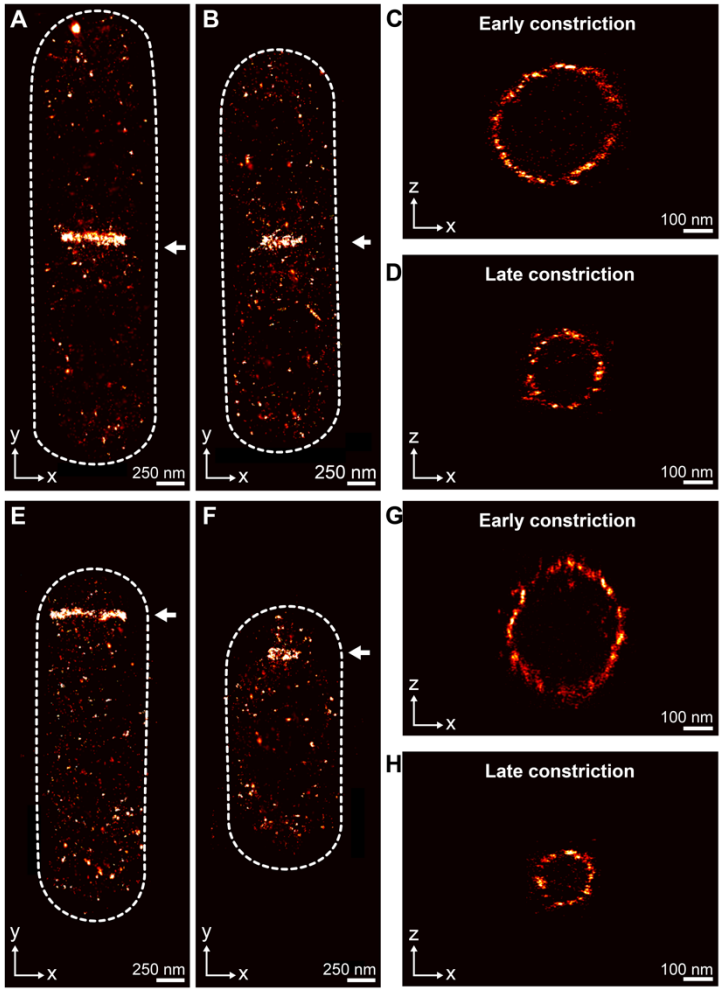

Supplementary Figure 3 | DNA-PAINT imaging of FtsZ in vegetative and sporulating *B. subtilis*. FtsZ imaging was implemented in strain KCB300 via anti-FtsZ primary antibodies and secondary nanobodies conjugated with a DNA-PAINT handle. (**A–D**) FtsZ localization in two vegetative cells. (**A**) DNA-PAINT imaging of FtsZ protein shows localization as a single band at the mid-cell, as expected. (**B**) DNA-PAINT imaging of FtsZ shows a "shorter" FtsZ band at the division septum when compared to **A**. (**C–D**) The zx-projections of the FtsZ bands in a and b are displayed in c and d, respectively. We show that both bands are indeed rings, and that the Z-ring displayed in **A** was fixed at an earlier stage of constriction compared to that of **B**. White arrows point to FtsZ bands. (**E–H**) Same as in **A–D** but for two sporulating cells. We visualize the Z-ring placed near a single cell pole, as expected.

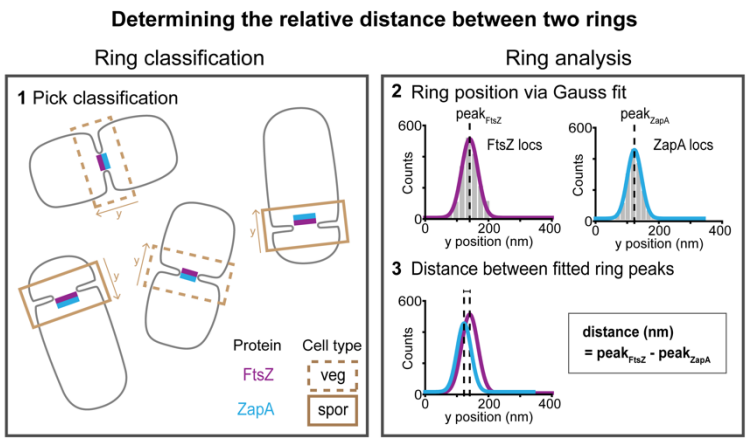

Supplementary Figure 4 | DNA-PAINT data analysis pipeline overview for determining the relative distance between two ring-shaped proteins in *B. subtilis.* (**1**) Rings are first classified via interactive "picking" in Picasso and saved with the corresponding cell type and protein classifier. In sporulating bacteria, the y-axis points towards the mother compartment, while no directionality exists for vegetative cells. (**2**) For each selected region, localizations are binned along the y-axis in the FtsZ and ZapA channel respectively. The positions of the FtsZ and ZapA rings are determined via Gaussian fits. (**3**) The peak position of ZapA was subtracted from the ring position of FtsZ to yield their distance. At sporulation septa, negative distance values indicate that the ZapA ring is closer to the mother cell compartment than the Z-ring and positive values indicate that ZapA is closer to the forespore than FtsZ. Analysis for FtsZ and SepF Exchange-PAINT data was performed analogously.

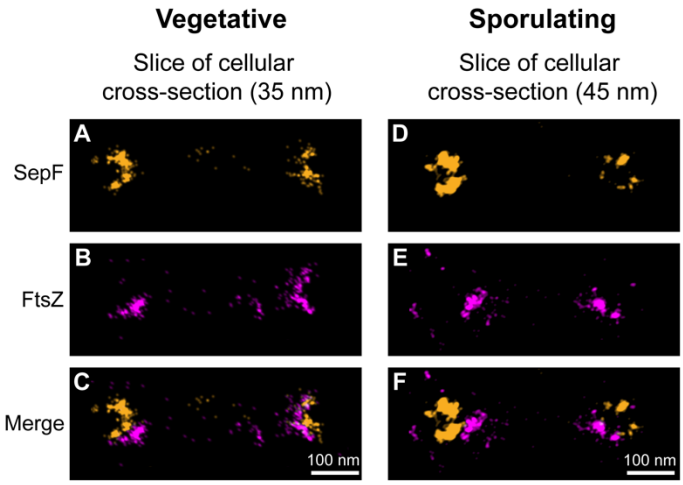

Supplementary Figure 5 | Single slice of 3D DNA-PAINT imaging of SepF and FtsZ in vegetative and sporulating *B. subtilis,* at the cellular cross-section. Imaging performed using strain KCB1113, SepF-sfGFP. FtsZ imaging performed via anti-FtsZ primary antibodies and secondary nanobodies conjugated with a DNA-PAINT handle. SepF imaging performed with anti-GFP nanobodies conjugated with a DNA-PAINT handle. (**A–C**) 35 nm slice of the division plane at the cellular cross-section in a vegetative cell. DNA-PAINT reveals (**A**) SepF assembles as arc shaped structures with endpoints facing away from the bacterial cytosol and (**B**) FtsZ as puncta or an arc shape at the cross-section of the division plane. (**C**) Merge image of **A** and **B** indicate FtsZ assemblies border or localize near to SepF arcs. (**D–F**) 45 nm slice of the division plane at the cellular cross-section in a sporulating cell. (**D**) Again, DNA-PAINT visualizes SepF as two arc shapes with endpoints facing away from the bacterial cytoplasm. (**E**) DNA-PAINT of FtsZ shows FtsZ assembly as puncta. (**F**) Merge image of d and e indicates FtsZ assemblies localize near to or adjoin SepF arcs. SepF in orange. FtsZ in magenta.

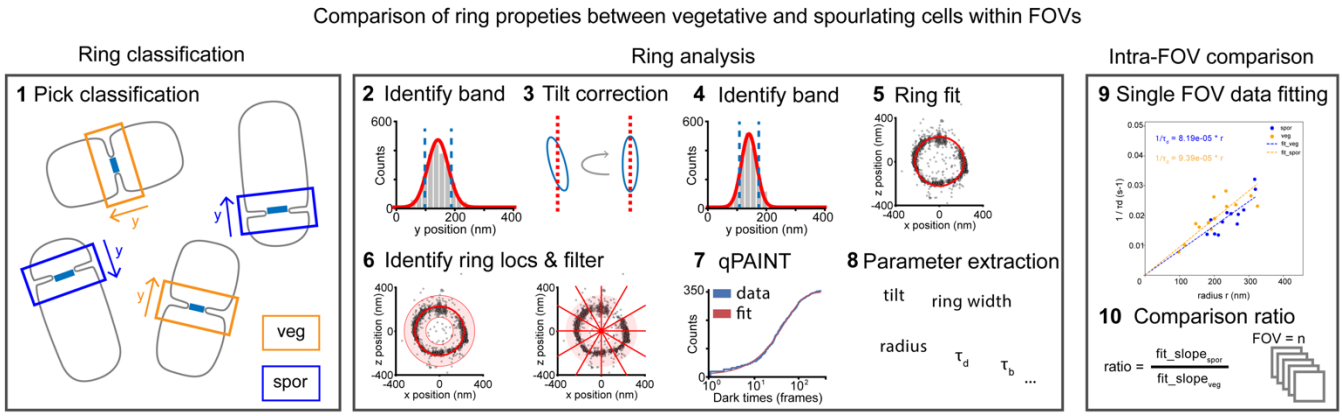

Supplementary Figure 6 | Comparison of ring properties between vegetative and sporulating cells. (**1**) Rings are first classified via interactive "picking" in Picasso and saved with the corresponding cell type classifier. (**2**) A histogram of localizations from an individual pick is calculated. The ring band is identified via a Gaussian fit and ring localizations are selected within a corridor around the peak position. The width of the corridor scales with the width of the Gauss fit. (**3**) Selected localizations are used to measure the tilt via singular value decomposition. The tilt is corrected for all localization in the pick via Rodrigues rotations. (**4**) Repeating the ring band identification on the tilt corrected data results in a narrower width of the Gauss fit and a more precise selection of ring localizations. (**5**) A circle is fitted to the selected ring localizations via least squares fit revealing the ring radius. (**6**) To reduce bias in the quantification of proteins amounts only localizations within ± 100 nm around the fitted ring radius (red shaded area, left panel) will be used. In addition, rings will be discarded if more than 20 % of localizations are outside of this ring region. Moreover, rings are further excluded if they are incompletely sampled along the ring circumference. To this aim the ring was split into 12 segments. A segment is considered to be sampled if it contains at least $N_{locs}/(4N_{segments})$ localizations. If at least 8 segments are sampled the ring is kept for further processing. (**7**) qPAINT was performed by fitting the cumulative distribution function of dark times yielding the mean dark time τ_d. (**8**) The determined ring parameters are saved for every selected ring in the FOV. (**9**) Protein amounts scale with $1/\tau_d$. In order to compare protein amounts the scaling of the inverse dark time with the ring radius was determined via a linear fit to all vegetative and sporulating rings, respectively, occurring in a single FOV. The slope of the linear fit represents protein densities. (**10**) The dark time as a metric for protein density varies with experimental conditions. To ensure comparability across FOVs the ratio between the sporulating and vegetative fit slopes is calculated, which measures the difference in protein amounts between both cell types.

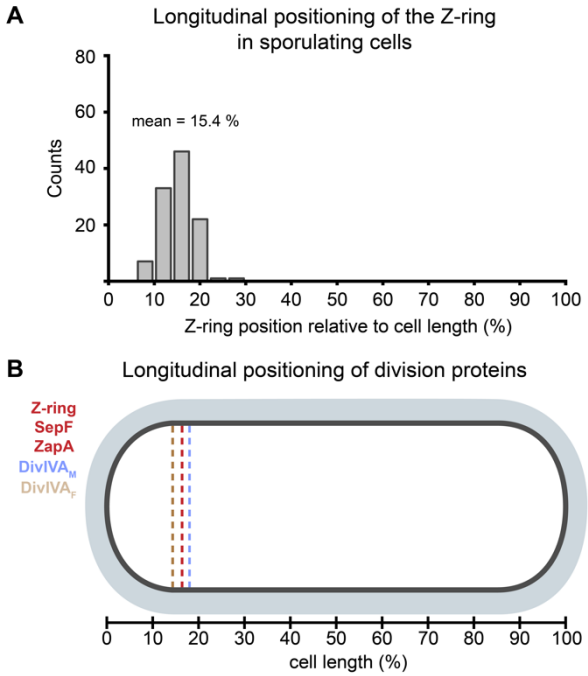

Supplementary Figure 7 | Longitudinal positioning of the Z-ring, SepF, ZapA, and DivIVA in sporulating cells. (**A**) Distribution of the longitudinal position of the Z-ring relative to cell length in individual sporulating *Bacillus subtilis* (KCB300). The Z-ring is typically positioned at 15 % ± 4 % (mean ± std, n = 110) of the cell length. (**B**) Schematic representation of the positioning of division proteins relative to cell length. Pictured cell is 2.8 μm long. SepF and ZapA rings are positioned with the Z-ring at approx. 15 % of the cell length (431 nm), indicated by red dotted line. Positioning of SepF and ZapA derived from results in **Fig. 3** of the Main text. Using the previously calculated mean distances of the Z-ring from rings DivIVA$_F$ and DivIVA$_M$ (see **Fig. 2**), DivIVA$_F$ and DivIVA$_M$ are positioned at approx. 13 % (360 nm) ± 1 % and 17 % (479 nm) ± 1 % of the cell length, respectively (mean ± std). Brown dotted line indicates positioning of DivIVA$_F$. Blue dotted line indicates mean positioning of DivIVA$_M$. DivIVA$_F$ refers to the DivIVA ring in the forespore compartment. DivIVA$_M$ refers to the DivIVA ring in the mother cell compartment. Cell membrane in black. Cell wall in grey. Cytoplasm in white. Cell length (%) refers to length of the cell body, excluding the cell wall.

Supplementary Table 1 | Strain information

Name	Genotype/Description	Reference or construction
168	Wild type (WT)	Burkholder et al(*45*)
KP161	*spoIIGB::erm*	Kenney et al(*46*)
KCB300	*divIVA::divIVA-GlyGlyGly-sfGFP spec*	pKCB300 → 168
KCB1113	*sepF::sepF- GlyGlyGly-sfGFP kan*	pKCB1113 → 168
KCB328	*zapA::zapA-ALFA kan*	pKCB328 → 168
KCB102	*zapA::zapA-ALFA kan* *divIVA::divIVA-GlyGlyGly-sfGFP spec*	gDNA KCB328 → 168

Supplementary Table 2 | Plasmid information

Name	Insert Description	Construction
pKCB300	divIVA-GlyGlyGly-sfGFP spec downstream-divIVA	Five-part Gibson Assembly
pKCB1113	sepF-GlyGlyGly-sfGFP kan downstream-sepF	Five-part Gibson Assembly
pKCB328	zapA-ALFA kan downstream-zapA	Gene block insertion into pMINI2.0 vector (NEB)

Supplementary Table 3 | Primer sequences

Name	Sequence (5' → 3')
JS029	AATTGGATGATATTTAGCGTATTTTGGAAAAGTTAATCG
JS030	GAATATCATTTGGCGTTAATGGCATGATCCCCGGGTACCGAGC
JS031	ATGCCATTAACGCCAAATG
KC050	CTTTGCTCATTCCTTTTCCTCAAATACAGC
KC051	AGGAAAAGGAGGAGGAGGAATGAGCAAAGGAGAAGAAC
KC052	ATTATACAGATTATTTGTAGAGCTCATCC
KC053	CTACAAATAATCTGTATAATAAAGAATAATTATTAATCTGTAG
JS036	TCAGAGAATTTATTAATTGAGAGAAGTTTCTATAGAATTTTTC
JS037	TTCTCTCAATTAATAAATTCTCTGATTATCTTGACATTTTC
11131F	ACAGGAGGCAGTAATTGGATGATATTTAGCGTATTTTGGAAAAGTTAATCGCCG
11131R	CCGCTCTGTCTCATGGATCCCCGGGTACCGAGC
11132F	CCCGGGGATCCATGAGACAGAGCGGGAATCTC
11132R	TCATACCGCCACCCCACCTCTGATGTTCGTCTTC
11133F	CATCAGAGGTGGGGTGGCGGTATGAGCAAAGG
11133R	AATACCAGAAAATTATTTGTAGAGCTCATCCATGCC
11134F	GCTCTACAAATAATTTTCTGGTATTTAAGGTTTTAG
11134R	TTGTGCCTTTGCCTAAAACAATTCATCCAGTAAAATATAATATTTTATTTTC
11135F	TGAATTGTTTTAGGCAAAGGCACAATATCAGCTTG
11135R	ATATCATCCAATTACTGCCTCCTGTGCTCTTTC
IKCB328A	CTGTACGTCATTTTCATTTGG
IKCB238B	CATCATTTGCTGCAACG

Supplementary Table S4| Imager and docking strand sequences

Name	Sequence (5' → 3')	Modifications	Vendor
R1 docking	TTTCCTCCT	5' C-3 azide	Metabion
R3 docking	TCCTCTCTC	5' C-3 azide	Metabion
5xR1 docking	TCCTCCTCCTCCTCCTCCT	5' C-3 azide	Metabion
5xR2 docking	ACCACCACCACCACCACCA	5' C-3 azide	Metabion
7xR3 docking	CTCTCTCTCTCTCTCTCTC	5' C-3 azide	Metabion
7xR4 docking	ACACACACACACACACACA	5' C-3 azide	Metabion
R1 imager	AGGAGGA	3'-Cy3B	Metabion
R2 imager	TGGTGGT	3'-Cy3B	Metabion
R3 imager	GAGAGAG	3'-Cy3B	Metabion
R4 imager	TGTGTGT	3'-Cy3B	Metabion

Supplementary Table S5 | DNA-PAINT imaging parameters

Target	Integration time	Number of frames	Imager concentration	Laser power at objective
DivIVA	100 - 200 ms	10,000 – 20,000	100 - 500 pM	20 - 25 mW
FtsZ	100 - 200 ms	10,000 – 20,000	75 - 300 pM	20 - 25 mW
ZapA	100 - 200 ms	10,000 – 20,000 per target	100 - 500 pM	20 – 25 mW
SepF	100 - 125 ms	10,000 – 20,000	100 - 500 pM	20 – 25 mW

Supplementary Table S6 | PAINT imaging parameters

Target	Integration time	Number of frames	Nile Red concentration	Laser power at objective	Localization precision
Membrane	40 ms	40,000	1.5 nM	45 mW	17.1 nm

Supplementary Table S7 | DNA sequence of gene block used to make pKCB328

Gene block sequence
CTGTACGTCATTTTCATTTGGTCAATAGCAGACAACGATACTTTTATCACTGAATGGGACACGTAATAATCTCC
TTTTTTTACACTTTTCGCTGTATATACCAGTGTATCATAACAGCGGGAGGCTCGTCTTTCCATTCATTTAATAA
ACGTGTTATGATAAGAACTAGGATTCTCGCGGAATGGAGGAGAAACGTTGTCTGACGGCAAAAAAACAAAAACA
ACCGTTGACATTTACGGCCAGCACTTCACGATTGTCGGTGAAGAAAGCAGAGCCCATATGAGGTATGTCGCCGG
AATTGTTGATGATAAAATGAGAGAAATCAATGAAAAAAATCCATACCTTGATATAAATAAACTTGCAGTGCTGA
CAGCGGTAAATGTGGTGCACGATTATGTCAAATTACAAGAGAAATGTGAAAAACTGGAGCGTCAGCTTAAAGAA
AAGGATCCTAGCCGTTTGGAAGAGGAACTGAGACGCCGTTTAACTGAATAATACCGTTCGTATAGCATACATTA
TACGAAGTTATTTTTCTGGTATTTAAGGTTTTAGAATGCAAGGAACAGTGAATTGGAGTTCGTCTTGTTATAAT
TAGCTTCTTGGGGTATCTTTAAATACTGTAGAAAAGAGGAAGGAAATAATAAATGGCTAAAATGAGAATATCAC
CGGAATTGAAAAAACTGATCGAAAAATACCGCTGCGTAAAAGATACGGAAGGAATGTCTCCTGCTAAGGTATAT
AAGCTGGTGGGAGAAAATGAAAACCTATATTTAAAAATGACGGACAGCCGGTATAAAGGGACCACCTATGATGT
GGAACGGGAAAAGGACATGATGCTATGGCTGGAAGGAAAGCTGCCTGTTCCAAAGGTCCTGCACTTTGAACGGC
ATGATGGCTGGAGCAATCTGCTCATGAGTGAGGCCGATGGCGTCCTTTGCTCGGAAGAGTATGAAGATGAACAA
AGCCCTGAAAAGATTATCGAGCTGTATGCGGAGTGCATCAGGCTCTTTCACTCCATCGACATATCGGATTGTCC

CTATACGAATAGCTTAGACAGCCGCTTAGCCGAATTGGATTACTTACTGAATAACGATCTGGCCGATGTGGATT
GCGAAAACTGGGAAGAAGACACTCCATTTAAAGATCCGCGCGAGCTGTATGATTTTTTAAAGACGGAAAAGCCC
GAAGAGGAACTTGTCTTTTCCCACGGCGACCTGGGAGACAGCAACATCTTTGTGAAAGATGGCAAAGTAAGTGG
CTTTATTGATCTTGGGAGAAGCGGCAGGGCGGACAAGTGGTATGACATTGCCTTCTGCGTCCGGTCGATCAGGG
AGGATATCGGGGAAGAACAGTATGTCGAGCTATTTTTTGACTTACTGGGGATCAAGCCTGATTGGGAGAAAATA
AAATATTATATTTTACTGGATGAATTGTTTTAGACAACTATGCTAGATATCATCATCTTAATCTTGCTCCTGAT
GGGGACTTTACTGGGGTTAAAACGCGGTTTTATCCTGCAGTTTATCCGCTTGACGAGCTTTATTTTATCAATTG
CCTTTGCGGCTTTATTCTATAAAAACGTGGCACCGCATTTACATTGGATTCCCGCACCCGATTTTTCAGCGGGA
CAGCCGGCTCTTTCTTTTTTTACGGGGAATTTGGAAGCAGCGTACTATAATGCGATTGCGTTTATCGTTTTATT
TATCATTGCTAAAATCTTACTGAGAATCATCGGCTCGTTCCTGAGTATTGTAGCCGGCATTCCGGTGATTAAAC
AAATCAACCAGATGCTGGGAGCCGTTCTCGGTTTTCTAGAAGTCTATTTATTTACATTTGTGCTGCTGTATGTC
GCATCCGTTCTGCCGGTAGACGCGTTGCAGCAAATGATG

Supplementary Table S8 | List of DNA-PAINT imaging datasets and their localization precisions

Dataset	Loc. Precision (nm)
230401_fov4_kcb1113_500pMr4_SepF_DP_1_drift_aligned_picked.hdf5	6.35
230518_artemis_kcb1113_fov4_140pM-r2_SepF_DP_1_drift_aligned_picked.hdf5	4.83
230518_artemis_kcb1113_fov1_150pM-r2_SepF_DP-2_1_drift_aligned_picked.hdf5	4.73
230310_kcb1113_2plex_spor_fov5_500pM-r3_SepF_DP_3_drift_picked.hdf5	6.47
230518_artemis_kcb1113_fov2_150pM-r2_SepF_DP_1_drift_aligned_picked.hdf5	5.22
230401_fov2_kcb1113_50pMr2_SepF_DP_1_drift_filter_sxsy_picked.hdf5	6.14
221015_2plex_rab7xR4_gfp5xR1_kcb1113-fov1-SepF_2_drift_aligned_picked.hdf5	5.27
230310_kcb1113_2plex_spor_fov3_500pM-r3_SepF_DP_1_drift_aligned_picked.hdf5	4.82
230401_fov4_kcb1113_500pMr4_SepF_DP_1_drift_aligned_picked.hdf5	6.28
230310_kcb1113_2plex_spor_fov3_500pM-r3_SepF_DP_1_drift_aligned_picked.hdf5	5.04
230518_artemis_kcb1113_fov2_150pM-r2_SepF_DP_1_drift_aligned_picked.hdf5	4.10
230401_fov1_kcb1113_500pMr4_SepF_DP_1_drift_filter-2_picked.hdf5	7.50
230518_artemis_kcb1113_fov3_150pM-r2_SepF_DP_1_drift_aligned_picked.hdf5	5.03
230401_fov2_kcb1113_50pMr2_SepF_DP_1_drift_filter_sxsy_picked.hdf5	6.74
230310_kcb1113_2plex_spor_fov4_500pM-r3_SepF_DP_1_drift_aligned_picked.hdf5	5.47
230518_artemis_kcb1113_fov4_140pM-r2_SepF_DP_1_drift_aligned_picked.hdf5	4.66
230310_kcb1113_2plex_spor_fov2_500pM-r3_SepF_DP_1_drift_aligned_picked.hdf5	5.56
230401_fov3_kcb1113_500pMr2_SepF_DP_1_drift_aligned_picked.hdf5	6.26
221015_2plex_rab7xR4_gfp5xR1_kcb1113-fov1-SepF_2_drift_aligned_picked.hdf5	7.56
230310_kcb1113_2plex_spor_fov2_500pM-r3_SepF_DP_1_drift_aligned_picked.hdf5	5.37
230518_artemis_kcb1113_fov1_150pM-r2_SepF_DP-2_1_drift_aligned_picked.hdf5	5.28
230310_kcb1113_2plex_spor_fov5_500pM-r3_SepF_DP_3_drift_picked.hdf5	6.77
230401_fov3_kcb1113_500pMr2_SepF_DP_1_drift_aligned_picked.hdf5	5.79
230518_artemis_kcb1113_fov3_150pM-r2_SepF_DP_1_drift_aligned_picked.hdf5	4.62
230310_kcb1113_2plex_spor_fov4_500pM-r3_SepF_DP_1_drift_aligned_picked.hdf5	5.73
230401_fov1_kcb1113_500pMr4_SepF_DP_1_drift_filter-2_picked.hdf5	6.33

230513_Gemini_fov3_Zring_200pM_FtsZ_DP_1_drift_picked.hdf5	5.01
221006_spor_KCB324_rab5xR2_GFP5xR1_fov2_FtsZ_1_aligned_picked.hdf5	6.03
200524_test_0p75_fov0_dp_ftsz_1_drift_picked.hdf5	5.72
221015_2plex_rab7xR4_gfp5xR1_kcb1113-fov3-FtsZ_1_drift_picked.hdf5	5.18
221006_spor_KCB324_rab5xR2_GFP5xR1_fov1_FtsZ_DP_1_aligned_PICKED.hdf5	9.10
200618_exchange1_fov7_ftsz_dp_1_drift_aligned_picked.hdf5	4.90
230314_kcb300_spor_RBnb5xr2_200pm-r2_fov2_FtsZ_DP_1_drift_picked.hdf5	5.31
230401_fov2_kcb1113_150pMr2_FtsZ_DP_1_drift_picked.hdf5	6.94
230513_artemis_Zring_fov3_200pM-r2_ftsz_DP_1_drift_picked.hdf5	5.66
230513_apollo_Zrings_fov1_r2-125pM_FtsZ_DP_1_drift_picked.hdf5	5.70
230513_artemis_Zring_fov8_300pM-r2_ftsz_DP_1_drift_picked.hdf5	5.39
200524_test_0p75_fov0_dp_ftsz_1_drift_picked.hdf5	4.58
230513_Gemini_fov3_Zring_200pM_FtsZ_DP_1_drift_picked.hdf5	5.01
220913_kcb306_spor_alfa2xr3_rab5xR2_fov2_200pM-R2_FtsZ_1_drift_aligned_PICKED.hdf5	5.17
230429_fov3_kcb300_115pM-r2_20mW_ftsz_DP_2_drift_aligned3_picked.hdf5	6.50
230513_Gemini_fov1_Zring_FtsZ_DP_1_drift_picked.hdf5	4.91
230513_artemis_Zring_fov8_300pM-r2_ftsz_DP_1_drift_picked.hdf5	4.94
230317_fov3_2plex_kcb1113_200pM-r2_DP_FtsZ_1_DRIFT_aligned_picked.hdf5	4.96
230309_kcb1113_veg_2plex_fov4_300pM-r2_FtsZ_DP_1_drift_picked.hdf5	5.11
230513_apollo_Zrings_fov7_r2-300pM_FtsZ_DP_1_drift_picked.hdf5	6.35
230513_Gemini_fov10_Zring_300pM_FtsZ_DP_1_drift_aligned_picked.hdf5	5.05
230429_fov1_kcb1113_200pM-r2_FtsZ_DP_1_drift_aligned_picked.hdf5	4.04
200716_exch_new_fov20_dp_ftsz_1_aligned_picked.hdf5	5.19
230513_Gemini_fov4_Zring_200pM_FtsZ_DP_1_MMStack_Pos0.ome_locs_picked.hdf5	5.02
230513_Gemini_fov6_Zring_300pM_FtsZ_DP_1_drift_picked.hdf5	4.77
220913_kcb306_spor_alfa2xr3_rab5xR2_fov1_200pM-R2_FtsZ_1_drift_picked.hdf5	4.71
230513_apollo_Zrings_fov9_r2-300pM_FtsZ_DP_1_drift_picked.hdf5	6.42
220429_kcb102_alfaP3-NBrabbit-7xr4_test_fov1-Ftsz_DP_1_drift_aligned_picked.hdf5	4.15
230513_apollo_Zrings_fov10_r2-300pM_FtsZ_DP_1_drift_picked.hdf5	6.64
220913_kcb306_spor_alfa2xr3_rab5xR2_fov2_200pM-R2_FtsZ_1_drift_aligned_PICKED.hdf5	4.44
230310_kcb1113_2plex_spor_fov5_200pM-r2_FtsZ_DP_1_drift_picked.hdf5	7.99
230314_kcb300_spor_RBnb5xr2_200pm-r2_fov4_FtsZ_DP_1_drift_picked.hdf5	4.69
220913_kcb306_spor_alfa2xr3_rab5xR2_fov1_200pM-R2_FtsZ_1_drift_picked.hdf5	4.82
220805_kcb102_fov2_3plex_nbRAB7xR5_FtsZ_1_aligned_PICKED.hdf5	6.31
200618_exchange1_fov8_ftsz_dp_1_aligned_picked.hdf5	4.37
230429_fov3_kcb1113_225pM-r2_ftsz_DP_1_drift_picked.hdf5	4.83
230513_apollo_Zrings_fov5_r2-300pM_FtsZ_DP_1_drift_picked.hdf5	6.26

230310_kcb1113_2plex_spor_fov2_160pM-r2_FtsZ_DP_1_aligned_picked.hdf5	5.98
220428_kcb102_AB-FtsZ_7xR4_50pM_fov1_DP_1_drift_filter_VEG-picked.hdf5	5.86
230429_fov3_kcb1113_225pM-r2_ftsz_DP_1_drift_picked.hdf5	4.49
230314_kcb300_spor_RBnb5xr2_200pm-r2_fov6_FtsZ_DP_1_drift_picked.hdf5	4.25
191218_ftsZ_ntsecondary_fov2_200pM_r3_23mW561_3dDP_1_1_drift - Copy_FtsZ_picked.hdf5	5.77
230513_artemis_Zring_fov5_200pM-r2_ftsz_DP_1_drift_picked.hdf5	4.44
230513_Gemini_fov6_Zring_300pM_FtsZ_DP_1_drift_picked.hdf5	5.07
230513_artemis_Zring_fov3_200pM-r2_ftsz_DP_1_drift_picked.hdf5	5.25
220913_kcb306_spor_alfa2xr3_rab5xR2_fov3_200pM-R2_FtsZ_2_drift_picked.hdf5	4.79
230401_fov3_kcb1113_112pMr2_FtsZ_DP_1_drift_aligned_picked.hdf5	6.62
221006_spor_KCB324_rab5xR2_GFP5xR1_fov3_FtsZ_1_drift_picked.hdf5	6.57
230314_kcb300_spor_RBnb5xr2_200pm-r2_fov2_FtsZ_DP_1_drift_picked.hdf5	4.87
200717_exch_kcb300_fov4_dp_ftsz_1_drift_align_picked.hdf5	4.34
220428_kcb102_AB-FtsZ_7xR4_50pM_fov1_DP_1_drift_filter_SPOR-picked.hdf5	5.42
230513_Gemini_fov2_Zring_FtsZ_DP_1_drift_picked.hdf5	4.62
230317_fov3_2plex_kcb1113_200pM-r2_DP_FtsZ_1_DRIFT_aligned_picked.hdf5	5.82
042320_fov2_exch_ftsz_dp_1_drift_FtsZ_spor_picked.hdf5	5.27
230513_apollo_Zrings_fov8_r2-300pM_FtsZ_DP_1_drift_picked.hdf5	5.71
230309_kcb1113_veg_2plex_100pM-R2_fov2_FtsZ_DP_1_drift_picked.hdf5	5.64
230401_fov1_kcb1113_150pMr2_FtsZ_DP_1_drift_aligned_picked.hdf5	6.69
230513_Gemini_fov7_Zring_300pM_FtsZ_DP_1_MMStack_Pos0.ome_locs_picked.hdf5	5.59
230310_kcb1113_2plex_spor_fov5_200pM-r2_FtsZ_DP_1_drift_picked.hdf5	8.26
221015_2plex_rab7xR4_gfp5xR1_kcb1113-fov3-FtsZ_1_drift_picked.hdf5	5.17
200619_exchange2_fov1_ftsZ_dp_1_aligned_picked.hdf5	4.85
230513_Gemini_fov7_Zring_300pM_FtsZ_DP_1_MMStack_Pos0.ome_locs_picked.hdf5	5.25
221006_spor_KCB324_rab5xR2_GFP5xR1_fov2_FtsZ_1_aligned_picked.hdf5	5.77
042620_spor_exh_fov2_60min_ftsz_dp_1_drift_early_sporsept.hdf5	5.64
200717_exch_kcb300_fov2_dp_ftsz_1_aligned_picked.hdf5	3.83
230401_fov5_kcb1113_115pMr2_FtsZ_DP_1_MMStack_Pos0.ome_locs_picked.hdf5	7.00
200524_test_2pt0_fov0_dp_ftsz_1_aligned_picked.hdf5	6.23
230317_fov1_2plex_kcb1113_200pM-r2_DP_FtsZ_1_drift_aligned_picked.hdf5	6.19
230513_Gemini_fov8_Zring_300pM_FtsZ_DP_1_drift_picked.hdf5	4.77
230513_apollo_Zrings_fov8_r2-300pM_FtsZ_DP_1_drift_picked.hdf5	5.92
230513_artemis_Zring_fov6_200pM-r2_ftsz_DP_1_drift_picked.hdf5	4.57
230429_fov1_kcb1113_200pM-r2_FtsZ_DP_1_drift_aligned_picked.hdf5	3.65
230513_apollo_Zrings_fov2_r2-200pM_FtsZ_DP_1_drift_picked.hdf5	6.02
230513_Gemini_fov2_Zring_FtsZ_DP_1_drift_picked.hdf5	4.86
230429_fov2_kcb300_200pM-r2_20mW_FtsZ-DP_1_drift_aligned_picked.hdf5	5.14

230513_artemis_Zring_fov10_300pM-r2_ftsz_DP_1_drift_picked.hdf5	4.69
230310_kcb1113_2plex_spor_fov1_100pM-r2_FtsZ_DP_1_drift_aligned_picked.hdf5	5.39
191218_ftsZ_ntsecondary_fov3_dp_r3_antiftsz_100pM_100mWset561_drift - Copy_picked.hdf5	5.61
230513_Gemini_fov8_Zring_300pM_FtsZ_DP_1_drift_picked.hdf5	5.04
230513_Gemini_fov4_Zring_200pM_FtsZ_DP_1_MMStack_Pos0.ome_locs_picked.hdf5	5.50
230513_artemis_Zring_fov9_300pM-r2_ftsz_DP_1_drift_picked.hdf5	4.68
230513_apollo_Zrings_fov6_r2-300pM_FtsZ_DP_1_drift_picked.hdf5	5.38
200716_exch_new_test_fov1_dp_ftsz_1_aligned_picked.hdf5	4.39
230513_apollo_Zrings_fov4_r2-200pM_FtsZ_DP_1_drift_picked.hdf5	6.48
230314_kcb300_spor_RBnb5xr2_200pm-r2_fov3_FtsZ_DP_1_drift_picked.hdf5	4.56
230513_apollo_Zrings_fov3_r2-200pM_FtsZ_DP_1_drift_picked.hdf5	6.15
230429_fov1_kcb300true_200pM-r2_20mW_FtsZ-DP_1_Mdrift_aligned_picked.hdf5	5.25
230513_Gemini_fov5_Zring_300pM_FtsZ_DP_1_drift_picked.hdf5	4.90
230513_artemis_Zring_fov1_125pM-r2_ftsz_DP_2_drift_picked.hdf5	4.77
220805_kcb102_fov1_3plex_nbGFP5xR1_FtsZ-2_1_drift_aligned_picked.hdf5	6.72
200716_exch_new_fov23_dp_ftsz_2_drift_aligned_picked.hdf5	6.52
230429_fov2_kcb300_200pM-r2_20mW_FtsZ-DP_1_drift_aligned_picked.hdf5	5.34
042320_fov1_exch_ftsz_DP_1_1_drift_aligned_picked.hdf5	4.48
230310_kcb1113_2plex_spor_fov3_200pM-r2_FtsZ_DP_1_drift_aligned_picked.hdf5	6.24
200717_exch_kcb300_fov1_dp_ftsz_1_drift_aligned_picked.hdf5	4.27
230513_apollo_Zrings_fov3_r2-200pM_FtsZ_DP_1_drift_picked.hdf5	6.16
230317_fov1_2plex_kcb1113_200pM-r2_DP_FtsZ_1_drift_aligned_picked.hdf5	6.63
221015_2plex_rab7xR4_gfp5xR1_kcb1113-fov1-FtsZ_1_drift_aligned_picked.hdf5	5.53
230429_fov4_kcb1113_400pM-r2_ftsz_dp_2_drift_aligned_picked.hdf5	5.27
230401_fov3_kcb1113_112pMr2_FtsZ_DP_1_drift_aligned_picked.hdf5	6.86
230513_apollo_Zrings_fov2_r2-200pM_FtsZ_DP_1_drift_picked.hdf5	5.59
230401_fov5_kcb1113_115pMr2_FtsZ_DP_1_MMStack_Pos0.ome_locs_picked.hdf5	6.40
230513_apollo_Zrings_fov6_r2-300pM_FtsZ_DP_1_drift_picked.hdf5	5.83
230314_kcb300_spor_RBnb5xr2_200pm-r2_fov3_FtsZ_DP_1_drift_picked.hdf5	4.81
042620_spor_exh_fov5_60min_ftsz_dp_1_drift_FtsZ_prox_picked.hdf5	5.05
230314_kcb300_spor_RBnb5xr2_200pm-r2_fov1_FtsZ_DP_1_drift_picked.hdf5	5.33
200619_exchange2_fov4_ftsz_dp_1_drift_aligned_picked.hdf5	3.62
230513_apollo_Zrings_fov10_r2-300pM_FtsZ_DP_1_drift_picked.hdf5	6.66
230401_fov2_kcb1113_150pMr2_FtsZ_DP_1_drift_picked.hdf5	6.70
200522_test_fov1000_ftsz_1_drift_aligned_picked.hdf5	11.53
230513_apollo_Zrings_fov9_r2-300pM_FtsZ_DP_1_drift_picked.hdf5	6.51
230429_fov2_kcb1113_200pM-r2_FtsZ_DP_1_drift_aligned_picked.hdf5	10.73
230513_apollo_Zrings_fov7_r2-300pM_FtsZ_DP_1_drift_picked.hdf5	5.68

221006_spor_KCB324_rab5xR2_GFP5xR1_fov4_FtsZ_1_drift_picked.hdf5	6.27
230429_fov1_kcb300true_200pM-r2_20mW_FtsZ-DP_1_Mdrift_aligned_picked.hdf5	5.13
200716_exch_old_fov2_dp_ftsz_1_drift_aligned_picked.hdf5	5.26
042320_fov3_exch_ftsz_dp_1_DRIFT_FtsZ_spor_picked.hdf5	4.94
200716_exch_new_fov21_dp_ftsz_1_aligned_picked.hdf5	4.75
230513_apollo_Zrings_fov5_r2-300pM_FtsZ_DP_1_drift_picked.hdf5	6.20
230513_apollo_Zrings_fov1_r2-125pM_FtsZ_DP_1_drift_picked.hdf5	6.53
230401_fov1_kcb1113_150pMr2_FtsZ_DP_1_drift_aligned_picked.hdf5	6.32
230513_Gemini_fov5_Zring_300pM_FtsZ_DP_1_drift_picked.hdf5	5.30
042620_spor_exh_fov3_60min_ftsz_dp_1_drift_ftsz_spor_picked.hdf5	4.77
221006_spor_KCB324_rab5xR2_GFP5xR1_fov4_FtsZ_1_drift_picked.hdf5	6.34
230513_artemis_Zring_fov6_200pM-r2_ftsz_DP_1_drift_picked.hdf5	5.20
042620_spor_exh_fov8_60min_ftsz_dp_1_drift_FtsZ_spor_picked.hdf5	4.63
042620_spor_exh_fov4_60min_ftsz_dp_1_drift_FtsZ_prox_picked.hdf5	5.29
230310_kcb1113_2plex_spor_fov3_200pM-r2_FtsZ_DP_1_drift_aligned_picked.hdf5	4.87
042620_spor_exh_fov6_60min_ftsz_dp_1_drift_FtsZ_prox_picked.hdf5	4.95
230314_kcb300_spor_RBnb5xr2_200pm-r2_fov1_FtsZ_DP_1_drift_picked.hdf5	5.40
200618_exchange1_fov2_redo_ftsz_dp_1_drift_aligned_picked.hdf5	3.28
230429_fov2_kcb1113_200pM-r2_FtsZ_DP_1_drift_aligned_picked.hdf5	4.40
200717_exch_kcb300_fov3_dp_ftsz_1_align_picked.hdf5	4.16
230310_kcb1113_2plex_spor_fov2_160pM-r2_FtsZ_DP_1_aligned_picked.hdf5	5.59
230429_fov4_kcb1113_400pM-r2_ftsz_dp_2_drift_aligned_picked.hdf5	5.39
200717_exch_kcb300_fov5_dp_ftsz_1_DRIFT_aligned_picked.hdf5	4.07
230513_artemis_Zring_fov1_125pM-r2_ftsz_DP_2_drift_picked.hdf5	5.46
200522_fov1002_bf_dp_ftsz_1_drift_aligned_picked.hdf5	6.27
230513_artemis_Zring_fov2_125pM-r2_ftsz_DP_1_drift_picked.hdf5	5.33
221015_2plex_rab7xR4_gfp5xR1_kcb1113-fov1-FtsZ_1_drift_aligned_picked.hdf5	4.89
230513_artemis_Zring_fov10_300pM-r2_ftsz_DP_1_drift_picked.hdf5	4.59
230513_Gemini_fov10_Zring_300pM_FtsZ_DP_1_drift_aligned_picked.hdf5	4.93
042320_fov3_exch_ftsz_dp_1_DRIFT_picked.hdf5	5.53
200619_exchange2_fov2_ftsz_dp_1_drift_aligned_picked.hdf5	4.34
230310_kcb1113_2plex_spor_fov1_100pM-r2_FtsZ_DP_1_drift_aligned_picked.hdf5	5.72
200618_exchange1_fov1_ftsz_DP_1_drift_aligned_picked.hdf5	4.28
230513_artemis_Zring_fov5_200pM-r2_ftsz_DP_1_drift_picked.hdf5	4.75
230314_kcb300_spor_RBnb5xr2_200pm-r2_fov6_FtsZ_DP_1_drift_picked.hdf5	4.85
230314_kcb300_spor_RBnb5xr2_200pm-r2_fov4_FtsZ_DP_1_drift_picked.hdf5	4.66
230429_fov3_kcb300_115pM-r2_20mW_ftsz_DP_2_drift_aligned3_picked.hdf5	7.15
200524_2pt0_fov2_dp_ftsz_1_drift_aligned_picked.hdf5	9.65
220913_kcb306_spor_alfa2xr3_rab5xR2_fov3_200pM-R2_FtsZ_2_drift_picked.hdf5	4.79

230513_Gemini_fov1_Zring_FtsZ_DP_1_drift_picked.hdf5	4.80
221006_spor_KCB324_rab5xR2_GFP5xR1_fov1_FtsZ_DP_1_aligned_PICKED.hdf5	9.12
042320_fov1_exch_ftsz_DP_1_1_drift_FtsZ_spor_picked.hdf5	4.36
230513_apollo_Zrings_fov4_r2-200pM_FtsZ_DP_1_drift_picked.hdf5	6.31
230513_artemis_Zring_fov9_300pM-r2_ftsz_DP_1_drift_picked.hdf5	4.38
230516_artemis_kcb102_fov3_1nM-r3_ZapA_DP_1_drift_aligned_picked.hdf5	10.33
230516_artemis_kcb102_fov1_1nM-R3_ZapA_DP_1_drift_aligned_picked.hdf5	5.85
230510_fov6_kcb328_2per_20mW_1nM-r3_ZapA_DP_1_drift_filter_picked.hdf5	5.61
230510_fov2_kcb328_2per_20mW_1nM-r3_ZapA_DP_2_drift_picked.hdf5	7.43
230516_artemis_kcb102_fov3_1nM-r3_ZapA_DP_1_drift_aligned_picked.hdf5	7.95
230510_fov2_kcb328_2per_20mW_1nM-r3_ZapA_DP_2_drift_picked.hdf5	7.70
230510_fov4_kcb328_2per_20mW_1nM-r3_ZapA_DP_1_drift_aligned_filter_picked.hdf5	5.58
230512_fov2_kcb102_1nM-R3_ZapA_DP_1_drift_aligned_filter_picked.hdf5	5.99
230516_artemis_kcb102_fov1_1nM-R3_ZapA_DP_1_drift_aligned_picked.hdf5	6.12
230512_fov2_kcb102_1nM-R3_ZapA_DP_1_drift_aligned_filter_picked.hdf5	6.63
230512_fov1_kcb102_1nM-R3_ZapA_DP_1_drift_aligned_filter_picked.hdf5	8.26
220805_kcb102_fov1_3plex_ALFA2xR3_ZapA_1_drift_aligned_picked.hdf5	6.28
230510_fov6_kcb328_2per_20mW_1nM-r3_ZapA_DP_1_drift_filter_picked.hdf5	4.82
230516_artemis_kcb102_fov4_1nM-r3_ZapA_DP_1_drift_aligned_filter_picked.hdf5	8.39
230510_fov4_kcb328_2per_20mW_1nM-r3_ZapA_DP_1_drift_aligned_filter_picked.hdf5	6.05
230516_artemis_kcb102_fov4_1nM-r3_ZapA_DP_1_drift_aligned_filter_picked.hdf5	7.52
220721_kcb102_spor_ZapA_2xR3_fov2-DP_1_drift_picked.hdf5	7.16
220805_kcb102_fov1_3plex_ALFA2xR3_ZapA_1_drift_aligned_picked.hdf5	6.12
230512_fov1_kcb102_1nM-R3_ZapA_DP_1_drift_aligned_filter_picked.hdf5	8.45
042620_spor_exh_fov3_60min_div_dp_1_drift_aligned_picked.hdf5	6.89
042620_spor_exh_fov3_60min_div_dp_1_drift_aligned_picked.hdf5	5.42
200619_exchange2_fov2_ftsz_dp_1_drift_aligned_picked.hdf5	4.03
042320_fov1_exch_DIV_DP_1_1_drift_aligned_picked_DivIVA_avg3.hdf5	4.41
200717_exch_kcb300_fov2_dp_ftsz_1_aligned_picked_avg3.hdf5	6.85
042620_spor_exh_fov8_60min_ftsz_dp_1_aligned_picked_ftsz.hdf5	4.27
042620_spor_exh_fov8_60min_ftsz_dp_1_aligned_picked_avg3.hdf5	4.27
200618_exchange1_fov1_DivIVA_DP_1_drift_aligned_picked.hdf5	6.20
200717_exch_kcb300_fov2_dp_ftsz_1_aligned_picked_avg3.hdf5	9.70
200717_exch_kcb300_fov5_dp_DivIVA_1_DRIFT_aligned_picked_Div.hdf5	5.69
200717_exch_kcb300_fov2_dp_ftsz_1_aligned_picked.hdf5	9.71
200717_exch_kcb300_fov1_dp_DivIVA_1_drift_aligned.hdf5	4.01
200618_exchange1_fov1_DivIVA_DP_1_drift_aligned_picked_avg3.hdf5	5.19

042620_spor_exh_fov3_60min_div_dp_1_drift_aligned_picked_avg3.hdf5	5.42
200717_exch_kcb300_fov4_dp_diviva_1_drift_align_picked.hdf5	9.09
042320_fov1_exch_DIV_DP_1_1_drift_aligned_picked_DivIVA.hdf5	4.41
200717_exch_kcb300_fov2_dp_ftsz_1_aligned_picked.hdf5	6.85
200618_exchange1_fov1_ftsz_DP_1_drift_aligned_picked_avg3.hdf5	4.67
042620_spor_exh_fov8_60min_diviva_dp_1_aligned_picked.hdf5	7.96
200619_exchange2_fov2_ftsz_dp_1_drift_aligned_picked_avg3.hdf5	4.03
200717_exch_kcb300_fov5_dp_DivIVA_1_DRIFT_aligned_picked_Ftsz.hdf5	11.00
042620_spor_exh_fov8_60min_diviva_dp_1_aligned_picked_avg3.hdf5	7.96
200717_exch_kcb300_fov1_dp_DivIVA_1_drift_aligned_avg3.hdf5	5.80
042620_spor_exh_fov8_60min_diviva_dp_1_aligned_picked_Div.hdf5	7.81
200619_exchange2_fov2_diviva_dp_1_drift_aligned_picked_avg3.hdf5	3.88
042320_fov1_exch_ftsz_DP_1_1_drift_aligned_picked_FtsZ_avg3.hdf5	3.00
200717_exch_kcb300_fov4_dp_diviva_1_drift_align_picked_avg3.hdf5	9.09
042620_spor_exh_fov3_60min_div_dp_1_drift_aligned_picked_avg3.hdf5	6.89
042320_fov1_exch_ftsz_DP_1_1_drift_aligned_picked_FtsZ.hdf5	3.00
200717_exch_kcb300_fov4_dp_ftsz_1_drift_align_picked.hdf5	5.11
200717_exch_kcb300_fov1_dp_DivIVA_1_drift_aligned.hdf5	5.80
200618_exchange1_fov1_ftsz_DP_1_drift_aligned_picked.hdf5	4.67
200619_exchange2_fov2_diviva_dp_1_drift_aligned_picked.hdf5	3.88
042620_spor_exh_fov8_60min_ftsz_dp_1_aligned_picked.hdf5	4.27
200717_exch_kcb300_fov1_dp_DivIVA_1_drift_aligned_avg3.hdf5	4.01
200717_exch_kcb300_fov4_dp_ftsz_1_drift_align_picked_avg3.hdf5	5.12
200203_CONDTN2_fov1_diviva_1_drift_Picklocs.hdf5	9.45
042620_spor_exh_fov3_60min_div_dp_1_drift_DivIVA_dualprox.hdf5	5.74
042620_spor_exh_fov1_15min_diviva__1_drift_DivIVA_dualprox_picked.hdf5	6.48
042320_fov2_exch_div_dp_1_DRIFT_diviva_dualprox_picked.hdf5	5.62
042320_fov1_exch_DIV_DP_1_1_DRIFT_Div_dualprox_picked.hdf5	4.56
042620_spor_exh_fov8_60min_diviva_dp_1_drift_DivIVA_dualprox_picked.hdf5	5.74
200220_Round5_kcb300_fov2_diviva_1_DRFIT_dualDivprox_picked.hdf5	6.45
200130_kcb300_fov1_DIVIVA_1_drift_SingleCell_DivIVAprox_picked.hdf5	7.00
042620_spor_exh_fov2_60min_diviva_dp_1_rift_DivIVA_dualprox_picked.hdf5	6.35
200203_CONDTN1_fov2_diviva_1_MMStack_Pos0.ome_locs_dualDivprox_picked.hdf5	13.40
042620_spor_exh_fov4_60min_div_dp_1_drift_DivIVA_Dualprox_picked.hdf5	7.51
042620_spor_exh_fov6_60min_div_1_drift_DivIVA_dualprox_picked.hdf5	5.14
042320_fov3_exch_div_dp_1_DRIFT_DivIVA_dualprox_picked.hdf5	4.92
042320_fov24_DIVIVAonly_multifov_dp_1_driftr_DivIVA_dualprox_picked.hdf5	6.49
042320_fov24_DIVIVAonly_multifov_dp_1_MMStack_fov20.ome_DivIVA_dualprox_picked.hdf5	5.53

200220_Round6_kcb300_fov1_R1diviva_1_DRIFT_singlecell_1DivProx_LocsPicked.hdf5	5.39
042220_kcb300_spor_dp__1_MMStack_fov100.ome_DRIFT_DivIVA_dualprox_picked.hdf5	5.98
042220_kcb300_spor_dp__1_MMStack_fov102.ome_DRIFT_DivIVA_dualproxpicked.hdf5	5.69
042620_spor_exh_fov5_60min_diviva_dp_1_drift_DivIVA_dualprox_picked.hdf5	6.84
200717_exch_kcb300_fov1_dp_DivIVA_1_drift_aligned_picked.hdf5	6.22
200716_exch_new_test_fov1_dp_DivIVA_1_aligned_picked.hdf5	6.83
200717_exch_kcb300_fov4_dp_DivIVA_1_drift_align_picked.hdf5	7.33
200619_exchange2_fov1_DivIVA_dp_1_aligned_picked.hdf5	6.06
042620_spor_exh_fov2_60min_DivIVA_aligned_picked.hdf5	6.31
042620_spor_exh_fov6_60min_DivIVA_dp_1_drift_aligned_picked.hdf5	5.13
200522_test_fov1000_DivIVA_1_drift_aligned_picked.hdf5	6.96
042320_fov3_exch_DivIVA_dp_1_DRIFT_align_picked.hdf5	4.44
042620_spor_exh_fov4_60min_DivIVA_dp_picked.hdf5	7.55
200717_exch_kcb300_fov2_dp_DivIVA_1_aligned_picked.hdf5	5.97
200618_exchange1_fov2_redo_DivIVA_dp_1_drift_aligned_picked.hdf5	4.72
200618_exchange1_fov7_DivIVA_dp_1_drift_aligned_picked.hdf5	7.98
200717_exch_kcb300_fov3_dp_DivIVA_1_align_picked.hdf5	5.54
200619_exchange2_fov2_DivIVA_dp_1_drift_aligned_picked.hdf5	4.63
200618_exchange1_fov1_DivIVA_DP_1_drift_aligned_picked.hdf5	5.68
200203_CONDTN2_fov1_DivIVA_1_drift_aligned_picked.hdf5	9.37
042620_spor_exh_fov5_60min_DivIVA_dp_1_picked.hdf5	7.12
200716_exch_new_fov21_dp_DivIVA_1_aligned_picked.hdf5	6.92
042320_fov2_exch_DivIVA_dp_1_drift_aligned_picked.hdf5	6.34
042620_spor_exh_fov8_60min_DivIVA_dp_1_aligned_picked.hdf5	6.06
200716_exch_new_fov23_dp_DivIVA_2_drift_aligned_picked.hdf5	9.04
200716_exch_old_test_fov1_dp_1_DivIVA_aligned_picked.hdf5	5.10
200716_exch_new_fov20_dp_DivIVA_1_aligned_picked.hdf5	6.03
200524_test_2pt0_fov0_dp_DivIVA_1_aligned_picked.hdf5	7.08
200716_exch_old_fov2_dp_DivIVA_1_drift_aligned_picked.hdf5	5.32
200524_2pt0_fov2_dp_diviva_1_drift_aligned_picked.hdf5	4.62
200524_test_0p75_fov0_dp_DivIVA_1_aligned_picked.hdf5	6.56
200717_exch_kcb300_fov5_dp_DivIVA_1_DRIFT_aligned_picked.hdf5	5.80
200619_exchange2_fov4_DivIVA_dp_1_drift_aligned_picked.hdf5	3.76
042620_spor_exh_fov3_60min_DivIVA_picked.hdf5	5.81
200522_fov1002_bf_dp_DivIVA_1_drift_aligned_picked.hdf5	8.15
200717_exch_kcb300_fov2_dp_ftsz_1_aligned_picked.hdf5	3.83
200717_exch_kcb300_fov3_dp_ftsz_1_align_picked.hdf5	4.16

042620_spor_exh_fov5_60min_ftsz_dp_1_picked.hdf5	5.57
042320_fov2_exch_ftsz_dp_1_drift_aligned_picked.hdf5	5.37
042320_fov3_exch_ftsz_dp_1_DRIFT_align_picked.hdf5	4.42
042620_spor_exh_fov2_60min_ftsz_aligned_picked.hdf5	5.14
200524_test_0p75_fov0_dp_ftsz_1_aligned_picked.hdf5	4.98
200716_exch_new_test_fov1_dp_ftsz_1_aligned_picked.hdf5	4.39
042620_spor_exh_fov8_60min_ftsz_dp_1_aligned_picked.hdf5	4.86
200716_exch_new_fov20_dp_ftsz_1_aligned_picked.hdf5	5.19
042620_spor_exh_fov3_60min_ftsz_picked.hdf5	4.48
200524_test_2pt0_fov0_dp_ftsz_1_aligned_picked.hdf5	6.23
200203_CONDTN2_fov1_ftsz_1_drift_aligned_picked.hdf5	6.21
200619_exchange2_fov2_ftsz_dp_1_drift_aligned_picked.hdf5	4.34
200618_exchange1_fov8_ftsz_dp_1_aligned_picked.hdf5	4.37
200618_exchange1_fov2_redo_ftsz_dp_1_drift_aligned_picked.hdf5	3.28
200716_exch_new_fov21_dp_ftsz_1_aligned_picked.hdf5	4.75
200618_exchange1_fov1_ftsz_DP_1_drift_aligned_picked.hdf5	4.28
200716_exch_old_test_fov1_dp_1_ftsz_aligned_picked.hdf5	5.11
200716_exch_new_fov23_dp_ftsz_2_drift_aligned_picked.hdf5	6.52
200619_exchange2_fov4_ftsz_dp_1_drift_aligned_picked.hdf5	3.62
200717_exch_kcb300_fov4_dp_ftsz_1_drift_align_picked.hdf5	4.34
042620_spor_exh_fov4_60min_ftsz_dp_picked.hdf5	5.15
200717_exch_kcb300_fov1_dp_ftsz_1_drift_aligned_picked.hdf5	4.27
200717_exch_kcb300_fov5_dp_ftsz_1_DRIFT_aligned_picked.hdf5	4.07
200524_2pt0_fov2_dp_ftsz_1_drift_aligned_picked.hdf5	9.65
200619_exchange2_fov1_ftsZ_dp_1_aligned_picked.hdf5	4.85
200716_exch_old_fov2_dp_ftsz_1_drift_aligned_picked.hdf5	5.26
200522_fov1002_bf_dp_ftsz_1_drift_aligned_picked.hdf5	6.27
042620_spor_exh_fov6_60min_ftsz_dp_1_drift_aligned_picked.hdf5	4.21
200618_exchange1_fov7_ftsz_dp_1_drift_aligned_picked.hdf5	4.90
200522_test_fov1000_ftsz_1_drift_aligned_picked.hdf5	11.53
042620_spor_exh_fov3_60min_DivIVA_dp_1_drift_aligned_picklocs.hdf5	6.92
200716_exch_old_fov2_dp_DivIVA_1_drift_aligned_picklocs.hdf5	5.61
200716_exch_new_fov23_dp_DivIVA_1_aligned_picklocs.hdf5	9.19
042320_fov3_exch_DivIVA_dp_1_DRIFT_align_picked.hdf5	4.97
200717_exch_kcb300_fov2_dp_DivIVA_1_drift_aligned_picklocs.hdf5	6.34
200203_CONDTN2_fov1_diviva_1_drift_veg_picklocs.hdf5	11.02
200716_exch_old_test_fov1_dp_1_DivIVA_drift_aligned_picklocs.hdf5	6.11
200618_exchange1_fov2_redo_DivIVA_dp_1_aligned_pickregs.hdf5	5.73
200213_fov1_200pmR1_DivIVA_1_drift_veg_picklocs.hdf5	9.98

200717_exch_kcb300_fov4_dp_DivIVA_1_align_picklocs.hdf5	11.72
042320_fov2_exch_DivIVA_dp_1_DRIFT_aligned_picklocs.hdf5	6.29
042620_spor_exh_fov6_60min_DivIVA_dp_1_drift_aligned_picklocs.hdf5	5.59
200130_kcb300_fov1_DIVIVA_1_drift_veg_picklocs.hdf5	8.08
200717_exch_kcb300_fov5_dp_DivIVA_1_DRIFT_aligned_pickregs.hdf5	5.40
042320_fov1_exch_DivIVA_DP_1_1_DRIFT_aligned_picked.hdf5	4.84
042620_spor_exh_fov4_60min_DivIVA_dp_1_aligned_picklocs.hdf5	8.38
200716_exch_new_test_fov1_DivIVA_2_drift_aligned_picklocs.hdf5	7.56
200618_exchange1_fov1_DivIVA_DP_1_drift_aligned_picklocs.hdf5	5.24
200717_exch_kcb300_fov3_dp_DivIVA_1_drift_align_pickregs.hdf5	5.21
200716_exch_new_fov20_dp_DivIVA_1_drift_aligned_picklocs.hdf5	8.16
200717_exch_kcb300_fov6_dp_DivIVA_1_aligned_picklocs.hdf5	7.93
230530_kcb102_Gemini_fov1_2plex_r4-150pM_FtsZ_DP_2_drift_aligned_picked.hdf5	4.23
230516_artemis_kcb102_fov3_180pM-r5_FtsZ_DP_1_drift_aligned_picked.hdf5	7.23
230530_kcb102_Gemini_fov1_2plex_r3-800pM_ZapA_DP_1_drift_aligned_picked.hdf5	4.75
230516_artemis_kcb102_fov1_1nM-R3_ZapA_DP_1_drift_aligned_picked.hdf5	5.63
230516_artemis_kcb102_fov3_1nM-r3_ZapA_DP_1_drift_aligned_picked.hdf5	9.90
230517_apollo_kcb102_fov4_r5-180pM_FtsZ_DP_1_drift_aligned_picked.hdf5	6.12
230516_artemis_kcb102_fov1_1nM-R3_ZapA_DP_1_drift_aligned_picked.hdf5	5.90
230512_fov1_kcb102_1nM-R3_ZapA_DP_1_drift_aligned_ZapA_picked.hdf5	7.68
230516_artemis_kcb102_fov4_1nM-r3_ZapA_DP_1_drift_aligned_picked.hdf5	7.90
230512_fov2_kcb102_1nM-R3_ZapA_DP_1_drift_aligned_filter_picked.hdf5	6.66
230512_fov2_kcb102_125pM-R2_FtsZ_DP_1_drift_aligned_picked.hdf5	6.12
230512_fov2_kcb102_1nM-R3_ZapA_DP_1_drift_aligned_filter_picked.hdf5	6.33
230516_artemis_kcb102_fov1_180pM-R5_FtsZ_DP_1_drift_aligned_picked.hdf5	5.83
230512_fov1_kcb102_1nM-R3_ZapA_DP_1_drift_aligned_ZapA_picked.hdf5	8.11
230516_artemis_kcb102_fov3_180pM-r5_FtsZ_DP_1_drift_aligned_picked.hdf5	7.92
230512_fov1_kcb102_125pM-R4_FtsZ_DP_1_drift_aligned_FtsZ_picked.hdf5	6.61
230516_artemis_kcb102_fov3_1nM-r3_ZapA_DP_1_drift_aligned_picked.hdf5	8.05
230516_artemis_kcb102_fov4_1nM-r3_ZapA_DP_1_drift_aligned_filter_picked.hdf5	7.52
230516_artemis_kcb102_fov4_180pM-r5_FtsZ_DP_1_drift_aligned_picked.hdf5	6.90
230517_apollo_kcb102_fov4_r3-1nM_ZapA_DP_1_drift_aligned_filter_picked.hdf5	6.94
230517_apollo_kcb102_fov4_r3-1nM_ZapA_DP_1_drift_aligned_filter_picked.hdf5	6.85
230516_artemis_kcb102_fov1_180pM-R5_FtsZ_DP_1_drift_aligned_picked.hdf5	5.77
230517_apollo_kcb102_fov4_r5-180pM_FtsZ_DP_1_drift_aligned_picked.hdf5	6.71
230512_fov1_kcb102_125pM-R4_FtsZ_DP_1_drift_aligned_FtsZ_picked.hdf5	7.21
230512_fov2_kcb102_125pM-R2_FtsZ_DP_1_drift_aligned_picked.hdf5	6.25
230621_apollo_kcb328_fov1_2plex_r4-170pM_DP_FtsZ_1_drift_aligned_picked.hdf5	5.73
230621_apollo_kcb328_fov1_2plex_r3-1nM_DP_ZapA_1_drift_aligned_picked.hdf5	7.28

230530_kcb102_Gemini_fov1_2plex_r4-150pM_FtsZ_DP_2_drift_aligned_picked.hdf5	4.23
230530_kcb102_Gemini_fov1_2plex_r3-800pM_ZapA_DP_1_drift_aligned_picked.hdf5	4.75
230530_kcb102_Gemini_fov3_2plex_r4-170pM_FtsZ_DP_1drift_aligned_picked.hdf5	4.91
230530_kcb102_Gemini_fov3_2plex_r3-800pM_ZapA_DP_1_drift_aligned_picked.hdf5	5.79
230621_kcb328_veg_fov1_r4-170pM_DP_FtsZ_1_drift_aligned_picked.hdf5	4.04
230621_kcb328_veg_fov1_2_r3-1nM_DP_ZapA_1_drift_aligned_picked.hdf5	5.60
230530_kcb102_Gemini_fov2_2plex_r3-800pM_ZapA_DP_1_drift_aligned_picked.hdf5	6.44
230530_kcb102_Gemini_fov2_2plex_r4-170pM_FtsZ_DP_1_drift_aligned_picked.hdf5	4.85
230401_fov2_kcb1113_50pMr2_SepF_DP_1_drift_aligned_picked.hdf5	6.21
230518_artemis_kcb1113_fov3_150pM-r2_SepF_DP_1_drift_aligned_picked.hdf5	5.05
230518_artemis_kcb1113_fov2_180pM-r5_FtsZ_DP_1_aligned_picked.hdf5	5.52
230518_artemis_kcb1113_fov3_150pM-r2_SepF_DP_1_drift_aligned_picked.hdf5	4.63
230518_artemis_kcb1113_fov3_180pM-r5_FsZ_DP_1_drift_aligned_picked.hdf5	4.43
230518_artemis_kcb1113_fov4_180pM-r5_FsZ_DP_1_drift_aligned_picked.hdf5	4.40
230310_kcb1113_2plex_spor_fov3_500pM-r3_SepF_DP_1_drift_aligned_picked.hdf5	5.05
230401_fov2_kcb1113_150pMr2_FtsZ_DP_1_drift_aligned_picked.hdf5	6.46
230401_fov2_kcb1113_50pMr2_SepF_DP_1_drift_aligned_picked.hdf5	6.86
230518_artemis_kcb1113_fov1_150pM-r2_DP-2_1_drift_aligned_picked.hdf5	4.78
230518_artemis_kcb1113_fov4_140pM-r2_SepF_DP_1_drift_aligned_picked.hdf5	5.08
230518_artemis_kcb1113_fov1_180pM-r5_DP-2_1_drift_aligned_picked.hdf5	4.80
230401_fov1_kcb1113_500pMr4_SepF_DP_1_drift_filter-2_aligned_picked.hdf5	6.55
230401_fov2_kcb1113_150pMr2_FtsZ_DP_1_drift_aligned_picked.hdf5	7.28
230401_fov3_kcb1113_500pMr2_SepF_DP_1_drift_aligned_filter_picked.hdf5	6.23
230518_artemis_kcb1113_fov2_150pM-r2_SepF_DP_1_drift_aligned_picked.hdf5	4.80
230518_artemis_kcb1113_fov1_150pM-r2_DP-2_1_drift_aligned_picked.hdf5	5.36
230401_fov3_kcb1113_112pMr2_FtsZ_DP_1_drift_aligned_picked.hdf5	6.76
230317_fov1_2plex_kcb1113_375pM-r3_DP_1_drift_aligned_picked.hdf5	5.19
230518_artemis_kcb1113_fov4_140pM-r2_SepF_DP_1_drift_aligned_picked.hdf5	4.32
230310_kcb1113_2plex_spor_fov3_500pM-r3_SepF_DP_1_drift_aligned_picked.hdf5	4.70
230518_artemis_kcb1113_fov1_180pM-r5_DP-2_1_drift_aligned_picked.hdf5	4.77
230401_fov1_kcb1113_150pMr2_FtsZ_DP_1_drift_aligned_picked.hdf5	7.41
230317_fov1_2plex_kcb1113_200pM-r2_DP_1_drift_aligned_picked.hdf5	6.16
230401_fov3_kcb1113_112pMr2_FtsZ_DP_1_drift_aligned_picked.hdf5	6.35
230518_artemis_kcb1113_fov2_180pM-r5_FtsZ_DP_1_aligned_picked.hdf5	5.83
230310_kcb1113_2plex_spor_fov3_200pM-r2_FtsZ_DP_1_drift_aligned_picked.hdf5	4.72
230310_kcb1113_2plex_spor_fov3_200pM-r2_FtsZ_DP_1_drift_aligned_picked.hdf5	5.21
230317_fov1_2plex_kcb1113_375pM-r3_DP_1_drift_aligned_picked.hdf5	5.32
230401_fov1_kcb1113_500pMr4_SepF_DP_1_drift_filter-2_aligned_picked.hdf5	7.79
230518_artemis_kcb1113_fov3_180pM-r5_FsZ_DP_1_drift_aligned_picked.hdf5	4.48

230401_fov1_kcb1113_150pMr2_FtsZ_DP_1_drift_aligned_picked.hdf5	6.43
230401_fov3_kcb1113_500pMr2_SepF_DP_1_drift_aligned_filter_picked.hdf5	6.14
230518_artemis_kcb1113_fov2_150pM-r2_SepF_DP_1_drift_aligned_picked.hdf5	5.04
230317_fov1_2plex_kcb1113_200pM-r2_DP_1_drift_aligned_picked.hdf5	6.63
230518_artemis_kcb1113_fov4_180pM-r5_FsZ_DP_1_drift_aligned_picked.hdf5	3.94

REFERENCES

1. E. F. Bi, J. Lutkenhaus, FtsZ ring structure associated with division in Escherichia coli. *Nature* **354**, 161–164 (1991).

2. J. Errington, L. J. Wu, Cell cycle machinery in *Bacillus subtilis*. *Subcell. Biochem.* **84**, 67–101 (2017).

3. P. Gamba, J. W. Veening, N. J. Saunders, L. W. Hamoen, R. A. Daniel, Two-step assembly dynamics of the *Bacillus subtilis* divisome. *J. Bacteriol.* **191**, 4186–4194 (2009).

4. L. G. Monahan, A. Robinson, E. J. Harry, Lateral FtsZ association and the assembly of the cytokinetic Z ring in bacteria. *Mol. Microbiol.* **74**, 1004–1017 (2009).

5. R. Duman, S. Ishikawa, I. Celik, H. Strahl, N. Ogasawara, P. Troc, J. Lowe, L. W. Hamoen, Structural and genetic analyses reveal the protein SepF as a new membrane anchor for the Z ring. *Proc. Natl. Acad. Sci. U.S.A.* **110**, E4601–E4610 (2013).

6. P. Szwedziak, Q. Wang, T. A. Bharat, M. Tsim, J. Lowe, Architecture of the ring formed by the tubulin homologue FtsZ in bacterial cell division. *eLife* **3**, e04601 (2014).

7. T. Mohammadi, G. E. Ploeger, J. Verheul, A. D. Comvalius, A. Martos, C. Alfonso, J. van Marle, G. Rivas, T. den Blaauwen, The GTPase activity of Escherichia coli FtsZ determines the magnitude of the FtsZ polymer bundling by ZapA in vitro. *Biochemistry* **48**, 11056–11066 (2009).

8. S. O. Jensen, L. S. Thompson, E. J. Harry, Cell division in *Bacillus subtilis*: FtsZ and FtsA association is Z-ring independent, and FtsA is required for efficient midcell Z-Ring assembly. *J. Bacteriol.* **187**, 6536–6544 (2005).

9. S. Pichoff, J. Lutkenhaus, Tethering the Z ring to the membrane through a conserved membrane targeting sequence in FtsA. *Mol. Microbiol.* **55**, 1722–1734 (2005).

10. N. Pende, A. Sogues, D. Megrian, A. Sartori-Rupp, P. England, H. Palabikyan, S. K. R. Rittmann, M. Grana, A. M. Wehenkel, P. M. Alzari, S. Gribaldo, SepF is the FtsZ anchor in archaea, with features of an ancestral cell division system. *Nat. Commun.* **12**, 3214 (2021).

11. M. Wenzel, I. N. Celik Gulsoy, Y. Gao, Z. Teng, J. Willemse, M. Middelkamp, M. G. M. van Rosmalen, P. W. B. Larsen, N. N. van der Wel, G. J. L. Wuite, W. H. Roos, L. W. Hamoen, Control of septum thickness by the curvature of SepF polymers. *Proc. Natl. Acad. Sci. U.S.A.* **118**, e2002635118 (2021).

12. K. Khanna, J. Lopez-Garrido, J. Sugie, K. Pogliano, E. Villa, Asymmetric localization of the cell division machinery during *Bacillus subtilis* sporulation. *eLife* **10**, e62204 (2021).

13. P. Eswaramoorthy, P. W. Winter, P. Wawrzusin, A. G. York, H. Shroff, K. S. Ramamurthi, Asymmetric division and differential gene expression during a bacterial developmental program requires DivIVA. *PLOS Genet.* **10**, e1004526 (2014).

14. J. H. Cha, G. C. Stewart, The divIVA minicell locus of *Bacillus subtilis*. *J. Bacteriol.* **179**, 1671–1683 (1997).

15. D. H. Edwards, J. Errington, The *Bacillus subtilis* DivIVA protein targets to the division septum and controls the site specificity of cell division. *Mol. Microbiol.* **24**, 905–915 (1997).

16. I. Barak, P. Prepiak, F. Schmeisser, MinCD proteins control the septation process during sporulation of *Bacillus subtilis*. *J. Bacteriol.* **180**, 5327–5333 (1998).

17. A. Lablaine, M. Serrano, C. Bressuire-Isoard, S. Chamot, I. Bornard, F. Carlin, A. O. Henriques, V. Broussolle, The morphogenetic protein CotE positions exosporium proteins CotY and ExsY during sporulation of Bacillus cereus. *mSphere* **6**, e00007-21 (2021).

18. J. Schnitzbauer, M. T. Strauss, T. Schlichthaerle, F. Schueder, R. Jungmann, Super-resolution microscopy with DNA-PAINT. *Nat. Protoc.* **12**, 1198–1228 (2017).

19. R. Jungmann, M. S. Avendano, M. Dai, J. B. Woehrstein, S. S. Agasti, Z. Feiger, A. Rodal, P. Yin, Quantitative super-resolution imaging with qPAINT. *Nat. Methods* **13**, 439–442 (2016).

20. R. Jungmann, M. S. Avendano, J. B. Woehrstein, M. Dai, W. M. Shih, P. Yin, Multiplexed 3D cellular super-resolution imaging with DNA-PAINT and Exchange-PAINT. *Nat. Methods* **11**, 313–318 (2014).

21. H. Gotzke, M. Kilisch, M. Martinez-Carranza, S. Sograte-Idrissi, A. Rajavel, T. Schlichthaerle, N. Engels, R. Jungmann, P. Stenmark, F. Opazo, S. Frey, The ALFA-tag is a highly versatile tool for nanobody-based bioscience applications. *Nat. Commun.* **10**, 4403 (2019).

22. M. E. Gundogdu, Y. Kawai, N. Pavlendova, N. Ogasawara, J. Errington, D. J. Scheffers, L. W. Hamoen, Large ring polymers align FtsZ polymers for normal septum formation. *EMBO J.* **30**, 617–626 (2011).

23. A. W. Bisson-Filho, Y. P. Hsu, G. R. Squyres, E. Kuru, F. Wu, C. Jukes, Y. Sun, C. Dekker, S. Holden, M. S. VanNieuwenhze, Y. V. Brun, E. C. Garner, Treadmilling by FtsZ filaments drives peptidoglycan synthesis and bacterial cell division. *Science* **355**, 739–743 (2017).

24. X. Yang, Z. Lyu, A. Miguel, R. McQuillen, K. C. Huang, J. Xiao, GTPase activity-coupled treadmilling of the bacterial tubulin FtsZ organizes septal cell wall synthesis. *Science* **355**, 744–747 (2017).

25. R. Pacheco-Gomez, X. Cheng, M. R. Hicks, C. J. Smith, D. I. Roper, S. Addinall, A. Rodger, T. R. Dafforn, Tetramerization of ZapA is required for FtsZ bundling. *Biochem. J.* **449**, 795–802 (2013).

26. P. Eswaramoorthy, M. L. Erb, J. A. Gregory, J. Silverman, K. Pogliano, J. Pogliano, K. S. Ramamurthi, Cellular architecture mediates DivIVA ultrastructure and regulates min activity in *Bacillus subtilis*. *MBio* **2**, e00257-11 (2011).

27. P. Guzman, J. Westpheling, P. Youngman, Characterization of the promoter region of the *Bacillus subtilis* spoIIE operon. *J. Bacteriol.* **170**, 1598–1609 (1988).

28. I. Barak, P. Youngman, SpoIIE mutants of *Bacillus subtilis* comprise two distinct phenotypic classes consistent with a dual functional role for the SpoIIE protein. *J. Bacteriol.* **178**, 4984–4989 (1996).

29. P. Caldas, M. Lopez-Pelegrin, D. J. G. Pearce, N. B. Budanur, J. Brugues, M. Loose, Cooperative ordering of treadmilling filaments in cytoskeletal networks of FtsZ and its crosslinker ZapA. *Nat. Commun.* **10**, 5744 (2019).

30. L. W. Hamoen, J. C. Meile, W. de Jong, P. Noirot, J. Errington, SepF, a novel FtsZ-interacting protein required for a late step in cell division. *Mol. Microbiol.* **59**, 989–999 (2006).

31. K. S. Ramamurthi, R. Losick, Negative membrane curvature as a cue for subcellular localization of a bacterial protein. *Proc. Natl. Acad. Sci. U.S.A.* **106**, 13541–13545 (2009).

32. J. Pogliano, N. Osborne, M. D. Sharp, A. Abanes-De Mello, A. Perez, Y. L. Sun, K. Pogliano, A vital stain for studying membrane dynamics in bacteria: A novel mechanism controlling septation during *Bacillus subtilis* sporulation. *Mol. Microbiol.* **31**, 1149–1159 (1999).

33. S. van Baarle, M. Bramkamp, The MinCDJ system in *Bacillus subtilis* prevents minicell formation by promoting divisome disassembly. *PLOS ONE* **5**, e9850 (2010).

34. E. Cendrowicz, S. P. van Kessel, L. S. van Bezouwen, N. Kumar, E. J. Boekema, D. J. Scheffers, *Bacillus subtilis* SepF binds to the C-terminus of FtsZ. *PLOS One* **7**, e43293 (2012).

35. R. M. Cleverley, J. R. Barrett, A. Basle, N. K. Bui, L. Hewitt, A. Solovyova, Z. Q. Xu, R. A. Daniel, N. E. Dixon, E. J. Harry, A. J. Oakley, W. Vollmer, R. J. Lewis, Structure and function of a spectrin-like regulator of bacterial cytokinesis. *Nat. Commun.* **5**, 5421 (2014).

36. G. A. Wilson, K. F. Bott, Nutritional factors influencing the development of competence in the *Bacillus subtilis* transformation system. *J. Bacteriol.* **95**, 1439–1449 (1968).

37. J. M. Sterlini, J. Mandelstam, Commitment to sporulation in *Bacillus subtilis* and its relationship to development of actinomycin resistance. *Biochem. J.* **113**, 29–37 (1969).

38. D. G. Gibson, L. Young, R. Y. Chuang, J. C. Venter, C. A. Hutchison, 3rd, H. O. Smith, Enzymatic assembly of DNA molecules up to several hundred kilobases. *Nat. Methods* **6**, 343–345 (2009).

39. K. Cramer, A. L. Bolender, I. Stockmar, R. Jungmann, R. Kasper, J. Y. Shin, Visualization of bacterial protein complexes labeled with fluorescent proteins and nanobody binders for STED microscopy. *Int. J. Mol. Sci.* **20**, 3376 (2019).

40. S. Sograte-Idrissi, N. Oleksiievets, S. Isbaner, M. Eggert-Martinez, J. Enderlein, R. Tsukanov, F. Opazo, Nanobody detection of standard fluorescent proteins enables multi-target DNA-PAINT with high resolution and minimal displacement errors. *Cell* **8**, 48 (2019).

41. U. Endesfelder, S. Malkusch, F. Fricke, M. Heilemann, A simple method to estimate the average localization precision of a single-molecule localization microscopy experiment. *Histochem. Cell Biol.* **141**, 629–638 (2014).

42. D. Comaniciu, P. Meer, Mean shift: A robust approach toward feature space analysis. *IEEE Trans. Pattern Anal. Mach. Intell.* **24**, 603–619 (2002).

43. F. Pedregosa, G. Varoquaux, A. Gramfort, V. Michel, B. Thirion, O. Grisel, M. Blondel, P. Prettenhofer, R. Weiss, V. Dubourg, J. Vanderplas, A. Passos, D. Cournapeau, M. Brucher, M. Perrot, E. Duchesnay, Scikit-learn: Machine learning in Python. *J Mach. Learn. Res.* **12**, 2825–2830 (2011).

44. P. Virtanen, R. Gommers, T. E. Oliphant, M. Haberland, T. Reddy, D. Cournapeau, E. Burovski, P. Peterson, W. Weckesser, J. Bright, S. J. van der Walt, M. Brett, J. Wilson, K. J. Millman, N. Mayorov, A. R. J. Nelson, E. Jones, R. Kern, E. Larson, C. J. Carey, I. Polat, Y. Feng, E. W. Moore, J. VanderPlas, D. Laxalde, J. Perktold, R. Cimrman, I. Henriksen, E. A. Quintero, C. R. Harris, A. M. Archibald, A. H. Ribeiro, F. Pedregosa, P. van Mulbregt; SciPy 1.0 Contributors, SciPy 1.0: Fundamental algorithms for scientific computing in Python. *Nat. Methods* **17**, 261–272 (2020).

45. P. R. Burkholder, N. H. Giles, Jr., Induced biochemical mutations in *Bacillus subtilis*. *Am. J. Bot.* **34**, 345–348 (1947).

46. T. J. Kenney, C. P. Moran, Jr., Organization and regulation of an operon that encodes a sporulation-essential sigma factor in *Bacillus subtilis*. *J. Bacteriol.* **169**, 3329–3339 (1987).

Publication 3: The Role of Nanoscale Distribution of Fibronectin in the Adhesion of Staphylococcus aureus Studied by Protein Patterning and DNA-PAINT

The Role of Nanoscale Distribution of Fibronectin in the Adhesion of Staphylococcus aureus Studied by Protein Patterning and DNA-PAINT

Heba Khateb, Rasmus S. Sørensen, Kimberly Cramer, Alexandra S. Eklund, Jorgen Kjems, Rikke L. Meyer, Ralf Jungmann, and Duncan Sutherland

ACS Nano
2022
16(7),10392–10403
doi: 10.1021/acsnano.2c00630

ACSNANO

www.acsnano.org

ARTICLE

The Role of Nanoscale Distribution of Fibronectin in the Adhesion of *Staphylococcus aureus* Studied by Protein Patterning and DNA-PAINT

Heba Khateb, Rasmus S. Sørensen, Kimberly Cramer, Alexandra S. Eklund, Jorgen Kjems, Rikke L. Meyer, Ralf Jungmann, and Duncan S. Sutherland*

Cite This: *ACS Nano* 2022, 16, 10392−10403

Read Online

ACCESS | Metrics & More | Article Recommendations | Supporting Information

ABSTRACT: ***Staphylococcus aureus*** **is a widespread and highly virulent pathogen that can cause superficial and invasive infections. Interactions between *S. aureus* surface receptors and the extracellular matrix protein fibronectin mediate the bacterial invasion of host cells and is implicated in the colonization of medical implant surfaces. In this study, we investigate the role of distribution of both fibronectin and cellular receptors on the adhesion of *S. aureus* to interfaces as a model for primary adhesion at tissue interfaces or biomaterials. We present fibronectin in patches of systematically varied size (100−1000 nm) in a background of protein and bacteria rejecting chemistry based on PLL-*g*-PEG and studied *S. aureus* adhesion under flow. We developed a single molecule imaging assay for localizing fibronectin binding receptors on the surface of *S. aureus* via the super-resolution DNA points accumulation for imaging in nanoscale topography (DNA-PAINT) technique. Our results indicate that *S. aureus* adhesion to fibronectin biointerfaces is regulated by the size of available ligand patterns, with an adhesion threshold of 300 nm and larger. DNA-PAINT was used to visualize fibronectin binding receptor organization *in situ* at ∼7 nm localization precision and with a surface density of 38−46 μm^{-2}, revealing that the engagement of two or more receptors is required for strong *S. aureus* adhesion to fibronectin biointerfaces.**

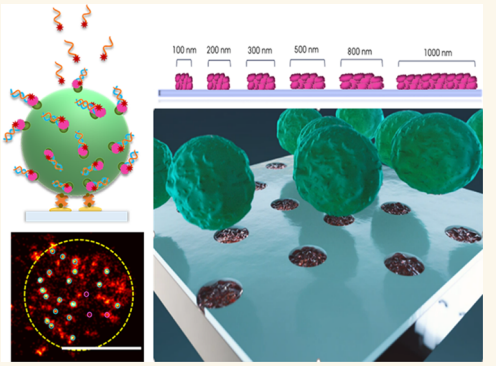

KEYWORDS: *protein nanopattern, fibronectin, fibronectin binding protein localization, DNA-PAINT, Staphylococcus aureus adhesion, colloidal lithography*

Bacterial infections are one of the major concerns in healthcare-associated challenges today.[1−5] *Staphylococcus aureus* is a commensal organism which is carried in the nostrils of 30% of healthy adults,[6] but is a widespread and highly virulent pathogen[7−9] that can cause superficial and invasive infections.[10,11] *S. aureus* has been isolated from infections of damaged tissue or implanted materials[12] and is considered as a dominant cause of acute infective endocarditis[13] with associated mortality rates of 20%−40%. Staphylococci were identified in the majority (nearly 80%) of prosthetic implant-associated infections,[14,15] where in orthopedic infections *S. aureus* and *Staphylococcus epidermidis* together account for two out of three cases.[15]

The pathogenicity of *S. aureus* is caused by a broad range of virulence factors[16−18] including cell wall anchored proteins used for attachment to the host.[19−22] The microbial surface component recognizing adhesive matrix molecules (MSCRAMMs) mediate attachment of *S. aureus*[23,24] to host ECM proteins, such as collagen, fibrinogen, and fibronectin (Fn)[25] as a required first step in biofilm formation, e.g., on the surface of medical implants. Adhesion to Fn also promotes internalization of *S. aureus* by mammalian cells.[25−29] Like biofilm formation, internalization by nonphagocytic host cells is an important mechanism to avoid detection by the host immune system.[30]

S. aureus interacts with Fn using several MSCRAMMs, such as FnBPA and FnBPB[25] and Ebh, Emb, and Aaa.[31] Fibronectin has

Received: January 19, 2022
Accepted: July 5, 2022
Published: July 8, 2022

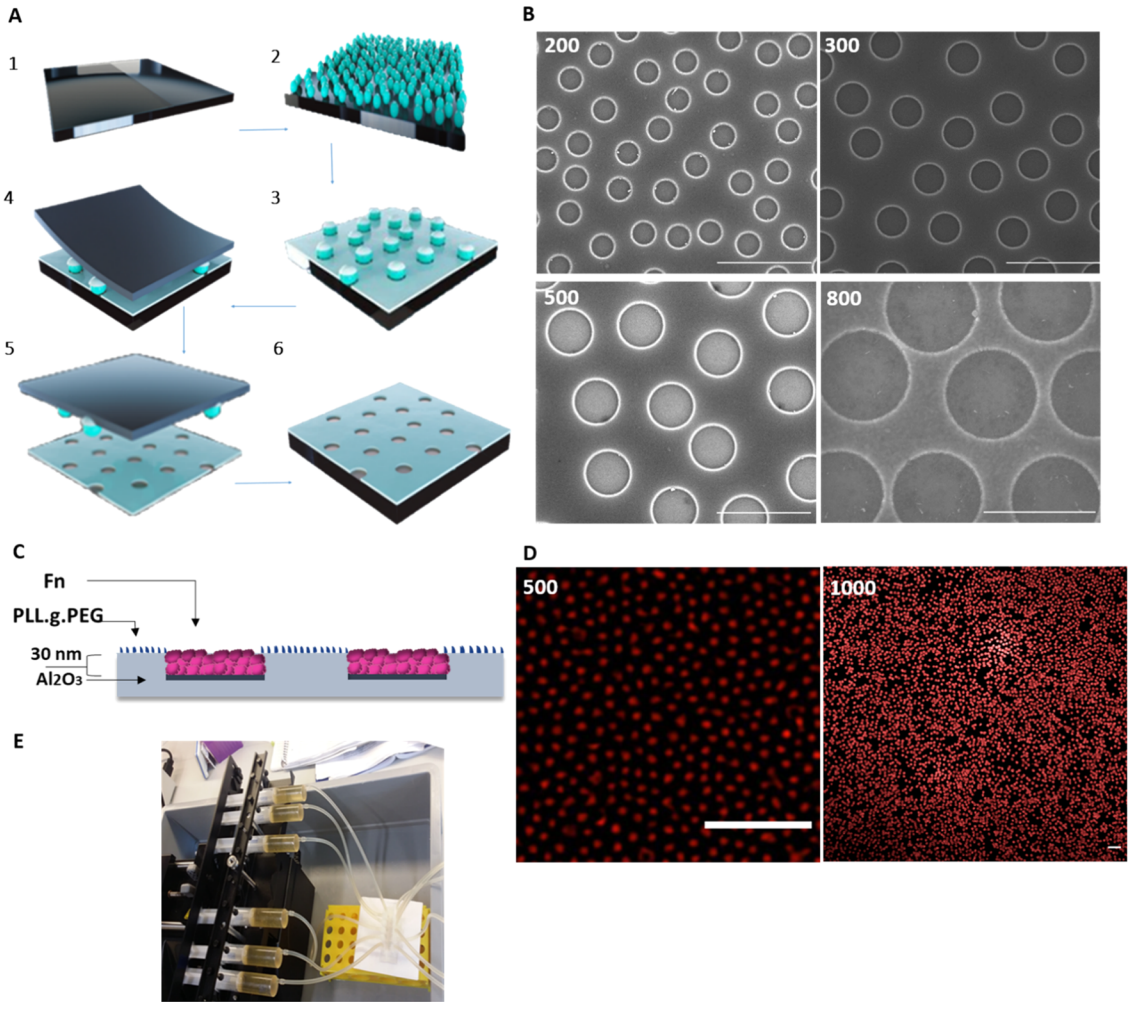

Figure 1. Schematic representation illustrating the generation of a series of protein patterns. (A) (1) Al (3 nm) precovered glass substrate. (2) Self-assembled polystyrene nanoparticle mask. (3) 2 nm Ti and 30 nm SiO_2 deposited onto the surface. (4 and 5) Particle mask removed by taped stripping. (6) Al_2O_3/SiO_2 patterned substrate. (B) SEM images of holes with diameters of 100, 300, 500, and 800 nm (scale bars: 1 μm). (C) Schematic sideview Fn/PLL-*g*-PEG nanopatterns. (D) Immunofluorescence of Fn patterns, 500 nm pattern (left, SIM image) and1000 nm pattern (right, CLSM image) (scale bars: 5 μm). (E) Image of the used flow system.

multiple bacterial binding domains at the N-terminal, which contains five sequential (1−5) Fn type 1 modules.[32] FnBPs contain multiple nonidentical fibronectin binding regions (FnBr) binding specifically to type 1 Fn modules in up to 11 binding repeats (FnBPA with 11 repeats and FnBPB with 10 repeats).[32,29] Increased avidity of the interactions between multiple FnBr domains in individual bacterial surface proteins and Fn bound at surfaces, or in solution, plays a role in increasing bacterial adhesion[25,33] and can mediate interactions with integrins at the surface of mammalian cells. The interaction forms an extended tandem β-zipper bound to multiple Fn type 1 domains on one or more Fn molecules.[32,34] While there has been a significant research effort to understand the role of the FnBr domains in individual FnBps in mediating receptor binding, much less focus has been placed on the local distribution of MSCRAMMS at the bacterial surface and of the ligands (e.g., Fn) on the surface to which it adheres.[23] Fibronectin and other ECM proteins have been widely studied in relation to biomaterials due to their important role in influencing cell behavior around biomedical implants,[35] highlighting that the loss of Fn-binding proteins reduced the cell adhesion onto surfaces during the primary adhesion[36,37] and a key finding has been the critical importance of nanoscale organization of specific proteins such as Fn, Vn, and Ln on the adhesion, signaling, and differentiation of mammalian cells,[38−40] particularly when the patterns are on length scales well below that of the cells. Multiple mechanisms of altered interaction have been proposed from minimum ligand spacings,[41,42] minimum ligand numbers, or patch areas.[43,44,38] While there is a significant body of work investigating eukaryote interactions, to date no similar investigations have been carried out for the role of ECM protein patterns on prokaryote adhesion. Exploring and understanding the relevant length scale of distribution of Fn binding proteins[45] at the bacterial surface and Fn availability at a biointerface will provide a molecular insight into the primary adhesion of *S. aureus* at the inhomogeneous surfaces of medical implants or organized ECM in host tissues. A clear challenge when studying prokaryotes comes from their small size where application of traditional wide-field and confocal fluorescence microscopes (with diffraction limited resolutions in the range 250−500 nm) to the study at subcellular dimensions becomes difficult. To date, there are no fluorescence studies showing the distribution of FnBP receptors at the surface of *S. aureus*.

https://doi.org/10.1021/acsnano.2c00630
ACS Nano 2022, 16, 10392−10403

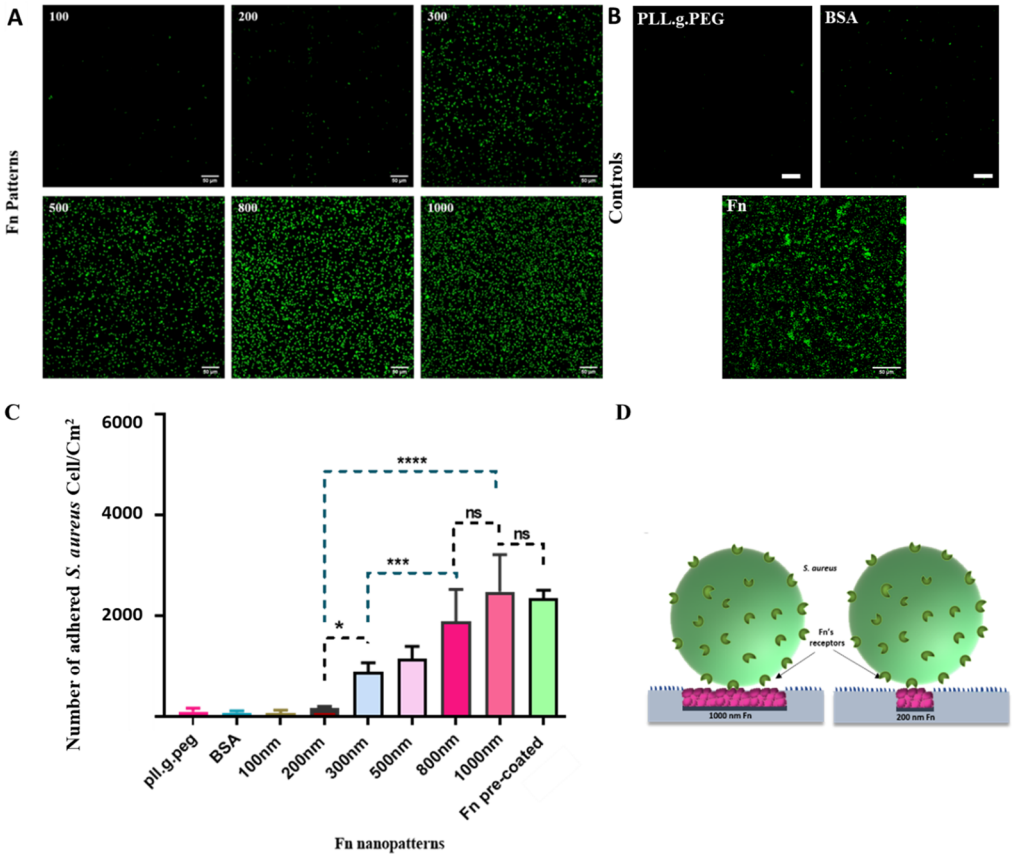

Figure 2. (A) Representative CLSM images of the *S. aureus* adhesion to Fn patterns (nominal diameters (nm) indicated). (B) Control measurements for *S. aureus* adhesion to glass surfaces coated with PLL-*g*-PEG, BSA, and Fn (scale bar 50 μm). (C) Number of bacterial cells/mm^2 on different Fn nanopattern compared to controls surfaces. Bars show mean ± s.d. of five independent experiments. $^{(n.s.)}p < 0.5$, $^{*}p < 0.05$, $^{**}p < 0.01$, $^{***}p > 0.001$, $^{****}p < 0.0001$. (D) Schematic representation of *S. aureus* interaction with Fn patches of different size.

Advances in super-resolution imaging in the past decade have enabled fluorescence microscopy approaches to provide spatial information characterizing cellular structures far below the diffraction limit. These methods include stimulated emission depletion microscopy,[46] photoactivated localization microscopy,[47] single-molecule localization microscopy,[48,49] and stochastic optical reconstruction microscopy.[50] These techniques all rely on switching molecules between on and off fluorescence states to obtain subdiffraction limit image resolution, but suffer from bleaching effects limiting the resolution and applicability of these approaches. A recently developed approach called DNA points accumulation for imaging in nanoscale topography (DNA-PAINT)[51] overcomes this limit by utilizing transiently binding fluorescent probes through weak DNA−DNA interactions, or more recently, peptide coil−coil interactions,[52] to provide robust single molecule localization[23−28,52] with few nanometer resolution.

In this study, we investigated the role of Fn surface distribution for the adhesion of *S. aureus* to interfaces as a model for primary adhesion at tissue interfaces or protein covered biomaterials by applying nanopatterning and super-resolution microscopy techniques. We presented Fn in patches of varying size (100−1000 nm) in a background of protein and bacteria rejecting chemistry based on PLL-*g*-PEG and studied primary adhesion of *S. aureus*. A clear role for protein patch size in controlling adhesion was observed with a threshold for adhesion requiring Fn patches larger than 200 nm. The range of Fn pattern sizes studied went from a pattern comparable to the size of the bacterium (~1 μm) down to close to the size scale of individual receptors (~20−50 nm). To visualize Fn binding receptor distributions on bacterial cells at super resolution, we developed the DNA-PAINT technique. Here, oligonucleotide-labeled Fn was used as an imaging probe for Fn binding proteins in the membrane of wild-type *S. aureus*. The measured receptor density suggests that the adhesion of *S. aureus* requires the engagement of multiple FnBPs for strong adhesion rather than single high-affinity interactions.

RESULTS AND DISCUSSION

Developments in the field of nanotechnology have enabled new approaches to study topics such as cellular adhesion via both fabrication approaches to define materials with nanoscale organization and new tools to characterize at the nanoscale. Here, we have developed and utilized colloidal lithography techniques[53] combined with site-specific material modification to generate a series of protein patterns of Fn on transparent substrates to explore the role of ligand organization on *S. aureus* adhesion. In parallel, we have applied the super-resolution imaging approach DNA-PAINT[54,55] to visualize the distribution of Fn receptors on the surface of *S. aureus*.

Nanopatterned Fibronectin. Materials with defined nanoscale distributions of Fn on transparent substrates were prepared for use in bacterial adhesion studies in microfluidic channels. Sparse colloidal lithography[56] was used to prepare glass cover slides with surface chemistry defined regions of protein rejecting (PEG-based) or protein binding character and

https://doi.org/10.1021/acsnano.2c00630
ACS Nano 2022, 16, 10392−10403

used to direct the physical adsorption of Fn into circular patterns of size 100 nm up to 1000 nm. These cover slides could be attached to commercial fluidic channels and used in studies of bacterial adhesion under flow.

Dense short-range ordered arrays of circular domains of Al_2O_3 chemistry in a background of SiO_2 were produced using dispersed colloidal monolayer masks. The process is schematically shown in Figure 1A. In brief, glass cover slides (60 μm thick) were coated with 3 nm-thick aluminum layers by physical vapor deposition (PVD) and fully oxidized by oxygen plasma to produce a transparent aluminum oxide layers which gave the surface a positive charge at neutral pH. Negatively charged sulfate-modified polystyrene nanoparticles were allowed to adsorb to the surface from dilute aqueous solution to form a complete dispersed short-ranged ordered monolayer where the distribution is well described by random sequential adsorption[53] with a characteristic spacing but no long-range order. The distribution of particles is maintained during drying by using a predrying heating process to raise the particles above the glass transition for the polymer (heated to >120 °C in a pressure chamber) to increase the surface interaction and prevent capillary-force induced aggregation. Thereafter, a 30 nm silicon dioxide layer with a 2 nm titanium adhesion layer was deposited by PVD, and the particles were removed by tape stripping to reveal alumina patches with the diameter of the particles. In a final step, the sample was cleaned with oxygen plasma before use. Scanning electron microscopy (SEM) was used for characterization and verification of a range of the different hole sizes. Figure 1B shows different nanopatterns with circular Al_2O_3 domains in a background of SiO_2 (a wider range of nanopatterns is shown in Figure S1). We confirmed the full oxidation of the aluminum layer and the stability of the layer after exposure to media by XPS (see Figure S1). The SiO_2 regions were subsequently chemically modified with PLL-*g*-PEG by the electrostatic assembly to prevent nonspecific protein adsorption to the background regions. The positively charged PLL backbone adsorbs strongly to negatively charged metal oxides, forming a dense brush of PEG extending from the surface. For this polymer under these conditions, the amount of protein binding is reduced by >97%.[57] The positively charged (at neutral pH) alumina surface prevents adsorption of the PLL groups, meaning that while protein is prevented from adsorbing to the silica surface after PLL-*g*-PEG treatment, protein can readily adsorb to the alumina surface. Fibronectin was allowed to adsorb to the surface and defined into patterns or onto homogeneous surfaces by adhesion to the Al_2O_3 surfaces (Figure 1C). High-quality protein patterns of Fn were successfully demonstrated by immunofluorescence (Figure S2) and (Figure 1D). Patterns of proteins have previously been formed in this way at gold/silica surfaces where the gold had been modified to be hybrophobic[43] or positively charged.[58] Here, they are prepared on fully transparent substrates.

Bacterial Adhesion. The nanopatterned samples together with homogeneous surfaces were mounted on Ibidi sticky slide slides with 6 channels per slide. Chemical functionalization and protein deposition were carried out within the channels, and the final patterns were washed with buffer before exposure to a 0.15 μL/min flow of *S. aureus* (optical density at 600 nm (OD_{600}) of 0.1) for 30 min (Figure 1E). Each channel on a sample was exposed to independently grown bacterial cultures to account for biological variation. After rinsing with PBS for 10 min with the same flow rate, the attached bacterial cells were stained with SYBR Green I from Invitrogen and imaged by confocal laser fluorescence microscopy (CLSM). Control measurements with different surface treatments were carried out, so several surfaces, precoated with BSA or PLL-*g*-PEG, were exposed to a flow of bacterial cells. Representative fluorescence images are shown in Figure 2A,B. Five independent experiments were carried out for each fabricated surface, and five random regions were imaged for each experiment.

There was no significant bacterial attachment to Fn-coated surfaces with the 100 and 200 nm pattern sizes compared to the Fn-free negative control surfaces coated with either PLL-*g*-PEG or BSA(Figure 2). An increasing number of bacteria attached to Fn-coated surfaces with larger size of Fn patches from 300 nm patches and up. At the largest patch sizes (800 and 1000 nm), bacterial attachment was comparable to the homogeneous Fn samples, even though the amount of Fn on homogeneous samples was 3 fold higher (Table S1).

The cells were counted using ImageJ software. The database was analyzed by (Graph-Pad Prism, 8). The data in (Figure 2C) shows a comparison between the numbers of attached *S. aureus* on different Fn nanopatterns and control samples. The variation between the replicates is plotted as a standard deviation between the means from each channel. A threshold for bacterial attachment appeared between 200 and 300 nm-sized patches, with a significant but intermediate number of bacteria seen at 300 nm surfaces which in general increases as the pattern size increases. No difference is seen between 800 or 1000 nm samples and the homogeneous surface, despite there being approximately 3 times more Fn-coated area available for binding at the homogeneous surfaces (Table S1), which indicates that it is not the global protein available that is important, but the locally available ligands. The global coverage of ligand for the 200 and 300 nm samples is similar (18% vs 24%); however, we cannot rule out that the increased global coverage plays a role in the increasing binding seen from 300 nm up to 1000 nm. Bacteria can in many situations adhere strongly to materials surfaces through nonspecific interactions. Here, the polymeric (PLL-*g*-PEG) and protein coatings are intended to reduce nonspecific interactions. For the functionalized surfaces, essentially no adherent cells are seen at the PLL-*g*-PEG surface indicating that chemistry successfully prevents bacterial attachment under these conditions. Similarly, no binding was seen at BSA-coated glass surfaces, which indicate that protein layers could mask the underlying chemistry and limit nonspecific interactions and that the binding observed to Fn patterns required Fn.

The protein patterns formed here were made from chemically nanostructured materials formed from holes that were 32 nm deep (30 nm SiO_2 and 2 nm Ti). Fibronectin is expected to form a maximum of 15−20 nm-thick layers so will not have extended above the silica surface, although bacterial receptors can likely extend into the holes. To explore if the aspect ratio (diameter/height) of the holes, which was lower for the smaller diameter holes compared to the larger diameter holes, influenced the results, experiments were carried out for 15 nm-thick silica layers for the 200 nm diameter patterns which showed similar low levels of binding (Figure S4), indicating that the threshold seen between 200 and 300 nm was not caused by any steric effects. A conclusion from the experimental results is that *S. aureus* requires a Fn patch area larger than 200 nm for significant strong interactions.

S. aureus binds to Fn via the cell wall anchored FnBP's using a tandem β-zipper mechanism.[25,32,29] Interestingly, it has been found that low binding affinity of FnBPs results when binding to

https://doi.org/10.1021/acsnano.2c00630
ACS Nano 2022, 16, 10392−10403

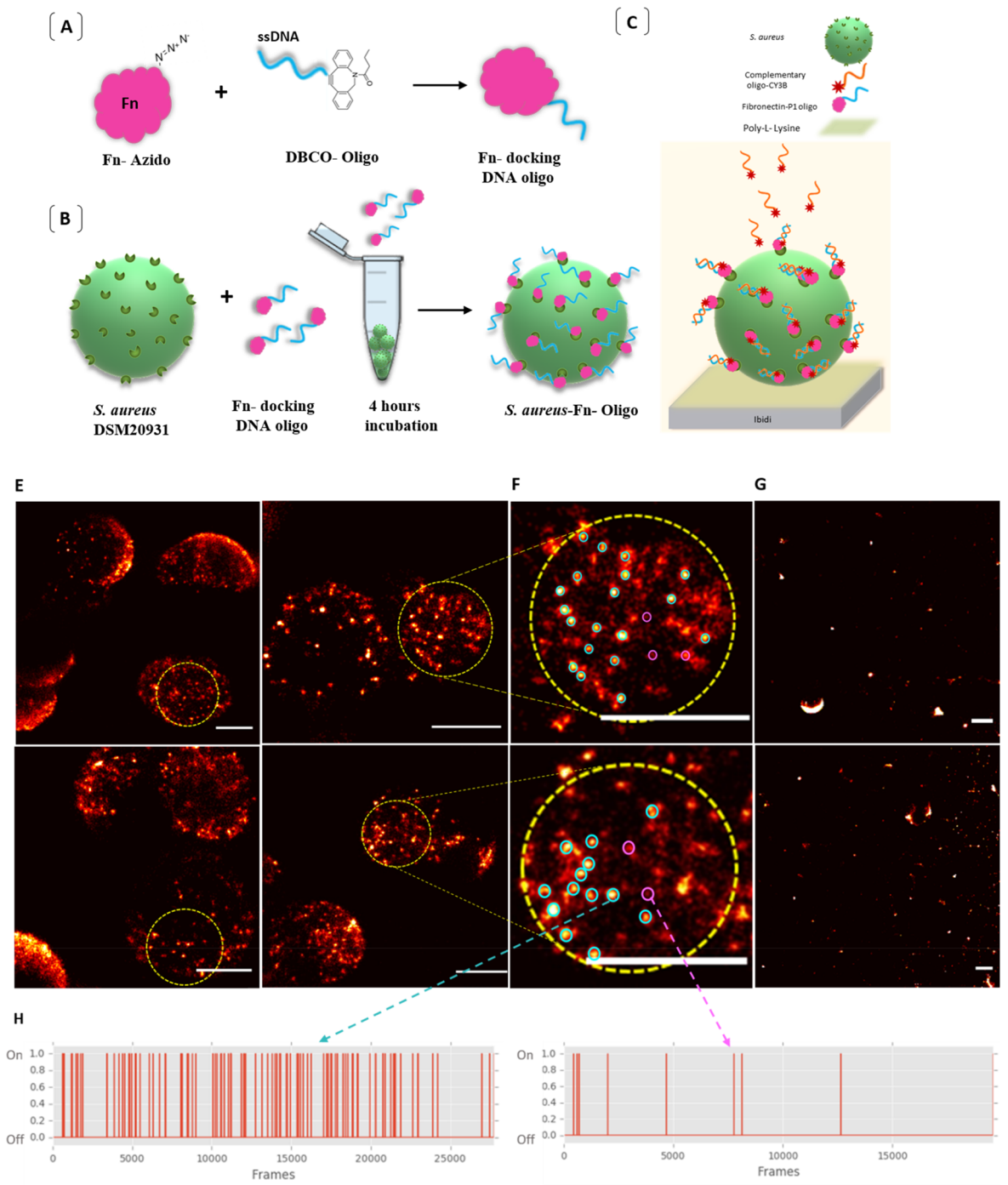

Figure 3. Characterization of FnBPs on *S. aureus* single cells using DNA-PAINT. (A) Schematic diagram depicting the functionalization of Fn with PS3 DNA-PAINT docking strand. (B) Diagram illustrating the binding of Fn at the surface of *S. aureus*. (C) Schematic diagram depicting the approach for cell immobilization via PLL and single-molecule localization of FnBPs at single *S. aureus* bacteria via an imager DNA strand. (D) DNA-PAINT super-resolution images visualizing the localization of FnBPs on single *S. aureus* bacteria. The highlighted areas correspond to ~0.36 μm^2. (E) Zoom-in of highlighted areas shows examples of the localized spots in cyan and of unspecific background features in magenta. Image resolution: 39 nm (scale bars: 500 nm). (F) Negative control of the complementary DNA-PAINT imager strands PS3* added onto bare immobilized *S. aureus* cells lacking the Fn-docking strand PS3 (scale bars: 500 nm). (G) Time traces of spots with repetitive binding events in cyan (left) and of unspecific background features in magenta (right).

individual short type 1 Fn modules, in contrast to neighboring arrayed Fn type 1 domains which result in high affinity, implying that avidity plays an important role.[59] In studies carried out with mammalian cells, ligand spacing, ligand number, and area of ligand patch were all seen as important for determining the cellular adhesion. Here, the density of ligands at the surface is high, but the density of Fn ligands at the surface of the bacteria may be limited.

The curvature of the outer wall of *S. aureus* (around 1 μm in diameter) will make it likely that each bacterium interacts with a single or, at most, a few patches. The contact region of *S. aureus* at material surfaces has been estimated to be in the range of

https://doi.org/10.1021/acsnano.2c00630
ACS Nano 2022, 16, 10392−10403

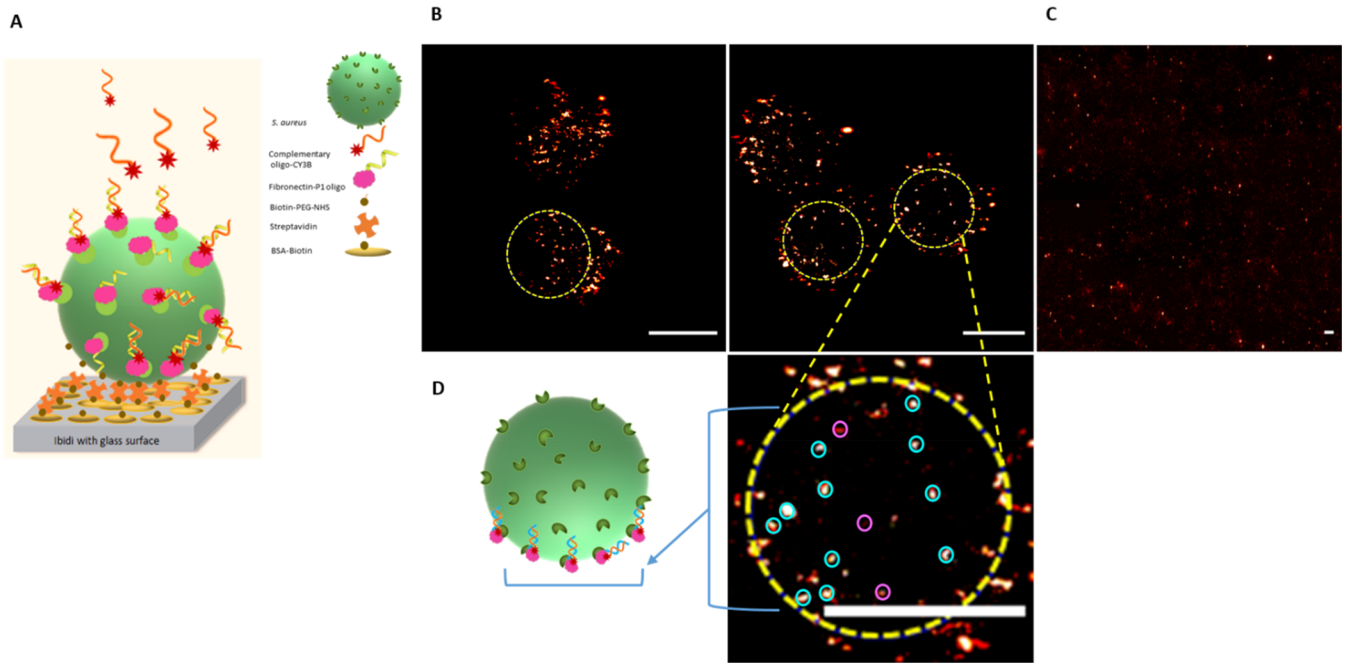

Figure 4. Characterization of FnBPs onto *S. aureus* single cell via DNA-PAINT. (A) Schematic diagram of the tethering approach and imager strand localization. (B) DNA-PAINT images at ~8 nm super-resolution visualizing the localization of FnBPs at *S. aureus* cells (scale bars: 500 nm). The highlighted areas show ~0.31 μm^2. (C) Negative control of the complementary DNA-PAINT imager strands R3* added onto the bare immobilized *S. aureus* cell lacking the Fn-docking strand R3 (scale bars: 1000 nm). (D) (left) Schematic representation illustrating the region of the cell analyzed; (right) zoom-in of the bottom of the cell. Examples of the localized spots in cyan and of unspecific background features in magenta (scale bars: 500 nm).

200−300 nm in diameter when interacting via nonspecific interactions.[60] Figure 2D shows a schematic that represents the relative sizes of the *S. aureus* bacteria and patches. Only adhesion receptors on the *S. aureus* surface which are close to the contact region are likely to be able to bind to the Fn. The different nanopatterned surfaces present slightly different global areas of Fn (~12% for 100 nm structures and ~36% for 1000 nm structures see Table S1 and Figure S3). However, this difference in global presentation is unlikely to provide the experimental outcome first because the 1000 nm structures give the same adhesion as the homogeneous Fn surfaces which have 100% coverage and ~3 times higher area available, and second because the 200 and 300 nm surfaces on either side of the threshold for adhesion have similar global coverage of Fn ~18 and 22% respectively. By contrast, the local coverage will play a role in that a bacterium that lands within a 1000 nm patch has likely a sufficiently large area available to accommodate all the FnBPs that can reach the surface, while the smaller patch sizes will restrict access to Fn for some of these FnBPs and thus the number of FnBPs that can be engaged, since the local area of available Fn will be reduced. The number of Fn molecules available in a 200 nm patch is likely already quite large (>100 Fn's) which should be compared to the ~6−8 Fn molecules that are estimated to be able to bind to an individual FnBPA protein[61] so there are easily sufficient ligands to engage with many individual FnBP's within a single patch. While there are high numbers of Fn molecules within a patch, there must be FnBPs to interact with them. We hypothesize that the threshold behavior of adhesion with Fn patch size results from a threshold number of FnBPs being required to give sufficient adhesive strength to keep the bacterium at the surface in our conditions (under flow). The concentration of FnBPs at the surface of *S. aureus* would provide a finite number of ligand binding molecules that would be available above an individual Fn patch. We propose that the number of FnBPs able to interact with the surface falls below a critical threshold for 200 nm patches, meaning that bacterial attachment becomes too weak to keep the bacterium at the surface. To examine this assumption, we localized the Fn receptors on single *S. aureus* cells via the super-resolution imaging approach, DNA PAINT.

FnBP Localization. Since *S. aureus* has several different fibronectin binding proteins (FnBPA and FnBPB), we developed a single-molecule binding assay utilizing Fn as the readout probe for the localization of Fn binding proteins. Using DNA-PAINT, we achieved images with localization precision (NeNA) down to 7 nm.

In this assay, Fn conjugated to a DNA-PAINT docking sequence (PS3 or R3) was used as a readout for FnBP localization. Thus, transient binding of the PS3 or R3 extension using complementary Cy3B-labeled imager strands enabled single-molecule imaging and localization.

Fibronectin was labeled with DNA-PAINT docking sequences (PS3 or R3) via a click-chemistry reaction. First, the Fn was functionalized with NHS-PEG4-azide groups followed by linking the azide with DBCO-oligos for the conjugation with the DNA-PAINT docking strand (Figure 3A, Figure S5). The Fn is likely functionalized with 3−5 docking strands which increased sampling and thus overall image quality.

In order to image bacterial cells with DNA-PAINT, the cells must be tethered to a surface with sufficient mechanical stability. The final image is based on the overlay of thousands of frames, meaning that any undesirable cell mobility can significantly reduce the image quality and reconstruction fidelity. Two different immobilization assays were explored in this study to overcome the significant challenge of holding the spherical cells stationary while limiting background fluorescence. In the first

https://doi.org/10.1021/acsnano.2c00630
ACS Nano 2022, 16, 10392−10403

assay, 0.01% poly-L-lysine (PLL) was used to coat a coverslip surface for 30 min. Thereafter, the fixed cells were added to the 6-channel 400 um height (IV 0.4) ibidi flow chambers, subsequently centrifugation of the ibidi slide at 3700 rpm[62] was applied, and the nonimmobilized cells were removed with PBS washing steps (Figure 3C). DNA-PAINT was then performed using 5 nM Cy3B-labeled complementary imager strands of PS3. The fluorescence emission upon binding was detected using highly inclined and laminated optical sheet microscopy.[63] This enabled imaging of horizontal slices of the bacteria slightly above the glass slide surface. A challenge with the use of PLL was background fluorescence from the PLL-coated glass surface, which could be avoided by imaging the bacteria in a plane above the surface. Some of the bacteria in this protocol appeared to be suspended above the surface apparently attached to other cells. Only cells appearing roughly in the lower 200 nm from the glass surface were considered for further quantification purposes (Figure 3D).

Intensity vs time traces for each apparent cluster of binding events were analyzed for repetitive binding, subsequently retained for further data quantification (while rejecting non-specific events). Specific areas of 0.36 μm^2 were analyzed from multiple cells, and the average number of bound Fn molecules were quantified to estimate the FnBPs localization (Figure 3E). We assume that all FnBPs have a bound Fn so this represents a lower limit. Images of *S. aureus* cells without preincubation with the Fn for the same conditions were taken, and only few, mostly unspecific binding sites, were observed (Figure 3F). A comparison between traces of an identical localizing point (G, left) and unspecific background features (G, right) in time shows a significant difference through the imaged frames.

The second cell immobilization protocol we developed relied on tethering the cells onto the bottom of ibidi chamber slides via biotin−streptavidin binding, to avoid the fluorescent background observed with PLL and thus resulting in increased image quality (Figure 4). Briefly, the cells were reacted with the functionalized fibronectin Fn-R3, and before fixation, the cells were biotinylated with NHS-dPEG$_4$-biotin. Ibidi chambers with glass slides were prepared by precoating them with BSA-biotin followed by streptavidin before exposure to the biotinylated *S. aureus* (Figure 4A). DNA-PAINT imaging was performed at the surface of the bacteria close to the coverslip, near total internal reflection conditions. The biotin-streptavidin immobilization method generally demonstrated better mechanical stability with reduced fluorescence background (Figure 4B). The DNA-PAINT images using this bacterial immobilization protocol reached a significantly better localization precision (NeNA) of 7 and 9.3 nm, compared to 12.8 and 15 nm for the immobilization approach based on PLL. The binding quantification was estimated in an identified area of 0.31 μm^2 at each image from multiple cells (Figure 4B).

The density of FnBPs receptors was estimated on six *S. aureus* cells from three independent experimental sets using two different imager strands of PS3 or R3, giving ∼38−46 receptors per μm^2 area and an average number of FnBPs on a single cell of ∼130 receptors. Lower et al.[64] utilizing force spectroscopy with Fn functionalized AFM tips proposed 36 FnBP's per μm^2 (around 110 per bacterium) for *S. aureus* adsorbed to Fn-coated glass, which is in good agreement with our findings. Here, the studied bacteria were in stationary phase, adhesion studies in an in vivo situation have shown higher rates of adhesion, and a higher surface density of FnBPs for *S. aureus* during the exponential phase compared to stationary phase may be expected.[65] In this bacterial adhesion study, the limiting area of Fn available in a single patch will have limited the number of FnBPs able to engage with Fn bound to the surface. Geometric considerations indicate that for 130 receptors per bacterium, there are on average ∼1.2−1.4 FnBPs available per 200 nm patch of Fn, at which condition we did not see any adhesion. The 2.25 times larger 300 nm patches would have provided access to ∼2.7−3.2 FnBPs. These data suggest that a minimum of two or three FnBP molecules were needed to give sufficient binding strength for attachment under flow conditions. Since the distribution of FnBPs was not homogeneous and the binding increased with increasing Fn patch size above 300 nm, a larger number of interacting FnBP's are likely required for stronger adhesion. We suggest that the limiting factor for adhesion of *S. aureus* on 100 and 200 nanopatterns of Fn is due to the density of FnBPs at the cell surface, largely limiting the interaction to single FnBPs, and that single FnBP engagement was not enough to provide strong binding.

Interestingly, the lack of *S. aureus* binding to Fn nanopatterns to patterns below 300 nm can be compared to mammalian cell adhesion to similar-sized patterns, where epidermal stem cells show adhesion already from 100 nm patterns,[38] to help shape the future of bioconstructive materials that can promote tissue integration but prevent bacterial colonization.

CONCLUSION

In this work, we have applied advanced nanoscale fabrication and characterization approaches to study *S. aureus* adhesion to ECM. We investigated the interaction of *S. aureus* with nanoscale distributions of Fn prepared by colloidal lithography. We observed a threshold behavior in adhesion of *S. aureus* to nanoscale distributions of Fn with minimal adhesion to patches with diameters up to 200 nm. DNA-PAINT characterization of distributions of Fn binding proteins at the surface of *S. aureus* suggested that the threshold behavior in adhesion resulted from too few receptors being available above individual patches. Geometric considerations indicated that engagement of more than one FnBP with surface bound Fn is required for strong adhesion. These results provide insight into bacterial adhesion to the extracellular matrix and to the design of biomedical implant material surfaces promoting cellular adhesion but limited bacterial adhesion. The methods developed and demonstrated in this work with *S. aureus* can have application to study a broad range of bacterial interactions with ECM and mammalian cell membrane proteins.

MATERIALS AND METHODS

Materials. Poly(dimethylammonium chloride) (PDDA) and poly-(sodium-4-styrenesulfonate) (PSS) were purchased from Sigma-Aldrich (DK). Polyammonium chloride (PAX-XL60) was purchased from Kemira Miljo (DK) and sulfate modified polystyrene colloidal particles in water were purchased from Invitrogen. *S. aureus* DMS 20231 was purchased form DSMZ, Germany. Human fibronectin protein was purchased from R&D systems (USA). All standard DNA oligonucleotides DBCO-PS3d, DBCO-R3, PS3i-CyB3, and R3-CyB3 sequences were purchased from IDT (DK). DBCO-NHS A124 was obtained from the click chemistry tool. PLL P8920, streptavidin 189730, biotin-NHS H1759-5MG, glycin50046, TBE buffer T4415-1L, and TSB medium were obtained from Sigma-Aldrich (DK). Biotin-BSA 29130 and SDS-PAGE (EA03552BOX) were obtained from Thermo Fisher. NHS-dPEG$_4$-biotin (BD1-A0401-045) from quantabiodesign (USA). μ-Slide VI 0.4 and ibidi μ-slide VI 0.5 glass bottom channel slide cat. no. 80607 from ibidi (DK). NHS-PEG4-azide (CLK-AZ103-100) was obtained from Jena bioscience (DE).

https://doi.org/10.1021/acsnano.2c00630
ACS Nano 2022, 16, 10392−10403

Methods. *Sparse Colloidal Lithography.* Monolayers of adsorbed dispersed colloidal nanoparticles were used as masks for pattern transfer by PVD as described previously.[44] Negatively charged colloidal particles (sulfate modified polystyrene) were deposited on oppositely charged substrates by electrostatic self-assembly. The substrates (glass coverslides with thin aluminum oxide overlayers) were given a stable positive charge by sequential deposition of three different charged polyelectrolyte layers PDDA, PSS, and PAX in an aqueous solution where the third layer had a positive charge at neutral pH. Colloidal particles of different sizes 100−1000 nm were used to form transparent chemical patterns of aluminum oxide/silicon dioxide. Later exposure to PLL-*g*-PEG could direct the PLL-*g*-PEG to the silicon dioxide parts of the surface.

The process of formation of hole patterns is shown in Figure 1. Glass substrates of size 25 × 60 mm were cleaned with acetone followed by oxygen plasma cleaning, 100 W, 25 mTorr for 15 min (Vision 300 Mark II, Advanced Vacuum AB Sweden). A thin layer of aluminum was deposited onto the surface via physical vapor deposition (electron beam stimulated thermal evaporation, Cyrofox GLAD, Polyteknik A/S DK, 0.1 nm/s base pressure <10−7 Torr), which is used later for creating positively charged aluminum oxide regions to electrostatically repel PLL-*g*-PEG and interact with the adsorbing protein. Different layers thicknesses were examined in terms of stability with different buffer treatments and also transparency. Therefore, a 3 nm aluminum layer was chosen which was then oxidized to form aluminum oxide (alumina) by exposure to oxygen plasma (50 W, 25 mTorr for 2 min) (Figure 1A). The surface was coated with three sequentially deposited polyelectrolyte layers (PDDA, PSS, PAX). Electrostatically charged (negative) particles adsorb directly onto the opposite charged (positive) surface (Figure 1B). Colloidal monolayers of charged polystyrene particles with different diameters were formed (100, 200, 300, 500, 800, 1000 nm using bulk nanoparticle concentrations of 0.2% volume for the three smallest diameters, 0.5% for 500 nm, 1% for 800 nm, and 2% for 1000 nm) by assembly onto a preformed triple layer of polyelectrolytes. After the particle deposition (2 min for 100 and 200 nm particles and overnight for 300−1000 nm particles), the samples were carefully rinsed, followed by transfer into a pressure chamber containing deionized water which was then heated to 120 °C to increase nanoparticle adhesion to the surface in order to prevent aggregation during subsequent drying. The coating process of the pretreated glass samples continued with the deposition of 2 nm Ti and 30 nm of SiO_2 in the same process run (Ti deposition rate 0.02 nm/s, SiO_2 deposition rate 0.1 nm/s, base pressure <10^{-7} Torr) by PVD (Figure 1C). The particles were removed by tape stripping followed by oxygen plasma cleaning (50 W, 25 mTorr for 10 min) (Figure 1E). Afterward, samples were rinsed with acetone, ethanol, and deionized water, respectively, under sonication until any remaining particles were removed. The samples were then dried under a stream of nitrogen gas followed by cleaning for 30 min in UV/ozone. SEM was used for characterization of the samples to determine holes size, surface coverage, and interhole distances from 4 images per sample type (50K magnification for 100 nm structures and 10K magnification for the other structure sizes).

Fibronectin Nanopatch Preparation. The fabricated surfaces with patterns of different diameters were sterilized in 70% EtOH. Then the samples were attached to ibidi chambers. Thereafter, 100 μL of 0.25 mg/mL PLL-*g*-PEG in 10 mM HEPES pH 7.4 was injected into each chamber and heated to 60 °C for 30 min. The surfaces were rinsed with HEPES (10 mM) and Tris buffer (2.7 Mm), respectively, and then incubated with bovine Fn (1030-FN, R&D Biotech) 20 μg/mL in Tris buffer (2.7 mM) overnight. Next day, the samples were rinsed with Tris buffer, followed by blocking for unspecific binding with 2% BSA in Tris buffer for 30 min at room temperature. Then, the surfaces were washed with Tris buffer and used immediately.

Flow Experiment. A colony of *S. aureus* DSM 20231 was inoculated into tryptic soy broth and incubated overnight at 37 °C with gentle shaking (130 rpm). Whole genome analysis of this strain showed the presence of the genes for the fibronectin binding protein FnBPA, FnBPB, and Ebh and the fibrinogen binding proteins ClfA and ClfB.[66] Five independently grown cultures were prepared for each experiment. The bacteria concentration was adjusted with fresh media to an OD of 0.1 at a wavelength of 600 nm which corresponds to ∼5 × 10^7 CFU/mL.

The adjusted cultures were inserted into a syringe pump to which the ibidi chamber was connected. The flow was adjusted to 0.15 μL/min for 30 min followed by rinsing with PBS for 10 min at the same flow rate (shear stress ∼1.8−1.9 μdyn/cm^2) . The remaining bacterial cells were stained with SYBR Green I 1× working concentration according to manufacturers instructions.

Microscopy and Data Analysis. The adhered cells were imaged in PBS using by CLSM (Zeiss LSM700), 20× Plan-Neofluoar and 63× Plan-Apochromat NA1.4 objective, using 488 nm excitation. At least 5 images were taken for each ibidi channel for each of the sample types. Images with 20× magnification were randomly chosen in each of the ibidi channels, whereas the 63× magnification images were manually chosen as representative of the population on the surface. The number of bacterial cells was determined with ImageJ software using the particle count protocol. Prior to the automatic analysis, a color threshold was set manually for the images.

Statistical Analysis. One-way analysis of variance was performed for the difference between the number of adhered cells onto each Fn patch size, followed by Tukey's test for multiple comparisons using (GraphPad Prism,8) to visualize the significant differences at the 0.05 level.

Immunofluorescence of Fibronectin. Primary antifibronectin antibody (anti-Fn1 antibody produced in rabbit, AV41490 Sigma) was diluted 1:500 in PBS, then added to the adsorbed Fn patches for 5 h followed by rinsing with PBS buffer. The secondary antibody, (anti-rabbit IgG (Fc specific)-Rhodamine antibody produced in goat, SAB3700846 Sigma), was diluted in PBS (1:200) and then added to the samples and incubated for 1 h, and the biointerface was rinsed with PBS for confocal imaging.

Fluorescence experiments to image the Fn patches were performed using a custom-modified N-SIM (Nikon) microscope with 100× oil immersion objective (NA 1.49). Excitation was done using 561 nm laser diodes (ps) operating on cw mode. The emission light was collected in EMCCD camera through a band-pass filter allowing 570−640 nm light, and images were captured in wide-field mode. The 1000 nm Fn patches were imaged with CLSM using a Zeiss LSM700 CLSM, a 488 nm laser for excitation, and a 63× Plan-Apochromat NA 1,4 objective for visualization.

DNA-PAINT for Visualizing the Organization of FnBPs on S. aureus Cell Membrane. The DNA-PAINT imaging concept relies on labeling the target molecule with single-stranded DNA, then transient binding of a complementary imager strand which is labeled with a fluorophore induces the blinking phenomena subsequently used to isolate and localize individual fluorophore molecules and reconstruct super-resolution images. Here, we used click chemistry to conjugate a docking DNA strand to Fn via a two-step reaction which involved first labeling the synthesized DNA with NHS-DBCO and then clicking it to Fn prefunctionalized with NHS-azide. The two docking oligos that used in this study (PS3d[67] and R3[68]) are the reversed complement to PS3i and R3i which in turn are used as PAINT imager strands conjugated with Cy3B. The docking oligos were first conjugated with DBCO-NHS-ester, the heterobifunctional linker, at the 5′-amine end (reagents purchased from IDT DK).

Fn-PEG4-azide Conjugation. Fn was functionalized with NHS-PEG4-azide by mixing at a 1:10 molar ratio followed by incubation for 5 h at 25 °C with a vortex at 700 rpm in a thermomixer. Unreacted NHS-PEG4-azide was removed using a 100 K Amicon centrifuge filter. The absorption was measured at A_{280} to calculate the product concentration. The purified functionalized Fn was verified by sodium dodecyl sulfate-polyacrylamide gel electrophoresis (SDS-PAGE).

Fn-oligos Conjugation. Subsequently, the functionalized Fn-EG4-azide in PBS was reacted with DBCO-oligos in a 1:5 ratio followed by incubation for 5 h at 25 °C/700 rpm. The reaction was followed by 100 K Centerfuge Amicon filtration. The spectral measurement was taken at A_{280} to calculate the concentration.

Preparation of S. aureus Cells for DNA-PAINT Imaging. Two protocols for cell immobilization were developed: One was based on biotinylation of the cells followed by immobilization on streptavidin-

https://doi.org/10.1021/acsnano.2c00630
ACS Nano 2022, 16, 10392−10403

Table 1. Imaging Parameters for DNA-PAINT Images

image	integration time	frames	laser power	imager concentration	imager	localization precision (NeNA)[69]
Figure 3e	150 ms	30,000	34 mW	5 nM	PS3	12.75 nm
Figure 3f	150 ms	30,000	18.1 mW	5 nM	PS3	15 nm
Figure 4b (right)	200 ms	10,000	110 mW	300 pM	7xR3	9.3 nm
Figure 4b (left)	100 ms	20,000	110 mW	300 pM	7xR3	7 nm
Figure 4c	200 ms	2,000	110 mW	250 pM	7xR3	14 nm

coated ibidi slide, and the other was based on immobilizing cells onto PLL-coated ibidi slides.

Cell Culture. One colony of *S. aureus* DSM20231 was inoculated into TSB medium and incubated overnight at 37 °C with shaking at 180 rpm The OD was adjusted to 0.1 at 600 nm, 1 mL of the culture was centrifuged at 5000×*g* for 10 min, and the pellet was resuspended and washed three times with PBS.

S. aureus Binding with the Functionalized Fibronectin (Fn-PS3d or Fn-R3d). The functionalized Fn with one of the oligos (PS3d or R3d) were added to *S. aureus* cells to a final concentration of 30 μg/mL in PBS, then the mixture was incubated for 4 h at 25 °C with a vortex at 300 rpm. The mixture was spun down at 5000×*g* for 10 min, and the pellet was resuspended and washed three times with PBS to remove the excess of (Fn-PS3d or Fn-R3d). The washed pellet was resuspended in ∼50 μL of PBS.

Biotin-Labeling of S. aureus. Three μL of 100 mM biotin-NHS was added to the *S. aureus* in PBS to a final concentration of 5 mM. The mixture was incubated for 15 min at 25 °C with a vortex at 300 rpm. The cell mixture was diluted to 950 μL with PBS to be fixed with 3% PFA + 0.07glutaraldehyde for 30 min at 37 °C and vortexed at 300 rpm in a thermomixer. Then the reaction was stopped by adding glycine to a final concentration of 15 mM and incubated for 30 min at 25 °C with a vortex at 300 rpm. The mixture was spun down at 2000×*g* for 10 min, the pellet was resuspended and washed three with PBS, and then the cells pellet was resuspended in 100 μL PBS.

Slide Preparation. Streptavidin-Coated Channel Slide Preparation. 60 μL of 1 mg/mL biotin-BSA was added to the ibidi μ-Slide VI 0.5 glass bottom channel slide for 10 min, followed by washing three times with PBS (with 0.05% Tween-20) to remove the unbounded biotin-BSA. Then 60 μL of 0.5 mg/mL streptavidin was added to the channel for 10 min, followed by washing three times with PBS (with 0.05% Tween-20) to remove unbound streptavidin.

Treated S. aureus Cells' Immobilization. 60 μL of *S. aureus* suspension was added onto the channel slide for 30 min before centrifuging the channel slide in a swinging bucket at 3700 rpm for 10 min to spin down the cells onto the surface. The excess cells were removed from the surface by washing three times with PBS. Then 60 μL of 3% BSA was added into the channel for 2 h.

Alternative Protocol for Cell Immobilization Based on Poly-L-lysine-Coated Ibidi Slides. The *S. aureus* cells were treated with the functionalized Fn (Fn-PS3d or Fn-R3d) to a final concentration of 30 μg/mL in PBS and incubated for 4 h at 25 °C with a vortex at 300 rpm. The mixture was spun-down at 5000×*g* for 10 min, and the pellet was resuspended and washed three times with PBS to remove the excess of (Fn-PS3d or Fn-R3d). The washed pellet was resuspended in ∼50 μL of PBS. The cells mixture was diluted to 950 μL with PBS to be fixed with 3% PFA + 0.07 glutaraldehyde for 30 min at 37 °C and vortexed at 300 rpm in a thermomixter. The reaction was stopped by adding glycine to a final concentration of 15 mM and incubated for 30 min at 25 °C with a vortex at 300 rpm. The mixture was spun down at 2000×*g* for 10 min, the pellet was resuspended and washed three with PBS, and then the cells pellet was resuspended in 100 μL PBS.

A PLL (Sigma P8920) solution was diluted first to 1:10 of which 100 μL was added into the ibidi chamber at 4 °C. After 30 min, the channel was rinsed three times with Milli-Q water to remove unbound PLL solution.[62] Then the fixed cells were added into the PLL-coated ibidi chambers for 30 min. The ibidi chamber was centrifuged in the swinging pocket centrifuge at 3700 rpm for 10 min. The non-immobilized cells were removed by rinsing three times with PBS.

DNA-PAINT Sample Preparation and Imaging. First, 50 μL of 1:4 AuNPs (∼25 μM) was added to the channels and incubated for 15 min. Second, the C-TAD solution was prepared by mixing 380 μL of buffer C (PBS with 0.5 M NaCl, 0.05% Tween-20), 4 μL of 0.1 M Trolox, 10 μL of 0.1 M PCA, and 4 μL of 1 μM PCD. The mixed solution was incubated in the dark for at least 5 min before adding 1 μL of 1 uM the fluorophore-oligo (Cy3B-R3 or Cy3B-PS3 imager strands) to 250 μL of the C-TAD solution to prepare PAINT imaging solution with 4 nM concentration. Eventually, 70 μL imaging solution was added into the chamber's channel.

DNA-PAINT imaging was carried out on an inverted microscope (Nikon Instruments, Eclipse Ti) with the Perfect Focus System, applying an objective-type TIRF configuration equipped with an oil-immersion objective (Nikon Instruments, Apo SR TIRF 100×, NA 1.49, oil). A 561 nm laser (Coherent Sapphire, 200 mW) was used for excitation and was coupled into a single-mode fiber. The laser beam was passed through cleanup filters (Chroma Technology, ZET561/10) and coupled into the microscope objective using a beam splitter (Chroma Technology, ZT561rdc). Fluorescence light was spectrally filtered with an emission filter (Chroma Technology, ET600/50m) and imaged with a sCMOS camera (Andor, Zyla 4.2plus) without further magnification, resulting in an effective pixel size of 130 nm after 2 × 2 binning. The camera readout sensitivity was set to 16-bit and readout bandwidth to 540 MHz.

Imaging parameters for DNA-PAINT images in all figures are provided in Table 1.

Image Analysis. Raw fluorescence data from DNA-PAINT imaging were subjected to super-resolution reconstruction using the "Picasso" software package[51] (latest version available on https://github.com/jungmannlab/picasso). Drift correction was performed with a redundant cross-correlation and gold nanoparticles as fiducials. DNA-PAINT signal from labeled FnBPs was selected manually using Picasso's "pick tool" and the circle pick option. Density of FnBPs per μm^2 was calculated for circular regions (area 0.36 μm^2 or 0.31 μm^2 the polylysine or streptavidin immobilized bacteria, respectively). Six cells were studied, e.g., as indicated in Figures 3 and 4, giving a range of values. Total number of FnBPs per bacteria was calculated assuming spherical bacteria 1 μm in diameter.

ASSOCIATED CONTENT

Supporting Information

The Supporting Information is available free of charge at https://pubs.acs.org/doi/10.1021/acsnano.2c00630.

SEM images of the complete range of nanopatterns. Quantification of nanopattern size, coverage and patch spacing. XPS characterization of Al surfaces before and after exposure to media. SIM images of 100 and 200 nm Fn patterns. Flourescence images and quantification of *S. aureus* adhesions to nanopatterns with a thinner silica layer. SDS gels demonstrating functionalization of FN with DNA oligos (PDF)

Schematic visualization of the sample fabrication process and the bacterial adhesion (MP4)

https://doi.org/10.1021/acsnano.2c00630
ACS Nano 2022, 16, 10392−10403

AUTHOR INFORMATION

Corresponding Author

Duncan S. Sutherland − *Interdisciplinary Nanoscience Center (iNANO), Aarhus University, Aarhus C 8000, Denmark;* orcid.org/0000-0002-5045-9915; Email: duncan@inano.au.dk

Authors

Heba Khateb − *Interdisciplinary Nanoscience Center (iNANO), Aarhus University, Aarhus C 8000, Denmark;* orcid.org/0000-0002-9166-8991

Rasmus S. Sørensen − *Interdisciplinary Nanoscience Center (iNANO), Aarhus University, Aarhus C 8000, Denmark*

Kimberly Cramer − *Max Planck Institute of Biochemistry, Martinsried 82152, Germany*

Alexandra S. Eklund − *Max Planck Institute of Biochemistry, Martinsried 82152, Germany;* orcid.org/0000-0003-1047-2100

Jorgen Kjems − *Interdisciplinary Nanoscience Center (iNANO) and Department of Molecular Biology and Genetics, Aarhus University, Aarhus C 8000, Denmark*

Rikke L. Meyer − *Interdisciplinary Nanoscience Center (iNANO), Aarhus University, Aarhus C 8000, Denmark*

Ralf Jungmann − *Max Planck Institute of Biochemistry, Martinsried 82152, Germany; Faculty of Physics and Center for Nanoscience, Ludwig Maximilian University, Munich 80539, Germany;* orcid.org/0000-0003-4607-3312

Complete contact information is available at: https://pubs.acs.org/10.1021/acsnano.2c00630

Author Contributions

H.K. and D.S. conceived and designed the study. H.K. conducted all the surface fabrications, protein engineering, characterization, bioconjugation, and bacterial experiments. H.K., D.S., and R.L.M. contributed to the data interpretation. H.K., K.C., A.K., and R.S. conducted the DNA-PAINT imaging. H.K. and D.S. drafted the manuscript, and all authors commented on the draft manuscript and approved submission.

Notes

The authors declare no competing financial interest.

ACKNOWLEDGMENTS

This work was financially supported by the Danmarksgrundforskningsfond center grant DRF135 CellPAT. R.L.M. acknowledges the Carlsberg Foundation grant number CF16-0342 for support.

REFERENCES

(1) Centers for Disease Control and Prevention. *Antibiotic resistance threats in the United States*; Centers for Disease Control and Prevention: Atlanta, GA, 2013; pp 11−28.

(2) Bally, C.; Meyssonnier, V.; Bricaire, F. Evolution Of Virulence in Epidemic Community-associated Methicillin-resistant Staphylococcus aureus. *Med. Mal. Infect.* **2011**, *41*, 346−348.

(3) Pang, Y. Y.; Schwartz, J.; Thoendel, M.; Ackermann, L. W.; Horswill, A. R.; Nauseef, W. M. Agr-dependent Interactions Of Staphylococcus aureus USA300 With Human Polymorphonuclear Neutrophils. *J. Innate Immun.* **2010**, *2*, 546−559.

(4) Wenzel, R. P. Health Care−Associated Infections: Major Issues in the Early Years of the 21st Century. *Clin. Infect. Dis.* **2007**, *45*, S85−S88.

(5) World Health Organization. *Report on the Burden of Endemic Health Care-Associated Infection Worldwide; Clean Care is Safer Care*; World Health Organization: Geneva, Switzerland, 2011; pp 1−40.

(6) Kluytmans, J.; Van Belkum, A.; Verbrugh, H. Nasal Carriage of Staphylococcus aureus: Epidemiology, Underlying Mechanisms, and Associated Risks. *Clin. Microbiol. Rev.* **1997**, *10*, 505−520.

(7) Lowy, F. Staphylococcus aureus Infections. *N. Engl. J. Med.* **1998**, *339*, 520−532.

(8) Balasubramanian, D.; Harper, L.; Shopsin, B.; Torres, V. J. Staphylococcus aureus Pathogenesis in Diverse Host Environments. *Pathog. Dis.* **2017**, *75*, ftx005.

(9) Malachowa, N.; Deleo, F. R. Mobile Genetic Elements of Staphylococcus aureus. *Cell. Mol. Life Sci.* **2010**, *67*, 3057−3071.

(10) Thomer, L.; Schneewind, O.; Missiakas, D. Pathogenesis of Staphylococcus aureus Bloodstream Infections. *Annu. Rev. Pathol.* **2016**, *11*, 343−364.

(11) Tong, S. Y. C.; Davis, J. S.; Eichenberger, E.; Holland, T. L.; Fowler, V. G. Staphylococcus aureus Infections: Epidemiology, Pathophysiology, Clinical Manifestations, and Management. *Clin. Microbiol. Rev.* **2015**, *28*, 603−661.

(12) Park, K.-H.; Lee, Y.-M.; Hong, H.-L; Kim, T.; Park, H. J.; Park, S.-Y.; Moon, S. M.; Chong, Y. P.; Kim, S.-H.; Lee, S.-O.; Choi, S.-H.; Jeong, J.-Y.; Kim, M.-N.; Woo, J. H.; Kim, Y. S. Persistent Catheter-Related Staphylococcus aureus Bacteremia after Catheter Removal and Initiation of Antimicrobial Therapy. *PLoS One* **2012**, *7*, No. e46389.

(13) Cabell, C. H.; Jollis, J. G.; Peterson, G. E.; Corey, G. R.; Anderson, D. J.; Sexton, D. J.; Woods, C. W.; Reller, L. B.; Ryan, T.; Fowler, V. G. Changing Patient Characteristics and the Effect On Mortality In Endocarditis. *Arch. Int. Med.* **2002**, *162*, 90−94.

(14) Tschudin-Sutter, S.; Frei, R.; Dangel, M.; Jakob, M.; Balmelli, C.; Schaefer, D.J.; Weisser, M.; Elzi, L.; Battegay, M.; Widmer, A.F. Validation of a Treatment Algorithm For Orthopaedic Implant-related Infections With Device-retention-results From a Prospective Observational Cohort Study. *Clin. Microbiol. Infect.* **2016**, *22*, 457.e1.

(15) Campoccia, D.; Montanaro, L.; Arciola, C. R. The Significance of Infection Related to Orthopedic Devices and Issues of Antibiotic Resistance. *Biomaterials* **2006**, *27*, 2331−2339.

(16) Kane, T. L.; Carothers, K. E.; Lee, S. W. Virulence Factor Targeting of the Bacterial Pathogen Staphylococcus aureus for Vaccine and Therapeutics. *Curr. Drug Targets* **2018**, *19*, 111−127.

(17) Oliveira, D.; Borges, A.; Simões, M. Staphylococcus aureus Toxins and Their Molecular Activity in Infectious Diseases. *Toxins (Basel)* **2018**, *10*, 252.

(18) Archer, G. L. Staphylococcus aureus: A Well-Armed Pathogen. *Clin. Infect Dis.* **1998**, *26*, 1179−1181.

(19) Geoghegan, J. A.; Foster, T. J. Cell Wall-Anchored Surface Proteins of Staphylococcus aureus: Many Proteins, Multiple Functions. *Curr. Top. Microbiol. Immunol.* **2015**, *409*, 95−120.

(20) Josse, J.; Laurent, F.; Diot, A. Staphylococcal Adhesion and Host Cell Invasion: Fibronectin-Binding and Other Mechanisms. *Front. Microbiol.* **2017**, *8*, 1−8.

(21) Foster, T. J.; Höök, M. Surface Protein Adhesins of Staphylococcus aureus. *Trends Microbiol.* **1998**, *6*, 484−488.

(22) McCarthy, A. J.; Lindsay, J. A. Genetic Variation in Staphylococcus aureus Surface and Immune Evasion Genes is Lineage Associated: Implications for Vaccine Design and Host-Pathogen Interactions. *BMC Microbiol.* **2010**, *10*, 173.

(23) Pietrocola, G.; Nobile, G.; Alfeo, M. J.; Foster, T. J.; Geoghegan, J. A.; De Fillippis, V.; Speziale, P. Fibronectin-Binding Protein B (FnBPB) from Staphylococcus aureus Protects Against the Antimicrobial Activity of Histones. *J. Biol. Chem.* **2019**, *294*, 3588−3602.

(24) Pollitt, E. J. G.; Szkuta, P. T.; Burns, N.; Foster, S. J. Staphylococcus aureus Infection Dynamics. *PLoS Pathog.* **2018**, *14*, e1007112.

(25) Foster, T. J.; Geoghegan, J. A.; Ganesh, V. K.; Höök, M. Adhesion, Invasion and vasion: The Many Functions of the Surface Proteins of Staphylococcus aureus. *Nat. Rev. Microbiol.* **2014**, *12*, 49−62.

(26) Dziewanowska, K.; Patti, J. M.; Deobald, C. F.; Bayles, K. W.; Trumble, W. R.; Bohach, G. A. Fibronectin Binding Protein and Host Cell Tyrosine Kinase are Required for Internalization of Staph-

ylococcus aureus by Epithelial Cells. *Infect. Immun.* **1999**, *67*, 4673−4678.
(27) Sinha, B.; Francois, P. P.; Nusse, O.; Foti, M.; Hartford, O. M.; Vaudaux, P.; Froster, S. J.; Lew, D. P.; Herrmann, M.; Krause, B. H. Fibronectin-Binding Protein Acts as Staphylococcus aureus Invasin Via Fibronectin Bridging to Integrin alpha5beta1. *Cell Microbiol.* **1999**, *1*, 101−117.
(28) Nallapareddy, S. R.; Weinstock, G. M.; Murray, B. E. Clinical Isolates of Enterococcus Faecium Exhibit Strain-Specific Collagen binding Mediated by Acm, a New Member of the MSCRAMM Family. *Mol. Microbiol.* **2003**, *47*, 1733−1747.
(29) Peacock, S. J.; Foster, T. J.; Cameron, B. J.; Berendt, A. R. Bacterial Fibronectin-Binding Proteins and Endothelial Cell Surface Fibronectin Mediate Adherence of S. aureus to Resting Human Endothelial cells. *Microbiology.* **1999**, *145*, 3477−3486.
(30) Pickering, A. C.; Vitry, P.; Prystopiuk, V.; Garcia, B.; Höök, M.; Schoenebeck, J.; Geoghegan, J. A.; Dufrene, Y. F.; Fitzgerald, J. R. Host-Specialized Fibrinogen-Binding by a Bacterial Surface Protein Promotes Biofilm Formation and Innate Immune Evasion. *PLoS Pathog.* **2019**, *15*, e1007816.
(31) Henderson, B.; Nair, S.; Pallas, J.; Williams, M. A. Fibronectin: A Multidomain Host Adhesin Targeted by Bacterial Fibronectin-Binding Proteins. *FEMS Microbiol. Rev.* **2011**, *35*, 147−200.
(32) Schwarz-Linek, U.; Werner, J. M.; Pickford, A. R.; Gurusiddappa, S.; Kim, J. H.; Pilka, E. S.; Briggs, J. A. G.; Gough, T. S.; Hook, M.; Campbell, I. D.; Potts, J. R. Pathogenic Bacteria Attach to Human Fibronectin Through a Tandem b-Zipper. *Nature* **2003**, *423*, 177−181.
(33) Mongodin, E.; Bajolet, O.; Cutrona, J.; Bonnet, N.; Dupuit, F.; Puchelle, E.; De Bentzmann, S. Fibronectin-Binding Proteins of Staphylococcus aureus are Involved in Adherence to Human Airway Epithelium. *Infect. Immun.* **2002**, *70*, 620−630.
(34) Speziale, P.; Pietrocola, G. The Multivalent Role of Fibronectin-Binding Proteins A and B (FnBPA and FnBPB) of Staphylococcus aureus in Host Infections. *Front. Microbiol.* **2020**, *11*, 1−13.
(35) Khalili, A. A.; Ahmad, M. R. A Review of Cell Adhesion Studies for Biomedical and Biological Applications. *Int. J. Mol. Sci.* **2015**, *16*, 18149−18184.
(36) McCourt, J.; O'Halloran, D. P.; McCarthy, H.; O'Gara, J. P.; Geoghegan, J. A. Fibronectin-Binding Proteins are Required for Biofilm Formation by Community-Associated Methicillin-Resistant Staphylococcus aureus Strain LAC. *FEMS Microbiol. Lett.* **2014**, *353*, 157−164.
(37) Buck, A. W.; Fowler, V. G.; Yongsunthon, R.; Liu, J.; DiBartola, A. C.; Que, Y.-A; Moreillon, P.; Lower, S. K. Bonds Between Fibronectin and Fibronectin-Binding Proteins on Staphylococcus aureus and Lactococcus lactis. *Langmuir.* **2010**, *26*, 10764−10770.
(38) Gautrot, J. E.; Malmström, J.; Sundh, M.; Margadant, C.; Sonnenberg, A.; Sutherland, D. S. The Nanoscale Geometrical Maturation of Focal Adhesions Controls Stem Cell Differentiaion and Mechanotransduction. *Nano Lett.* **2014**, *14*, 3945−3952.
(39) Théry, M. Micropatterning as a Tool to Decipher Cell Morphogenesis and Functions. *J. Cell Sci.* **2010**, *123*, 4201−4213.
(40) Amin, Y. Y. I.; Runager, K.; Simoes, F.; Celiz, A.; Taresco, T.; Rossi, R.; Enghild, J. J.; Abildtrup, L. A.; Kraft, D. C. E.; Sutherland, D. S.; Alexander, M. R.; Foss, M.; Ogaki, R. Combinatorial Biomolecular Nanopatterning for High-Throughput Screening of Stem-Cell Behavior. *Adv. Mater.* **2016**, *28*, 1472−1476.
(41) Trappmann, B.; Gautrot, J. E.; Connelly, J. T.; Strange, D. G. T.; Li, Y.; Oyen, M. L.; Cohen Stuart, M. A.; Boehm, H.; Li, B.; Vogel, V.; Spatz, J. P.; Watt, F. M.; Huck, W. T. S. Extracellular-Matrix Tethering Regulates Stem-Cell Fate. *Nat. Mater.* **2012**, *11*, 642−649.
(42) Cavalcanti-Adam, E. A.; Volberg, T.; Micoulet, A.; Kessler, H.; Geiger, B.; Spatz, J. P. Cell Spreading and Focal Adhesion Dynamics are Regulated by Spacing of Integrin Ligands. *Biophys. J.* **2007**, *92*, 2964−2974.
(43) Malmström, J.; Christensen, B.; Jakobsen, H. P.; Lovmand, J.; Foldbjerg, R.; Sørensen, E. S.; Sutherland, D. S. Large Area Protein Patterning Reveals Nanoscale Control of Focal Adhesion Development. *Nano Lett.* **2010**, *10*, 686−694.
(44) Malmström, J.; Lovmand, J.; Kristensen, S.; Sundh, M.; Duch, M.; Sutherland, D. S. Focal Complex Maturation and Bridging on 200 nm Vitronectin But Not Fibronectin Patches Reveal Different Mechanisms of Focal Adhesion Formation. *Nano Lett.* **2011**, *11*, 2264−2271.
(45) Mao, X.; Kim, J.; Zhang, Q.; Jiang, T.; Ahn, D. O.; Jung, Y.; Matsushita, M.; Bae, T.; Lee, B. L. The N2N3 Domains of ClfA, FnbpA and FnbpB in Staphylococcus aureus Bind to Human Complement Factor H, and Their Antibodies Enhance the Bactericidal Capability of Human Blood. *J. Biochem.* **2021**, *169*, 543−553.
(46) Hell, S. W.; Wichmann, J. Breaking the Diffraction Resolution Limit by Stimulated Emission: Stimulated-Emission-Depletion Fluorescence Microscopy. *Opt. Lett.* **1994**, *19*, 780.
(47) Betzig, E.; Patterson, G. H.; Sougrat, R.; Lindwasser, O. W.; Olenych, S.; Bonifacino, J. S.; Davidson, M. W.; Lippincott-Schwartz, J.; Hess, H. F. Imaging Intracellular Fluorescent Proteins at Nanometer Resolution. *Science* **2006**, *313*, 1642−1645.
(48) Dai, M.; Jungmann, R.; Yin, P. Optical Imaging of Individual Biomolecules in Densely Packed Clusters. *Nat. Nanotechnol.* **2016**, *11*, 798.
(49) Xu, K.; Babcock, H. P.; Zhuang, X. Dual-Objective STORM Reveals Three-Dimensional Filament Organization in the Actin Cytoskeleton. *Nat. Methods* **2012**, *9*, 185.
(50) Heilemann, M.; Van De Linde, S.; Schüttpelz, M.; Kasper, R.; Seefeldt, B.; Mukherjee, A.; Tinnefeld, P.; Sauer, M. Subdiffraction-Resolution Fluorescence Imaging With Conventional Fluorescent Probes. *Angew. Chem., Int. Ed.* **2008**, *47*, 6172−6176.
(51) Schnitzbauer, J.; Strauss, M. T.; Schlichthaerle, T.; Schueder, F.; Jungmann, R. Super-Resolution Microscopy with DNA-PAINT. *Nat. Protoc.* **2017**, *12*, 1198−1228.
(52) Eklund, A. S.; Ganji, M.; Gavins, G.; Seitz, O.; Jungmann, R. Peptide-PAINT Super-Resolution Imaging Using Transient Coiled Coil Interactions. *Nano Lett.* **2020**, *20*, 6732−6737.
(53) Hanarp, P.; Sutherland, D. S.; Gold, J.; Kasemo, B. Control of Nanoparticle Film Structure for Colloidal Lithography. *Colloids Surf., A* **2003**, *214*, 23−36.
(54) Jungmann, R.; Avendano, M. S.; Woehrstein, J. B.; Dai, M.; Shih, W. M.; Yin, P. Multiplexed 3D Cellular Super-Resolution Imaging with DNA-PAINT and Exchange-PAINT. *Nat. Methods* **2014**, *11*, 313−318.
(55) Jungmann, R.; Steinhauer, C.; Scheible, M.; Kuzyk, A.; Tinnefeld, P.; Simmel, F. C. Single-Molecule Kinetics and Super-Resolution Microscopy by Fluorescence Imaging of Transient Binding on DNA Origami. *Nano Lett.* **2010**, *10*, 4756−4761.
(56) Haynes, C. L.; Van Duyne, R. P. Nanosphere Lithography: A Versatile Nanofabrication Tool for Studies of Size-Dependent Nanoparticle Optics. *J. Phys. Chem. B* **2001**, *105*, 5599−5611.
(57) Malmström, J.; Agheli, H.; Kingshott, P.; Sutherland, D. S. Viscoelastic Modeling of Highly Hydrated Laminin Layers at Homogeneous and Nanostructured Surfaces: Quantification of Protein Layer Properties Using QCM-D and SPR. *Langmuir* **2007**, *23*, 9760−9768.
(58) Andersen, A. S.; Aslan, H.; Dong, M.; Jiang, X.; Sutherland, D. S. Podosome Formation and Development in Monocytes Restricted by the Nanoscale Spatial Distribution of ICAM1. *Nano Lett.* **2016**, *16*, 2114−2121.
(59) Casolini, F.; Visai, L.; Joh, D.; Conaldi, P. I.; Toniolo, A.; Höök, M.; Speziale, P. Antibody Response to Fibronectin-Binding Adhesin FnbpA in Patients with Staphylococcus aureus Infections. *Infect. Immun.* **1998**, *66*, 5433−5442.
(60) Spengler, C.; Thewes, N.; Jung, P.; Bischoff, M.; Jacobs, K. Determination of the Nano-scaled Contact Area of Staphylococcal Cells. *Nanoscale* **2017**, *9*, 10084−10093.
(61) Bingham, R. J.; Rudino-Pinera, E.; Meenan, N. A. G.; Schwarz-Linek, U.; Turkenburg, J. P.; Hook, M.; Garman, E. F.; Potts, J. R. Crystal Structures of Fibronectin-Binding Sites From Staphylococcus aureus FnBPA in Complex With Fibronectin Domains. *Proc. Natl. Acad. Sci. U. S. A.* **2008**, *105*, 12254−12258.
(62) Stockmar, I.; Feddersen, H.; Cramer, K.; Gruber, S.; Jung, K.; Bramkamp, M.; Shin, J. Y. Optimization of Sample Preparation and

https://doi.org/10.1021/acsnano.2c00630
ACS Nano 2022, 16, 10392−10403

Green Color Imaging Using the mNeonGreen Fluorescent Protein in Bacterial Cells for Photoactivated Localization Microscopy. *Sci. Rep.* **2018**, *8*, 1−11.
(63) Tokunaga, M.; Imamoto, N.; Sakata-Sogawa, K. Highly Inclined Thin Illumination Enables Clear Single-Molecule Imaging in Cells. *Nat. Methods* **2008**, *5*, 159−161.
(64) Lower, S. K.; Yongsunthon, R.; Casillas-Ituarte, N. N.; Taylor, E. S.; DiBartola, A. C.; Lower, B. H.; Beveridge, T. J.; Buck, A. W.; Fowler, V. G. A Tactile Response in Staphylococcus aureus. *Biophys. J.* **2010**, *99*, 2803−2811.
(65) Kerdudou, S.; Laschke, M. W.; Sinha, B.; Priessner, K. T.; Menger, M. D.; Herrmann, M. Fibronectin Binding Proteins Contribute to the Adherence of Staphylococcus aureus to Intact Endothelium In Vivo. *Thromb. Haemost.* **2006**, *96*, 183−189.
(66) Shiroma, A.; Terabayashi, Y.; Nakano, K.; Shimoji, M.; Tamotsu, H.; Ashimine, N.; Ohki, S.; Shinzato, M.; Teruya, K.; Satou, K.; Hirano, T. First Complete Genome Sequences of Staphylococcus aureus Subsp. aureus Rosenbach 1884 (DSM 20231T), Determined by PacBio Single-Molecule Real-Time Technology. *Genome Announc.* **2015**, *3*, e00800.
(67) Schueder, F.; Stein, J.; Stehr, F.; Auer, A.; Sperl, B.; Strauss, M. T.; Schwille, P.; Jungmann, R. An Order of Magnitude Faster DNA-PAINT Imaging by Optimized Sequence Design and Buffer Conditions. *Nat. Methods* **2019**, *16*, 1101−1104.
(68) Strauss, S.; Jungmann, R. Up to 100-fold Speed-Up and Multiplexing in Optimized DNA-PAINT. *Nat. Methods* **2020**, *17*, 789−791.
(69) Endesfelder, U.; Malkusch, S.; Fricke, F.; Heilemann, M. A Simple Method to Estimate the Average Localization Precision of a Single-Molecule Localization Microscopy Experiment. *Histochem. Cell Biol.* **2014**, *141*, 629−638.

https://doi.org/10.1021/acsnano.2c00630
ACS Nano 2022, 16, 10392−10403

Supporting Information

The role of nanoscale distribution of fibronectin in the adhesion of *Staphylococcus aureus* studied by protein patterning and DNA-PAINT

Heba Khateb[1], Rasmus S. Sørensen[1], Kimberly Cramer[2], Alexandra S. Eklund[2], Jorgen Kjems[1,4], Rikke L. Meyer[1], Ralf Jungmann[2,3] and Duncan S. Sutherland[1]

[1] Interdisciplinary Nanoscience Center (iNANO) Aarhus University Gustav Wieds Vej 14, Aarhus C, 8000, Denmark. [2] Max Planck Institute of Biochemistry, Martinsried, 82152, Germany. [3] Faculty of Physics and Center for Nanoscience, Ludwig Maximilian University, Munich, 80539, Germany. [4]Department of Molecular Biology and Genetics Aarhus University Aarhus C, 8000, Denmark

Corresponding Author

Duncan S. Sutherland

Email: duncan@inano.au.dk.

Nominal size/nm	**Average diameter/nm**	**s.d./nm (polydispersity)**	**Area fraction**	**Characteristic center to center distance/nm**
100	105	7	0.12	123
200	200	8	0.18	153
300	302	14	0.22	179
500	449	10	0.23	253
800	718	26	0.33	204
1000	923	31	0.36	221

Table S1 Characteristics of nanopatterns quantified from SEM images of nanopatterned materials. Data calculated from 4 images of each sample type.

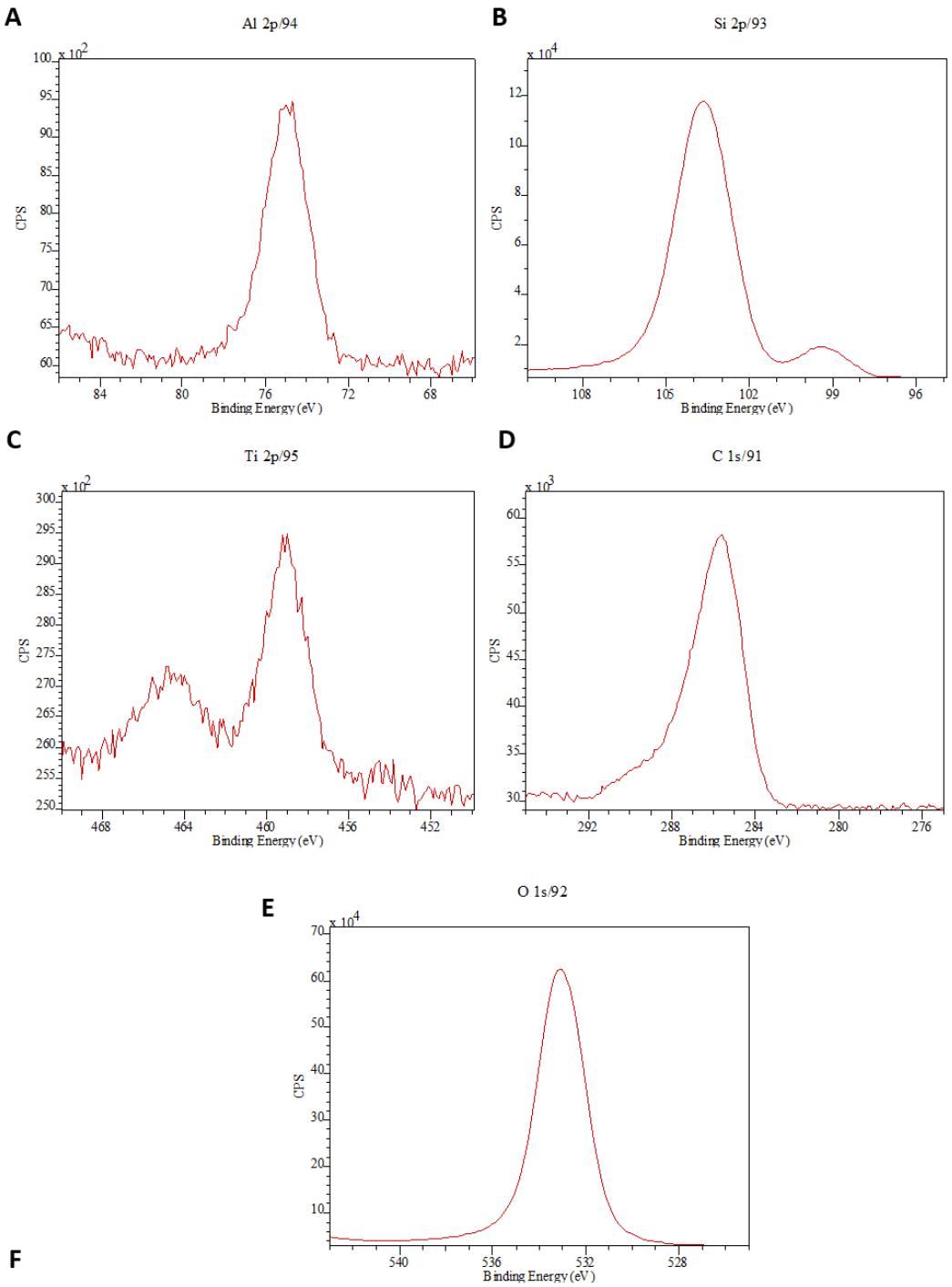

	%	Al	Si	O	C	Ti
As prepared	Average	1.38	27.9	59.8	10.8	0.20
	s.d	0.16	0.2	0.9	0.7	0.04
24 hours in media	Average	1.18	29.1	59.8	9,74	0.19
	s.d.	0.07	0.1	0.5	0.55	0.03

Figure S1: XPS surface analysis from nanopatterned 100nm samples. Spectra show sample after exposure to media for 24 hours. (A) Al2p region, (B) Si2p/Al2s region (Al2s at ~99eV), (C) Ti2p region, (D) C1s region, (E) O1s region (F). Quantification of the relative surface elemental composition for samples before and after exposure to media (n=3).

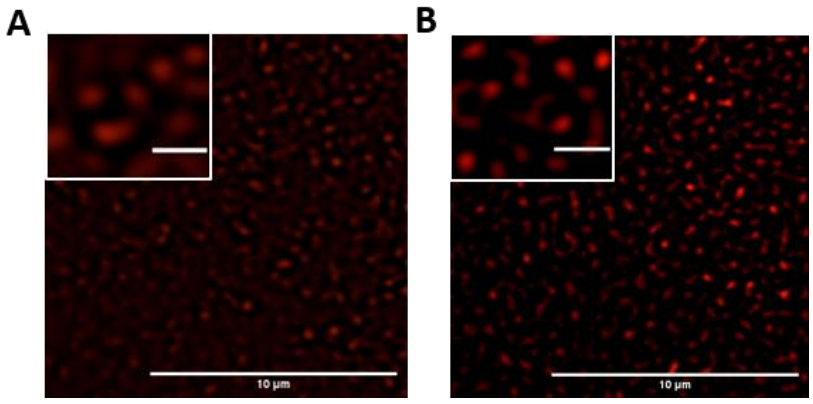

Figure S2: Immunofluorescence of fibronectin patterns. (A) SIM image for 100 nm pattern (Scale bar 10 micron) with a zoom in on the left corner (scale bar 1 micron).(B) SIM image for 200 nm pattern (Scale bar 10 micron) with a zoom in on the left corner (scale bar 1 micron).

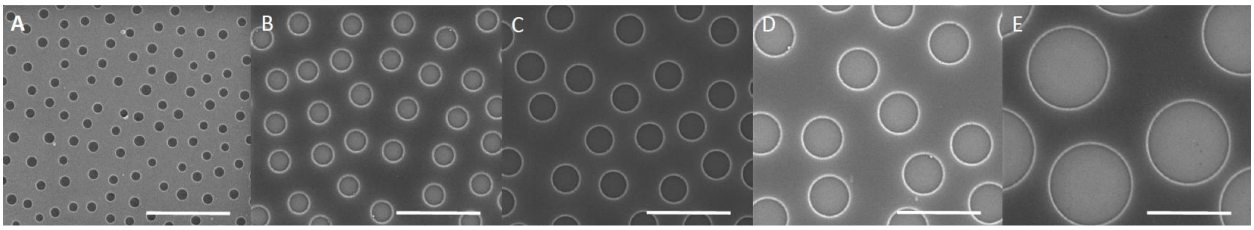

Figure S3: SEM images of Nanopatterned Al_2O_3 holes in $Si0_2$ film . (A) 100nm (B) 200nm (C) 300nm (D) 500nm (E) 1000nm. Scale bar 1000nm.

(A)

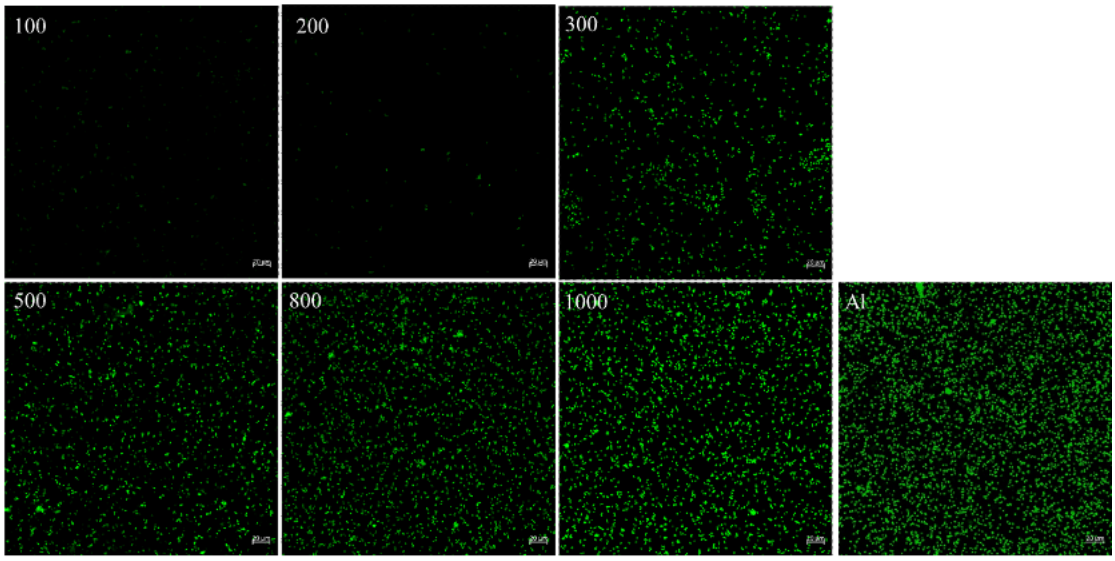
100
200
300
500
800
1000
Al

(B)

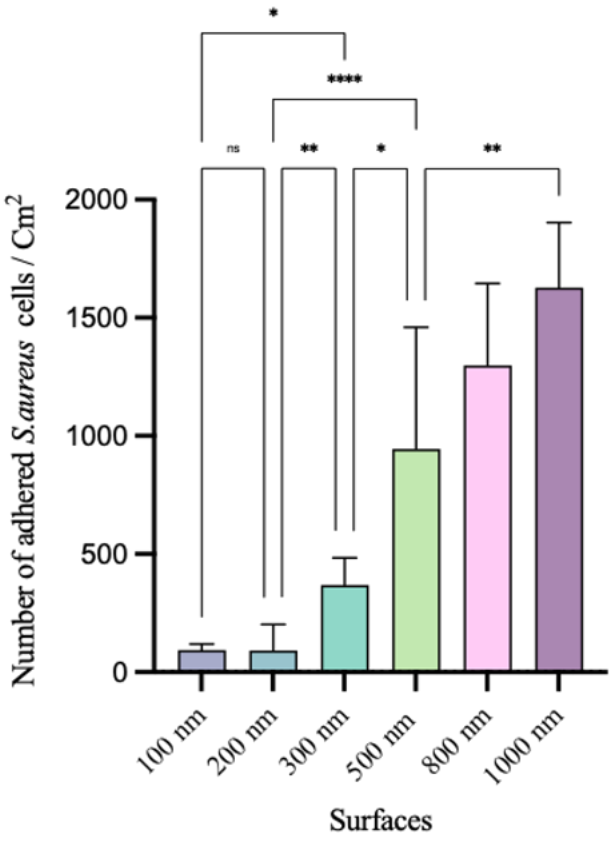
*
****
ns
**
*
**
2000
1500
1000
500
0
Number of adhered S.aureus cells / Cm2
100 nm
200 nm
300 nm
500 nm
800 nm
1000 nm
Surfaces

Figure S4: (A) Representative CLSM images of the *S. aureus* adhesion to Fn patterns with 15 nm depth (nominal diameters (nm) indicated) (Scale bar 20µm). (C) Number of bacterial cells/mm^2 on different Fn nanopattern compared to controls surfaces. Bars show mean ± s.d. of 2 independent experiments (3 images for each) for 100 nm Fn pattern with 15 nm depth, 3 independent experiments (5 images for each) for 200, 300 , 500, 800 and 1000 nm Fn patterns with 15 nm with 15 nm depth. $^{(n.s)}p<0.5$, * P<0.05, ** P<0.01, *** P>0.001, p<0.0001 (****).

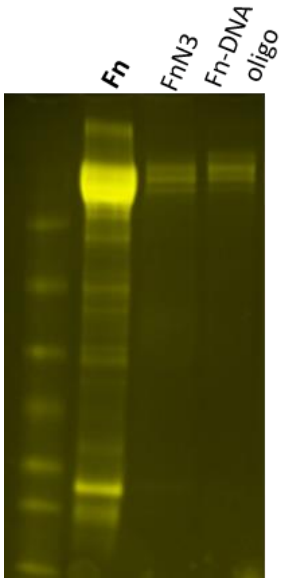

Figure S5: SDS gel electrophoresis demonstrating the expected band shift of the DNA-conjugated fibronecting in comparison to the pure fibronecting.

Discussion & Outlook

Publication 1: Visualization of Bacterial Protein Complexes Labeled with Fluorescent Proteins and Nanobody Binders for STED Microscopy

In Publication 1, I present a methodology for STED imaging of bacterial proteins using nanobody binders. Visualizing protein assemblies in bacteria presents several challenges such as their small size, the lack of commercially available primary binders against bacterial proteins, and the physical barrier of the bacterial cell wall. Thus, even though organic dyes have superior photophysical properties for super-resolution microscopy applications, targets are commonly imaged using fluorescent protein tags. We determined nanobody binders (NBs) against the common tags GFP and RFP could be used for successful STED microscopy imaging of the intracellular proteins DivIVA and FtsZ in *B. subtilis* and *E. coli,* respectively. We evaluated the unspecific binding of the GFP and RFP nanobodies and characterized the effects of organic dye selection on STED microscopy in *B. subtilis,* determining that ATTO 647N was the highest performing STED dye.

Influence of dye selection on nanobody performance in *B. subtilis*

We show that the dye coupled to a nanobody (NB) binder can influence NB performance. We quantified the cellular background and signal-to-noise ratios of nanobodies conjugated with the organic dyes ATTO 647N, ATTO 594, STAR 600, and STAR 635P. The tested STED dyes had net charges in the range of -3 to +1 [66-68]. Cellular background of the GFP nanobody (NB_{GFP}) significantly varied when conjugated to different STED dyes. NB_{GFP}-ATTO 647N resulted in cellular background levels of 11%, while NB_{GFP}-STAR 635P resulted in 34% background. When imaging with NB_{GFP}-ATTO 594, the cellular background was so high that STED imaging was unsuccessful. Cellular background levels were calculated by dividing fluorescent signal outside of the division septum by fluorescent signal at the division septum. Thus, lower cellular background levels indicate more signal was present at the division septum than the cytoplasm. ATTO 647N has a positive net charge (+1) while the other dyes tested, ATTO 585 and STAR 635P have net charges of (-1) and (-3). It could be that the chemistry of NB_{GFP}-ATTO 647N increased binder penetration to the crowded division septum. Another possibility is that the positive net charge reduced unspecific binding in the bacterial cytoplasm. We note ATTO 647N was also the best performer for RFP protein imaging, however, it ranked marginally ahead the second best performer, ATTO 594. NB_{RFP}-STAR600 performed slightly worse. Therefore, dye choice heavily influenced NB_{GFP} performance, and NB_{RFP} performance was not very sensitive to dye choice. Overall, data suggested that STED dye choice can influence NB performance and determined ATTO 647N was the best performing STED dye for *B. subtilis* imaging.

Methodology Establishment

We used the cell division protein DivIVA in the gram-positive bacteria *B. subtilis* and FtsZ in the gram-negative bacteria *E. coli* as proof-of-concept (POC) proteins for methodology establishment. DivIVA appears as a single band when visualized using diffraction-limited microscopy. The true structure of DivIVA, two rings flanking division sites [54], can only be resolved using super-resolution microscopy methods, making it an ideal POC target. Furthermore, DivIVA is a high copy number protein, ~ 1700 proteins/cell, that is present during sporulation and vegetative division modes and has been extensively tagged with fluorescent proteins [69]. Sample preparation or imaging artifacts would have likely been detected via aberrations of the DivIVA dual ring structure during 3D imaging since rings have a constant diameter (~800 nm). DivIVA isn't present in the gram-negative bacteria *E. coli*. Therefore, we used the protein FtsZ to establish STED imaging with nanobody binders. Like DivIVA, FtsZ is a high-copy number protein whose localization has been extensively studied [53,54,59,61,70,71]. We visualized FtsZ as a patchy band at the mid-cell, agreeing with previous results. Unlike *B. subtilis*, we did not compare the performance of dye-labeled RFP and GFP nanobody binders in *E. coli*, primarily because future research plans focused on *B. subtilis* imaging. Future studies could characterize NB performance in *E. coli* by creating strains expressing FtsZ fusion proteins and following the methodology presented in our study.

We created an optimized immunolabeling protocol for intracellular bacterial protein imaging. Unlike mammalian cells, bacteria have a cell wall that requires digestion for effective intracellular delivery of exogenous molecules, *e.g.* antibody or nanobody binders. Detergents such as Triton-X-100 and Tween20 are typically used for membrane permeabilization of microscopy specimens. We found that the use of Tween20 alone was not sufficient for cell permeabilization in the gram-positive bacteria *B. subtilis* (Publication 1, SM Fig. 1). This was most likely due to the thick layer (30 – 60 nm) of peptidoglycan surrounding the *B. subtilis* cell membrane [72]. The enzyme lysozyme hydrolyzes the linkages between peptidoglycan molecules, effectively creating gaps or holes. In live cells, incubation with high enough lysozyme concentrations can lead to loss of turgor pressor and cell lysis. We found that lysozyme incubation after fixation enabled NB entry into *B. subtilis* (Publication 1, SM Fig. 1). Increasing the concentration of lysozyme used during sample preparation increased fluorescent signal from the dye-labeled NB, suggesting that increased lysozyme concentrations ultimately increased the amount of NB entering bacteria. For all conditions, we incubated the sample with detergent, which permeabilizes cell membranes [73], during the NB incubation step, strongly suggesting that fixation and detergent treatment isn't sufficient for membrane permeabilization. However, fixation with 2% formaldehyde preserved cell integrity during lysozyme treatments (Publication 1, SM Fig. 1). It's likely

that cell wall proteins crosslinked together by fixation form a stable mesh withstand lysozyme and detergent treatment, allowing both sample preservation and subsequent immunolabeling.

Outlook

This thesis presents a methodology for STED microscopy imaging of intracellular bacterial proteins using fluorescent proteins and nanobody binders. The performance of various nanobody-dye combinations for STED microscopy in *B. subtilis* was evaluated. Results were presented for nanobody binders against GFP and RFP tags, which are commonly used as fluorescent protein tags in microbiology, and four STED dyes. However, characterizations of additional nanobody-dye combinations could greatly benefit researchers. Several companies now offer a large library of nanobodies against protein tags and comprehensive information about their performance. Also, nanobodies can be purchased conjugated to a dye of choice. Thus, systematic evaluation of a larger range of nanobody-dye combinations for STED microscopy of bacteria is feasible. It would also be interesting to asses nanobody-dye combinations systematically across not only *B. subtilis* but other commonly used bacteria species (*e.g. E. coli, S. aureus, and C. cresentus*), ultimately providing a guidebook for STED super-resolution microscopy applications in bacteria.

Publication 2: Comparing Divisome Organization Between Vegetative and Sporulating Bacillus subtilis at the Nanoscale using DNA-PAINT

In Publication 2, I present my research investigating potential differences between divisome organization in vegetative and sporulating *B. subtilis* at the nanoscale. Previously, it was reported that the Z-ring, the foundation of the bacterial divisome, was positioned differently within the division plane dependent on division mode [74]. The research presented in this thesis investigates whether other divisome proteins are positioned or organize differently dependent on division mode. Super-resolution microscopy offered valuable insights because it combines nanoscale resolutions, <20 nm, with target identification and target quantification capabilities. The nanoscale positioning, assemblies, and distribution of four key division proteins in vegetative and sporulating cells were mapped and compared using DNA-PAINT super-resolution microscopy (DNA-PAINT) and quantitative analyses. The long-debated assembly of SepF was revealed as arcs *in cellulo*. We determined that asymmetric placement of early divisome proteins is a characteristic of sporulating *B. subtilis* and found evidence that regulation of division septum thickness differs between division modes.

DNA-PAINT for intracellular bacterial protein imaging

We ultimately chose to use DNA-PAINT super-resolution microscopy to visualize bacterial division proteins. Comparing divisome protein organization required a microscopy method with nanoscale resolution (<20 nm), quantitative capabilities, multiplexed 3D imaging, and usability. While standard

STED microscopy enabled visualization of dual DivIVA rings (Publication 1), the resolutions we achieved, ~50 nm in the xy-plane, were not sufficient for nanoscale mapping of the positioning and architecture of division proteins. Furthermore, 3D imaging was needed to image the entire divisome, which has a maximum of ~800 nm diameter. 3D imaging is possible with standard STED microscopy using z-stacks, *i.e.* sequential imaging of the z-plane in slices of a predefined size (typically ~250 nm for bacterial imaging). However, photobleaching can occur during z-stack acquisition as multiple images are taken at a single field-of-view, potentially resulting in undercounting of target molecules. PALM, (d)STORM, and DNA-PAINT can reach a sample depth of ~ 1 μm using TIRF or HILO illumination methods (Introduction), which is sufficient for *B. subtilis* imaging. However, target quantification using both dSTORM and PALM can present challenges due to photobleaching, repetitive blinking, overlapping emitters, or failed activation [75]. The inherent properties of DNA-PAINT minimized or abolished these challenges, as DNA-PAINT contains a virtually unlimited photon budget due to the repetitive cycling of fresh imager strands binding and unbinding docking strands. Furthermore, blinking density can be controlled by the concentration of imager strands in solution. While two-target imaging using PALM or dSTORM experiments is well established, corrections for chromatic aberration are necessary to eliminate shifts between channels. DNA-PAINT can perform multi-target imaging using the same dye, *e.g.* Cy3B, for all targets. Since our project focused on quantification of targets and revealing nanoscale differences in protein distribution, we ultimately chose DNA-PAINT. We achieved on average 6 nm localization precision, or ~ 14 nm resolution in the xy-plane (Publication 2, SM Table S8) and performed 2-plex imaging via Exchange-PAINT [32].

One challenge was developing the sample preparation protocol for intracellular protein labeling of vegetative and sporulating *B. subtilis*. Intracellular bacterial targets can be visualized using either direct or indirect labeling (1.1 Fluorescence). We previously developed a methodology for indirect labeling of intracellular proteins in vegetative cells, Publication 1. When naïvely performing the same sample preparation protocol used for vegetative cells on sporulating *B. subtilis*, DNA-PAINT imaging was unsuccessful and STED imaging successful. Compared to the DNA-PAINT protocol for vegetative cells, the optimized protocol for sporulating cells required harsher permeabilization and improved washing steps. While a dye is coupled to nanobody binders for STED microscopy, DNA-PAINT requires nanobody coupling to DNA oligonucleotides. It's possible that the chemistry of a DNA-labeled nanobody binder is different than that of a dye-labeled nanobody. DNA is negatively charged, and organic dyes have various charges, e.g. STAR 635P at -3, ATTO 647N at +1 [66,67], which could influence unspecific binding and binder entry through the thick *B. subtilis* cell wall. Another exacerbating factor is that the constricting septum contains not only division proteins, but biomolecules involved in the processes of septal thinning and DNA translocation during sporulation, and these processes are absent

in vegetative cells [76,77]. We used harsher washing and lysozyme treatments, which might have removed biomolecules concentrated around the division septum that perturbed entry of the DNA-labeled nanobody. When applying an immunolabeling protocol that was optimized using dye-labeled binders, one might anticipate slight protocol changes in the washing and or permeabilization steps when switching to DNA-labeled binders.

Nanoscale positioning of early divisome proteins is dictated by division mode

We mapped the nanoscale positioning of four bacterial division proteins by performing Exchange-PAINT [32] on two division proteins at a time (Fig. 3). DNA-PAINT offers theoretically unlimited multiplexing capabilities, however, imaging more than two tagged protein targets can have disadvantages. Integration of a protein tag at endogenous gene loci might reduce or abolish protein functionality [78]. This affect is amplified when creating strains with multiple protein tags, especially when targets comprise the same macromolecular complex or perform similar functions. The proteins of interest SepF and ZapA both bind and stabilize the Z-ring [79,80], which forms the foundational scaffold structure of the divisome [53]. The protein of interest DivIVA is a component of the regulatory Min system, which prevents aberrant Z-ring assembly and was shown to flank the Z-ring in vegetative cells but not directly interact with the Z-ring [54]. Therefore, we designed DNA-PAINT experiments for two target imaging of the Z-ring with SepF, ZapA, or DivIVA, or performed one target imaging. By pinpointing the position of the Z-ring between dual DivIVA rings in sporulating cells and then the placement of SepF and ZapA relative to the Z-ring, we mapped the relative placement of divisome proteins at division septa. In theory it would be possible to use primary antibodies in combination with secondary nanobodies to circumvent protein tagging, an approach that was recently used for 30 target DNA-PAINT imaging in neurons [33]. However, commercially available antibodies against bacterial proteins are scare in comparison to those for mammalian proteins. Out of the four protein targets investigated in *B. subtilis*, there was a commercially available primary binder against one protein, an anti-serum against FtsZ protein. Additionally, our proteins of interest belonged to a small ring shaped macromolecular complex, ~800 nm diameter. It's likely that simultaneous labeling using multiple tags, antibodies, and nanobodies against many targets would reduce target accessibility because of steric hinderance. Our imaging approach, in which a single target of interest was imaged using a positional reference target, could be extended to map the nanoscale positioning of additional divisome proteins. Our results suggest that the early divisome proteins, also called Z-ring binding proteins (ZBPs), are necessary for cell division in sporulating *B. subtilis*. ZBPs are the first set of proteins recruited to the division plane during vegetative division and include proteins SepF, EzrA, and SepF. It was recently determined that Z-ring condensation by ZBPs is essential for cell division in vegetative *B. subtilis* [46], however the localization and function of ZBPs during sporulation remained relatively unexplored. Co-

localization of ZBPs with the Z-ring in sporulating cells would suggest ZBPs perform similar functions during sporulation. At the time of this thesis whether or not SepF appeared at the division septum in sporulating cells had not been determined, and super-resolution imaging of ZapA during sporulation was not yet performed [81]. We found that the SepF and ZapA rings are positioned together with the Z-ring (Fig. 3) towards the mother cell of sporulating cells during division. These findings show that the co-positioning of ZBPs with the Z-ring in sporulating cells is similar to that of vegetative cells, suggesting ZBPs perform similar functions in sporulating and vegetative cells, namely Z-ring condensation and stabilization. Future experiments testing the effect of various ZBPs knock out strains on Z-ring condensation and cell growth, with similar methodology to previous work [46], could be performed in the future.

How sporulating cells asymmetrically position the divisome is not known. However, recent evidence indicates that the protein SpoIIE is a key player. In *ΔspoIIE* strains, sporulating cells position the Z-ring symmetrically at the mid-septum like in vegetative cells [74] and in wild-type cells, SpoIIE preferentially localizes to the forespore side of the division septum before membrane constriction [50]. However, the mechanism behind the effect of SpoIIE on divisome positioning is not clear. At the onset of sporulation, the Z-ring and SpoIIE are redeployed from the mid-cell to the cell poles in a spiral-like intermediate [49]. However, there are currently no known SpoIIE localization cues at the cell pole. Perhaps SpoIIE leads the Z-ring to the future division site via an unidentified topological marking. Once at the cell pole, SpoIIE might sequester currently unidentified proteins involved in asymmetric Z-ring placement. It's also possible that SpoIIE spatially excludes proteins from localizing to the forespore side of the septum during divisome assembly, helping create asymmetry at the division septum. Interestingly, SpoIIE interacts with the Min system via DivIVA in sporulating cells [50]. Identification of additional factors affecting the nanoscale positioning of the divisome will help researchers describe a mechanism for asymmetric Z-ring placement.

Why the asymmetric placement of the division machinery occurs is also unclear. During sporulation, there is a second division site at the opposite cell pole that is typically dissolved prior to forespore engulfment [82]. Placement of the divisome towards the mother cell compartment could promote division machinery assembly at the second potential division site of the sporulating cell, which is also in the mother cell compartment. Asymmetric positioning of divisome proteins could ensure adequate amounts of division proteins present in the mother cell for redistribution to the second division site in case division fails at the first site. Asymmetric positioning of divisome proteins could also be a consequence of the processes of DNA translocation and septal thinning, which require multiple components to localize at the division septum and occur exclusively in sporulating cells. Clearly, there

are many avenues of exploration open to elucidate the mechanism behind asymmetric Z-ring positioning in *B. subtilis* and why it occurs.

SepF arcs inform mechanisms of septal thickness regulation in vegetative and sporulating *B. subtilis*

We revealed that SepF protein forms arcs that encircle the invaginating septum in vegetative and sporulating cells (Fig. 4). SepF is a widely conserved across gram-positive bacteria, archaea, and cyanobacteria, and emerged before the divergence of Archea and Bacteria[83]. The *in vivo* organization of SepF at the division septum has long been debated. SepF anchors FtsZ to the cell membrane via its N-terminal membrane binding domain and has a C-terminal FtsZ binding domain. While SepF forms ring shaped polymers *in vitro*, the membrane binding domain localizes at the inner surface of the polymer rings [80]. Therefore, it seems unlikely that SepF assembles into rings *in vivo*, *since* the membrane binding domain would not be accessible to the cell membrane. In the "clamp model" [84], SepF forms arcs that encircle the invaginating septum to align the FtsZ protofilaments that lie perpendicularly across them. In this model, SepF controls septum thickness by controlling the width of FtsZ protofilaments at the division site. Using DNA-PAINT, we revealed that SepF assembles as arcs with endpoints that face away from the cytoplasm at division septa in vegetative and sporulating cells. This protein organization supports the SepF clamp model. However, if this model holds true for both division modes, the diameters of SepF arcs should correlate with septal thickness. This is particularly interesting because the constricting septum is ~ 50 nm wide in vegetative cells and ~25 nm wide in sporulating cells. We determined that SepF arc diameter is similar, ~50 nm, at vegetative and sporulating division septa. This value is similar to the thickness of the septum in vegetatively dividing cells, supporting the clamp model. However, SepF arc diameter (50 nm) cannot be the determinant of septum thickness (25 nm) in sporulating cells. Our findings strongly suggest that the thickness of the constricting septum is not controlled by the curvature of SepF assemblies in sporulating cells and support the SepF clamp model in which SepF arc curvature is a determinant of septal thickness in vegetative cells.

Data presented in this thesis suggest the thickness of the division septum is controlled by different mechanisms dependent on division mode, however, the mechanisms behind septal thickness regulation remain unknown. Cryo-focused ion beam cryo-electron tomography (cryo-FIB-ET) studies determined that *B. subtilis* strains with knock-outs of SpoIIE protein contain division thicker division septa than wild-type strains [74,77,85], strongly suggesting SpoIIE affects septal thickness regulation in sporulating cells. However, the thickness of septa in wild-type sporulating cells (~25 nm) was still thinner than septa in Δ*spoIIE* cells (~40 nm), strongly suggesting additional proteins are involved in

septal thickness regulation. Future studies should identify and knock out candidate factors to determine their effect on septal thickness.

Recent research suggests that the number of FtsZ filaments at the division site correlates with septum thickness during cell division [74]. Researchers used Cryo-FIB-ET to visualize FtsZ filaments in vegetative and sporulating cells and measured FtsZ filament length at division septa. They found that the length of FtsZ filaments was ~50% longer in vegetative cells, correlating with the difference in septum thickness between division modes. To explore this hypothesis, we compared the amount of FtsZ within Z-rings between division modes and found that Z-rings in sporulating cells contained 10% less FtsZ compared to vegetative cells. Since the division septum is ~50% thinner in sporulating than vegetative cells, our results suggest that the quantity of FtsZ within the Z-ring isn't a key determinant of division septum thickness. We note that unlike the previous study, we were able to analyze the entire Z-ring volume and had improved statistics, since tens of cells are within single field-of-view. Additionally, we normalized FtsZ protein content values for Z-ring diameter, since rings containing larger diameters will contain larger amounts of protein. There is still much to be understood about interplay of the divisome with septal thickness regulation in *B. subtilis*.

Protein content of ring assemblies dependent on vegetative or sporulating division mode

DNA-PAINT imaging revealed that protein distribution within DivIVA assemblies differs dependent on *B. subtilis* division mode (Fig. 1). We found that the DivIVA ring in the forespore (ringF) contained approximately 30% more DivIVA than its counterpart in the mother cell compartment (ringM) during cell division, *i.e.* when the Z-ring was present. DivIVA is a component of the *B. subtilis* Min system, which regulates divisome assembly [86]. DivIVA is recruited to the division site upon membrane constriction via the appearance of negative membrane curvature, which occurs at the division septum and at a second potential division site at the opposite cell pole [54 82]. Upon septum completion at the first division site in wild-type cells, septum formation has begun at the second division site in ~10% of cells, termed disporic cells [82]. Our results suggest that DivIVA in ringM could be undergoing redistribution to the second division site, at the opposite cell pole, during division at the first site. Since not all cells are disporic, our results also suggest that less protein is recruited to ringM compared to ringF during dual DivIVA ring assembly in dividing cells. Interestingly, a prior study reported DivIVA was exclusively present on the forespore side of the division plane after septum elaboration [50]. Taken together, it seems likely that less protein is recruited to ringM compared to ringF during dual DivIVA ring assembly, and ringM is completely disassembled shortly before or immediately after the septum is elaborated and or redistributed to the second potential division site. A contributing factor to the uneven distribution of protein between DivIVA dual rings could be the membrane geometry of the forespore compartment, which presents negative curvature at the septum's lateral edge. Notably, the

forespore side of the septum appears more concave than the mother cell side due to the rounded forespore shape [74], potentially promoting DivIVA assembly.

We determined that protein content within the ring assemblies of SepF and FtsZ is dependent on division mode. Specifically, SepF rings in sporulating cells contained approximately 30% less protein compared to those in vegetative cells. Given that SepF, EzrA, and FtsA all bind to the same 20-amino acid FtsZ protein domain, there might be competition among these early divisome proteins for FtsZ binding. Smaller amounts of SepF might suggest that EzrA and or FtsA outcompete SepF for the binding domain. Additionally, during sporulation, proteins localize to the division plane for sporulation-specific processes such as DNA translation or septal thinning, creating competition for space at the septum [53]. Thus, there might be less space available at the septa of sporulating cells for SepF to bind the membrane. In future studies, it might be interesting to quantify the relative amounts of EzrA and FtsA between division modes, as increased amounts would suggest EzrA or FtsA outcompetes SepF for FtsZ-binding. The implications of different Z-ring protein content between vegetative and sporulating cells was discussed previously.

We determined that ring assemblies of SepF, FtsZ, and DivIVA contain different amounts of protein dependent on division mode by comparing protein content of cells within the same field-of-view. Using a naïve approach, we could have compared divisome protein content between cells across all field-of-views. However, this approach would likely result in higher experimental fluctuations because samples would be imaged on different dates, immunolabeled with different antibody or nanobody stocks, and prone to variations caused by general human error. To determine protein abundance, we used DNA-PAINT dark time (τ_d) as a readout of protein content since it scales inversely with target protein amount (Introduction). The size of our imaging field-of-view was 65 x 65 μm and 30 – 70 cells were present in a typical image.

Outlook

A major contribution of this thesis was the finding that the positioning of the early division machinery depends on division mode in *B. subtilis*. A natural continuation of this research would be to map and compare the nanoscale positioning of additional divisome proteins between vegetative and sporulating division modes. Recent models of bacterial cell division are split on whether FtsZ filament treadmilling drives septal wall synthases circumferentially around the division site or if peptidoglycan synthesis is responsible [44,47,48,87]. Thus, it would be especially interesting to see if peptidoglycan synthases localize asymmetrically with FtsZ in sporulating cells or exclusively at areas of constricting membrane. According to cell division models in which FtsZ-treadmilling drives septal wall synthase motion, the Z-ring should be positioned with the peptidoglycan synthases in both division modes [44,47]. The biological mechanisms responsible for asymmetric placement of division machinery in sporulating

cells remain elusive. Such mechanisms could be identified by determining the effect knock-out strains have on the positioning of the Z-ring at division septa via DNA-PAINT as presented in Publication 2. Alternatively, cryo-FIB-ET could be used [74]. Identification of currently undiscovered proteins affecting divisome positioning might also be required. If a perfect knock out system is identified, *i.e.* a viable strain enabling completely symmetric placement of the division machinery in sporulating cells, the functional relevance of asymmetric divisome positioning in sporulating *B. subtilis* should also be explored.

Innovations in bacterial membrane labeling will be important for revealing the interplay between divisome protein architecture and cell wall synthesis. The state-of-art bacterial membrane dye is Nile Red, which has achieved resolutions of ~ 30 nm [25]. A nanoscale image of division proteins and the membrane was not achievable in our hands due to a low spatial resolution of Nile Red, ~40 nm. Nile Red typically remains immobilized on the membrane after binding and bleaches. In contrast, the transient binding of imager and docking sequences in DNA-PAINT leads to multiple localizations per binding site, creating a virtually unlimited photon budget. Additional challenges faced using Nile Red based membrane imaging were difficulties achieving background free staining in 3D and the fact that Nile Red cannot be washed out of samples after use. The ideal bacterial membrane stain would enable nanoscale resolutions (<20 nm) in three dimensions and have increased usability. Glycan or lectin based imaging probes offer a promising approach, but target selection should be informed to ensure presentation on the newly synthesized cell wall [88]. Improved membrane staining would be especially interesting in the case of SepF, which we found to form arc assemblies that likely encircle the invaginating septum, and as a general tool to study protein and membrane dynamics during the entire process of sporulation. To the best of my knowledge, only the *B. subtilis* division proteins FtsZ and FtsA can be visualized at the division septum using electron microscopy approaches due to their high staining contrast [74]. Correlative light and electron microscopy (CLEM) is another possible approach to achieve nanoscale membrane and protein staining. However, CLEM presents challenges such as identifying fluorescent probes compatible with light and electron microscopy sample preparations, overlaying light and electron microscopy images, achieving high resolutions in light microscopy data, and the general constraints of its required sample sectioning [89]. Knowledge from chemists, microbiologists, and microscopists will be necessary to create the ideal tool for bacterial membrane visualization at the nanoscale.

The ultimate goal would be to generate a 3D model of how divisome proteins organize and perform division at the nanoscale in vegetative and sporulating cells. A combination of super-resolution imaging, genetic engineering, biochemistry, and microbiology will be required for success. The methodology and analysis pipelines presented in this thesis can be directly applied to additional

division proteins to determine their protein content, organization, nanoscale positioning at the division septum, and assembly properties. This methodology is currently optimized for *B. subtilis*, but could be extended to other bacterial species by modifying the sample preparation steps for DNA-PAINT imaging, particularly the fixation and permeabilization steps. Divisome components could be imaged at nanoscale resolutions in wild-type cells and as part of functionality assays. The diameter of the Z-ring can be used as a clock to pinpoint division stage in fixed samples. Imaging probes such as nanobodies against protein tags or primary antibodies can be used to visualize proteins of interest, however, care should be taken to ensure that protein tagging doesn't influence their functionality. Imaging probe creation using AI based approaches such as AlphaFold presents an intriguing opportunity [90]. The dynamics of divisome components should also be studied using single-molecule tracking in live cells as previously performed [46]. Overall, a 3D nanoscale model of how divisome proteins organize and perform division is not too far out of reach.

Publication 3: The Role of Nanoscale Distribution of Fibronectin in the Adhesion of Staphylococcus aureus Studied by Protein Patterning and DNA-PAINT

In Publication 3, I present results from visualization of the protein fibronectin (Fn) to cell surface receptors on the bacteria *Staphylococcus aureus* with DNA-PAINT. *S. aureus* is a highly virulent pathogen that can cause both superficial and invasive infections. The interactions between surface receptors of *S. aureus* and the extracellular matrix protein fibronectin play a crucial role in bacterial invasion of host cells and are associated with the colonization of medical implants. We looked at the impact of fibronectin and cellular receptor distribution on *S. aureus* adhesion to biointerfaces, serving as a model for initial adhesion at tissue interfaces or biomaterials. We found *S. aureus* adhesion to fibronectin biointerfaces is influenced by the size of available ligand patches, with an adhesion threshold of 300 nm or larger patches. We then determined the surface density of FnBPs on the *S. aureus* surface, ranging from 38 to 46 μm^{-2}. Taken together, we found that the engagement of two or more receptors is necessary for *S. aureus* adhesion to fibronectin biointerfaces.

The nanoscale distribution of fibronectin binding proteins on the *S. aureus* surface

We determined 2.7–3.2 FnBPs on the cell surface are needed for strong *S. aureus* adhesion. Several fibronectin binding proteins (FnBPA and FnBPB) are present on the *S. aureus* cell surface. Therefore, we used a single-molecule binding assay employing the FnBP receptor ligand fibronectin (Fn). During sample preparation, live *S. aureus* were incubated with Fn conjugated to DNA-PAINT docking handles, fixed, and immobilized on coverslips for imaging. Therefore, unlike the results presented in Publication 1 and 2, no cell permeabilization was required. We determined each bacterium contained approximately 130 FnBP receptors by counting DNA-PAINT localizations on the *S. aureus* surface. It

could be possible that Fn ligands did not bind every FnBP receptor, leading to target undercounting. However, we note our findings agree with a previous study that calculated ~110 FnBP per bacterium [91] using a functionalized atomic force microscopy (AFM) tip. We determined that at least 2.7–3.2 FnBPs are required for strong *S. aureus* adhesion to surfaces by combining results from fibronectin-coated biointerface studies and DNA-PAINT studies. The lower limit of engagement was 2.7–3.2 FnBPs for strong *S. aureus* adhesion, *i.e.* adhesion under flow conditions. This suggests that the lack of *S. aureus* adhesion on Fn patches below 300 nm most likely resulted from too few receptors being available on the cell surface for binding to the smaller Fn patches.

Outlook

We determined the adhesion properties of FnBP, a microbial surface components recognizing adhesive matrix molecule (MSCRAMM), in the pathogenic bacteria *S. aureus* via protein patterning and DNA-PAINT. The methodology presented could be extended to characterize the adhesion properties of additional MSCRAMMs in *S. aureus*. Indeed, the mechanisms behind adhesion of the MSCRAMMs SdrD, SdrC, and ClfA remain elusive [92]. It might also be interesting to map and compare the distribution of multiple MSCRAMMS on the cell surface under various adhesion conditions and in combination with human immune cells. Our imaging approach incubates the DNA-conjugated ligand with live cells. This might be disadvantageous when assessing the effect of a single ligand on the distribution of multiple MSCRAMMs. Therefore, the effect of fixation on DNA-conjugated ligands could be assessed and optimized to enable multi-target imaging of MSCRAMMs. Future studies might also aim to directly calculate the distribution of MSCRAMMs by genetically engineering the MSCRAMM under investigation with a small tag instead of using the ligand as a readout for receptor localization. In this case, proper localization and functionality of tagged proteins should be assessed. If readily available, antibodies or smaller affinity reagents against MSCRAMMs have great potential as imaging probes.

Concluding Remarks

Overall, the findings of this thesis contribute a methodology for STED microscopy of bacteria using fluorescent protein tags and nanobodies, increase our understanding of divisome protein organization in the vegetative and sporulating division modes of *Bacillus subtilis*, incite investigations comparing divisome organization between division modes, and present DNA-PAINT super-resolution microscopy as a useful tool for investigating bacteria at the nanoscale.

Acknowledgements

I'd like to start by thanking Ralf for taking me in as a PhD student. Your supervision and support over the years was invaluable. I am grateful for the many opportunities you afforded me during my PhD time.

I'd like to thank my parents who have done nothing but support my education and personal development my entire life. Without you this PhD would've never happened. I dedicate this dissertation to you both.

I'd like to thank my husband Fatih for his endless support in every possible way. You keep me calm and motivate me to do better. Thank you for your understanding and patience during my PhD journey.

I'd like to thank Jae for taking me in and teaching me about bacterial cell division and microscopy sample preparation during my Masters and first PhD year. Your mentorship helped me immensely on my journey.

I'd like to thank Susanne for being an excellent teammate. Thank you for your great work and camaraderie while working on the sporPAINT paper.

I'd like to thank Alex Auer for his contributions to the sporPAINT paper.

Thank you to Anna-Lena, Robert, Iris, and Heba for being great collaborators.

I'd like to thank my Thesis Advisory Committee members Prof. Petra Schwille and Prof. Marc Bramkamp for helpful discussions, advice, and input over the years.

Thanks to the OG Girl's Office (R.I.P.) members Isabelle and Taisha for making work so fun. I doubt I'll ever have a workplace vibe like that again.

I'd like to thank all my lab mates. You made this PhD process not only rewarding but fun. Thank you Monique and Ana for fun and interesting discussions. Thank you Philipp, Rafal, and Shuhan for always making me laugh. Thank you Eduard for the easy camaraderie over the years. Thank you Max Strauß for answering my endless questions about Picasso and microscopes when I first joined the lab. Thank you Luciano for your insights.

Thank you Martin Spitaler and the members of the MPIB Imaging Facility for training me on and helping me troubleshoot a plethora of different microscopes over the years.

Thank you Jürgen and Sebastian for giving me the opportunity to intern at Massive Photonics GmbH during my PhD.

Thank you to everyone, including those not mentioned by name, who has supported me during my PhD.

References

1 Jablonski, A. Efficiency of Anti-Stokes Fluorescence in Dyes. *Nature* **131**, 839-840 (1933). https://doi.org/10.1038/131839b0

2 Lakowicz, J. R. Principles of frequency-domain fluorescence spectroscopy and applications to cell membranes. *Subcell Biochem* **13**, 89-126 (1988). https://doi.org/10.1007/978-1-4613-9359-7_3

3 Stokes, G. G. XXX. On the change of refrangibility of light. *Philosophical Transactions of the Royal Society of London* **142**, 463-562 (1852). https://doi.org/doi:10.1098/rstl.1852.0022

4 Heim, R., Prasher, D. C. & Tsien, R. Y. Wavelength mutations and posttranslational autoxidation of green fluorescent protein. *Proc Natl Acad Sci U S A* **91**, 12501-12504 (1994). https://doi.org/10.1073/pnas.91.26.12501

5 Rodriguez, E. A. *et al.* The Growing and Glowing Toolbox of Fluorescent and Photoactive Proteins. *Trends Biochem Sci* **42**, 111-129 (2017). https://doi.org/10.1016/j.tibs.2016.09.010

6 Lang, K. *et al.* Genetic Encoding of bicyclononynes and trans-cyclooctenes for site-specific protein labeling in vitro and in live mammalian cells via rapid fluorogenic Diels-Alder reactions. *J Am Chem Soc* **134**, 10317-10320 (2012). https://doi.org/10.1021/ja302832g

7 Leenaars, M. & Hendriksen, C. F. M. Critical Steps in the Production of Polyclonal and Monoclonal Antibodies: Evaluation and Recommendations. *ILAR Journal* **46**, 269-279 (2005). https://doi.org/10.1093/ilar.46.3.269

8 Sograte-Idrissi, S. *et al.* Correction: Circumvention of common labelling artefacts using secondary nanobodies. *Nanoscale* **12**, 24543 (2020). https://doi.org/10.1039/d0nr90279a

9 Opazo, F. *et al.* Aptamers as potential tools for super-resolution microscopy. *Nat Methods* **9**, 938-939 (2012). https://doi.org/10.1038/nmeth.2179

10 Pleiner, T., Bates, M. & Görlich, D. A toolbox of anti-mouse and anti-rabbit IgG secondary nanobodies. *J Cell Biol* **217**, 1143-1154 (2018). https://doi.org/10.1083/jcb.201709115

11 Schlichthaerle, T. *et al.* Site-Specific Labeling of Affimers for DNA-PAINT Microscopy. *Angew Chem Int Ed Engl* **57**, 11060-11063 (2018). https://doi.org/10.1002/anie.201804020

12 Strauss, S. *et al.* Modified aptamers enable quantitative sub-10-nm cellular DNA-PAINT imaging. *Nat Methods* **15**, 685-688 (2018). https://doi.org/10.1038/s41592-018-0105-0

13 Tokunaga, M., Imamoto, N. & Sakata-Sogawa, K. Highly inclined thin illumination enables clear single-molecule imaging in cells. *Nature Methods* **5**, 159-161 (2008). https://doi.org/10.1038/nmeth1171

14 Fish, K. N. Total internal reflection fluorescence (TIRF) microscopy. *Curr Protoc Cytom* **Chapter 12**, Unit12.18 (2009). https://doi.org/10.1002/0471142956.cy1218s50

15 Abbe, E. Beiträge zur Theorie des Mikroskops und der mikroskopischen Wahrnehmung. *Archiv für Mikroskopische Anatomie* **9**, 413-468 (1873). https://doi.org/10.1007/BF02956173

16 Rayleigh. XV. On the theory of optical images, with special reference to the microscope. *The London, Edinburgh, and Dublin Philosophical Magazine and Journal of Science* **42**, 167-195 (1896). https://doi.org/10.1080/14786449608620902

17 Gustafsson, M. G. Surpassing the lateral resolution limit by a factor of two using structured illumination microscopy. *J Microsc* **198**, 82-87 (2000). https://doi.org/10.1046/j.1365-2818.2000.00710.x

18 Hell, S. W. & Wichmann, J. Breaking the diffraction resolution limit by stimulated emission: stimulated-emission-depletion fluorescence microscopy. *Opt. Lett.* **19**, 780-782 (1994). https://doi.org/10.1364/OL.19.000780

19 Hell, S. W. Far-Field Optical Nanoscopy. *Science (New York, N.Y.)* **316**, 1153-1158 (2007). https://doi.org/doi:10.1126/science.1137395

20 Westphal, V. *et al.* Video-Rate Far-Field Optical Nanoscopy Dissects Synaptic Vesicle Movement. *Science (New York, N.Y.)* **320**, 246-249 (2008). https://doi.org/doi:10.1126/science.1154228

21 Thompson, R. E., Larson, D. R. & Webb, W. W. Precise nanometer localization analysis for individual fluorescent probes. *Biophys J* **82**, 2775-2783 (2002). https://doi.org/10.1016/s0006-3495(02)75618-x

22 Betzig, E. *et al.* Imaging Intracellular Fluorescent Proteins at Nanometer Resolution. *Science (New York, N.Y.)* **313**, 1642-1645 (2006). https://doi.org/doi:10.1126/science.1127344

23 Rust, M. J., Bates, M. & Zhuang, X. Sub-diffraction-limit imaging by stochastic optical reconstruction microscopy (STORM). *Nature Methods* **3**, 793-796 (2006). https://doi.org/10.1038/nmeth929

24 Heilemann, M. *et al.* Subdiffraction-Resolution Fluorescence Imaging with Conventional Fluorescent Probes. *Angewandte Chemie International Edition* **47**, 6172-6176 (2008). https://doi.org/https://doi.org/10.1002/anie.200802376

25 Sharonov, A. & Hochstrasser, R. M. Wide-field subdiffraction imaging by accumulated binding of diffusing probes. *Proceedings of the National Academy of Sciences* **103**, 18911-18916 (2006). https://doi.org/doi:10.1073/pnas.0609643104

26 Balzarotti, F. *et al.* Nanometer resolution imaging and tracking of fluorescent molecules with minimal photon fluxes. *Science (New York, N.Y.)* **355**, 606-612 (2017). https://doi.org/doi:10.1126/science.aak9913

27 Watson, J. D. & Crick, F. H. C. Molecular Structure of Nucleic Acids: A Structure for Deoxyribose Nucleic Acid. *Nature* **171**, 737-738 (1953). https://doi.org/10.1038/171737a0

28 Jungmann, R. *et al.* Single-Molecule Kinetics and Super-Resolution Microscopy by Fluorescence Imaging of Transient Binding on DNA Origami. *Nano Letters* **10**, 4756-4761 (2010). https://doi.org/10.1021/nl103427w

29 Schnitzbauer, J., Strauss, M. T., Schlichthaerle, T., Schueder, F. & Jungmann, R. Super-resolution microscopy with DNA-PAINT. *Nature Protocols* **12**, 1198-1228 (2017). https://doi.org/10.1038/nprot.2017.024

30 Ovesný, M., Křížek, P., Borkovec, J., Švindrych, Z. & Hagen, G. M. ThunderSTORM: a comprehensive ImageJ plug-in for PALM and STORM data analysis and super-resolution imaging. *Bioinformatics* **30**, 2389-2390 (2014). https://doi.org/10.1093/bioinformatics/btu202

31 Huang, B., Wang, W., Bates, M. & Zhuang, X. Three-Dimensional Super-Resolution Imaging by Stochastic Optical Reconstruction Microscopy. *Science (New York, N.Y.)* **319**, 810-813 (2008). https://doi.org/doi:10.1126/science.1153529

32 Jungmann, R. *et al.* Multiplexed 3D cellular super-resolution imaging with DNA-PAINT and Exchange-PAINT. *Nature Methods* **11**, 313-318 (2014). https://doi.org/10.1038/nmeth.2835

33 Unterauer, E. M. *et al.* Spatial proteomics in neurons at single-protein resolution. *bioRxiv*, 2023.2005.2017.541210 (2023). https://doi.org/10.1101/2023.05.17.541210

34 Jungmann, R. *et al.* Quantitative super-resolution imaging with qPAINT. *Nature Methods* **13**, 439-442 (2016). https://doi.org/10.1038/nmeth.3804

35 Cramer, K., Reinhardt, S. C. M., Auer, A., Shin, J. Y. & Jungmann, R. Comparing divisome organization between vegetative and sporulating Bacillus subtilis at the nanoscale using DNA-PAINT. *Science Advances* **10**, eadk5847 (2024). https://doi.org/doi:10.1126/sciadv.adk5847

36 Strauss, S. & Jungmann, R. Up to 100-fold speed-up and multiplexing in optimized DNA-PAINT. *Nature Methods* **17**, 789-791 (2020). https://doi.org/10.1038/s41592-020-0869-x

37 Silhavy, T. J., Kahne, D. & Walker, S. The bacterial cell envelope. *Cold Spring Harb Perspect Biol* **2**, a000414 (2010). https://doi.org/10.1101/cshperspect.a000414

38 MacDermott-Opeskin, H. I., Gupta, V. & O'Mara, M. L. Lipid-mediated antimicrobial resistance: a phantom menace or a new hope? *Biophys Rev* **14**, 145-162 (2022). https://doi.org/10.1007/s12551-021-00912-8

39 Browne, H. P. *et al.* Culturing of 'unculturable' human microbiota reveals novel taxa and extensive sporulation. *Nature* **533**, 543-546 (2016). https://doi.org/10.1038/nature17645

40 Carroll, K. C. *et al.* in *Jawetz, Melnick, & Adelberg's Medical Microbiology, 27e* (McGraw-Hill Education, 2019).
41 Sharpe Michaela, E., Hauser Philippe, M., Sharpe Robert, G. & Errington, J. Bacillus subtilis Cell Cycle as Studied by Fluorescence Microscopy: Constancy of Cell Length at Initiation of DNA Replication and Evidence for Active Nucleoid Partitioning. *Journal of bacteriology* **180**, 547-555 (1998). https://doi.org/10.1128/jb.180.3.547-555.1998
42 Bi, E. F. & Lutkenhaus, J. FtsZ ring structure associated with division in Escherichia coli. *Nature* **354**, 161-164 (1991). https://doi.org/10.1038/354161a0
43 Wang, X. & Lutkenhaus, J. The FtsZ protein of Bacillus subtilis is localized at the division site and has GTPase activity that is dependent upon FtsZ concentration. *Molecular microbiology* **9**, 435-442 (1993). https://doi.org/10.1111/j.1365-2958.1993.tb01705.x
44 Yang, X. *et al.* GTPase activity-coupled treadmilling of the bacterial tubulin FtsZ organizes septal cell wall synthesis. *Science (New York, N.Y.)* **355**, 744-747 (2017). https://doi.org/10.1126/science.aak9995
45 Gamba, P., Veening, J. W., Saunders, N. J., Hamoen, L. W. & Daniel, R. A. Two-step assembly dynamics of the Bacillus subtilis divisome. *Journal of bacteriology* **191**, 4186-4194 (2009). https://doi.org/10.1128/jb.01758-08
46 Squyres, G. R. *et al.* Single-molecule imaging reveals that Z-ring condensation is essential for cell division in Bacillus subtilis. *Nat Microbiol* **6**, 553-562 (2021). https://doi.org/10.1038/s41564-021-00878-z
47 Bisson-Filho, A. W. *et al.* Treadmilling by FtsZ filaments drives peptidoglycan synthesis and bacterial cell division. *Science (New York, N.Y.)* **355**, 739-743 (2017). https://doi.org/10.1126/science.aak9973
48 Whitley, K. D. *et al.* Peptidoglycan synthesis drives a single population of septal cell wall synthases during division in Bacillus subtilis. *Nature Microbiology* **9**, 1064-1074 (2024). https://doi.org/10.1038/s41564-024-01650-9
49 Ben-Yehuda, S. & Losick, R. Asymmetric cell division in B. subtilis involves a spiral-like intermediate of the cytokinetic protein FtsZ. *Cell* **109**, 257-266 (2002). https://doi.org/10.1016/s0092-8674(02)00698-0
50 Eswaramoorthy, P. *et al.* Asymmetric division and differential gene expression during a bacterial developmental program requires DivIVA. *PLoS Genet* **10**, e1004526 (2014). https://doi.org/10.1371/journal.pgen.1004526
51 Wu, L. J. & Errington, J. Coordination of cell division and chromosome segregation by a nucleoid occlusion protein in Bacillus subtilis. *Cell* **117**, 915-925 (2004). https://doi.org/10.1016/j.cell.2004.06.002
52 Wu, L. J. *et al.* Noc protein binds to specific DNA sequences to coordinate cell division with chromosome segregation. *Embo j* **28**, 1940-1952 (2009). https://doi.org/10.1038/emboj.2009.144
53 Errington, J. & Wu, L. J. Cell Cycle Machinery in Bacillus subtilis. *Subcell Biochem* **84**, 67-101 (2017). https://doi.org/10.1007/978-3-319-53047-5_3
54 Eswaramoorthy, P. *et al.* Cellular architecture mediates DivIVA ultrastructure and regulates min activity in Bacillus subtilis. *mBio* **2** (2011). https://doi.org/10.1128/mBio.00257-11
55 Patrick, J. E. & Kearns, D. B. MinJ (YvjD) is a topological determinant of cell division in Bacillus subtilis. *Molecular microbiology* **70**, 1166-1179 (2008). https://doi.org/https://doi.org/10.1111/j.1365-2958.2008.06469.x
56 Bramkamp, M. *et al.* A novel component of the division-site selection system of Bacillus subtilis and a new mode of action for the division inhibitor MinCD. *Molecular microbiology* **70**, 1556-1569 (2008). https://doi.org/10.1111/j.1365-2958.2008.06501.x
57 Biteen, J. S. *et al.* Super-resolution imaging in live Caulobacter crescentus cells using photoswitchable EYFP. *Nat Methods* **5**, 947-949 (2008). https://doi.org/10.1038/nmeth.1258

58 Greenfield, D. *et al.* Self-organization of the Escherichia coli chemotaxis network imaged with super-resolution light microscopy. *PLoS Biol* **7**, e1000137 (2009). https://doi.org/10.1371/journal.pbio.1000137
59 Fu, G. *et al.* In vivo structure of the E. coli FtsZ-ring revealed by photoactivated localization microscopy (PALM). *PLoS One* **5**, e12682 (2010). https://doi.org/10.1371/journal.pone.0012680
60 Dyba, M. & Hell, S. W. Photostability of a fluorescent marker under pulsed excited-state depletion through stimulated emission. *Appl Opt* **42**, 5123-5129 (2003). https://doi.org/10.1364/ao.42.005123
61 Jennings, P. C., Cox, G. C., Monahan, L. G. & Harry, E. J. Super-resolution imaging of the bacterial cytokinetic protein FtsZ. *Micron* **42**, 336-341 (2011). https://doi.org/10.1016/j.micron.2010.09.003
62 Carsten, A. *et al.* MINFLUX imaging of a bacterial molecular machine at nanometer resolution. *Methods and Applications in Fluorescence* **11**, 015004 (2023). https://doi.org/10.1088/2050-6120/aca880
63 Coltharp, C. & Xiao, J. Superresolution microscopy for microbiology. *Cell Microbiol* **14**, 1808-1818 (2012). https://doi.org/10.1111/cmi.12024
64 Strauss, M. P. *et al.* 3D-SIM super resolution microscopy reveals a bead-like arrangement for FtsZ and the division machinery: implications for triggering cytokinesis. *PLoS Biol* **10**, e1001389 (2012). https://doi.org/10.1371/journal.pbio.1001389
65 Stockmar, I. *et al.* Optimization of sample preparation and green color imaging using the mNeonGreen fluorescent protein in bacterial cells for photoactivated localization microscopy. *Sci Rep* **8**, 10137 (2018). https://doi.org/10.1038/s41598-018-28472-0
66 *abberior STAR 635P*, <https://abberior.shop/abberior-STAR-635P> (2024).
67 *Product Information: ATTO 647N*, <https://www.atto-tec.com/fileadmin/user_upload/Katalog_Flyer_Support/ATTO_647N.pdf> (2024).
68 *ATTO 594*, <https://www.atto-tec.com/ATTO-594.html?language=en#:~:text=ATTO%20594%20is%20a%20novel,stability%2C%20and%20excellent%20water%20solubility.> (2021).
69 Feddersen, H., Würthner, L., Frey, E. & Bramkamp, M. Dynamics of the Bacillus subtilis Min System. *mBio* **12** (2021). https://doi.org/10.1128/mBio.00296-21
70 Rowlett, V. W. & Margolin, W. 3D-SIM super-resolution of FtsZ and its membrane tethers in Escherichia coli cells. *Biophys J* **107**, L17-l20 (2014). https://doi.org/10.1016/j.bpj.2014.08.024
71 Söderström, B., Chan, H. & Daley, D. O. Super-resolution images of peptidoglycan remodelling enzymes at the division site of Escherichia coli. *Current Genetics* **65**, 99-101 (2019). https://doi.org/10.1007/s00294-018-0869-x
72 Graham, L. L. & Beveridge, T. J. Structural differentiation of the Bacillus subtilis 168 cell wall. *Journal of bacteriology* **176**, 1413-1421 (1994). https://doi.org/doi:10.1128/jb.176.5.1413-1421.1994
73 Jamur, M. C. & Oliver, C. Permeabilization of cell membranes. *Methods Mol Biol* **588**, 63-66 (2010). https://doi.org/10.1007/978-1-59745-324-0_9
74 Khanna, K., Lopez-Garrido, J., Sugie, J., Pogliano, K. & Villa, E. Asymmetric localization of the cell division machinery during Bacillus subtilis sporulation. *Elife* **10** (2021). https://doi.org/10.7554/eLife.62204
75 Lelek, M. *et al.* Single-molecule localization microscopy. *Nature Reviews Methods Primers* **1**, 39 (2021). https://doi.org/10.1038/s43586-021-00038-x
76 Wu, L. J., Lewis, P. J., Allmansberger, R., Hauser, P. M. & Errington, J. A conjugation-like mechanism for prespore chromosome partitioning during sporulation in Bacillus subtilis. *Genes Dev* **9**, 1316-1326 (1995). https://doi.org/10.1101/gad.9.11.1316

77 Illing, N. & Errington, J. Genetic regulation of morphogenesis in Bacillus subtilis: roles of sigma E and sigma F in prespore engulfment. *Journal of bacteriology* **173**, 3159-3169 (1991). https://doi.org/10.1128/jb.173.10.3159-3169.1991
78 Thorn, K. Genetically encoded fluorescent tags. *Mol Biol Cell* **28**, 848-857 (2017). https://doi.org/10.1091/mbc.E16-07-0504
79 Mohammadi, T. *et al.* The GTPase activity of Escherichia coli FtsZ determines the magnitude of the FtsZ polymer bundling by ZapA in vitro. *Biochemistry* **48**, 11056-11066 (2009). https://doi.org/10.1021/bi901461p
80 Duman, R. *et al.* Structural and genetic analyses reveal the protein SepF as a new membrane anchor for the Z ring. *Proceedings of the National Academy of Sciences of the United States of America* **110**, E4601-E4610 (2013). https://doi.org/10.1073/pnas.1313978110
81 Gueiros-Filho, F. J. & Losick, R. A widely conserved bacterial cell division protein that promotes assembly of the tubulin-like protein FtsZ. *Genes Dev* **16**, 2544-2556 (2002). https://doi.org/10.1101/gad.1014102
82 Pogliano, J. *et al.* A vital stain for studying membrane dynamics in bacteria: a novel mechanism controlling septation during Bacillus subtilis sporulation. *Molecular microbiology* **31**, 1149-1159 (1999). https://doi.org/10.1046/j.1365-2958.1999.01255.x
83 Pende, N. *et al.* SepF is the FtsZ anchor in archaea, with features of an ancestral cell division system. *Nat Commun* **12**, 3214 (2021). https://doi.org/10.1038/s41467-021-23099-8
84 Wenzel, M. *et al.* Control of septum thickness by the curvature of SepF polymers. *Proc Natl Acad Sci U S A* **118** (2021). https://doi.org/10.1073/pnas.2002635118
85 Barák, I. & Youngman, P. SpoIIE mutants of Bacillus subtilis comprise two distinct phenotypic classes consistent with a dual functional role for the SpoIIE protein. *Journal of bacteriology* **178**, 4984-4989 (1996). https://doi.org/10.1128/jb.178.16.4984-4989.1996
86 Lenarcic, R. *et al.* Localisation of DivIVA by targeting to negatively curved membranes. *Embo j* **28**, 2272-2282 (2009). https://doi.org/10.1038/emboj.2009.129
87 Schäper, S. *et al.* Cell constriction requires processive septal peptidoglycan synthase movement independent of FtsZ treadmilling in Staphylococcus aureus. *Nature Microbiology* **9**, 1049-1063 (2024). https://doi.org/10.1038/s41564-024-01629-6
88 Tra, V. N. & Dube, D. H. Glycans in pathogenic bacteria – potential for targeted covalent therapeutics and imaging agents. *Chemical Communications* **50**, 4659-4673 (2014). https://doi.org/10.1039/C4CC00660G
89 van den Dries, K., Fransen, J. & Cambi, A. Fluorescence CLEM in biology: historic developments and current super-resolution applications. *FEBS Lett* **596**, 2486-2496 (2022). https://doi.org/10.1002/1873-3468.14421
90 Jumper, J. *et al.* Highly accurate protein structure prediction with AlphaFold. *Nature* **596**, 583-589 (2021). https://doi.org/10.1038/s41586-021-03819-2
91 Lower, S. K. *et al.* A tactile response in Staphylococcus aureus. *Biophys J* **99**, 2803-2811 (2010). https://doi.org/10.1016/j.bpj.2010.08.063
92 Foster, T. J. The MSCRAMM Family of Cell-Wall-Anchored Surface Proteins of Gram-Positive Cocci. *Trends Microbiol* **27**, 927-941 (2019). https://doi.org/10.1016/j.tim.2019.06.007